

HZDR

 **HELMHOLTZ**
ZENTRUM DRESDEN
ROSSENDORF

 **TECHNISCHE
UNIVERSITÄT
DRESDEN**

Morphology-Induced Magnetic Phenomena Studied by Broadband Ferromagnetic Resonance

DISSERTATION

Zur Erlangung des akademischen Grades

Doctor rerum naturalium

(Dr. rer. nat.)

vorgelegt

der Fakultät Mathematik und Naturwissenschaften
der Technischen Universität Dresden

von

Michael Körner

geboren am 18.08.1982 in Wismar

Eingereicht am 07.05.2013

Die Dissertation wurde in der Zeit von 01/2009 bis 05/2013 im Institut
für Ionenstrahlphysik und Materialforschung am Helmholtz-Zentrum
Dresden-Rossendorf e. V. angefertigt.

1. Gutachter: Prof. Dr. J. Faßbender, Helmholtz-Zentrum Dresden-Rossendorf e. V.
 2. Gutachter: Prof. Dr. J. Wosnitza, Helmholtz-Zentrum Dresden-Rossendorf e. V.
- Datum der Verteidigung: 02.09.2013

Abstract

In the present work, the influence of the morphology of thin ferromagnetic films on their static as well as dynamic magnetic properties was investigated by means of broadband ferromagnetic resonance (FMR). Using an ion beam erosion process the surface of the substrates was periodically modulated (ripples), where the modulation wavelength is determined by the ion energy. In this way a well-controllable roughness profile evolves ranging from a few ten up to several hundreds of nanometers in wavelength. The substrate's surface profile in turn is repeated by films grown on top offering an easy and fast approach to investigate morphology influences on the magnetic properties. This work aims on modifications of the magnetic anisotropy as well as the FMR linewidth of the magnetic relaxation process.

Prior to magnetic investigations the existing FMR setup was extended to measure FMR spectra at a fixed microwave frequency while sweeping the external magnetic field. Furthermore, a software toolbox was developed to perform the data processing and evaluation.

Starting with the morphology influence on the magnetic anisotropy 10 nm thin Fe, Co, and Ni₈₁Fe₁₉ (Permalloy \equiv Py) films were deposited on rippled Si substrates. Due to Si displacements during ion erosion and natural oxidation the rippled Si substrates exhibit an amorphous surface causing a polycrystalline material growth. This leads to a suppression of magneto-crystalline anisotropy leaving only morphology-induced anisotropy contributions. Here, a uniaxial magnetic anisotropy (UMA) was observed that aligns its easy axis with the ripple ridges, whereas its strength decays with increasing ripple wavelength for all materials. From thickness-dependent measurements two characteristic regions were determined with competing uniaxial volume and surface anisotropy contributions. Underlined by micromagnetic simulations a dominant volume contribution was found in the thin region accompanied by magnetic moments nearly following the surface corrugation. In the thick region the UMA is controlled by dipolar stray fields at the surface.

In contrast to Si, ion eroded MgO keeps its crystal structure offering epitaxial growth of 10 nm thin single-crystalline Fe films. Consequently, a superposition of morphology-induced UMA and magneto-crystalline cubic anisotropy was observed. The direction of the ripple ridges is predetermined by the incident ion beam, which allows to freely orient the UMA's direction with respect to the cubic anisotropy, offering a possibility for anisotropy engineering. In comparison to the planar reference case rippled magnetic films exhibit lower intrinsic and extrinsic relaxation contributions.

For the final part, 30 nm Py was grown on rippled Si covering modulation wavelengths λ ranging from 27 to 432 nm. Using magnetic force microscopy and holography measurements the dipolar stray fields above and inside the magnetic layer were characterized. For $\lambda \geq 222$ nm, the stray fields act as scattering centers for spin waves triggering two-magnon scattering (TMS).

This causes an apparent line broadening generating distinct peaks in the frequency-dependent linewidth whose position can be tuned by altering λ . These effects are understood in the framework of a perturbation theory of spin waves in periodically perturbed films recently presented in the literature. Furthermore, the in-plane angular dependence of the linewidth revealed a two-fold symmetry, which is not present for vanishing TMS at small λ .

Kurzfassung

In Rahmen dieser Arbeit wurde der Einfluss der Morphologie eines dünnen ferromagnetischen Films auf dessen statische und dynamische Eigenschaften mittels breitbandiger ferromagnetischer Resonanz (FMR) untersucht. Durch Ionenstrahl-Erosion wurde die Oberfläche des verwendeten Substrats periodisch moduliert (Ripple), wobei die Wellenlänge der Modulation durch die Ionenenergie bestimmt ist. Dies ermöglicht die kontrollierte Herstellung rauher Oberflächen mit Wellenlängen zwischen wenigen zehn bis zu einigen hundert Nanometern. Werden auf diesen Oberflächen Filme abgeschieden, übernehmen diese die Modulation. Somit ergibt sich eine einfache und schnelle Untersuchungsmöglichkeit der magnetischen Filmeigenschaften in Hinblick auf die Morphologie. Das Ziel dieser Arbeit ist die Untersuchung von Morphologieeinflüssen auf die magnetische Anisotropie sowie FMR-Linienbreite.

Im Vorfeld der magnetischer Untersuchungen wurde der bestehende FMR-Aufbau um einen Messmodus erweitert, sodass Messungen bei fester Mikrowellenfrequenz und gleichzeitigem Durchfahren eines externen magnetischen Feldes möglich wurden. Weiterhin wurde ein Softwarepaket für die Datenauswertung entwickelt.

Beginnend mit dem Morphologieeinfluss auf die magnetische Anisotropie wurden 10 nm dünne Fe, Co und $\text{Ni}_{81}\text{Fe}_{19}$ (Permalloy \equiv Py) Filme auf periodisch moduliertem Si abgeschieden. Durch Versetzungen während der Ionenstrahl-Erosion und Bildung einer natürlichen Oxidschicht bildet sich bei den verwendeten Substraten eine amorphe Oberfläche, was zu polykristallinem Schichtwachstum führt. Dadurch wird die magneto-kristalline Anisotropie unterdrückt und morphologie-induzierte Beiträge bestimmen die Anisotropie. Beobachtet wurde eine induzierte uniaxiale magnetische Anisotropie (UMA), deren leichte Richtung sich entlang der Ripple-Wellenzüge ausrichtet. Mittels schichtdickenabhängigen Messungen wurden zwei charakteristische Regionen mit konkurrierender uniaxialer Volumen- und Oberflächenanisotropie ermittelt. Dabei ist die Volumenkomponente im Bereich dünner Schichten vorherrschend und die magnetischen Momente richten sich entlang der Oberflächenmodulation aus. Für dickere Schichten ist die UMA dahingegen durch dipolare Streufelder bestimmt. Die experimentellen Funde werden in beiden Bereichen durch mikromagnetische Simulationen untermauert.

Im Gegensatz zu erodiertem Si behält MgO seine Kristallstruktur, was epitaktisch gewachsene, einkristalline Fe-Schichten von 10 nm Dicke ermöglicht. Folglich wurde eine Überlagerung aus induzierter und kristalliner Anisotropie beobachtet. Dadurch, dass die Richtung der Ripple durch die Richtung des Ionenstrahls während der Erosion vorgegeben wird, lässt

sich die UMA frei gegen die kristalline Anisotropie drehen, was wiederum Möglichkeiten zur gezielten Beeinflussung der Anisotropie bietet. Im Hinblick auf die dynamischen magnetischen Eigenschaften führen Ripple zu einer Verringerung der intrinsischen und extrinsischen Relaxationsbeiträge.

Für den letzten Teil der Arbeit wurde 30 nm dünnes Py auf Si-Ripple gewachsen, wobei ein Wellenlängenbereich von $\lambda = 27$ nm bis 432 nm abgedeckt wurde. Mit Hilfe von magnetischer Kraftmikroskopie und Holographie wurden die dipolaren Streufelder über und in den Filmen untersucht. Ab $\lambda \geq 222$ nm ermöglichen diese dipolaren Felder eine Streuung von Spinwellen, sodass Zwei-Magnonen-Streuung (TMS) auftritt. Dies führt zu einer scheinbaren Linienverbreiterung und äußert sich durch einzelne Peaks in der frequenzabhängigen Linienbreite. Letztere lassen sich in ihrer Frequenzposition durch die Wellenlänge des Substrates beeinflussen und können mittels einer kürzlich in der Literatur veröffentlichten Störungstheorie für Spinwellen in periodisch gestörten Filmen erklärt werden. Weiterhin wurde in der winkelabhängigen Linienbreite eine zweifache Symmetrie beobachtet, welche durch die TMS hervorgerufen wird und folglich nicht bei kleinen Wellenlängen zu beobachten ist.

Contents

Abstract	iii
Kurzfassung	v
1 Introduction	1
2 Fundamentals	5
2.1 Magnetic anisotropy	5
2.1.1 Magnetic interactions	6
2.1.2 Phenomenological description	8
2.2 Magnetization dynamics	14
2.2.1 Equation of motion	14
2.2.2 Resonance condition and dynamic susceptibility	17
2.2.3 Spin waves	20
2.3 Magnetic relaxation	25
2.3.1 Phenomenological description	26
2.3.2 Physical origin of intrinsic processes	27
2.3.3 Extrinsic contributions — Two-magnon scattering	29
2.4 Ion beam erosion	34
3 Ferromagnetic resonance	37
3.1 Cavity-based FMR	38
3.2 Vector network analyzer FMR	40
3.2.1 Coplanar waveguide	40
3.2.2 Vector network analysis	41
3.2.3 Experimental setup	43
3.3 VNA-FMR operation modes	45
3.3.1 Frequency-sweep VNA-FMR	46
3.3.2 Field-sweep VNA-FMR	50
3.3.3 Influence of stripline measurements	55

4	Morphology-induced magnetic uniaxial anisotropy in polycrystalline thin films	61
4.1	Sample preparation and characterization	62
4.1.1	Preparation procedure	62
4.1.2	Basics of surface characterization	64
4.1.3	Substrate characterization	66
4.2	Induced uniaxial magnetic anisotropy	69
4.3	Thickness dependence of the induced UMA	73
4.3.1	Thickness-dependent magnetization reversal	73
4.3.2	Micromagnetic simulations	75
4.3.3	Thickness evolution of the anisotropy	79
5	Epitaxial iron on ion beam eroded single-crystalline substrates	83
5.1	Sample structure	85
5.2	VNA-FMR investigations	89
5.2.1	Direction-dependent g -factor	90
5.2.2	In-plane anisotropy	91
5.3	FMR linewidth	99
6	Extrinsic control of magnetic properties in NiFe thin films	103
6.1	Perturbation theory	104
6.2	Substrate characterization	110
6.3	Dipolar stray field observation	111
6.3.1	Lamella preparation	113
6.3.2	Sample structure at high wavelengths	114
6.3.3	Fields above and inside the magnetic layer	118
6.4	Ripple-induced two-magnon scattering	124
7	Summary and outlook	139
A	Software toolbox for FMR data evaluation	145
	Bibliography	153
	Publications	171
	Acknowledgments	175

1 Introduction

Over the past decades magnetism has attracted growing attention in research and technology and has become an integral part of our daily life. In almost every area applications rely on the unique properties of ferromagnetic materials. To name but a few fields, magnetic materials are present in telecommunication, sensors, electric motors, medical imaging, energy supply, or in information technology in general [1, 2]. In the latter, for decades only the charge property of electrons was used to build logic circuits and process information, while magnetic materials were applied for nonvolatile data storage. However, since electrons carry not only a charge but also a magnetic momentum (caused by its spin), new possibilities arise by combining these two degrees of freedom in a new research field called spintronics [3, 4]. As prominent examples the giant magneto-resistance [5] or the interlayer exchange coupling [6] may be mentioned. Furthermore, considering the spin offers new directions to circumvent scaling limits in present technology that are arising in charge-only based electronics [7, 8] as well as to implement new data storage concepts like magnetic random access memory [4, 9].

Independently of the purpose, in nearly all these new applications thin magnetic films or even patterned magnetic elements play a crucial role. With ongoing miniaturization the spatial limitations of the magnetic volume in turn increases the importance of the bordering interface or edge effects of confined magnetic structures by approaching intrinsic magnetic length scales such as exchange length or domain wall width [10]. Accordingly, questions arise concerning the role of the interface and associated roughness. Among others, the technological importance of magnetism as well as basic research interests in general lead to widely spread activities on this topic dealing for example with the influence of roughness on the static magnetic properties in single magnetic layers [11–16] and multilayer stacks [17–21], as well as the roughness impact on the magnetization dynamics [22–24]. Summarizing the roughness influence, dipolar magnetic fields are most important since they influence the ferromagnet’s energetic configuration—and hence the ground state—as well as mediate coupling between magnetic elements [25, 26] and different spin wave modes in the magnetization dynamics [22].

From the wide area of research topics magnetic anisotropy as well as the relaxation behavior are possibly the most prominent ones, since the first determines the spatial orientation of the magnetization [27] and the latter for example the switching speed in magnetization reversal processes [28]. Controlling these properties opens the possibility for artificially tailoring the

static and dynamic magnetic behavior.

The aim of this thesis is to study the roughness effects, mediated by dipolar fields, with respect to magnetic anisotropy and magnetization dynamics. Furthermore, the surface roughness is used to specifically tailor both properties extrinsically. As main experimental technique broadband ferromagnetic resonance (FMR) [29] was used giving direct access to both properties simultaneously.

To correlate the magnetic properties with roughness effects, a well-defined method is mandatory modulating the interface of a magnetic film. Since electron lithography patterning [30] is quite time consuming and not suitable for large-area manipulation a self-organized approach based on ion beam erosion was used. Starting from a planar substrate ion beam erosion leads to a periodic surface pattern (ripple) exhibiting a well-defined surface roughness [31]. In addition, the periodicity of the pattern, given by the wavelength λ , is simply set by the ion energy, and thus, scalable over a wide range starting at a few nanometers and ranging to several hundreds [32]. Magnetic films grown on top take over the surface corrugation of the substrate, and thus, exhibit two modulated interfaces [33], which increases the roughness contribution to the magnetic properties. In contrast to approaches eroding the ferromagnetic layer directly [34,35] the film thickness is much better controllable and the roughness quality can be determined prior to the film growth. Furthermore, the crystal structure of the eroded substrate can be used to predetermine the structure of the grown layer and specifically induce or suppress magneto-crystalline anisotropy contributions. In this way the substrate's roughness is used in the present work to determine the role of evolving dipolar fields and to tailor the magnetic anisotropy as well as relaxation behavior extrinsically. A detailed review on the state of the art in research will be given at the beginning of every experimental chapter.

The thesis is divided into five main chapters. Starting with the theoretical backgrounds in Chapter 2, the basics of magnetic anisotropy, magnetization dynamics and accompanied relaxation processes, as well as the sputter erosion process are reviewed. Since the investigations performed made it necessary to implement a broadband FMR setup operating in field-sweep mode Chapter 3 aims on FMR techniques by comparing classical cavity setups with the currently applied stripline technique. The latter in turn can be operated in two modes (field or frequency sweep), where a comparison reveals the mode most suitable for the purpose of this work. Additionally, the stripline geometry requires a discussion with respect to influences on the acquired data.

In the first experimental part, Chapter 4, ion eroded Si substrates are used as templates for growing magnetic materials. There the focus is initially set on the substrate properties using atomic force microscopy (AFM) before the magnetic properties are discussed. The investigated

magnetic materials exhibit a polycrystalline structure and thus allow to study the evolving uniaxial magnetic anisotropy (UMA) as a function of film thickness and ripple wavelength (up to 90 nm) by suppressing intrinsic magnetic anisotropies. Finally, the UMA is correlated with dipolar fields created by the roughness.

In a next step, Fe is epitaxially grown on rippled MgO substrates, which is presented in Chapter 5. Due to the epitaxial relation the magneto-crystalline anisotropy is combined with the uniaxial one creating a model system to tailor magnetic anisotropies. In this framework, the magnetic relaxation is analyzed with respect to influences caused by the ripple morphology.

Finally, in Chapter 6 the influence of long-wavelength rippled Si substrates (λ up to 432 nm) on the magnetization dynamics of Ni₈₁Fe₁₉ (Permalloy \equiv Py) is discussed. Starting point is the theory of spin waves in periodically disturbed magnetic films presented by Landeros and Mills aiming on surface stripe defects. These defects create periodic dipolar fields and by this enable spin wave scattering. To confirm the existence of these fields in rippled magnetic films magnetic force microscopy (MFM) measurements were performed imaging the dipolar stray fields above the sample as well as holography measurements to access the fields in a cross-sectional view. The results are compared with micromagnetic simulations and used to adapt the model of Landeros and Mills to the case of rippled perturbations.

The scientific part of the thesis closes with a summary and an outlook and is followed by an appendix describing the developed software tools, used to evaluate the FMR measurements.

All calculations and equations in this work are based on the SI unit system. Vectors are printed in bold type and scalars in italics.

2 Fundamentals

Within this chapter fundamental concepts of magnetic anisotropy, magnetization dynamics and relaxation, as well as for ion beam erosion will be introduced. Presented calculations are based on a spherical coordinate system, as depicted in Fig. 2.1. All azimuthal angles are counted from the [100] direction and are denoted by φ_i . In contrast, polar angles are represented by θ_i , counted from the surface's normal [001]. The subscript i accounts either for the external magnetic field \mathbf{H} ($i = H$), an in-plane uniaxial anisotropy ($i = u$), or vanishes in case of the magnetization \mathbf{M} . To express vectors with respect to the [100] orientation, the normalized direction cosines

$$\alpha_x = \sin \theta \cos \varphi, \quad \alpha_y = \sin \theta \sin \varphi, \quad \alpha_z = \cos \theta \quad (2.1)$$

are used.

2.1 Magnetic anisotropy

Below a critical temperature, the Curie temperature T_C , ferromagnetic materials exhibit a spontaneous collective ordering of its permanent magnetic moments μ_i . These moments are formed by the spin and orbital momentum of the electrons and average over the volume V

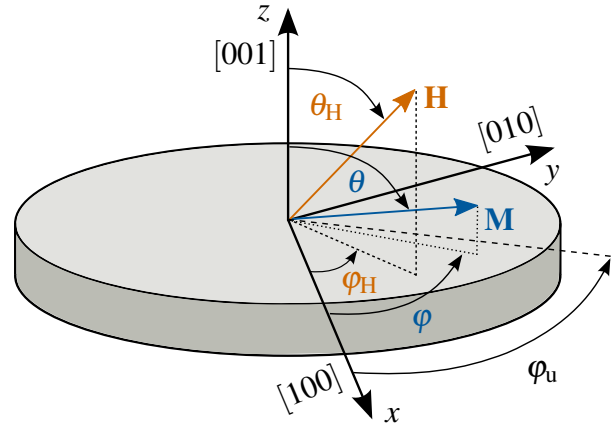


Figure 2.1: Spherical coordinate system containing magnetization \mathbf{M} , external magnetic field \mathbf{H} , and an in-plane uniaxial anisotropy direction φ_u .

to the sample's magnetization $\mathbf{M} = \sum \boldsymbol{\mu}_i/V$. The orientation of \mathbf{M} within the sample shows energetically favorable directions, the easy axes (minimal energy), and non-favorable ones named hard axes (maximum energy). This directional dependence of the magnetization is called magnetic anisotropy. The energy needed to change \mathbf{M} from an easy axis alignment into another direction, e. g. by applying an external magnetic field \mathbf{H} , is denoted as magnetic anisotropy energy. To describe the response of the magnetization to an external magnetic field the sum of all energetic contributions, the total magnetic energy E_{tot} of the system, has to be taken into consideration. In a single ferromagnetic layer it mainly depends on anisotropy, exchange interaction, and the interaction with an external field. The magnetic anisotropy is affected by the crystal structure and the sample shape. Further anisotropy contributions, e. g. induced by stress (magnetostriction), are negligible in this work. In order to modify anisotropic behavior in magnetic films a detailed understanding of the underlying processes as well as a suitable model for analytical description is required. Subsequently, the physical origins of the collective ordering and its anisotropic behavior as well as a phenomenological description of anisotropy will be discussed.

2.1.1 Magnetic interactions

Exchange interaction

The exchange interaction gives rise to the collective ordering in magnetic materials. It is of quantum mechanical nature and in its simplest form a direct overlap of the wave functions of localized electrons with spins \mathbf{s}_i will be considered. As a result of the generalized Pauli principle (antisymmetric overall wave function $|\Psi\rangle$), together with the electron's Coulomb repulsion, the corresponding Hamiltonian is equivalent to an effective spin-spin interaction

$$\hat{H}_{\text{exch}} = -2 \sum_{i < j} J_{ij} \mathbf{s}_i \cdot \mathbf{s}_j \quad (2.2)$$

and gives rise to the exchange energy $E_{\text{exch}} = \langle \Psi | \hat{H}_{\text{exch}} | \Psi \rangle$. Here, J_{ij} is the exchange integral describing the overlap in wave functions of the i -th with the j -th spin. An antiparallel alignment is obtained for $J_{ij} < 0$ whereas $J_{ij} > 0$ aligns neighboring spins parallel. In the magnetic materials Fe, Ni, and Co the magnetism is determined by the spin momentum of the delocalized $3d$ electrons. In this case an indirect exchange has to be considered that leads to itinerant magnetism [36].

However, the scalar product of $\mathbf{s}_i \cdot \mathbf{s}_j$ is invariant with respect to the choice of the coordinate system. Hence, the spin-spin exchange energy is isotropic in space and does not contribute to the magnetic anisotropy. Instead, the symmetry breaking, shown by van Vleck [37], is caused by relativistic corrections to the Hamiltonian modeling the magnetic system. These are on the

one hand dipole-dipole and spin-orbit interactions on the other hand. Both contribute to a quite small correction (three up to four orders of magnitude less than the exchange energy) in the total magnetic energy and lead to the magnetic anisotropy.

Dipole-dipole interaction

With every magnetic moment a dipolar magnetic field H_d is associated. In a classical approach the strength of the dipolar field at a distance \mathbf{r}_i ($|\mathbf{r}_i| = r_i$) from the dipole $\boldsymbol{\mu}_i$ is given by

$$H_d(\mathbf{r}_i) = \frac{\mu_0}{4\pi} \frac{3(\boldsymbol{\mu}_i \cdot \mathbf{r}_i)\mathbf{r}_i - r_i^2 \boldsymbol{\mu}_i}{r_i^5}, \quad (2.3)$$

with μ_0 being the magnetic constant. In an ensemble of magnetic moments dipolar interactions between moments and the field, created by the surrounding moments, occur. By summing up the entire interactions between moments and surrounding fields one finds the classical dipolar energy of the sample by

$$E_{\text{dip}} = \frac{\mu_0}{4\pi} \sum_{i \neq j} \frac{1}{r_{ij}^3} \left(\boldsymbol{\mu}_i \cdot \boldsymbol{\mu}_j - 3 \frac{(\mathbf{r}_{ij} \cdot \boldsymbol{\mu}_i)(\mathbf{r}_{ij} \cdot \boldsymbol{\mu}_j)}{r_{ij}^2} \right), \quad (2.4)$$

where \mathbf{r}_{ij} is the distance between two moments. Note that in case of itinerant electrons carrying the magnetism, e. g. in Fe, Ni, and Co, the dipolar interaction is mediated by a local magnetization density instead of locally fixed moments. A relativistic description covering this case was done by Jansen using density functional theory [38].

Since the dipolar energy in Eq. (2.4) depends on the scalar product of $\boldsymbol{\mu}_i$ with $\boldsymbol{\mu}_j$ it in turn communicates a coupling between these moments. As mentioned above the influence is far below the exchange interaction. Nevertheless, the dipolar interaction is of long-range order causing the sum in Eq. (2.4) to converge slowly. So the dipolar field within the magnetic volume depends strongly on the volume's shape and gives rise to shape anisotropy. For example, inside a magnetic volume with cubic crystal structure dipolar fields at each lattice point are canceled out by neighboring moments. However, in presence of surfaces or interfaces the cancellation vanishes, which leads to emerging magnetic poles and, therefore, an energetic contribution that depends on the shape, called shape anisotropy [27].

If magnetic moments are localized at the atomic sites a multipole expansion of non-spherical magnetization densities leads to a dependence of the dipolar energy with respect to the crystal direction. Hence, the dipolar interaction adds a contribution to the magneto-crystalline anisotropy. Due to symmetry reasons the influence arises for cubic systems from higher orders in the multipole expansion of the magnetization density and is, therefore, negligible [39, 40].

Spin-orbit interaction

An energetically favorable alignment of \mathbf{M} with respect to the sample's crystallographic axes is achieved by coupling the electron's spin with its orbital momentum. The theoretical description relies on Dirac's equation [41], the base equation of relativistic quantum theory that explains the existence of a spin associated with each particle. By expanding the Dirac equation to the limit of low velocities ($v^2/c^2 \ll 1$) a relativistic spin-orbit correction adds to the classical Hamiltonian that reads for a single electron

$$\hat{H}_{LS} = \xi \hat{l} \cdot \hat{s}, \quad (2.5)$$

where \hat{s} and \hat{l} are the operators for the spin and orbital momentum, respectively. ξ is the spin-orbit constant that depends on the potential ϕ_{e^-} , which is seen by the electrons and generated by surrounding charges of electrons and atoms. In a simple classical picture this is understood as correlation between the spin momentum of an electron with the magnetic field created by the electron's movement around the atom. Since the movement is determined by the seen potential ϕ_{e^-} a coupling between spin and crystal lattice is achieved. Hence, the crystal structure and its symmetry influences the magnetic anisotropy, adding a magneto-crystalline anisotropy contribution [40].

2.1.2 Phenomenological description

Energy density

Since the magnetic interactions introduced above are difficult to calculate analytically (e. g. due to many-particle interactions in the Hamiltonian) it is usually more suitable to use a phenomenological description based on the total energy density $\varepsilon_{\text{tot}} = E_{\text{tot}}/V$. According to the introduced magnetic interactions, ε_{tot} is a sum of magneto-crystalline anisotropy density, dipolar energy density (including shape influences), and exchange energy density [42]

$$\varepsilon_{\text{ex}} = \frac{A}{V} \int_V [\nabla \mathbf{m}(\mathbf{r})]^2 dV. \quad (2.6)$$

A , the exchange stiffness constant, is a material parameter describing the spin-spin coupling and depends on temperature and exchange constant J [cf. Eq. (2.2)]. Furthermore, Eq. (2.6) depends on the local direction of the normalized magnetization $\mathbf{m}(\mathbf{r})/M_s$ with M_s being the saturation magnetization. Therefore, ε_{ex} reaches its minimum for locally parallel aligned magnetic moments and increases if magnetic domains are present. Likewise its origin [given in Eq. (2.2)], exchange energy is isotropic in space. In the following, all considerations will be carried out for uniform magnetized samples $\mathbf{M}(\mathbf{r}) = \mathbf{M}$, neglecting domain effects. In this

way the exchange energy reduces to a constant contribution that will be neglected in further discussions. Besides this, the sample temperature is assumed to be well below the Curie temperature to avoid magnetization fluctuations.

If a system with constant particle number and temperature is considered the thermodynamic potential F (free energy density) can be introduced. It describes a change in energy density caused by work W performed on the system to realign the magnetization from an initial to a final state, where $dF = -dW$ applies. $F = F(M_s, \mathbf{e}_M, T, \zeta)$, the difference in total energy density between two states, depends on internal sample parameters such as magnetization magnitude M_s and its direction \mathbf{e}_M , the temperature T , and strain ζ [27, 39, 40]. The latter will be neglected in further discussions. Changing the magnetization's alignment usually is achieved by applying an external magnetic field $\mathbf{H}(\mathbf{r})$, which gives rise to an extrinsic energy density contribution, namely the Zeeman energy density

$$\varepsilon_{Zee} = -\frac{\mu_0}{V} \int_V \mathbf{M} \mathbf{H}(\mathbf{r}) dV \quad (2.7)$$

that favors a parallel alignment of magnetization and external field. This implies $\mathbf{M} = M_s \mathbf{e}_M$ being controlled indirectly by the external field, turning F into an inappropriate thermodynamic potential since the absolute value of \mathbf{M} changes with respect to the external field direction. Instead, Gibbs' free energy density \mathcal{G} , linked to F via the Legendre transformation [43] $\mathcal{G} = F - \mu_0 \mathbf{H} \mathbf{M}$, is the appropriate thermodynamic potential. From the transformation one finds \mathcal{G} being the free energy density F expanded by the Zeeman term [cf. Eq. (2.7) with $\mathbf{H}(\mathbf{r}) = H \mathbf{e}_H$ assumed to be uniform over the sample]. Expressed in polar coordinates using Eq. (2.1) the Zeeman energy density for a uniform magnetized sample in a uniform field is given by:

$$\varepsilon_{Zee} = -\mu_0 M_s H [\sin \theta \sin \theta_H \cos(\varphi - \varphi_H) + \cos \theta \cos \theta_H]. \quad (2.8)$$

However, often F is used instead of \mathcal{G} as symbol for the free energy density including a Zeeman term. In order to avoid confusions with literature F , will be used as symbol throughout the whole thesis.

Shape anisotropy

An analytic expression of the shape-dependent part of F is derived from the dipolar field [Eq. (2.3)] integrated over the whole sample using a continuum approximation, justified by the long-range order of dipolar interaction. In this case, the solution of Maxwell's equations

$$\nabla \times \mathbf{H}_d = 0 \quad \text{and} \quad \nabla \cdot \mathbf{H}_d = -\nabla \cdot \mathbf{M} \quad (2.9)$$

leads to a demagnetizing field \mathbf{H}_d inside the sample [40]. Since it originates from surface charges created by the magnetization its intensity in general is position dependent with opposing orientation to \mathbf{M} . Outside the magnetic volume \mathbf{H}_d continues as dipolar stray field. The associated dipolar energy density is formed by \mathbf{M} interacting with its generated demagnetizing field [analog to Eq. (2.4)] and reads

$$\varepsilon_{\text{shape}} = -\frac{\mu_0}{2V} \int_V \mathbf{M}(\mathbf{r}) \mathbf{H}_d(\mathbf{r}) dV \quad (2.10)$$

in its general term.

Considering a special case of a uniformly magnetized ellipsoid, \mathbf{H}_d is directly proportional to the magnetization with

$$\mathbf{H}_d = -\hat{\mathbf{N}}\mathbf{M}, \quad (2.11)$$

where $\hat{\mathbf{N}}$ is called demagnetizing tensor including the shape. Transformed to the three principle sample axes, $\hat{\mathbf{N}}$ can be expressed by a diagonalized form given by:

$$\hat{\mathbf{N}} = \begin{pmatrix} N_x & 0 & 0 \\ 0 & N_y & 0 \\ 0 & 0 & N_z \end{pmatrix}. \quad (2.12)$$

The demagnetization factors N_x, N_y, N_z fulfill the relation $N_x + N_y + N_z = 1$ and are obtained numerically for complex shapes or analytically, e. g. for prisms [44]. In the simplest case of a sphere $N_x = N_y = N_z = 1/3$ applies by reasons of symmetry. The relevant experimental case of a flat film (surface normal parallel to the z direction) is approximated by a semi-infinite plane where charges at the edges are vanishing as boundaries are separated infinitely. As a result surface charges may only occur perpendicularly to the film plane simplifying the components of $\hat{\mathbf{N}}$ to [40, 42, 45]:

$$N_x = N_y = 0 \quad \text{and} \quad N_z = 1. \quad (2.13)$$

Together with Eqs. (2.1) and (2.11) the energy density of the shape anisotropy (2.10) reduces to

$$\varepsilon_{\text{shape}} = \frac{\mu_0}{2} M_s^2 \cos^2 \theta. \quad (2.14)$$

As a consequence for flat films, the shape contribution favors an in-plane magnetization alignment with a hard axis perpendicular to the plane.

Magneto-crystalline anisotropy

Magnetic anisotropy arising from crystal structure is closely linked to the difficulty in finding precisely the electronic configuration. Because the origin of magneto-crystalline anisotropy, the spin-orbit interaction [37], is a small contribution to the total magnetic energy of a ferromagnet

it can be treated by perturbation theory [46, 47]. Unfortunately, this relatively easy approach reflects only the order of magnitude of the anisotropy. More promising results are carried out by *ab-initio* calculations [48–51], e. g. by using density functional theory. Nevertheless, from an experimental point of view a universal and fast description of the situation is needed. Hence, a phenomenological approach for the free energy density is used for decades. It is based on a power series expansion of α_i [see Eq. (2.1)] of the magnetization direction $\mathbf{e}_M = (\alpha_x, \alpha_y, \alpha_z)$ with respect to the crystallographic axes [52]:

$$F = K_0 + K_1 f_1(\alpha_x^{h_1}, \alpha_y^{k_1}, \alpha_z^{l_1}) + K_2 f_2(\alpha_x^{h_2}, \alpha_y^{k_2}, \alpha_z^{l_2}) + \dots \quad (2.15)$$

It directly reflects the symmetry of the described crystal structure by the exponents h_i, k_i, l_i , where functions f_i group terms of the same order [53]. K_i are phenomenological anisotropy constants having, except symmetry, a priori no physical correlation to microscopic sample properties, but are widely used to describe very well experimental situations and the interplay of energetics in ferromagnets [40]. Terms in Eq. (2.15) exhibiting no angular dependence, e. g. K_0 , do not contribute to anisotropy and will be neglected in the following. Furthermore, the subscripts to K are chosen in a way to reflect the symmetry of the described anisotropy, where \parallel (\perp) means an in-plane (out-of-plane) anisotropy axis and 2 (4) a two-fold (four-fold) symmetry, respectively.

In the simplest case a magnetic easy axis is aligned in the film plane. This two-fold symmetry is also referred as uniaxial anisotropy. By reasons of symmetry only even powers of α_i are allowed since odd ones would change the magnetization direction by 180° if α_i reverses sign [$F(\alpha_i) = F(-\alpha_i)$]. The corresponding energy density is given in first order by

$$\begin{aligned} F_{\text{uni},\parallel} &= -K_{2\parallel} \alpha_x^2 \\ &= -K_{2\parallel} \sin^2 \theta \cos^2(\varphi - \varphi_u). \end{aligned} \quad (2.16)$$

The in-plane uniaxial anisotropy constant $K_{2\parallel}$ sets the easy axis along φ_u (counted from the $[100]$ direction, as depicted in Fig. 2.1) for $K_{2\parallel} > 0$. For negative $K_{2\parallel}$ this axis becomes a hard axis. Further on, a uniaxial anisotropy perpendicular to the film plane reads

$$\begin{aligned} F_{\text{uni},\perp} &= -K_{2\perp} \alpha_z^2 - K_{4\perp} \alpha_z^4 \\ &= K_{2\perp} \sin^2 \theta - K_{4\perp} \cos^4 \theta, \end{aligned} \quad (2.17)$$

taking the first two non-vanishing orders into account, where $K_{i\perp} > 0$ sets the easy axis perpendicularly to the film plane.

The case of cubic symmetry will be considered next. Here, based on the same symmetry argument as for uniaxial symmetry, odd powers of direction cosines α_i as well as mixed terms $\alpha_i \alpha_j$ vanish, too. Additionally, also the second-order term in α_i must vanish due to

indistinguishable indices i of equal cubic axes. Restricting the free energy density to the fourth order it shows to be [27]:

$$\begin{aligned} F_{\text{cubic}} &= K_4 (\alpha_x^2 \alpha_y^2 + \alpha_x^2 \alpha_z^2 + \alpha_y^2 \alpha_z^2) \\ &= K_4 \sin^2 \theta - \frac{1}{8} K_4 (\cos 4\varphi + 7) \sin^4 \theta. \end{aligned} \quad (2.18)$$

A positive four-fold anisotropy constant K_4 leads to easy axes along the $\langle 100 \rangle$ directions, whereas a negative value determines the $\langle 111 \rangle$ directions to be easy axes. Note that in case of cubic symmetry only one four-fold anisotropy constant for in- as well as out-of-plane anisotropy appears due to crystallographic equivalent $\langle 100 \rangle$ directions. To distinguish between different strengths of in-plane and out-of-plane four-fold anisotropy, a tetragonally distorted crystal system must be considered. This system is of particular interest for thin films where the in-plane lattice constant may differ from the out-of-plane one, as it is achieved by epitaxial growth of a material on a substrate with slightly different lattice parameters. By breaking the symmetry of crystallographic equivalent directions the tetragonal system is described up to the fourth order by [27]:

$$\begin{aligned} F_{\text{tet}} &= -K_{2\perp} \alpha_z^2 - \frac{1}{2} K_{4\perp} \alpha_z^4 - \frac{1}{2} K_{4\parallel} (\alpha_x^4 + \alpha_y^4) \\ &= K_{2\perp} \sin^2 \theta - \frac{1}{2} K_{4\perp} \cos^4 \theta - \frac{1}{8} K_{4\parallel} (3 + \cos 4\varphi) \sin^4 \theta. \end{aligned} \quad (2.19)$$

Of course, even if the description of magneto-crystalline anisotropy [Eqs. (2.16)–(2.19)] is based on crystal symmetry it is yet still derived by a phenomenological strategy, which finally allows to adopt it to polycrystalline or morphology-induced anisotropies exhibiting the same anisotropic symmetry but missing the far-ordered crystal structure.

Total free energy density

Finally, the free energy density of a tetragonally distorted magnetic film can be constructed including intrinsic contributions such as uniaxial in-plane (2.16), out-of-plane (2.17), shape (2.14) and magneto-crystalline anisotropy (2.19), and the Zeeman term (2.8):

$$\begin{aligned} F &= -\mu_0 M_s H [\sin \theta \sin \theta_H \cos(\varphi - \varphi_H) + \cos \theta \cos \theta_H] \\ &\quad - \left(\frac{1}{2} \mu_0 M_s^2 - K_{2\perp} \right) \sin^2 \theta - K_{2\parallel} \sin^2 \theta \cos^2(\varphi - \varphi_u) \\ &\quad - \frac{1}{2} K_{4\perp} \cos^4 \theta - \frac{1}{8} K_{4\parallel} (3 + \cos 4\varphi) \sin^4 \theta. \end{aligned} \quad (2.20)$$

Knowing the system's free energy density gives the possibility to calculate the orientation of the magnetization within the sample in presence of external magnetic fields and anisotropies.

The latter in turn gives rise to anisotropy fields, defined by [10]:

$$H_{K_i} = \frac{2K_i}{\mu_0 M_s}. \quad (2.21)$$

These fields can be treated as internal fields, offering the possibility to compare anisotropy-generated effects with external field effects by their strengths. The overall effective field (sum of external and internal fields) acting on the magnetization can be derived from [42, 54]:

$$\mathbf{H}_{\text{eff}} = -\frac{1}{\mu_0} \frac{\partial F}{\partial \mathbf{M}}. \quad (2.22)$$

In equilibrium the magnetization aligns parallel with the effective field, which means that the torques exerted by \mathbf{H}_{eff} onto the magnetization vanishes:

$$\mu_0 \mathbf{M} \times \mathbf{H}_{\text{eff}} = 0. \quad (2.23)$$

The equilibrium position of \mathbf{M} , denoted by polar angle θ and azimuthal angle φ , is determined by the minimum state of the free energy density:

$$\left. \frac{\partial F}{\partial \theta} \right|_{\theta} \stackrel{!}{=} 0 \quad \text{and} \quad \left. \frac{\partial F}{\partial \varphi} \right|_{\varphi} \stackrel{!}{=} 0. \quad (2.24)$$

Depending on the strength of the external field with respect to the anisotropy fields the free energy density in Eq. (2.20) may have multiple minima resulting in a hysteretic behavior of the magnetization reversal curve¹ $M(H)$. In saturation \mathbf{H} is dominant over anisotropy contributions forcing \mathbf{M} towards its direction causing F to exhibit only a global minimum with distinct equilibrium orientation. By modeling magnetization reversal curves² the contributions to \mathbf{H}_{eff} and hence the anisotropy constants can be determined from measurements. At the same time, however, it should be noted that magnetization reversal curves include unsaturated regimes, where magnetic domains (esp. if measuring off the hard axes) might be present. The domain switching is determined by external contributions such as pinning centers or impurities, which in turn makes it challenging for modeling. Methods that rely on saturated samples, e. g. dynamic methods like ferromagnetic resonance (FMR), circumvent this disadvantages and will be introduced later.

In experimental situations, effective anisotropy constants are determined containing information from bulk and surface/interface effects. Disentangling both contributions can be achieved by determining the thickness dependence of K and using the relation:

$$K = K^V + \frac{2K^S}{d}. \quad (2.25)$$

¹For $M(H)$ curves the magnitude of the projection of \mathbf{M} onto the external field direction is measured by sweeping \mathbf{H} from negative to positive saturations values and back.

²Using Eqs. (2.20) and (2.24) allows to calculate the projection of \mathbf{M} onto \mathbf{H} . For further details see Ref. 10.

Here, K^V is the volume anisotropy part and $2K^S$ the surface/interface contribution originating from both sides of the film with thickness d [40].

Due to magnetic interactions several characteristic length scales can be introduced. For example, if only exchange and dipolar interaction are considered in F , the exchange length follows [55, 56]:

$$\Lambda_{\text{ex}} = \sqrt{\frac{2A_{\text{ex}}}{\mu_0 M_s^2}}. \quad (2.26)$$

The competition between both interactions leads to a coherent alignment of moments below this length, whereas above dominating dipolar interactions may start to tilt magnetic moments against each other. Note that the definition of the exchange length may be different to Eq. (2.26) [10]. Further details on length scales are provided by Refs. 10, 57.

2.2 Magnetization dynamics

Up to now, magnetic properties have only been considered as being static, where the alignment of magnetic moments and resulting magnetization is caused by a time-independent effective field \mathbf{H}_{eff} . Of course experimental situations exist, where the equilibrium condition (2.23), due to changes in magnitude or direction of \mathbf{H}_{eff} , is violated, which leads to a relaxation mechanism of \mathbf{M} back to its equilibrium position. For example, in FMR experiments the magnetization is excited resonantly [in the radio frequency (rf) range] by a microwave field $\mathbf{h}_{\text{rf}}(t)$ to precess around the effective field. The condition under which precession takes place is determined by the sample properties and is described by the resonance condition, a result of solving the equation of motion. In addition, the width of the resonance peak (referred to as linewidth), visible if the microwave absorption is recorded as a function of external field or applied microwave frequency, can be related to losses of the precessional energy due to damping in the magnetic system.

2.2.1 Equation of motion

To gain an understanding of the underlying processes first a single atom with magnetic moment $\boldsymbol{\mu}$ in a magnetic field \mathbf{H} is considered. The field leads to Zeeman splitting of the atomic energy levels into so-called Zeeman multiplets, where the energy difference between level i and k is given by $\Delta E_{ik} = g\mu_B \Delta m_{ik} \mu_0 H$. Here, g is the Landé factor, also referred to as spectroscopic splitting factor, which depends on the ratio of spin and orbital momentum [58, 59]. Furthermore, μ_B is the Bohr magneton, and Δm_{ik} the difference in magnetic quantum numbers of the considered states i and k , respectively. A transition between both states is induced by resonant

absorption of microwave energy of $\Delta E_{i,k} = \hbar\omega_{ik}$, with \hbar being the reduced Planck constant. For example, in an electronic system with spin quantum number $s = 1/2$ the induced transition occurs between $m_i = 1/2$ and $m_k = -1/2$, which corresponds to a spin flip. Determined by selection rules transitions are only possible that satisfy $|\Delta m_{ik}| = 1$. Furthermore, this sets the polarization plane of emitted microwaves perpendicularly to \mathbf{H} . That in turn defines the geometry for an absorption experiment under the resonant condition:

$$\omega = \gamma\mu_0 H. \quad (2.27)$$

Here, the direction of the exciting microwave field with resonant frequency $f = \omega/(2\pi)$ has to be perpendicular to the applied field [58]. Eq. (2.27) includes the gyromagnetic ratio $\gamma = g|e|\hbar/(2m_{e^-})$ that in turn includes the electron mass m_{e^-} and charge e . Typically, magnetic resonance experiments are carried out on an ensemble of atoms, showing a magnetic moment. If these moments are uncoupled and no internal fields are present (paramagnetic case) one speaks of electron paramagnetic resonance. For ferromagnetic samples having internal fields and exchange interaction the method is referred to as ferromagnetic resonance, which will be considered in the following.

It was pointed out by Landau and Lifschitz in 1935 that the intrinsic ferromagnetic interactions occurring during resonance can be simply taken into account by replacing the external field in Eq. (2.27) by the effective field [58, 60]. The induced motion of the magnetization, whether by simply tilting the effective field away from the magnetization orientation or by resonant excitation of transitions in the Zeeman multiplets, is described by the Landau-Lifschitz equation of motion:

$$\frac{d\mathbf{M}}{dt} = -\gamma\mu_0 \mathbf{M} \times \mathbf{H}_{\text{eff}}. \quad (2.28)$$

It describes the time evolution of \mathbf{M} caused by the totally acting torque. Due to the large number of moments involved in the process the correspondence principle applies and the classical [55] as well as quantum mechanical description [10] of the motion become equivalent. Fig. 2.2(a) depicts the motion described by Eq. (2.28). The cross product of \mathbf{M} with \mathbf{H}_{eff} describes a torque acting on the magnetization forcing it to precess around the effective field. For purely isotropic samples the motion is circular around \mathbf{H}_{eff} , but it becomes elliptic if the acting field is anisotropic.

As the cross product $\mathbf{M} \times \mathbf{H}_{\text{eff}}$ is the only contribution that acts on the magnetization (tangential to its trajectory) the Landau-Lifschitz equation misses a damping term which relaxes \mathbf{M} back to its equilibrium position, parallel to \mathbf{H}_{eff} . The lack of damping would cause \mathbf{M} to precess for infinity³ which of course does not reflect the reality. Therefore, it was the research interest of various authors to add a damping contribution to Eq. (2.28). In 1935 Landau

³An infinite lifetime of such an excited state would also correspond to an infinite narrow linewidth (δ -function).

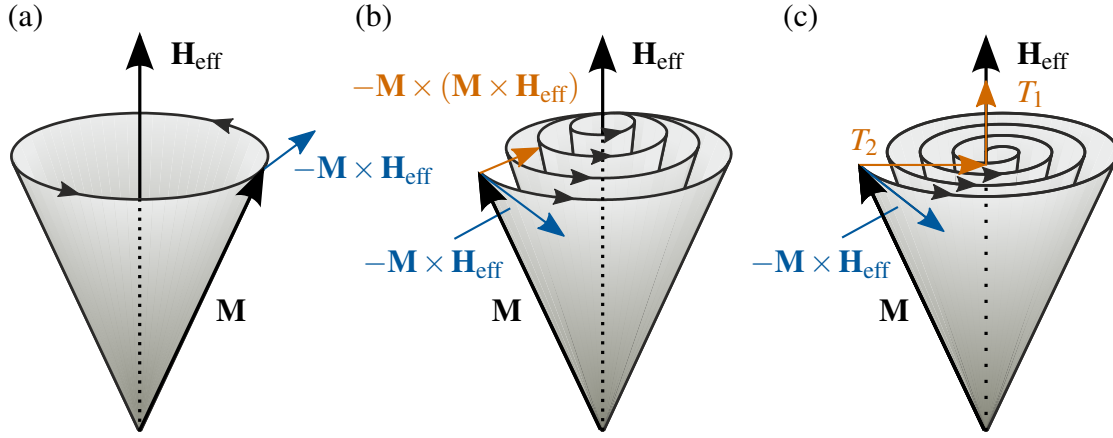


Figure 2.2: Precessional motion of magnetization \mathbf{M} in an effective field \mathbf{H}_{eff} , once tipped out of its equilibrium position. Sketched are (a) an undamped motion, (b) a damped motion with constant magnitude (Landau-Lifschitz-Gilbert) of \mathbf{M} , and (c) a damped motion with longitudinal T_1 and transversal T_2 relaxation times (Bloch-Bloembergen). For a better visualization the opening angle $\angle(\mathbf{M}, \mathbf{H}_{\text{eff}})$ is grossly exaggerated. Adapted from Ref. 59.

and Lifschitz added a phenomenological damping term to Eq. (2.28) that is proportional to $-\mathbf{M} \times (\mathbf{M} \times \mathbf{H}_{\text{eff}})$ and the damping constant λ_{LL} . Thus, damping occurs perpendicularly to the driving torque pointing towards the effective field [60]:

$$\frac{d\mathbf{M}}{dt} = -\gamma\mu_0\mathbf{M} \times \mathbf{H}_{\text{eff}} - \frac{\lambda_{\text{LL}}}{M_s^2}\mathbf{M} \times (\mathbf{M} \times \mathbf{H}_{\text{eff}}). \quad (2.29)$$

A visualization of the resulting motion of \mathbf{M} , tipped once out of its equilibrium position, is shown in Fig. 2.2(b). Due to the fact that the damping term in Eq. (2.29) points perpendicularly to \mathbf{M} it does not change the absolute value of the magnetization leading to a spiral motion towards the effective field orientation.

A slightly different formulation was proposed by Gilbert in 1955 introducing a relaxation term that is proportional to the change of \mathbf{M} with time [54]:

$$\frac{d\mathbf{M}}{dt} = -\gamma\mu_0\mathbf{M} \times \mathbf{H}_{\text{eff}} + \frac{\alpha}{M_s}\mathbf{M} \times \frac{d\mathbf{M}}{dt}. \quad (2.30)$$

This equation is known as Landau-Lifschitz-Gilbert (LLG) equation containing the dimensionless damping parameter α . It can be shown that the viscous damping term (velocity-proportional) is equivalent to the one proposed by Landau and Lifschitz for small damping parameters ($\alpha < 0.1$), which is satisfied by almost every experiment [58]. Commonly, α is substituted by $\alpha = G/(\gamma\mu_0 M_s)$ to express damping in terms of relaxation rates using the Gilbert damping parameter G . The reason why the LLG equation is preferred over Eq. (2.29) is

of physical nature. For high damping parameters λ_{LL} an unphysical short relaxation time is predicted, whereas high α values still give reasonable relaxation behavior [61].

Lastly, to complete the picture of relaxation, a model containing spatially different relaxation times will be discussed. It has been first introduced by Bloch [62] in 1946 to explain nuclear magnetic resonance and was later adapted by Bloembergen [63, 64] to explain absorption in ferromagnets:

$$\frac{d\mathbf{M}}{dt} = -\gamma\mu_0\mathbf{M} \times \mathbf{H}_{\text{eff}} - \frac{M_x}{T_2}\mathbf{e}_x - \frac{M_y}{T_2}\mathbf{e}_y - \frac{M_z - M_s}{T_1}\mathbf{e}_z. \quad (2.31)$$

Its relaxation term splits into three contributions connected with a longitudinal and transversal relaxation time T_1 and T_2 , which makes it possible to account for different relaxation mechanisms [65]. The length of \mathbf{M} during relaxation is preserved [as in Eqs. (2.29), (2.30)] only for the case of $T_2 = 2T_1$ [66]. In Fig. 2.2(c) the process is shown for a scattering event that distributes the energy to the transverse components of \mathbf{M} while ensuring a constant projection of \mathbf{M} onto the effective field axis (along z) [59]. Different phenomena leading to different relaxation mechanisms [phenomenologically covered by the Eqs. (2.30) and (2.31)] are described in section 2.3.

2.2.2 Resonance condition and dynamic susceptibility

The equations of motion offer the opportunity to calculate the condition under which resonant absorption, caused by a microwave field $\mathbf{h}_{\text{rf}}(t)$, appears. First attempts to explain the experimental observation were done by Kittel in 1947 [67]. An extension of this theory led to the prediction of a resonance condition dependent on the sample shape and crystal structure [68]. However, the theory was still limited to fixed measurement geometries.

The general case is obtained considering the free energy density of the system. The effective field acting on \mathbf{M} consists of an externally applied field, anisotropy fields, and the applied microwave field. Under resonant excitation the torque generated by the microwave field balances the damping term and the remaining equation of motion is equal to Eq. (2.28), forcing a precession at the eigenfrequency of the system. Expressed in terms of spherical coordinates (cf. Fig. 2.1) and under the assumption of a uniform magnetization with constant magnitude it reads [58]:

$$\frac{d\theta}{dt} = \gamma\mu_0 H_{\text{eff},\varphi} \quad \text{and} \quad \frac{d\varphi}{dt} \sin\theta = -\gamma\mu_0 H_{\text{eff},\theta}. \quad (2.32)$$

$H_{\text{eff},\theta}$ and $H_{\text{eff},\varphi}$ are the polar and azimuthal components of the effective field. In thermodynamic equilibrium these components vanish since the magnetization is aligned parallel to \mathbf{H}_{eff} . The equilibrium angles θ and φ can be easily found from Eq. (2.24). However, when exposed to a microwave field, \mathbf{M} precesses around its equilibrium position, described by the angles

$\theta(t) = \theta + \delta\theta$ and $\varphi(t) = \varphi + \delta\varphi$, which causes non-vanishing angular components of \mathbf{H}_{eff} . Expressing Eq. (2.22) in spherical coordinates gives [58]

$$H_{\text{eff},\theta} = -\frac{1}{\mu_0 M_s} F_\theta \quad \text{and} \quad H_{\text{eff},\varphi} = -\frac{1}{\mu_0 M_s \sin \theta} F_\varphi, \quad (2.33)$$

where $F_i = \frac{\partial F}{\partial i}$ is used to abbreviate the partial derivative of F with respect to i . To derive the latter it is linearly expanded around the equilibrium position θ, φ assuming small deflections $\delta\theta, \delta\varphi$ yielding $F_\theta = F_{\theta\theta}\delta\theta + F_{\theta\varphi}\delta\varphi$ and $F_\varphi = F_{\varphi\varphi}\delta\varphi + F_{\varphi\theta}\delta\theta$. Again, second partial derivatives of F are abbreviated by F_{ij} . By this, Eq. (2.32) can be solved using (2.33) together with a periodic ansatz for the deflections $\delta\theta, \delta\varphi \sim \exp(i\omega t)$, which results in the resonance condition [58] formulated by Smit and Beljers in 1955 [69]:

$$\begin{aligned} \omega &= \gamma \mu_0 H_{\text{eff}} \\ &= \frac{\gamma}{M_s \sin \theta_0} \sqrt{F_{\theta\theta} F_{\varphi\varphi} - F_{\theta\varphi}^2}. \end{aligned} \quad (2.34)$$

This equation was also derived by Suhl at the same time [70]. However, even if Eq. (2.34) allows to calculate the resonance condition for any experimental situation knowing F , it is still physically not convenient due to occurring singularities e. g. for $\theta = 0$. Instead Baselgia *et al.* found a new expression circumventing this problem [71]:

$$\left(\frac{\omega}{\gamma}\right)^2 = \frac{1}{M_s^2} \left[F_{\theta\theta} \left(\frac{F_{\varphi\varphi}}{\sin^2 \theta} + \frac{\cos \theta}{\sin \theta} F_\theta \right) - \left(\frac{F_{\theta\varphi}}{\sin \theta} - \frac{\cos \theta}{\sin \theta} \frac{F_\varphi}{\sin \theta} \right)^2 \right]. \quad (2.35)$$

Experimentally two possibilities exist to fulfill the resonance condition: (i) choosing a fixed microwave frequency ω while simultaneously sweeping the external magnetic field (H -sweep), or (ii) sweeping the microwave frequency (f -sweep) and keeping the external field constant.

An alternative approach to calculate resonance conditions is achieved by separating magnetization and magnetic field into static and dynamic components: $\mathbf{M}(t) = \mathbf{M}_{\text{stat}} + \mathbf{m}_{\text{dyn}}(t)$, $\mathbf{H}_{\text{eff}}(t) = \mathbf{H}_{\text{stat}} + \mathbf{h}_{\text{rf}}(t)$. Inserting this ansatz into the equation of motion (2.30) and solving the linearized problem for small perturbations yields a linear relation between the dynamic components, connected by the dynamic susceptibility tensor $\hat{\chi}$ [72]:

$$\mathbf{m}_{\text{dyn}} = \hat{\chi} \mathbf{h}_{\text{rf}}. \quad (2.36)$$

This expression was first obtained by Polder when considering undamped precessional motion described by Eq. (2.28) [73]. In the general case including damping the components of $\hat{\chi}$ become complex. To make this explicit, an isotropic magnetic film saturated by an external field along the z direction as well as a periodic microwave field \mathbf{h}_{rf} oriented perpendicularly

to \mathbf{H} will be discussed. For small perturbation the z component of \mathbf{M} is unchanged and the precessional motion takes places in the xy plane. Then Eq. (2.36) is given by:

$$\begin{pmatrix} m_x \\ m_y \end{pmatrix} = \begin{pmatrix} \chi & i\kappa \\ -i\kappa & \chi \end{pmatrix} \begin{pmatrix} h_x \\ h_y \end{pmatrix}. \quad (2.37)$$

This case applies only for spherical precession in an isotropic medium. If the magnetic system includes anisotropies, the precession becomes elliptic and the diagonal components of $\hat{\chi}$ differ from each other. The complex components of $\hat{\chi}$ are

$$\chi = \frac{(\omega_H + i\omega\alpha)\omega_M}{(\omega_H + i\omega\alpha)^2 - \omega^2} \quad \text{and} \quad \kappa = \frac{\omega\omega_M}{(\omega_H + i\omega\alpha)^2 - \omega^2}, \quad (2.38)$$

with the abbreviations [74]:

$$\omega_M = \gamma\mu_0 M_s \quad \text{and} \quad \omega_H = \gamma\mu_0 H. \quad (2.39)$$

Both, $\chi = \chi' - i\chi''$ and $\kappa = \kappa' - i\kappa''$ can be split into real and imaginary part describing dispersion and absorption of the microwave signal, respectively. Since every contribution on its own depends on the microwave frequency ω (and hence on the resonance field) it is sufficient to measure only one component in a resonance experiment to gain the magnetic response. This can be achieved by choosing the direction of the microwave field parallel to the corresponding component of the susceptibility. The components of χ are

$$\chi' = \frac{\omega_M\omega_H [\omega_H^2 - (1 - \alpha^2)\omega^2]}{[\omega_H^2 - (1 + \alpha^2)\omega^2]^2 + 4\alpha^2\omega^2\omega_H^2}, \quad \chi'' = \frac{\alpha\omega_M\omega [\omega_H^2 + (1 + \alpha^2)\omega^2]}{[\omega_H^2 - (1 + \alpha^2)\omega^2]^2 + 4\alpha^2\omega^2\omega_H^2}. \quad (2.40)$$

A detailed derivation as well as the components of κ can be found elsewhere [72, 74].

In a FMR experiment the external frequency (or field) is swept through the resonance of the susceptibility. By considering the f -sweep case the resonance position⁴ of Eq. (2.40) is found at $\omega_{\text{res}} = \frac{\omega_H}{1 + \alpha^2}$. To the lowest-order approximation the influence of the damping constant α on the resonance position is negligible ($1 + \alpha^2 \approx 1$), since α is usually a small quantity. The evolving line shapes, when going through resonance, are shown in Fig. 2.3 for dispersion (χ') and absorption (χ''), respectively. Next to the resonance position ω_{res} the linewidth $\Delta\omega$ is of importance. It is defined as half width of the absorption curve at its half amplitude $\chi_{\text{max}}/2$ (HWHM) and is directly proportional to the relaxation [74]:

$$\Delta\omega = \alpha\omega_{\text{res}}. \quad (2.41)$$

⁴The index “res” denotes the resonance position of a swept quantity. For simplicity it is omitted in $f(H)$ and thus valid for f - and H -sweep measurements. The same holds true for the resonance condition $\omega(H)$.

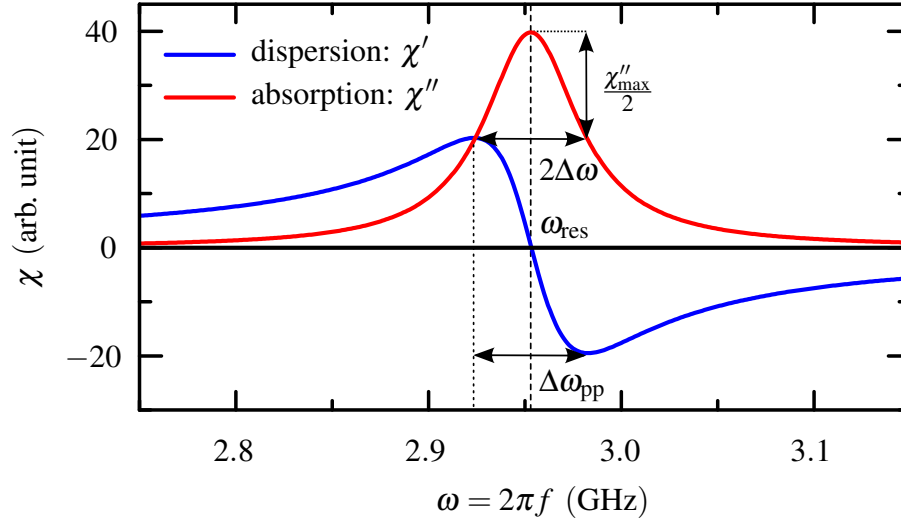


Figure 2.3: Real (blue line) and imaginary (red line) part of the dynamic susceptibility χ . The magnetic response is shown for a magnetic thin film ($\mu_0 M_s = 1$ T, $\alpha = 0.01$, and $\gamma = 185.55$ GHz/T) in an external field of $\mu_0 H = 0.1$ T while the excitation frequency is swept.

For small damping constants α the line shape represents a Lorentzian resonance curve, but becomes asymmetric with increasing damping [74]. To extract linewidth and resonance position from measured curves usually a Lorentzian model function is used that allows a parameter determination without knowledge of the exact magnetic response function. Usually there the peak-to-peak linewidth $\Delta\omega_{pp}$ is used, as it is easier to determine. A detailed discussion on this will be given in Chapter 3.

In comparison to Eq. (2.35) the susceptibility approach provides not only the resonance condition (and hence the anisotropy constants), but also the line shape of the measured magnetic response.

2.2.3 Spin waves

The nonequilibrium state discussed so far was a result of a spatially homogeneous excitation field $\mathbf{h}_{rf}(\mathbf{r}, t) = \mathbf{h}_{rf}(t)$ which again causes a homogeneous precession of the magnetization $\mathbf{M}(\mathbf{r}, t) = \mathbf{M}(t)$. This precessional mode is called uniform or FMR mode since all spins are exposed to the same exciting force and, hence, precess parallel at the same phase [see Fig. 2.4(a)]. However, if real experimental situations are considered nonuniform time-dependent fields, e. g. arising from dipolar interactions at the sample's boundaries or by inhomogeneous excitation fields, are present that lead to spatially nonuniform magnetization distributions. Excited spin states that exhibit a well-defined spatial correlation are called spin waves. Of course, effects acting on the spin system can be treated in a quantum mechanical fashion, but are in agreement

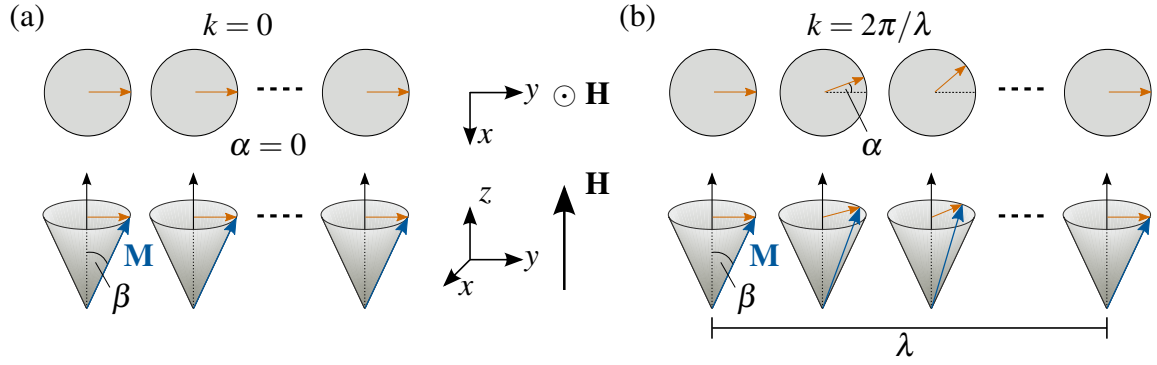


Figure 2.4: Illustration of precessional modes of \mathbf{M} with opening angle β counted from the external field \mathbf{H} : (a) uniform precession with wave number $k = 0$ and (b) spin wave with wavelength λ where neighboring spins are tilted by α . Adapted from Ref. 75.

with a simple picture of classical treatment [75] obtained from a macrospin model with continuous states. The validity of the macrospin model is a consequence of the correspondence principle. A detailed quantum mechanical approach is e. g. given by Sparks [75].

First a spin system, excited to precess around an external field \mathbf{H} , is considered which contains only exchange and Zeeman interaction (see section 2.1.1). In its energetic minimum (ground state with uniform mode), all spins are aligned parallel to each other and a precession in phase takes place, depicted in Fig. 2.4(a). This parallel alignment corresponds to an infinite wavelength λ and zero wave number, $k = 0$. The first excited state in the spin system corresponds to a single spin flip, which, due to strongly increased exchange energy, is energetically unfavorable. Instead, the potential energy is kept small by introducing a constant tilt α between neighboring spins. In addition, each spin is tipped out of its equilibrium position by β . Due to the high number of spins in the system quasi-continuous spin states evolve and, consequently, the situation forms a spin wave with wavelength $\lambda = 2\pi/k$ (wave number k), as shown in Fig. 2.4(b). As a result of tilting away from the external field by the angle β , the observed magnetic moment μ_H along the field direction is reduced by $\Delta\mu_H$ from its saturation value $M_s V$. Turning to the quantum mechanical picture, a quantized spin wave causing a reduction in μ_H , equal to a single spin flip, is called magnon. In an electronic system with spin quantum number $1/2$ a single magnon reduces μ_H by $g\mu_B$. If more than one magnon state is present, $\Delta\mu_H$ is comprised by the number of magnons n_k having wave vectors k [75]:

$$\mu_H = M_s V - g\mu_B \sum_k n_k. \quad (2.42)$$

The energy of a magnon is caused by the exchange interaction between neighboring spins ($\mathbf{s}_i \cdot \mathbf{s}_j$) and thus is proportional to the tilt $\cos \alpha$. For small precession angles $\cos \alpha \approx 1 - \alpha^2/2$

continues to apply. Furthermore, a higher wavelength λ is equivalent to a smaller tilt angle α , or $\alpha \sim k$. This finally results in a direct proportionality of the magnon energy to the wave number, $\hbar\omega_{\text{magnon}} \sim k^2$. By taking dipolar effects between spins as well as an externally applied field into account one finds the spin wave dispersion relation for an infinite ferromagnetic medium having no anisotropy [76, 77]:

$$\left(\frac{\omega(k)}{\gamma}\right)^2 = (\mu_0 H + Dk^2) (\mu_0 H + Dk^2 + \mu_0 M_s \sin^2 \varphi_{\mathbf{k}}). \quad (2.43)$$

The spin wave stiffness constant $D = 2A/M_s$ includes the exchange interaction, whereas $\mu_0 M_s \sin^2 \varphi_{\mathbf{k}}$ accounts for dipolar effects of the spin motion. The dipole term strongly depends on the angle $\varphi_{\mathbf{k}}$ between the wave vector \mathbf{k} and \mathbf{M} . If both are aligned parallel to each other the dipolar influence on the dispersion relation vanishes, whereas a perpendicular alignment shifts the magnonic states to higher energies.

Next, boundary conditions (limited film thickness d) need to be included to advance to realistic systems, which evolves in different spin wave modes. Of particular importance is the relation between exchange and dipolar contribution, distinguishing between the limits of so-called dipolar- and exchange-dominated modes. Dipolar spin waves, also referred to as magnetostatic waves, are present for spin waves with large wavelength, whereas short wavelengths result in exchange-dominated modes. A detailed review on the nature of spin waves can be found in Refs. 78, 79. In the following, an overview of spin wave modes appearing in ultrathin films will be discussed. A formalism covering a variety of modes may be found in Refs. 80, 81.

Magnetostatic modes

Starting with dipolar modes, a dispersion relation is obtained by solving Maxwell's equations in a magnetostatic approximation. Assuming negligible displacement currents, spin waves with wavelengths much shorter than the exciting electromagnetic wave (of equal frequency), and including the dynamic susceptibility leads to three modes [72, 82], shown in Fig. 2.5.

Forward volume magnetostatic waves (FVMSW) are modes with in-plane propagation direction $\mathbf{e}_{k_{\parallel}} = \mathbf{k}_{\parallel}/k_{\parallel}$ within an out-of-plane magnetized film. An approximation of the dispersion is given by:

$$\left(\frac{\omega(k_{\parallel})}{\gamma}\right)^2 = \mu_0 H \left[\mu_0 H + \mu_0 M_s \left(1 - \frac{1 - \exp(-k_{\parallel} d)}{k_{\parallel} d} \right) \right]. \quad (2.44)$$

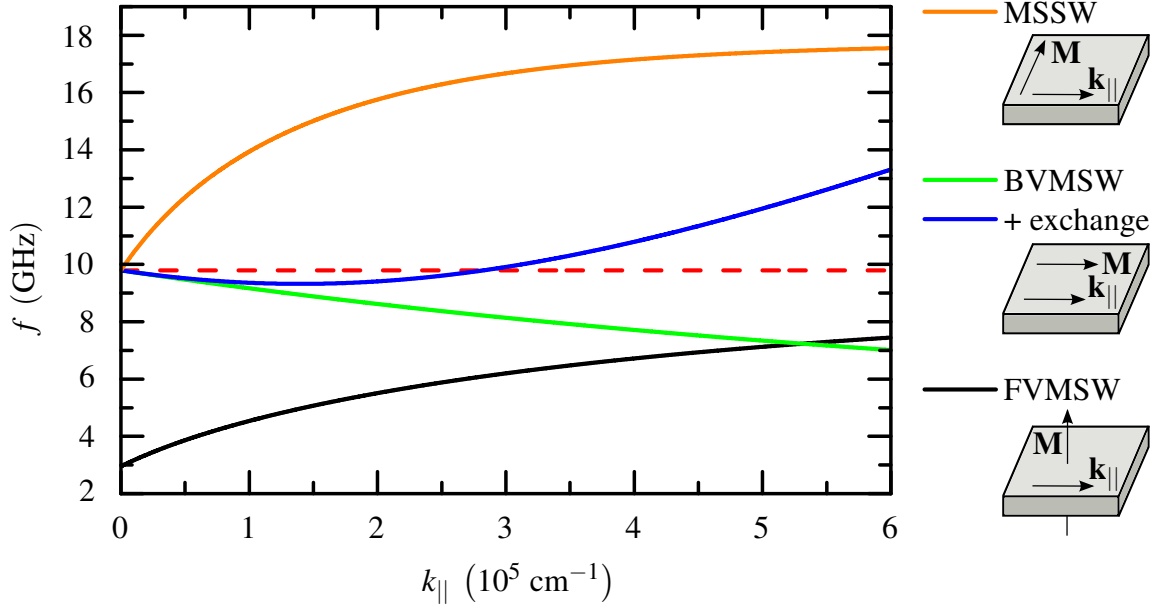


Figure 2.5: Spin wave dispersion relation for in-plane propagating modes in a thin $\text{Ni}_{81}\text{Fe}_{19}$ film ($\mu_0 M_s = 1$ T, $d = 30$ nm, $g = 2.11$, $D = 34$ T nm², $K_{2\perp} = 0$) in an external field of $\mu_0 H = 0.1$ T. The red dashed line corresponds to the uniform mode, whereas the remaining spin wave modes are described by Eqs. (2.44)–(2.47), and (2.49).

Important characteristics of these modes are their independence of in-plane propagation direction and precessional amplitudes that are distributed over the whole magnetic volume. Since phase ($v_p = \omega/k$) and group ($v_g = \partial\omega/\partial k$) velocity of the mode are pointing in the same direction these mode are called forward modes.

Backward volume magnetostatic waves (BVMSW) likewise propagate in-plane and parallel to the in-plane oriented magnetization. These modes, too, are distributed over the whole volume, but exhibit oppositely oriented group and phase velocity, which characterizes them as backward volume modes. The negative group velocity is caused by a negative slope in the dispersion relation that is approximated by:

$$\left(\frac{\omega(k_{\parallel})}{\gamma}\right)^2 = \mu_0 H \left[\mu_0 H + \mu_0 M_s \left(\frac{1 - \exp(-k_{\parallel} d)}{k_{\parallel} d} \right) \right]. \quad (2.45)$$

Note that in the limit of $k_{\parallel} d \ll 1$ dipolar interactions lead to a dispersion linear in k_{\parallel} , which is a unique feature of propagation in two dimensions [66]. Also for $k_{\parallel} \rightarrow 0$ the resonance frequency approaches the frequency of the uniform mode $(\omega/\gamma)^2 = \mu_0 H (\mu_0 H + \mu_0 M_s)$, as it can be derived from Eq. (2.35) using (2.20) while neglecting any anisotropy contributions ($K_i = 0$).

Magnetostatic surface waves (MSSW) mainly propagate at the surface and are present if spin wave propagation direction and magnetization are in-plane and perpendicular to each other. Approximately, the dispersion can be calculated by:

$$\left(\frac{\omega(k_{\parallel})}{\gamma}\right)^2 = \mu_0 H (\mu_0 H + \mu_0 M_s) + \frac{(\mu_0 M_s)^2}{4} [1 - \exp(-2k_{\parallel}d)]. \quad (2.46)$$

These waves are named Damon-Eshbach modes, who described them first [83]. For $k_{\parallel} \rightarrow 0$, like backward volume modes, these modes are equal to the uniform mode.

Exchange-dominated in-plane modes

Next, spin wave modes with non-negligible exchange interaction will be discussed for in-plane propagating waves. An approximation of the dispersion relation, including dipolar and exchange effects in ultrathin films ($k_{\parallel}d \ll 1$), is given by Arias and Mills [22]:

$$\begin{aligned} \left(\frac{\omega(k_{\parallel}, \varphi_{\mathbf{k}_{\parallel}})}{\gamma}\right)^2 &= \left(\frac{\omega}{\gamma}\right)^2 - \frac{\mu_0 M_s}{2} [\mu_0 H - (\mu_0 H + \mu_0 M_{\text{eff}}) \sin^2 \varphi_{\mathbf{k}_{\parallel}}] k_{\parallel}d \\ &+ (2\mu_0 H + \mu_0 M_{\text{eff}}) D k_{\parallel}^2. \end{aligned} \quad (2.47)$$

Here, $(\omega/\gamma)^2 = \mu_0 H (\mu_0 H + \mu_0 M_{\text{eff}})$ is the resonance condition of the uniform mode of an ultrathin film with perpendicular uniaxial anisotropy $K_{2\perp}$. The latter is included in the effective magnetization, which is the difference between shape and perpendicular uniaxial anisotropy:

$$\mu_0 M_{\text{eff}} = \mu_0 M_s - 2K_{2\perp}/M_s. \quad (2.48)$$

Positive values of $\mu_0 M_{\text{eff}}$ cause an orientation of the magnetization in the film plane, whereas negative values align \mathbf{M} perpendicularly. If high-order spin waves in the film plane are present ($k_{\parallel} \neq 0$) the last term in Eq. (2.47) accounts for the exchange interaction (isotropic in space) and causes a shift upwards in resonance frequency, since canting of neighboring spins costs energy. Furthermore, the dispersion relation includes the angle $\varphi_{\mathbf{k}_{\parallel}}$ measured between \mathbf{k}_{\parallel} and \mathbf{M} , both aligned in-plane. For vanishing exchange D and perpendicular anisotropy $K_{2\perp}$ as well as in the ultrathin-film limit Eq. (2.47) approximates magnetostatic backward volume (2.45) and surface modes (2.46) for $\varphi_{\mathbf{k}_{\parallel}} = 0$ and $\varphi_{\mathbf{k}_{\parallel}} = 90^\circ$, respectively. To expand Eq. (2.47) in the limit of BVMSW modes ($\varphi_{\mathbf{k}_{\parallel}} = 0$) in thicker films, the substitution

$$k_{\parallel}d \rightarrow 2 \left[1 - \frac{1 - \exp(-k_{\parallel}d)}{k_{\parallel}d} \right] \quad (2.49)$$

needs to be used.

The effect of exchange interaction on backward volume modes is of particular importance. The interplay of opposing slopes of dipolar ($\sim -k_{\parallel}$, for $k_{\parallel}d \ll 1$ in ultrathin films) and exchange ($\sim k_{\parallel}^2$) contribution creates a minimum in the dispersion leading to degenerate states in ω of the uniform mode ($k_{\parallel} = 0$). These degenerate states are of particular importance for magnetization relaxation effects (see section 2.3.3). A comparison between backward volume modes ($\varphi_{\mathbf{k}_{\parallel}} = 0$) with and without exchange interaction is depicted in Fig. 2.5. As the ultrathin film limit is not valid for the chosen parameters the substitution (2.49) is used.

Up to now, spin waves were discussed propagating in-plane encountering no lateral constraints since the only boundary was the film thickness. Turning the wave vector perpendicularly to the film limits the wavelength to discrete values having nodes at the film boundaries and forming standing waves. Fulfilling this boundary condition leads to discrete wave numbers $k_{\perp} = p\pi/d$, with mode numbers p of integer values greater than zero. Neglecting influences of in-plane modes leads to an approximated dispersion relation of so-called perpendicular standing spin waves (PSSW) [76]:

$$\left(\frac{\omega(k_{\perp})}{\gamma}\right)^2 = (\mu_0 H + Dk_{\perp}^2) \cdot (\mu_0 H + Dk_{\perp}^2 + \mu_0 M_s). \quad (2.50)$$

Here, the exchange interaction causes a constant upward shift of the mode frequency with increasing mode number. It was first predicted by Kittel to use the difference in resonance frequencies of different PSSW modes to determine the exchange stiffness constant D (so-called spin wave resonance) experimentally [84].

2.3 Magnetic relaxation

As already mentioned in section 2.2.1, magnetic moments in nonequilibrium with an effective field undergo a relaxation process back to parallel alignment. Additionally, in resonance experiments these moments are continuously excited resulting in magnons ($k = 0$ in case of FMR experiments), where the energy pumped into the spin system by resonant excitation via the microwave field is balanced by relaxation (damping) effects. In terms of magnons an annihilation process needs to take place transferring the introduced energy away from the spin system. A basic scheme of the involved relaxation channels is shown in Fig. 2.6. Two general channels can be deduced: (i) a transition of energy from the spin system into the lattice system (spin-lattice relaxation) and (ii) internal magnetic transitions (spin-spin relaxation). Referring to the second point the energy in the magnetic system is transferred from the initially excited $k = 0$ state to a degenerate magnon state e. g. via two-magnon scattering (TMS). Both mechanisms will

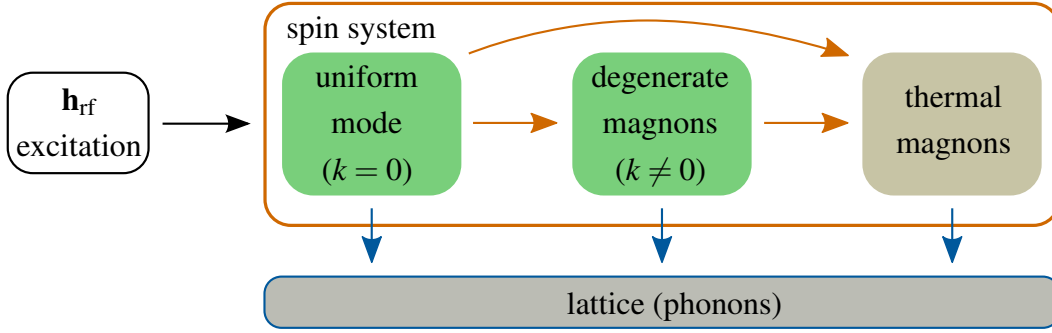


Figure 2.6: Relaxation channels of a spin system excited by a microwave field \mathbf{h}_{rf} . Orange colored transitions mark dissipations inside the magnonic system (spin-spin relaxation). Depicted in blue are relaxation paths transferring the energy to the lattice (magnon-phonon relaxation). Magnonic states of the same energy are colored green. Adapted from Ref. 75.

be described below. Additional magnon processes may follow, e. g. three-magnon processes splitting or confluence magnons, distributing the energy in the spin system until a thermal equilibrium is established. The thermalized spin system itself exhibits a higher temperature compared to the lattice. Hence, the energy is finally transferred via magnon-phonon processes to the thermal bath, simply speaking heating the sample. A detailed review of the relaxation channels is provided by Sparks [75].

An additional classification of relaxation channels is usually made concerning unavoidable, intrinsic and avoidable, extrinsic contributions [85]. In this framework major relaxation contributions will be discussed below, experimentally obtained by measuring the linewidth $\Delta H_{\text{pp}} = 2\Delta H/\sqrt{3}$ of the field-sweep resonance signal⁵. In general, relaxation rates are proportional to the frequency-sweep linewidth $\Delta\omega$, but can be converted using [75, 86, 87]

$$\Delta H = \frac{dH_{\text{res}}}{d\omega} \Delta\omega, \quad (2.51)$$

where the derivative has to be taken at resonance, as for example defined by Eq. (2.35). The only extrinsic relaxation contribution that will be discussed in this work is two-magnon scattering. Others, i. e., spin pumping may be found in Ref. 59.

2.3.1 Phenomenological description

A phenomenological description of intrinsic damping is based on the solution of the LLG equation (2.30). It describes the decay of $k=0$ magnons directly into the thermal bath (provided

⁵The factor $2/\sqrt{3}$ originates from the Lorentzian model function typically used to evaluate measured data and will be discussed in Chapter 3.

by the lattice). As a consequence of reducing the overall number of magnons, \mathbf{M} spirals towards the effective field while its length conserves, and hence, its projection onto \mathbf{H}_{eff} increases [see Fig. 2.2(b)]. The general, angle-dependent linewidth is derived by solving the LLG equation for small, damped oscillations providing the resonance condition $\omega(H)$ and the linewidth $\Delta\omega$. By using the conversion⁶ (2.51) one finds [58, 70, 88]:

$$\Delta H_{\text{pp}}^{\text{G}} = \frac{2}{\sqrt{3}} \frac{1}{\left| \frac{\partial \omega}{\partial H_{\text{res}}} \right|} \frac{G}{M_{\text{s}}^2} \left(\frac{\partial^2 F}{\partial \theta^2} + \frac{1}{\sin^2 \theta} \frac{\partial^2 F}{\partial \varphi^2} \right) \quad (2.52)$$

$$= \frac{2}{\sqrt{3}} \frac{G}{\gamma^2 M_{\text{s}}} \frac{\omega}{\Xi}. \quad (2.53)$$

Ξ is the dragging function, accounting for the fact that in a field-sweep resonance experiment the microwave frequency is fixed while the field changes in magnitude. Since the magnetization aligns with the effective field, which in turn depends on the anisotropy, its equilibrium position may not correspond to the external field direction but rather is dragged behind the field. A simple approximation for an in-plane angular dependence yields $\Xi \approx \cos(\varphi - \varphi_{\text{H}})$ [89]. Determining the Gilbert damping term under a fixed angle along an easy or hard magnetization direction yields a linear dependence on the microwave frequency since Ξ becomes unity. However, the linearity in ω is a consequence of the measurement setup sweeping the field. For other techniques measuring at fixed fields this relation becomes invalid [66].

While carrying out the conversion from frequency- to field-swept linewidth the resonance condition may exhibit anisotropy contributions depending on the resonance frequency ω . Such dependences may occur for a spatial distribution of the resonance condition, e. g. slightly varying anisotropy axes generated by roughness. As a result, local resonances at slightly different fields evolve, superimposing to a single line causing an increased field-sweep linewidth. This effect, called mosaicity or inhomogeneous broadening, is treated by taking the frequency dependence for additional parameters in the derivation of Eq. (2.51) into account [86]:

$$\Delta H_{\text{pp}}^{\text{mos}} = \Delta H_{\text{pp}}^{\text{inhom}} + \frac{2}{\sqrt{3}} \sum_i \left| \frac{\partial H_{\text{res}}}{\partial \Delta x_i} \right| \Delta x_i. \quad (2.54)$$

Here $\Delta x_i = \frac{\partial \Delta x_i}{\partial \omega} \Delta \omega$ is used as well as a frequency-independent inhomogeneous broadening $\Delta H_{\text{pp}}^{\text{inhom}}$.

2.3.2 Physical origin of intrinsic processes

Intrinsic damping, described by Gilbert damping using Eq. (2.53), has its origin in three major effects: (i) eddy currents, (ii) magnon-phonon interaction, and (iii) interactions of itinerant

⁶If $y = f(x)$ is a differentiable and invertible function, the relation $dx/dy = [dy/dx]^{-1}$ (for $dy/dx \neq 0$) applies to its inverse function $x = g(y)$.

electrons. In all these processes the energy is irreversibly transferred from the spin system to the lattice. Additionally, unavoidable perturbations add to purely intrinsic interaction, e. g. the presence of thermal magnons and phonons at finite temperatures, diffuse scattering at the film interfaces, and inhomogeneous electronic potentials in alloys. The following subsections will focus on two out of the three mentioned effects, since the magnon-phonon interaction is too small to explain the measured Gilbert damping [85,90].

Eddy currents

The precessional motion of the magnetization induces eddy currents in the sample that in turn influence the damping. Since the precession is caused by the microwave field, eddy currents depend strongly on the skin depth δ . It is defined as depth below the surface of a conductor at which the microwave amplitude decayed to $1/e$ of its original value from the surface:

$$\delta = \sqrt{\frac{2}{\omega\sigma\mu_r\mu_0}}. \quad (2.55)$$

σ denotes the electrical conductivity and $\mu_r = \mu/\mu_0 = 1 + \chi$ the relative permeability. For typical transition metals, δ is in the range of one micron if excited with 10 GHz [66].

However, in ferromagnetic materials the susceptibility strongly depends on frequency and increases when going through resonance. That in turn lowers the skin depth in FMR experiments. For the two materials used in this work to explore damping effects, Fe and Py, the role of eddy currents is insignificant below 25 and 100 nm, respectively, if excited at 10 GHz. A further decrease of eddy currents is achieved by decreasing the film thickness, since $G_{\text{eddy}} \sim d^2$ [66,91]. On the other hand, by increasing the excitation frequency ω a reduction of skin depth follows, as it can be seen easily from Eq. (2.55).

For films thicker or comparable to δ , the microwave field is inhomogeneous over the film thickness and exchange needs to be taken into consideration. Additionally, higher-order spin waves may be excited if the microwave field becomes inhomogeneous over the film thickness. Both, eddy currents and exchange coupling were first introduced by Ament and Rado [92]. The linewidth broadening due to eddy currents in the thick-film limit is proportional to $\sqrt{\sigma A}$, usually referred to as exchange conductivity.

In contrast, also in case of films with thickness smaller than the skin depth eddy currents may be important. In a theoretical study, Kostylev has shown that exciting bilayer films by microwaves incident on one surface may cause shielding effects due to eddy currents, which in turn give rise to an asymmetric resonance response. Thus, eddy currents may provide a possibility of studying buried interfaces [93].

Spin-orbit relaxation

As reviewed by Heinrich *et al.*, the main contribution to intrinsic damping originates from incoherent scattering of itinerant electrons by phonons and magnons, evolving in two relevant processes [85,90]:

(i) By coherently scattering magnons and itinerant electrons via s - d interaction a creation or annihilation of electron-hole pairs takes place. While s - d interaction conserves the angular momentum, magnon scattering causes a spin flip of the itinerant electron. In order to contribute to damping the coherent scattering needs to be disrupted to suppress the inverse scattering process that would re-emit an initial magnon. This happens by incoherently scattering the spin-flipped electron-hole pairs on thermally excited magnons or phonons and yields to a loss of the initial magnon and, hence, a damping of precessional motion [85,94]. For this, the relaxation of spin-flipped electron-hole pairs needs the inclusion of spin-orbit interaction. The finite lifetime τ_{sf} of the spin-flipped electron-hole pairs, as Elliot showed for simple metals [95], exhibits an inverse proportionality of the deviation of the g -factor from its purely electronic value ($g_e \approx 2$): $\tau_{\text{sf}} \sim \tau (\Delta g)^{-2}$. Here, τ determines the orbital momentum relaxation time. The damping constant G in turn is proportional to the spin-flip rate, thus: $G_{\text{LS}}^{\text{scatt}} \sim (\Delta g)^2 / \tau$.

(ii) The precessional motion of \mathbf{M} leads to a periodical distortion of the Fermi surface, since anisotropic spin-orbit interaction causes shifts in band energies of the electrons. This effect is referred to as breathing Fermi surface and causes a change in electron population due to shifting levels. As a consequence, a dissipative process happens mostly due to increased scattering probabilities within sub-bands of same spin states, which causes a delay in repopulation of the changing Fermi surface. The dissipative process leads to a damping of $G_{\text{LS}}^{\text{Fermi}} \sim \tau (\Delta g)^2$ [90,96].

Both processes exhibit phase lags, once between spin-flipped itinerant and localized electrons and on the other hand between distorted Fermi surface and magnetization precession, which is proportional to the microwave frequency ω . Thus, both processes lead to viscous, or Gilbert-like damping. In addition, τ enters the conductivity and causes G_{LS} in one case to (i) scale with resistivity and in the other (ii) with conductivity [85]. The damping constant also depends on the g -factor, which carries the spin-orbit interaction and should lead to an anisotropic damping described by a tensor $\hat{\mathbf{G}}$ rather than a scalar G . Nevertheless, it has been shown by Seib *et al.* that the anisotropic contribution in $\hat{\mathbf{G}}$ mostly averages out [97].

In fact, the outlined dependence on G_{LS} provides a rough estimation. More sophisticated treatments of spin-orbit interaction were performed e. g. by Kamberský [98,99].

2.3.3 Extrinsic contributions — Two-magnon scattering

First evidences of two-magnon scattering were observed in ferromagnetic insulators of bulk yttrium iron garnet (YIG) samples in 1958 [100]. A strong dependence of linewidth with respect

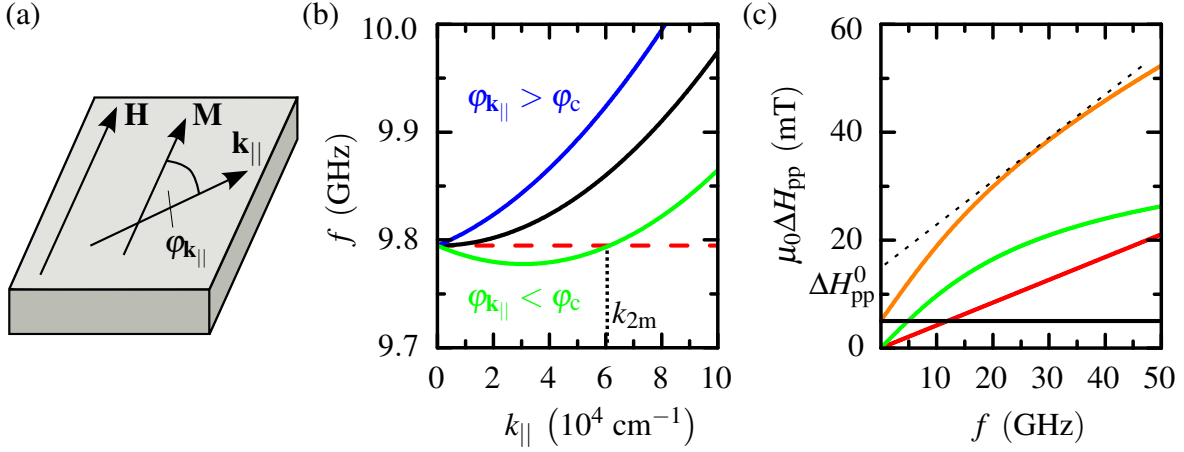


Figure 2.7: TMS in ultrathin films using Eq. (2.47). Except the film thickness, parameters are equal to Fig. 2.5. (a) In-plane geometry. (b) Dispersion relation for $\varphi_{\mathbf{k}_{\parallel}} < \varphi_c$ (green) exhibiting a degenerate state of wave number k_{2m} , $\varphi_{\mathbf{k}_{\parallel}} = \varphi_c$ (black), and $\varphi_{\mathbf{k}_{\parallel}} > \varphi_c$ (blue). The red dashed line corresponds to the FMR frequency. (c) Peak-to-peak linewidth along a principal magnetization axis (no influence of dragging): inhomogeneous broadening (black) with $\Delta H_{pp}^{\text{inh}} = 5$ mT, Gilbert damping (red) of $G = 2$ GHz, TMS (green) of $\gamma\Gamma = 5$ GHz, as well as the overall sum (orange). The dashed line shows the evaluation for Gilbert use only, resulting in a residual linewidth ΔH_{pp}^0 . Adapted from Ref. 105, 106.

to the sample's surface structure was seen, revealing the extrinsic nature of some contributing relaxation processes. Shortly thereafter, Sparks *et al.* developed a linewidth contribution based on defect-induced scattering of precessional energy of the uniform mode ($k_{\parallel} = 0$) into degenerate modes, well explaining the experimental observations on YIG samples [101]. An extension of the theory, among other things including thin films magnetized in an oblique out-of-plane direction, was presented by Hurben *et al.* [102, 103].

Although known since decades for bulk materials, the TMS relaxation channel was for a long time not considered for ultrathin films. Instead, the FMR community widely used the LLG approach for linewidth evaluations. In 1998 McMichael *et al.* presented a study of 10 nm ultrathin $\text{Ni}_{80}\text{Fe}_{20}$ films coupled to NiO, where the angular dependence was obtained by varying the magnetization from in-plane to out-of-plane orientation. The corresponding linewidth is in agreement with a presented two-magnon model of random perturbations originating from the coupling to the NiO underlayer [104]. Shortly thereafter, in 1999, Arias and Mills published their theory on TMS appearing in ultrathin films with in-plane magnetization [22]. In the following this theory and its conclusions will be discussed in detail, following the description of Refs. 22, 66.

Let's consider a film with perpendicular anisotropy $K_{2\perp}$, small enough to obtain an in-

plane magnetization orientation [see Eq. (2.48)]. Limiting the discussion to ultrathin films ($k_{\parallel}d \ll 1$) reduces the magnetic system to a quasi-two-dimensional system, where a variation of magnetization perpendicular to the film plane may be ignored. The confinement in addition influences the spin wave modes of the system. First, the ultrathin-film limit causes via exchange interaction an upward shift of the frequency of perpendicular standing spin waves with $k_{\perp} > 0$. This shift is above the FMR range and hence unimportant for relaxation [66]. A different picture emerges for in-plane propagating backward volume modes. A sketch of magnetization direction and spin wave propagation, including the angle $\varphi_{\mathbf{k}_{\parallel}}$ between both, is depicted in Fig. 2.7(a). Due to strong exchange interaction the usually parabolic spin wave dispersion ($\omega \sim k_{\parallel}^2$) exhibits an additional term linear in k_{\parallel} (for details see section 2.2.3). The situation is described by Eq. (2.47) and is shown in Fig. 2.7(b) for different propagation directions $\varphi_{\mathbf{k}_{\parallel}}$. For angles $|\varphi_{\mathbf{k}_{\parallel}}| < \varphi_c$ or $|\pi - \varphi_{\mathbf{k}_{\parallel}}| < \varphi_c$, where

$$\varphi_c = \sin^{-1} \sqrt{\frac{\mu_0 H}{\mu_0 H + \mu_0 M_{\text{eff}}}} \quad (2.56)$$

is the critical propagation angle, the term linear in k_{\parallel} in Eq. (2.47) is negative and causes a degeneration of the uniform precession mode at finite values of $k_{2\text{m}}$ [66]. Hence, it is possible to scatter energy from the initially excited $k = 0$ state into the degenerate magnon state $k = k_{2\text{m}}$. The energy pumped via resonant absorption into the magnetic system is transferred to the transverse components of \mathbf{M} by TMS. This reduces the number of uniform $k = 0$ magnons, but keeps the energy in the magnetic system as well as the overall number of magnons constant. As a consequence the LLG equation is inappropriate since it conserves the length of \mathbf{M} . Instead, Bloch-Bloembergen's equation (2.31) has to be used which provides two separate relaxation channels for longitudinal and transverse relaxation (see sect. 2.2.1). TMS only contributes to the latter channel by scattering energy into the transverse magnetization components and acts as a dephasing event. In contrast, the longitudinal component describes the relaxation to the thermal bath [59, 65, 66].

The presence of degenerate magnon states is associated with the external field. From Eq. (2.56) it is apparent that the critical angle φ_c decreases with magnitude of \mathbf{H} and finally, in the limit of $H \rightarrow 0$, the degeneration of the uniform mode is removed. Another limit arises from the direction of \mathbf{H} with respect to the film plane, as discussed by Erickson and Mills [107]. By tipping \mathbf{M} away from the surface degenerate FMR modes may only occur if $\eta_c < \pi/4$ is satisfied, where η_c is the angle between magnetization and film plane [66]. Especially the latter limitation provides an experimental proof for TMS in the film plane.

The theory on TMS, presented by Arias and Mills [22, 66], assumes rectangular bump- or island-like surface defects of random distribution with identical orientation and size, small compared to the wavelengths of involved modes. These surface or interfacial defects activate

the scattering process from the initially excited to the degenerate magnon state, conserving the energy rather than momentum. The coupling between both states is mediated by a matrix element, which is given by a Fourier transform (FT) of the defect structure [85]. Three contributions enter the matrix element: (i) a perturbation of the Zeeman energy, (ii) a distorted dipolar field from moving spins, and (iii) strong surface and interfacial anisotropies. Here, the latter has been identified to be the dominant contribution. By calculating the response function of the film one obtains the contribution to the linewidth. Because difficulties may arise in calculating the matrix element for realistic sample structures the linewidth for experimental situation with in-plane magnetization may be evaluated by using [22, 108]

$$\Delta H_{\text{pp}}^{2m} = \frac{2}{\sqrt{3}} \Gamma \sin^{-1} \sqrt{\frac{\sqrt{(\omega_0/2)^2 + \omega^2} - \omega_0/2}{\sqrt{(\omega_0/2)^2 + \omega^2} + \omega_0/2}}, \quad (2.57)$$

with $\omega_0 = \gamma\mu_0 M_{\text{eff}}$. The factor Γ is the squared matrix element responsible for the scattering and, therefore, depends on the sample's defect structure.

Apparent from Eq. (2.57), TMS—in contrast to Gilbert-like damping—is nonlinear in FMR frequency ω . In this way, a method for disentangling linewidth contributions measured by FMR is given by determining the frequency dependence of the linewidth. A schematic sketch comparing the frequency dependence of spin-spin and spin-lattice relaxation is shown in Fig. 2.7(c). Prior to the TMS theory of ultrathin films the community determined relaxation rates by applying Gilbert-like damping combined with a residual linewidth $\Delta H_{\text{pp}}^0 = \Delta H_{\text{pp}}(\omega = 0)$, only. The latter was assumed to contain extrinsic contributions resulting from inhomogeneities [109–111]. Together with the limited amount of data points, originating from conventional FMR setups having a fixed number of excitation frequencies (see sect. 3.1), the suggested linear behavior of linewidth vs. frequency may lead to a misinterpretation of linewidth and damping contributions [59, 65]. The dashed black line in Fig. 2.7(c) illustrates the misleading linear assumption.

The first confirmation of the TMS theory of Arias and Mills was done by studying the thickness dependence of Ni₅₀Fe₅₀ thin films observing influences on the field-sweep linewidth as well as on the resonance position [23]. Frequency-dependent investigations of ultrathin Ni₈₀Fe₂₀ samples measured with a sufficiently high number of points revealed a slightly nonlinear dependence of the linewidth if defects were introduced in the samples [112]. First quantitative evaluations of frequency-dependent linewidth taking TMS into account were done by Lindner *et al.* investigating Fe/V superlattices, pseudomorphically grown on MgO [106]. Fitting the data using Eqs. (2.57) and (2.53) revealed a reasonably well coincidence, where no residual linewidth ΔH_{pp}^0 was observed. Values for the squared matrix element Γ were directly obtained via fitting the data, circumventing the need of a specific model. Measurements along different directions revealed anisotropic TMS relaxation rates $\gamma\Gamma$ about two orders of magni-

tude faster than Gilbert damping [65, 106]. Measurements on an extended frequency range support these findings and, in addition, angle-dependent measurements proof the anisotropy of TMS [113]. Subsequent investigations on Fe₃Si proved TMS to be also present in ultrathin single ferromagnetic layers [86]. There as well, TMS relaxation was faster than Gilbert damping, although merely by one order of magnitude. But also in case of purely crystalline Fe ultrathin films TMS was observed, which was attributed to the presence of lattice defects [114].

However, both models discussed above have their justifications depending on the relative strength of local effective fields (influenced by perturbations) compared to magnetic interactions. Strong perturbations lead to a local variation of the effective field resulting in a superposition of noninteracting regions with slightly different resonances. If these local fields⁷ simply add up to the applied field, a constant contribution (mosaicity) adds to the linear⁸ Gilbert-like damping. In contrast, weak perturbations cause basically a uniform precession, where the perturbations trigger an energy transfer from the uniform mode to other spin wave modes (TMS) [115, 116]. As discussed in reference [116] Gilbert-like damping may also have a significant influence on TMS.

So far, TMS was considered as a consequence of random defects. However, by utilizing ordered defect structures McMichael *et al.* demonstrated a possibility to adjust TMS [117]. Two kinds of grooved substrates were produced, one using a lithographic approach and another by mechanical abrasion with subsequent deposition of a thin Ni₈₀Fe₂₀ layer (50 and 65 nm). At first, the lithographic approach showed a splitting of resonances as well as regions of increased linewidth in the in-plane angular dependence, qualitatively explained by superimposed resonances. Mechanically grooved sample in turn revealed an in-plane angle-dependent linewidth that is in good agreement with the model of TMS. The uniform precession is only scattered into degenerate spin wave modes if the corresponding wave vector is perpendicular to the grooves, which leads to an increase in linewidth [117]. Both in-plane angle-dependent linewidth measurements cannot be explained by a simple proportionality to local angular dispersion (mosaicity and intrinsic Gilbert damping). In addition, the frequency-dependent linewidth of this periodically perturbed film exhibits a linear dependence parallel to the grooves, but a nonlinear, non-monotonous bump-like behavior when measuring perpendicularly [112]. This dependence cannot be explained with the theory of random defects introduced above and will be addressed in Chapter 6.

It should be noted that TMS has not only a strong impact on linewidth, but it is also accompanied by a shift in resonance field [22, 66]. Such a shift is also the case for Gilbert-like damping, but negligible for all practical situations [66]. A simplified expression of the form

⁷compare with mosaicity (2.54)

⁸if $\mathbf{M} \parallel \mathbf{H}$ applies

derived in [22] is presented by Azevedo *et al.* [23]:

$$\delta H = \frac{16s}{\pi D} \ln \left(\sqrt{\frac{q_m}{q_0}} + \sqrt{1 + \frac{q_m}{q_0}} \right) H_{2\perp}^2. \quad (2.58)$$

The shift of the resonance position depends strongly on the surface anisotropy field $H_{2\perp} = 2K_{2\perp}/(\mu_0 M_s)$ [cf. Eq. (2.21)] and a geometrical factor covering surface roughness:

$$s = ph^2 \left(\left\langle \frac{a}{c} \right\rangle - 1 \right). \quad (2.59)$$

This factor in turn is composed out of the fraction p of the surface covered with defects (average height/depth h , and lateral dimensions a and c). In addition, Eq. (2.58) contains a characteristic volume mode wave number $q_0 = \mu_0 M_s d / (2D)$ and a cutoff wave number $q_m = 1/\langle a \rangle$. Considering a film with strong surface anisotropy of $H_{2\perp} = -0.31$ T, Azevedo and coworkers found a shift in δH of 7.7 mT in a $d = 2.7$ nm thin $\text{Ni}_{50}\text{Fe}_{50}$ film. In comparison, a shift attributed to Gilbert damping is in the order of 10^{-3} mT. Since the surface anisotropy is inversely proportional to the film thickness [see Eq. (2.25)] the effect is most important for ultrathin films.

Finally, Arias and Mills [22] discuss one further issue associated with TMS. As a result of surface defects internal magnetic fields are no longer uniform and, hence, may influence the shape of the response function and thus the FMR absorption line. An approximation for Fe films revealed a correction of integrated strength of the absorption signal by one percent as well as a quite small deviation from the symmetric Lorentzian line shape (see Chapter 3). Thus, in this case the effect plays a minor role.

In conclusion, the linewidth measured in FMR experiments may not be directly interpreted as magnetization damping, since damping describes the dissipation of energy from the excited spin system to the thermal bath of the lattice. Considering TMS in a FMR experiment, the energy pumped into the excited uniform mode ($k_{\parallel} = 0$) is distributed within the spin system to high-order spin wave modes ($k_{\parallel} \neq 0$). These modes are in turn coupled to the thermal bath or even scatter back to the uniform mode. Hence, the damping of $k_{\parallel} \neq 0$ modes needs to be taken into account as well. In addition, since TMS shifts/splits the resonance position an apparent line broadening may appear by superimposing adjacent lines.

2.4 Ion beam erosion

Ion beam processes offer a great variety of sample modifications. Directing a broad ion beam onto a surface causes, strongly dependent on the mass ratio between ions and target atoms,

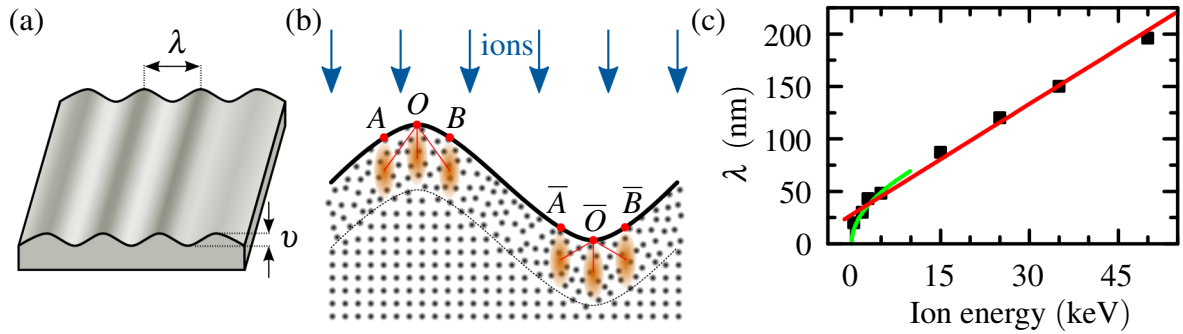


Figure 2.8: Ripple formation due to ion beam erosion. (a) Schematic sketch of a rippled Si surface (peak-to-peak amplitude v , wavelength λ). (b) Sketch of curvature-dependent energy deposition. The dashed line marks the transition from the amorphous surface region to crystalline bulk material. Collision cascades caused by ion strikes at the points A , B , and O (\bar{A} , \bar{B} , and \bar{O}) for the crests (troughs) are shown in orange. (c) Ripple wavelength λ in dependence on incident ion beam energy (by courtesy of S. Facsco and M. Fritzsche). Red and green lines represent the expected scaling behavior. Illustrations are adapted from Refs. 31, 32.

on the one hand ion implantation and surface erosion on the other hand. For instance, doping $\text{Ni}_{81}\text{Fe}_{19}$ thin films with Cr^+ ions results in a reduction of saturation magnetization as well as a modification of magnetic anisotropy and damping parameter α [118]. In order to obtain doping profiles numerical packages such as *TRIDYN* are available [119, 120]. This package also takes simple ion beam erosion effects into account. A special form of ion beam erosion leading to self-organized surface patterns will be discussed in the following by outlining the principle mechanisms.

Ions impacting the surface partially transfer their energy to atoms within the implantation range, which in turn may collide with others forming a collision cascade. By this, atoms may be accelerated towards the sample surface and leave the sample. In this case the corresponding atom is sputtered. Accompanied with this surface erosion smoothing or stochastic roughening can be induced. Especially surface roughening provides an excellent way to study morphology effects on magnetic layers.

Depending on the irradiation conditions periodic self-organized surface patterns evolve for instance into dots or ripples [121–123]. In a simple approximation the latter resemble sinusoidal surface modulations as shown in Fig. 2.8(a). However, due to the angle between incident ion beam and surface normal the ripple slopes become asymmetric in dependence of the primary ion energy. For simplicity the following explanation assumes sinusoidal modulations. The formation process was first described by Bradley and Harper (BH) [31] who combined surface diffusion with the sputter theory formulated by Sigmund [124]. Here the sputter yield, defined as ratio between incident ion flux and flux of emitted atoms, exhibits a curved dependence

that enhances the surface roughness. For more advanced theories the reader is referred to Refs. 121–123.

Starting with a crystalline Si semiconductor surface, ion bombardment leads to atomic displacements and consequently to an amorphous surface layer. Both, amorphous layer and crystalline bulk material are shown in Fig. 2.8(b), where the dashed line marks the transition region. Additionally, ion bombardment leads to sputtering and causes a stochastically surface roughening. Figure 2.8(b) also shows the spatial energy distribution of single ion impacts (orange ellipses) of assumed Gaussian shape. With respect to depth these profiles follow the surface corrugation caused by the same mean ion penetration $\rho(E)$, which depends on the ion energy E . Ions entering a crest at point A , B , or O deposit their energy at the same depth below these points. The same holds true for impacting ions in a trough (points \bar{A} , \bar{B} , and \bar{O}) causing the same deposited energy by ions striking in O and \bar{O} . However, the contribution to the sputter yield at the surface differs in troughs (point O) and crests (point \bar{O}). By comparing the mean deposited energy at O with \bar{O} one finds a greater contribution from ion impacts in \bar{A} , \bar{B} to the sputter yield in \bar{O} than caused by strikes in A , B contributing to sputtering in O . This curvature dependence is caused by a shorter distance from the mean energy deposition depth to \bar{O} in the crests compared to troughs. As a result the surface roughness is enhanced by an ion-induced surface instability, also known as surface micro-roughening. In competition with surface diffusion, whether thermally or ion induced, the most unstable wavelength grows fastest and forms the rippled surface pattern [31, 122].

With the presented approach some major experimental findings in the early stage of the pattern evolution, like ripple orientation with respect to incident ion beam and initial growth of ripple amplitude ν , are described. Also an expression for the wavelength λ can be given that depends on the mean ion penetration depth ρ and the sputter rate Y , where both quantities depend on the incident ion energy E [32]:

$$\lambda \sim \frac{\rho(E)}{\sqrt{Y(E)}}. \quad (2.60)$$

The experimentally observed energy dependence of the wavelength is depicted in Fig. 2.8(c) and has been obtained by irradiating Si with Ar^+ or Xe^+ ions under an angle of 67° with respect to the substrate's normal. In the low-energy range a square root behavior is observed (green curve), whereas the medium energy range exhibits a linear dependence (red curve) on the ion energy [32]. The ripple amplitude predicted by the BH theory should grow exponentially. In contrast, experimental observations with long sputtering times show a saturation leading to a fixed aspect ratio (amplitude/wavelength) of approximately 0.2. Using the energy dependence provides a powerful tool to change the surface morphology and, by this, influence the properties of magnetic layers deposited on top.

3 Ferromagnetic resonance

In the following chapter, the basics of ferromagnetic resonance and its experimental realizations are discussed. For this, the theoretical background of coplanar waveguides, its influence on the measurement, and network analysis under the use of a vector network analyzer (VNA) will be given. Then the arising measurement modes (field or frequency sweep) will be discussed and, based on preliminary measurements, a suitable mode will be selected in order to obtain precise results for anisotropy and linewidth of the investigated films.

With respect to anisotropy all investigated thin films can be described by a tetragonally distorted system with an in-plane uniaxial anisotropy. Based on Eqs. (2.20), (2.35), and (2.48) the resonance condition reads:

$$\begin{aligned}
 \left(\frac{\omega}{\gamma}\right)^2 = & \left\{ \mu_0 H [\sin \theta \sin \theta_H \cos(\varphi - \varphi_H) + \cos \theta \cos \theta_H] \right. \\
 & - \cos 2\theta \left[\mu_0 M_{\text{eff}} + \frac{2K_{2\parallel}}{M_s} \cos^2(\varphi - \varphi_u) + \frac{K_{4\parallel}}{4M_s} (3 + \cos 4\varphi) - \frac{K_{4\perp}}{M_s} \right] \\
 & \left. + \cos 4\theta \left[\frac{K_{4\parallel}}{4M_s} (3 + \cos 4\varphi) + \frac{K_{4\perp}}{M_s} \right] \right\} \\
 & \times \left\{ \mu_0 H [\sin \theta \sin \theta_H \cos(\varphi - \varphi_H) + \cos \theta \cos \theta_H] \right. \\
 & - \cos^2 \theta \left[\frac{K_{4\parallel}}{2M_s} (3 + 5 \cos 4\varphi) + \frac{2K_{2\parallel}}{M_s} \cos^2(\varphi - \varphi_u) + \mu_0 M_{\text{eff}} \right] \\
 & \left. + \cos^4 \theta \left[\frac{K_{4\parallel}}{2M_s} (3 + \cos 4\varphi) + \frac{2K_{4\perp}}{M_s} \right] + \frac{2K_{2\parallel}}{M_s} \cos 2(\varphi - \varphi_u) + \frac{2K_{4\parallel}}{M_s} \cos 4\varphi \right\} \\
 & - \left[\frac{K_{2\parallel}}{M_s} \sin 2(\varphi - \varphi_u) + \frac{3K_{4\parallel}}{2M_s} \sin 4\varphi \sin^2 \theta \right]^2 \cos^2 \theta. \tag{3.1}
 \end{aligned}$$

Here the geometry shown in Fig. 2.1 was assumed. To determine anisotropy using FMR the resonance condition shown above has to be evaluated for a set of different field angles (or frequencies) treating K_i as fit parameters. Varying the azimuthal angle φ_H or the polar angle θ_H allows to determine the in-plane or out-of-plane anisotropy, respectively. Alternatively, but accompanied by increased fit uncertainties, $f(H)$ curves can be recorded under fixed geometry. Whichever method is used, the saturation magnetization must be known in order to obtain anisotropy constants K_i . For unknown M_s anisotropy fields $2K_i/M_s$ are determined instead.

Only in special cases FMR is capable of measuring M_s directly, i. e., if $K_{2\perp}$ vanishes and the effective magnetization [cf. Eq. (2.48)] equals the saturation magnetization [125]. Otherwise a reference is needed [126].

As already mentioned in section 2.2.2 two possibilities exist to fulfill the resonance condition. In conventional, cavity-based FMR systems the excitation frequency is fixed while the field is swept (H -sweep mode), whereas broadband approaches sweep the frequency of the excitation field by keeping the external field constant (f -sweep mode). Usually the H -sweep mode is widely used since it is much easier to sweep a magnetic field rather than a microwave frequency. In addition, setups using a microwave cavity are limited to a narrow frequency range making it impossible to sweep the microwave frequency. With the rise in vector network analyzer techniques the possibility was given for a broadband microwave source that can be utilized for both methods. Although cavity-based FMR was not applied in the present work a brief overview on the technique will be given in order to get an impression on advantages and disadvantages about both methods and, more important, to gain an understanding of the recorded spectra. For detailed descriptions on cavity-based FMR the reader is referred to Refs. 29, 126–128. In the framework of this thesis, VNA-FMR was applied based on a coplanar waveguide (CPW) technique providing both sweep methods. These modes will be addressed as f -sweep and H -sweep VNA-FMR, respectively.

3.1 Cavity-based FMR

In this approach a microwave is generated by a klystron and sent through a waveguide to a splitter. There the signal is divided into measurement and reference signal. Subsequently, the measurement signal is attenuated and fed through a circulator into the cavity. The part of the microwave that is reflected by the cavity is passed by the circulator to a detection diode where it meets with the reference signal. Finally, the diode generates a voltage serving as measurement signal. Inside the cavity the injected microwave forms a standing electromagnetic wave. The coupling of microwaves to the cavity is tuned by matching the cavity's eigenfrequency with the excitation frequency, where in case of perfect coupling all microwave energy is absorbed. In general, the ratio of stored energy in the cavity and dissipated energy per time unit is described by the quality factor Q .

The cavity is placed inside the poles of an electromagnet that generates a magnetic field. By placing a magnetic sample inside the cavity it becomes detuned if the external field is swept and the sample goes through resonance. The power absorbed by the sample is proportional to χ'' . Moreover, the cavity detuning causes a reflection of microwave signal, which in turn generates the measurement signal. If the excitation frequency follows the eigenfrequency of the system

cavity/sample the quality factor is kept at its maximum and dispersive parts are stabilized out. Hence, an absorption spectrum is measured (see Fig. 2.3) corresponding to the change in Q . If instead the excitation frequency is fixed one observes either dispersion, absorption, or a mixture of both corresponding to the change of resonant frequency. The observed signal depends on the phase between measured and reference signal, where the phase of the latter can be adjusted when both are again mixed together [127].

Measurements are usually carried out by recording absorption spectra (see Fig. 2.3). As mentioned earlier, results obtained under small-enough microwave fields and damping correspond to a Lorentzian curve that is described by [127]:

$$L_{\text{abs}}(H) = -\frac{A_{\text{abs}}}{1 + \left(\frac{H-H_{\text{res}}}{\Delta H}\right)^2}. \quad (3.2)$$

Here, ΔH accounts for the half width half maximum linewidth, A_{abs} is the signal's amplitude, and H_{res} the resonance position. To enhance the measured signal lock-in techniques are widely used that modulate the external field. By this the derivative of the absorption signal will be measured, given by the expression [127]

$$\frac{dL_{\text{abs}}}{dH}(H) = -\tilde{A}_{\text{abs}} \frac{16 \frac{H-H_{\text{res}}}{0.5\Delta H_{\text{pp}}}}{\left[3 + \left(\frac{H-H_{\text{res}}}{0.5\Delta H_{\text{pp}}}\right)^2\right]^2}, \quad (3.3)$$

where \tilde{A}_{abs} is the function's amplitude. In contrast to the symmetric peak of an absorption signal its derivative has two peaks, antisymmetric with respect to resonance position and resembling that of a dispersion curve¹ (cf. Fig. 2.3). Due to that an alternative definition of linewidth, namely ΔH_{pp} , can be used that accounts for the H distance between these two peaks. By simple algebra one finds the connection to known linewidth values as [127]:

$$\Delta H_{\text{pp}} = \frac{2}{\sqrt{3}}\Delta H. \quad (3.4)$$

When recording dispersion signals the corresponding Lorentzian function reads [127]

$$L_{\text{disp}}(H) = -A_{\text{disp}} \frac{2 \frac{H-H_{\text{res}}}{\Delta H}}{1 + \left(\frac{H-H_{\text{res}}}{\Delta H}\right)^2}, \quad (3.5)$$

where A_{disp} is the function's amplitude. Note that the peak-to-peak linewidth of a dispersion curve equals twice the FWHM linewidth, as can be seen clearly from Fig. 2.3. Due to frequently used absorption-derivative measurements in the past it is common to determine peak-to-peak linewidth values as defined by Eqs. (3.3) and (3.4). Also in the present thesis linewidth values will be given as peak-to-peak distances referring to the width of an absorption-derivative signal.

¹Compared to dispersion curves the absorption derivative exhibits much broader peak widths in case of identical parameters.

3.2 Vector network analyzer FMR

The cavity approach of FMR limits the experiment to a single excitation frequency. Changing the frequency is always accompanied by a cavity and setup change. Such setup changes are not only time consuming, but in particular involve slight changes in the measurement geometry. If e. g. $f(H)$ curves are measured the external field configuration may slightly differ after changing the cavity, which limits the achievable accuracy. Instead, a broadband approach is much more convenient and is obtained by replacing the cavity by a coplanar waveguide. The latter is connected to a VNA, serving as broadband microwave source and detector simultaneously. Samples are placed upside-down onto the CPW so that the emitted microwave field permeates the magnetic layer and a change in microwave signal, dependent on the externally applied magnetic field, can be recorded. In the following section, the essential components of VNA-FMR will be introduced, followed by a description of the setup used in this thesis.

3.2.1 Coplanar waveguide

A coplanar waveguide consists of three conductors of thickness d aligned in a plane and placed on top of a dielectric substrate of thickness h . The microwave signal is applied to the center strip conductor (signal line) with width w . It in turn is separated by narrow gaps on each side followed by ground planes in the distance s .

A corresponding cross-sectional sketch of the geometry is shown in Fig. 3.1. In addition, the electromagnetic field configuration is shown for a quasi-static approximation. As sketched, the magnetic field evolves transversal to the conductor plane and is reversely oriented above the ground lines with respect to the signal line. Indeed, since the ground lines are much broader and carry just half the current of the center strip the field generated above these is much weaker. Between the conductors the magnetic field turns perpendicularly to the plane to reverse its direction. The propagation of the electromagnetic wave along the conductor lines takes place as transversal electromagnetic mode (TEM). However, since the electromagnetic field propagation appears in air as well as in the dielectric substrate, a longitudinal magnetic component evolves that is caused by different phase velocities. Mostly, the substrate is electrically thin enough ($h \ll \lambda$) ensuring negligible longitudinal components. For this case the propagation mode is referred to as quasi-TEM. Nevertheless, at sufficiently high frequencies the longitudinal components become non-negligible causing non-TEM propagation. Beyond, parasitic modes may propagate if e. g. a conductor backed (grounded) CPW is used for stability reasons [129]. To suppress these modes a set of construction efforts may be made, i. e., shields, microwave absorbers, or conducting bridges (vias) through the substrate to connect top and bottom ground

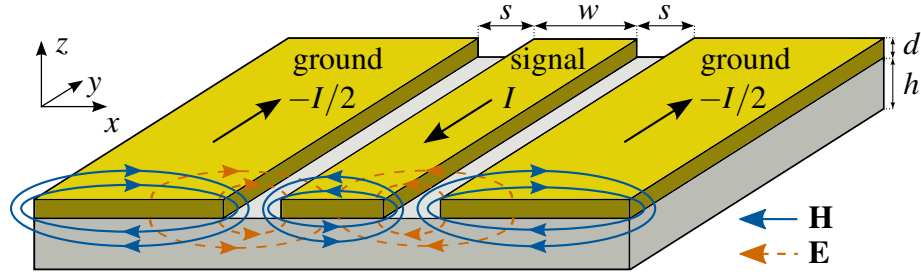


Figure 3.1: Cross-sectional geometry of a coplanar waveguide (after Ref. 129). Depicted are the electric and magnetic field components of the transversal electromagnetic wave in quasi-static approximation. For simplicity additional elements, such as bottom ground planes and vias, are not shown.

planes.

For effective microwave injection into the CPW with minimal losses its characteristic impedance has to match those of the microwave source and subsequent detector, which is usually 50Ω for microwave devices [130]. This can be achieved by properly designing the dimensions of substrate, conductors, and shields.

3.2.2 Vector network analysis

Together with the sample and connected transmission lines the CPW forms a two-port device that exhibits a characteristic frequency behavior. To specify the response of such an unknown linear² network at high frequencies (hf), the use of scattering parameters S is common. These have—in comparison to voltage and current measurements—the advantage of being quite easy to accomplish. In addition, connecting undesirable loads when measuring a device under test (DUT), or even short it, is not necessary. At this, S -parameters are defined in terms of voltage traveling waves. Following the generally used terms, waves entering the two-port device on port one (two) are denoted by a_1 (a_2), whereas waves leaving port one (two) are termed by b_1 (b_2), respectively. The transmission as well as reflection of incident waves is covered by the scattering matrix $\bar{\mathbf{S}}$ [131]:

$$\begin{pmatrix} b_1 \\ b_2 \end{pmatrix} = \bar{\mathbf{S}} \begin{pmatrix} a_1 \\ a_2 \end{pmatrix}, \quad \text{with} \quad \bar{\mathbf{S}} = \begin{pmatrix} S_{11} & S_{12} \\ S_{21} & S_{22} \end{pmatrix}. \quad (3.6)$$

²Linear devices apply magnitude and phase changes to incident waves, whereas nonlinear devices may shift the signal frequency and/or create new signals by intermodulation or in form of harmonics [130].

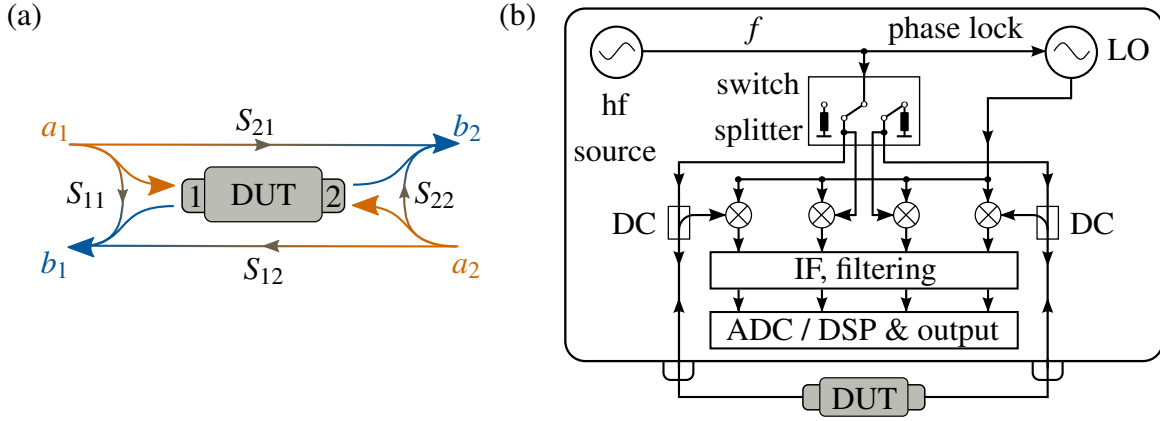


Figure 3.2: Network analysis on a two-port device under test (DUT). (a) Visualization of S -parameters S_{ij} and related complex incident a_j and outgoing waves b_i . Adapted from Ref. 130. (b) VNA architecture for measuring S -parameters on a two-port device. The used abbreviations are explained in the text. After Refs. 130, 133.

Here, a wave emitted on any port of the DUT is a linear combination of all incoming waves. The elements of $\bar{\mathbf{S}}$ are determined by

$$S_{ij} = \left. \frac{b_i}{a_j} \right|_{a_i=0}, \quad (3.7)$$

where two identical indices describe reflection, whereas different indices account for signal transmission. In this case $i(j)$ labels the port where the signal leaves (enters) the DUT [130, 131]. Hence, knowing the complete set of S -parameters fully characterizes any linear device. A sketch of the situation is shown in Fig. 3.2(a).

Depending on the characteristics of the network some simplifications apply to $\bar{\mathbf{S}}$ [131, 132]. Here, only the reciprocal network should be mentioned, exhibiting identical transmission characteristics independent on which port the signal is injected. As a result $S_{12} = S_{21}$ holds true, which is the case for networks that contain no active devices, ferrites, or plasmas [132].

The S -parameters are measured using a VNA that is connected to the two ports of the DUT, as it is depicted in Fig. 3.2(b). In this thesis, an Agilent PNA E8364B two-port VNA was used. While a (scalar) network analyzer measures only the signal magnitude, a vector network analyzer in addition provides phase information, which results in complex S_{ij} and enables the possibility of calculating the complex magnetic susceptibility. To measure all four S -parameters a built-in synthesized source provides a microwave at the desired frequency f . This signal is passed to a switch splitter that splits it into a reference and test signal. In addition it switches between port one and two of the VNA to enable forward and reverse measurements and internally terminating the currently inactive port. While the reference signal is routed

directly to the appropriate receiver, the test signal is passed through a directional coupler either out to port one or two, both connected to the DUT. Signals that are transmitted through or reflected from the DUT are passed by the directional couplers to the receivers [133].

For detecting high-frequency signals a tuned receiver is used where a local oscillator (LO) is phase locked with the reference signal mixing the input signal down to a lower intermediate frequency (IF). The IF signal then is bandpass filtered, sent to an analog-digital converter (ADC), and is finally digitally signal processed (DSP) in order to obtain magnitude and phase information. Details of the used VNA including all its components can be found in Ref. 130.

To reduce systematic errors, e. g. due to imperfections of VNA components and parasitic reflections at connections, the VNA provides the possibility for error correction and calibration (for further information see Refs. 134, 135). Parasitic reflections occur e. g. if the termination of the inactive VNA port does not match the connected load. In this case Eq. (3.7) is violated and incorrect results are obtained. A calibration can account for contributions caused by cables and connectors attached to the DUT, which moves the reference plane to the DUT and hence excludes setup influences in the obtained parameters. Therefore, a full two-port error correction is performed by connecting an electronic calibration (ECal) kit to the cables that are usually attached to the CPW. This ECal kit provides well-known standards for short, open, load, and through by which it is possible to characterize the occurring error terms and mathematically correct it in future measurements.

3.2.3 Experimental setup

In comparison to cavity-based FMR a VNA approach offers a broad microwave range under which the sample can be excited without the need of changing the setup. In contrast, the spatially limited excitation field of the CPW lowers, together with missing lock-in technique, the sensitivity of VNA-FMR measurements. Additionally, the nonuniform microwave field may influence the linewidth of the measured response. This issue will be discussed in section 3.3.3. Nevertheless, VNA-FMR offers the unique possibility to study ferromagnetic resonance either by sweeping the field or the frequency. Especially when investigating special magnetization states the external field needs to be kept constant or even set to zero, which is impossible with classical systems. In the following the utilized, fully automated, VNA-FMR setup is introduced. Constructional details can be found in the thesis of D. Markó [136].

Figure 3.3(a) shows a sketch of the utilized VNA-FMR setup with a photograph depicted in part (b). The external magnetic field is generated by a commercial electromagnet (Bruker B-E 25v) capable of generating fields up to $\mu_0 H = 2.2$ T at a pole spacing of 4 cm. The electromagnet is powered by a bipolar power supply (BSMPS BIP 200/60 4Q) whose control

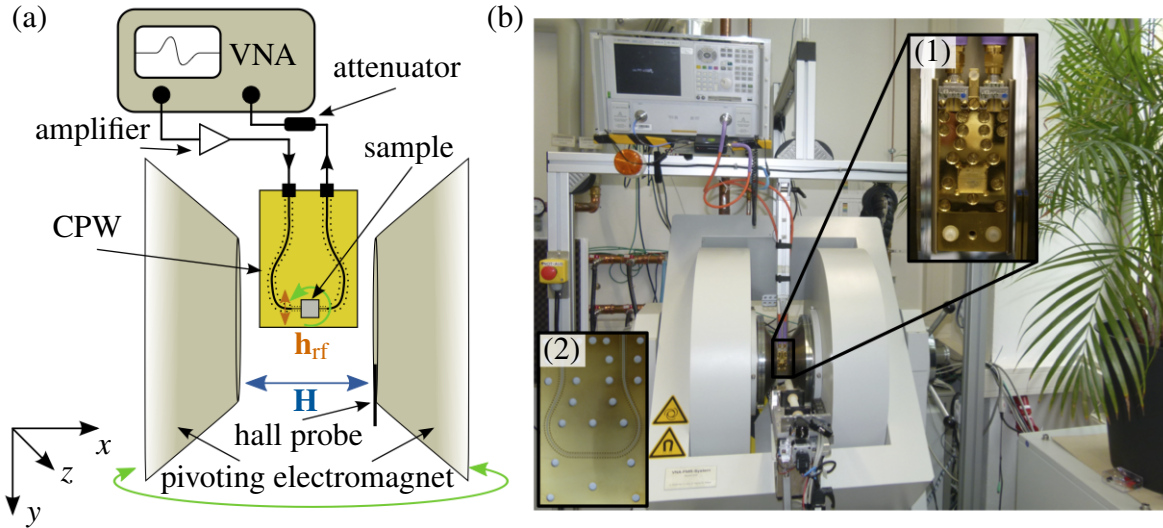


Figure 3.3: Experimentally used VNA-FMR setup. (a) System sketch containing the main components (amplifier and attenuator are used in H -sweep mode, only). Depicted in green are the rotational degrees of freedom. For simplicity control units and the sample holder are omitted. (b) Photograph of the system with insets showing (1) the shielded waveguide that is connected by transmission lines and (2) an unshielded CPW.

unit (B-EC1) allows either field- or current-swept measurements. The magnet itself is mounted on a pivot bearing that allows to rotate the magnetic field around the y axis. On one of the electromagnet's poles a hall probe of a digital teslameter (Projekt Elektronik Berlin FM 3000-BB-10) is attached and connected on the one hand to the magnet's control unit and on the other to a digital voltmeter (Keithley 3706 DMM). While the connection with the control unit enables an automatic field control, the voltmeter is used to measure quickly and much more precisely the actual magnetic field value. Between the poles the CPW is mounted whose shape is based on constructional issues. Due to limited space between the poles and to ensure rotational degrees of freedom, the microwave transmission lines have to enter from the top or bottom. However, because the microwave field has to be perpendicular to the external magnetic field in any measurement geometry, the sensitive part of the CPW needs to be parallel to \mathbf{H} . The CPW itself has an impedance of $Z_{\text{CPW}} = 50 \Omega$ and a metal ground on the backside, connected to the front ground planes by vias. Metalizations on both sides are made out of 50 nm TiW followed by 3 μm of Au. To have minimal losses only the straight center part at the bottom contains a narrow center conductor that is intended for measurements. At this position the center conductor has a width of $w = 80 \mu\text{m}$. Outside this area—the nonsensitive part—the width is increased up to $w = 500 \mu\text{m}$. Additionally, outside the sensitive area the whole plane is covered by a thick Au-plated copper plate to shield external rf fields. A detailed review on

the utilized CPW layout can be found in the thesis of D. Markó [136].

Finally, the waveguide is connected by nonmagnetic end launch connectors (Southwest Microwave 1492-04A-5) and transmission lines (MegaPhase RF Orange TM50-2125) to the two-port VNA (Agilent PNA E8364B) that provides microwaves in the frequency range between 10 MHz and 50 GHz with a maximum, frequency-dependent, output power between -10 dBm and $+5$ dBm. For transmission measurements only, an amplifier (Centellax TA0L50VA, amplification up to 27 dB) in front and a -20 dB attenuator behind the waveguide can optionally be inserted to enhance the magnitude of the generated microwave field. Behind the mount of the CPW a reference permanent magnet can be positioned pneumatically whose magnetic field is aligned parallel to the one created by the CPW and has a strength of approximately 100 mT at the sample's position. By that, necessary reference measurements for the f -sweep mode can be performed.

There are two ways for mounting the sample onto the CPW and realizing angle-dependent measurements. First, it can be fixed directly onto the waveguide. In this case the magnet has to rotate around the sample varying the field between in-plane and out-of-plane configuration. Such a measurement configuration will be termed as polar. The covered angular range extends from -40° to 195° and corresponds to a change of the magnetic field angle θ_H as depicted in Fig. 2.1. On a second holder the sample is mounted on a rod situated on a mechanical slider that presses the sample against the CPW. To change the in-plane orientation of the sample with respect to the CPW the slider lifts the sample and the rod rotates to the desired angular position. This configuration will be referred to as azimuthal. It covers the full angular range of 360° and changes the in-plane magnetic field angle φ_H , while $\theta_H = 90^\circ$ applies. Both holders are in addition suitable for frequency-dependent $f(H)$ measurements.

3.3 VNA-FMR operation modes

Since decades, owing to available setups, FMR was performed in H -sweep mode, insofar as it is much easier sweeping a magnetic field rather than a frequency. However, because the present setup is equipped with a network analyzer combined with a waveguide, additionally the f -sweep mode is an option that has to be considered when studying morphology-induced phenomena. To obtain best possible results both methods will be compared on practically relevant samples to finally decide for a measurement mode. Evaluation, visualization, and if necessary conversion of the measured data is carried out with a newly developed software package that will be introduced in appendix A.

3.3.1 Frequency-sweep VNA-FMR

Above all, the question arises how the measured scattering parameters are linked to the physical quantities of interest. Merely in the recent years, since this type of broadband FMR is relatively new, approaches have been developed to interpret the raw data. In a basic approach the magnetic susceptibility is given by the change in impedance over frequency caused by the presence of magnetic material attached to the waveguide [137]. Applying simple transmission line theory reveals the connection between S_{11} and impedance of the system and finally allows to calculate the complex susceptibility [138, 139]. However, this approach does not take wave propagation into account. In yet another approach simply the amplitude of the transmitted microwave signal S_{21} is considered [28]. There, the measured S_{21} peak width may not be directly related to the linewidth as the absorbed power can be influenced by $k \neq 0$ spin waves. The latter are caused by nonuniform excitations present in CPW structures and will be discussed in sect. 3.3.3. In addition, this approach does not provide complex-susceptibility calculations. Kalarickal *et al.* used transmission parameters to calculate a complex susceptibility while taking a reference measurement into account. Albeit, also in this case effects from reflections are neglected [87]. A full two-port treatment including wave propagation and reference measurements leading to a complex susceptibility was presented by Bilzer *et al.* [140, 141] and is based on permeability measurements presented decades ago [142, 143]. The authors, in addition, provide a comparison of their model with the two last-mentioned methods, finding well agreements for resonance frequencies (relative error $<1\%$), but a difference in linewidth of up to 10%. Hence, since this model accounts for more relevant effects, it will be the method of choice when analyzing f -sweep measurements.

To operate the introduced setup in f -sweep mode the amplifier as well as attenuator displayed in Fig. 3.3(a) have to be removed. The sample is placed with the magnetic film directly onto the sensitive part of the CPW to measure the full set of S -parameters at every excitation frequency while sweeping it through the desired range and keeping the external field constant. Measurements are carried out fully automatic using an available control software³ running in *LabVIEW*. In order to apply the susceptibility calculation introduced by Bilzer *et al.*, a two-port calibration of the VNA system was done as explained above. By this the reference plane is shifted from the VNA couple ports to the CPW connectors, which in turn means that the measured signal includes not only the magnetic but also the CPW response. To account for this the conversion algorithm uses two reference measurements: (i) a measurement done with an empty CPW and no external field, which captures the hf transmission characteristics of the waveguide and (ii) a measurement with the sample attached and saturated by the reference permanent magnet (the electromagnet is turned off). The reference magnet causes a static field

³for details see Ph.D thesis of D. Markó [136]

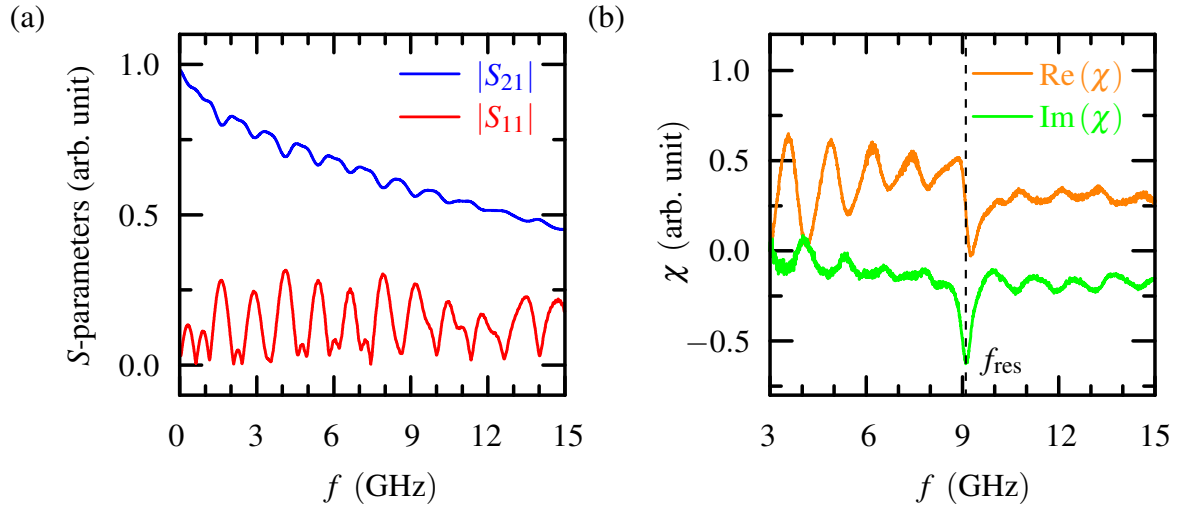


Figure 3.4: Frequency-swept VNA-FMR measurement of the ion beam patterned thin-film system Si/SiO₂/Py(30 nm)/Cr(3 nm), recorded under an external magnetic field of $\mu_0 H = 0.1$ T. (a) Absolute values of the microwave transmission S_{21} (blue line) and reflection S_{11} (red line) parameters. (b) Resulting real (orange line) and imaginary (green line) part of the susceptibility. In addition, the dashed line marks the film's resonance frequency f_{res} at this particular external field.

parallel to the exciting microwave field⁴ that suppresses resonances and is used to remove sample effects by subtracting the obtained background.

To illustrate the impact of this procedure, absolute values of measured scattering parameters will be compared against complex susceptibility determined on a sample of interest. The specimen used is made out of a 30 nm thin Py layer that was deposited on a naturally oxidized silicon substrate and subsequently capped by 3 nm of Cr. The final layer acts as protective barrier preventing the magnetic material from oxidation when exposed to ambient conditions. After layer deposition the sample has been partially irradiated with Cr⁺ ions to create a surface stripe pattern. Further details on the layout will be given later in section 6.1 or in Ref. 144. At this point of the discussion only the principle appearance of the measured spectra is of interest, which are recorded under comparable conditions, but using different sweep modes.

The measurement was done using an IF bandwidth of 1 kHz on the VNA, leading to a raw set of data as depicted in Fig. 3.4(a). For the sake of clarity, and because transmission and reflection parameters basically equal the case of reversed measurements, simply one set of

⁴This configuration is also known as parallel pumping and has to be repeated every time the sample position on the waveguide is altered. Alternatively, a measurement at high external fields, shifting the resonance out of the field of view, has a similar effect.

S -parameters, describing a microwave leaving port one, is shown. As it can be seen the raw data contain a strong background where basically no resonance signal can be distinguished. Only through the conversion to complex susceptibility, depicted in panel (b), a signal is observable. Due to strongly increased noise at low frequencies this part is cut out in the graph. In order to extract the signal's characteristic parameters the Lorentzian functions introduced above can be applied. In this place the absorption information is covered by the imaginary part of χ and hence fitted by using Eq. (3.2). Alternatively, the real part of χ corresponds to a dispersion signal and the fit-parameter extraction is done by use of Eq. (3.5), respectively. Both approaches lead to basically identical parameters, but it is often much easier to use the dispersion curve as its two antisymmetric peaks provide usually much better reference points for exact linewidth determination. However, since the background level is dominant it was often difficult to obtain precise parameters.

One reason for the relatively low signal-to-noise ratio (SNR) of this operation mode is certainly the constructionally enforced curved shape design of the CPW. On the one hand the bended layout may enhance reflection as on the other the tapering of the center conductor presumably does. This assumption is also indicated by measurements realized on an earlier version of the VNA-FMR setup, presented in the thesis of D. Markó [125, 136]. There, a straight CPW with constant center conductor width was utilized, where the same calibration procedure results in a much better SNR.

To enhance the signal quality a number of setup and evaluation improvements were made. One possibility is to change the IF bandwidth. By decreasing this value less high-frequency noise was achieved but resulted in an increased sweep time. On the other hand, by increasing the IF bandwidth faster measurements are possible that may be fast enough to circumvent low-frequency noise. In order to retain a reasonable signal-to-noise ratio subsequently recorded spectra have to be averaged. To a certain extent an optimization in this direction can give some improvement, but will not solve the general noise problem.

A different optimization approach was to subtract two susceptibility spectra from each other, where the subtrahend was recorded at a higher magnetic field and hence showed a resonance far above the one of interest. Nevertheless, the signal improvement was in general quite small since the background slightly starts to change if variations in external fields are too high.

In any case, the linewidth is highly sensitive to fluctuations of the magnetic field inasmuch as the resonance position depends on the field strength. Field fluctuations during a slow f -sweep will thus broaden the measured line. In contrast, fast recorded spectra may be unaffected by this fluctuations, but the necessary averaging will redeem that benefit. This effect is especially important at low-field values, as it is of interest for two-magnon scattering. To make this clear

a Py ($\mu_0 M_s = 1$ T, $g = 2.11$) film with vanishing anisotropy will be considered. Here, the resonance condition (2.35) simplifies to $(\omega/\gamma)^2 = \mu_0 H (\mu_0 H + \mu_0 M_s)$ and a measurement at $\mu_0 H = 0.03$ T gives a resonance frequency of $f \simeq 5.2$ GHz. Already a fluctuation in field of $3 \cdot 10^{-4}$ T shifts the resonance frequency by 26.7 MHz. That in turn corresponds to a relative shift in peak-to-peak linewidth of 10.7% if a typical value of $\Delta f_{pp} = 0.5$ GHz is assumed. Such systematic errors can only be prevented by rather long dwell times after a field value was set at the power supply.

Also tests with absorber materials attached to the nonsensitive CPW part, higher-quality microwave transmission lines, as well as a length reduction of the same did not lead to satisfactory result. The periodic noise in the raw S -parameters remains always and continues to the magnetic susceptibility. Here, the critical issue is the phase stability over the transmission lines and the sample. A particular conspicuous aspect is the observation of periodic noise that is most pronounced for reflection parameters S_{ii} leading to the suggestion of an insufficient VNA two-port calibration. Because electronic components are never perfect, directional couplers do not perfectly route reflected and emitted signals. This effect is called directivity, by which the reflected signal entering the coupler can be reduced by leakage from the initial signal. Usually this can be reduced by a two-port calibration [145]. Unfortunately, it is on the one hand impossible to conduct a calibration with the CPW connected. On the other hand just slight movements of the microwave transmission lines, or even thermal drift effects, will already influence the transmission characteristics (signal amplitude and phase). Hence, an effective directivity can occur that consists of corrected directivity and reflections from components introduced after calibration. Together with the reflected signal from the DUT it can add up in phase producing a peak in the reflection parameters or a dip if both signals partially cancel each other [130, 135].

Therefore, another measurement method was urgently needed to guarantee the necessary precision, where the solution was found in switching to H -sweep VNA-FMR. By this, another benefit emerged, namely the direct comparison to linewidth data obtained over decades with cavity FMR. Due to the widely spread usage of cavity FMR, a huge amount of linewidth theory has become available, although the physical meaning—namely the relaxation rate—is carried by Δf . Certainly, it should be mentioned that over the last years an increasing amount of publications focused on the evaluation of frequency-swept linewidth data [87, 112, 138, 146, 147], accounting for intrinsic damping [148] and two-magnon scattering [28]. Alternatively, it is of course possible to apply the linewidth conversion given by Eq. (2.51). To do so for angle-dependent measurements the anisotropy constants of the system must be known in order to calculate the slope from $f(H)$ curves via Eq. (2.35), which in turn introduces further uncertainties. On the other hand, by measuring $f(H)$ dependences this step can be skipped,

but still uncertainties from the resonance measurement remain. This all pleads in favor for the field-sweep mode, implemented during this thesis and introduced in the following.

3.3.2 Field-sweep VNA-FMR

In order to measure FMR in field-sweep mode using the previously introduced setup the available control software had to be extended to operate in the new mode. The basic idea behind this operation mode is rather simple: While ramping the magnetic field in small steps the field value as well as the selected S -parameter will be read out simultaneously. Both has to be done fast, so the IF bandwidth is set to 1 kHz, which enables single-point detection in 47.1 ms. For noise reduction subsequently recorded values, usually 5 points, were averaged. In consideration of achieving the same order of measurement time also for field measurements the built-in analog-digital converter of the magnet's power supply was too slow and was replaced by a Keithley 3706 digital multimeter, which reads out the teslameter signal directly and much quicker. That allowed fast enough and much more precise measurements⁵ at the same time. To bypass remanence and saturation effects of the electromagnet the magnetic field was controlled via the applied current. On the VNA side the mentioned amplifier as well as attenuator were added to the signal line in order to increase available microwave field strengths. Here, the attenuator is used to limit the power input at the VNA microwave detectors. Due to the additional components in the setup measurements are limited to transmission only, caused by the unidirectional amplifier.

Since field-sweep data recording works at a single microwave frequency VNA two-port error correction, the crucial point in f -sweep data acquisition, may be omitted. Here, the influence of reflections to the recorded spectrum should be negligible while the field is swept. Instead, offsets will occur between single spectra that can be corrected numerically. Nevertheless, also this method is naturally quite sensitive to drift effects associated, i. e., with movements of microwave transmission lines. Thus, in front of each measurement an idle time (usually up to three hours) is spent to gain a relaxed system.

Fig. 3.5 shows a direct comparison between frequency- and field-swept data acquisition. Here the same sample as before was measured, whereas this time not a single spectrum is depicted but rather a series of sweeps obtained under different constant field respectively frequency values. Also the usually applied combination of amplifier and attenuator was removed during the measurement to be able to compare signal amplitudes, both recorded at 1 mW of microwave power. Displayed are the absolute values of χ in panel (a) and the complex scattering parameter

⁵The voltage accuracy is in the order of 10^{-6} V ($1 \text{ V} \cong 1 \text{ T}$), whereas the teslameter has a measurement uncertainty below 0.01%.

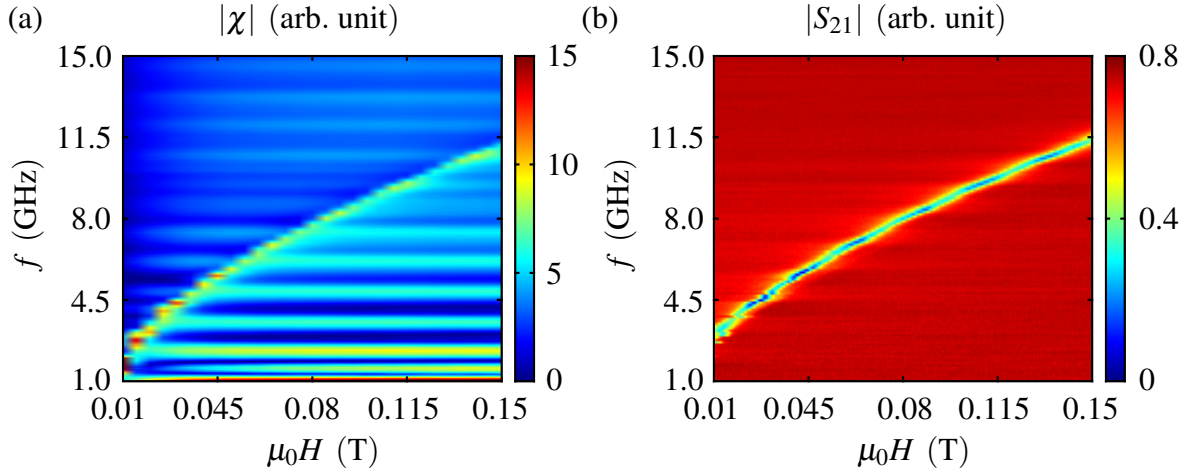


Figure 3.5: Comparison of available sweep techniques using the patterned thin-film system Si/SiO₂/Py(30 nm)/Cr(3 nm). Depicted are absolute values of (a) the dynamic susceptibility χ obtained by frequency-sweep and (b) the scattering parameter S_{21} recorded using field-sweep VNA-FMR.

S_{21} in panel (b), both shown as color-coded plot. Except an offset correction⁶ for field-swept data no other image processing was applied to maintain comparability. Note that the field axis of graph (b) displays average values, caused by varying field points during the H -sweep. Even so, the deviation of each measured point from the displayed average value is usually negligibly small⁷. In contrast, the frequency axis of graph (a) is exact since the VNA can be set to the same frequency values when recording a spectrum.

The first striking point when comparing both measurement modes is a quite considerable difference in signal-to-noise ratio. Here, the field-sweep measurement has a strongly reduced noise background leading to a considerably enhanced resonance signal⁸. Clearly the periodic background, as observed for f -sweep measurements, vanished, which was also confirmed by other sample systems. In addition, an increased SNR allows the observation of higher spin wave modes ($k \neq 0$), as it will be seen in later measurements. In contrast, at the very bottom of the f -sweep graph the previously mentioned strong increase in low-frequency noise is visible. Another difference between both modes is the step-like feature in the evolution of f -sweep resonances. This can simply be attributed to less dense field points.

Finally, the H -sweep signal amplitude shows an oscillatory behavior that can be directly correlated with the background oscillations of the f -sweep mode. Superimposing both plots

⁶Due to e. g. drift effects recorded spectra may be shifted against each other by an approximately fixed offset. The correction shifts the spectrum baseline back to zero, which is done using the toolbox introduced in appendix A.

⁷The deviation is provided by the evaluation software (see appendix A) that was used to produce the graphs.

⁸This is best seen if single spectra (not shown) are compared.

(not shown) makes clear that the minima in the H -sweep measurement ($|S_{21}|$) correspond to f -sweep minima ($|\chi|$). Furthermore, when considering Fig. 3.4(b) the dispersive part is much stronger than the absorptive one of χ . Thus, in this case extrema in $|\chi|$ are mainly caused by dispersion. Now, comparing Fig. 3.4(b) with (a) reveals minima in the dispersion where $|S_{21}|$ exhibits a maximum and $|S_{11}|$ a minimum. Hence, appearing minima of $|S_{21}|$ in Fig. 3.5(b), equivalent to enhanced microwave absorption (explained later in this section), can be directly related to minimal reflection losses of the microwave signal. Consequently, background oscillations as a function of microwave frequency also exist for the H -sweep mode, but are less important since the frequency is kept constant while recording a single spectrum. Note also that H -sweep measurements were done without any VNA error correction, which supports the argument given above of an interplay between reflections and directivity when using a calibration in f -sweep VNA-FMR.

The greatest advantage of broadband VNA-FMR over cavity-based field-sweep ferromagnetic resonance is the freedom of choice with respect to microwave frequency. Utilizing a stripline as an excitation source dates back to the 1960s [149, 150]. The crucial difference to cavity FMR is the way the signal is obtained. While in case of a cavity a pure absorption signal can be recorded, the sample attached to a stripline/CPW forms an electric two-port device whose resonant response is measured. To obtain the resonance curve $\chi(H)$ from complex transmission and reflection parameters S_{11} and S_{21} , respectively, the effective impedance of the sample needs to be considered as shown by Ding *et al.* [151]. This can be done by directly linking scattering parameters to the change of impedance of the system⁹ caused by the magnetic material, from which finally the susceptibility can be calculated [137, 138, 152, 153]. To further exclude nonmagnetic backgrounds the scattering parameters S_{ij} of the whole system are separated into desired magnetic contributions S_{ij}^m and a nonmagnetic part S_{ij}^0 with $S_{ij} = S_{ij}^0 + S_{ij}^m$. The nonmagnetic response can be measured by applying a strong-enough external magnetic field parallel to the microwave field while recording S_{ij}^0 . Treating sample and waveguide in an equivalent-circuit approach (substituting them by corresponding impedances, inductances, and capacities) results in a relation between wanted susceptibility and measured scattering parameters [151]:

$$\chi(H) = \chi_0 \left(\frac{1 + S_{11} - S_{21}}{1 - S_{11}} - \frac{1 + S_{11}^0 - S_{21}^0}{1 - S_{11}^0} \right). \quad (3.8)$$

Here, χ_0 summarizes experimental parameters such as film thickness, sample size, and characteristic impedance of the CPW. Further simplifications of Eq. (3.8) can be made by assuming

⁹Most commonly the sample is attached to a stripline or CPW that even can be shortcut, as well as coils may be utilized for this inductive method.

weak reflections $|S_{11}|$ of microwave power¹⁰ as well as considering a quasi-static limit. With this Nembach *et al.* found [154]:

$$\chi(H) \cong -\chi_0 [3(1 + S_{11}^0 - S_{21}^0)] S_{21}^m. \quad (3.9)$$

The equation presented above provides a direct connection between measured scattering parameters and magnetic susceptibility of the sample. Also a linear relation between susceptibility and magnetic part of the scattering parameter S_{21}^m can be found if perfect measurement conditions (100% transmission, no reflection) are present: $\chi(H) \cong -2\chi_0 S_{21}^m$ [154]. This reveals the crucial importance of measuring S_{21} when performing broadband H -sweep resonance experiments. Together with Eq. (2.40) it allows a direct determination of wanted sample parameters. However, solving the LLG equation to obtain a sample-dependent expression of the susceptibility (2.40) may become challenging and needs to be done for every single sample system. That is why a universal approach would be favorable and will be presented below.

Since the background function is usually quite small for the samples investigated in this thesis and because it strongly depends on temperature and other drift effects, it was decided not to use a background subtraction and evaluate S_{21} directly. Again, it should be pointed out that this measurement mode maps the complex magnetic susceptibility and, hence, a resonance curve. Thus, functions used for cavity-based FMR may be inappropriate since these reflect only absorption or dispersion, but never both simultaneously. In order to describe a complex resonance curve a complex Lorentzian ansatz is used:

$$L_{\text{compl}}(H) = \frac{A_{\text{compl}}}{\Delta R + i(H - H_{\text{res}})}. \quad (3.10)$$

Its definition contains the amplitude A_{compl} as well as the resonance position H_{res} and linewidth ΔR . By determining the real and imaginary part of L_{compl} one finds a match with the known Lorentzian functions of absorption and dispersion [Eqs. (3.2) and (3.5)] by what the linewidth is related to known quantities as follows:

$$\Delta R = \frac{\sqrt{3}}{2} \Delta H_{\text{pp}}. \quad (3.11)$$

In order to describe any intermediate state simply a phase factor $\exp(i\phi)$ is multiplied to the complex function given by Eq. (3.10). Subsequently, taking the real part finally provides the Lorentzian fit function used in the framework of this thesis

$$L_c(H) = \frac{A_c \Delta R [\cos \phi + (H - H_{\text{res}}) \sin \phi]}{\Delta R^2 + (H - H_{\text{res}})^2} \quad (3.12)$$

¹⁰Although reflections in the system are present, these still can be considered as being weak. This assumption is supported by Fig. 3.5(b), as oscillations—caused by reflections—of the signal's amplitude are rather small.

that covers all possible line shapes. Note that the imaginary part can be obtained by a phase offset of 90° . Again, A_c is the function's amplitude. In addition, to account for drift effects a linear background function will be superimposed on Eq. (3.12). The physical origin of ϕ arises, such as the phase shift in cavity experiments, from the phase relation between received microwave and the VNA's microwave source. As explained earlier the receiver built into the VNA is phase and frequency locked to the microwave source if no calibration is applied. Even by choosing a proper excitation frequency does not guarantee a fixed phase relation over the whole measurement range. Instead, a sample under resonant excitation can introduce changes and also an alternation of exciting microwave frequency or sample orientation introduces further shifts. Changing frequency apparently causes a phase shift due to a changes in the ratio between wavelength and transmission line length. Altering the sample's orientation on the CPW in contrast involves a change of effective sample length and thus alters the propagation properties, which in turn influences the phase relation between both signals.

One possibility to circumvent fitting the phase would be the evaluation of absolute values of S_{21} . Even so, in practice slight deviations from the perfect absorption respectively dispersion shape remain, for example caused by damping entering the resonance curve, that will complicate the evaluation and, hence, may increase especially the error in linewidth. In addition, higher-order spin wave modes ($k \neq 0$) may be phase shifted with respect to the FMR mode even if absolute values of S_{21} are considered. Accordingly, experiments will be evaluated through fitting the real part of S_{21} using the phase ϕ .

The application of fit function (3.12) is exemplary shown in Fig. 3.6 where the same sample was used as discussed above in this chapter. Depicted by red lines are fit results that perfectly overlap with the measured data, shown as open blue circles. Also, by comparing with Fig. 3.4 a strongly enhanced signal quality is visible where the noise of the measurement is much less than the symbol size. Further improvements of the SNR will be obtained for samples with bigger area (here $1 \times 1 \text{ mm}^2$, usually $1 \times 1 \text{ cm}^2$ in later experiments) and inserting the amplifier back into the signal line. The three different graphs show the resonance under three different phases, well modeled by the fit function. Note that the phase shifts shown do not correspond to a single oscillation. Because the microwave signal is mixed down to an intermediate frequency by the receiver, the phase oscillations are in the kHz to MHz regime, whereas the measurement shown has tenths of GHz between the recorded curves.

As a final remark it should be stressed that comparisons between the varieties of performing FMR had been the scope of investigations in the past as well. There, reasonably good agreements were found between f - and H -sweep FMR (broadband and cavity) with respect to resonance position and linewidth. Also other magnetization dynamic methods, such as pulsed

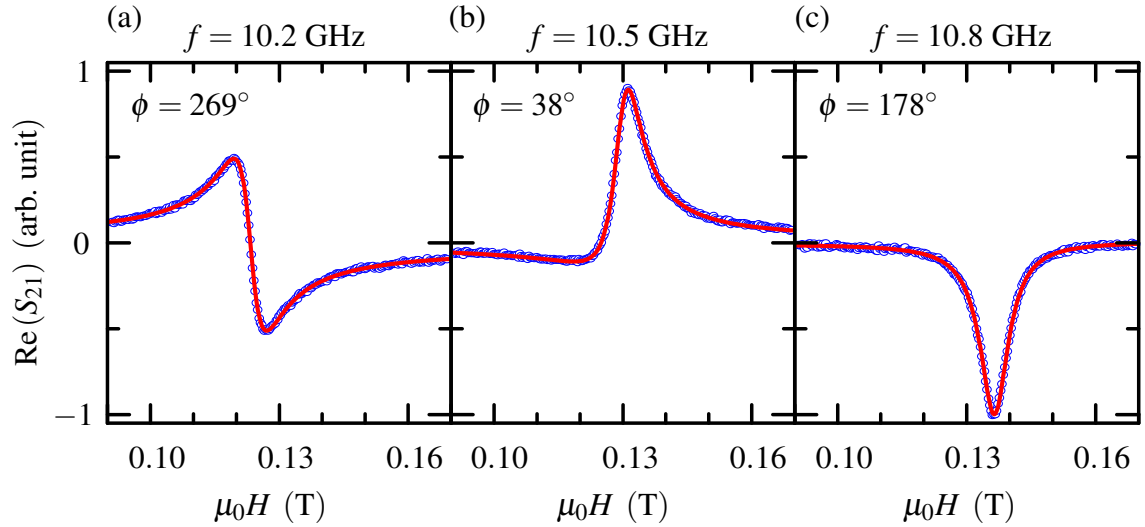


Figure 3.6: Measurement (blue open circles) and fit (red line) of the patterned Si/SiO₂/Py(30 nm)/Cr(3 nm) system in H -sweep mode using Eq. (3.12). Depicted are three different microwave excitation frequencies: (a) 10.2 GHz, (b) 10.5 GHz, and (c) 10.8 GHz. The signal amplitudes are normalized to one.

inductive microwave magnetometry (PIMM) or time-resolved magneto-optic Kerr effect, have been included in the studies, providing equivalent results [87, 147].

3.3.3 Influence of stripline measurements

The discussion regarding microwave excitation so far was determined by homogeneous fields. Certainly, by considering Fig. 3.1 it can be seen easily that CPWs do not provide a homogeneous microwave field. Caused by the narrow geometry of the center conductor the microwave field will be spatially limited being in-plane and perpendicular to the strip axis, but also out-of-plane components evolve. This is a fundamental difference to cavity created excitation fields, which can be considered as being homogeneous over the sample area. Only samples exhibiting thicknesses comparable to the skin depth will experience inhomogeneous excitations over their thickness. The same of course is true for samples with strong inhomogeneous dipolar fields, caused e. g. by spatial limitations.

Due to the inhomogeneous excitation field caused by the utilized CPW new challenges as well as possibilities arise. An inhomogeneous excitation may cause high-order spin waves (see sect. 2.2.3). By this, additional sample parameters such as exchange stiffness can be determined. In cavity-based FMR this is only possible by inhomogeneous fields caused e. g. at sample inhomogeneities or edges, which in turn can be too small to have an effect. Now, the excitation field serves as another seed, enhancing the generation of spin waves. As an example PSSW

modes have been observed in thin films, where the amplitude is remarkably larger in case of broadband FMR than in cavity experiments [155]. Furthermore, inhomogeneities will have a direct impact on resonance position and linewidth. Also, by applying stripline techniques only a small area of the sample is probed, by which inhomogeneous regions may get over- or underrepresented. The following section will examine the influence of the utilized waveguide geometry on sample systems investigated later on.

At first, the spatial distribution of the magnetic field, as created by the CPW, is of importance. For simplicity, only the center strip is taken into consideration. Fields evolving from the ground planes will be rather small compared to the ones of the center strip, because on the one hand the ground planes are much wider than the center conductor whereas the current passing them is smaller on the other hand. Therefore, the probed area is basically limited by the center strip area covering the sample. The field can be estimated by applying the Karlqvist equations [156], originally derived to obtain fields above a recording head. By adapting the boundary conditions, Silva *et al.* found an expression for the transversal magnetic field component above a uniform current strip oriented along the y direction in the xy plane [157]:

$$H_x^{\text{strip}}(I, y, z) = \frac{I}{2\pi w} \left[\arctan\left(\frac{w/2 + y}{z}\right) + \arctan\left(\frac{w/2 - y}{z}\right) \right]. \quad (3.13)$$

z accounts for the height above the strip whereas I represents the current sent through. The underlying geometry is shown in Fig. 3.1. In order to obtain values for the current a simple ohmic behavior $I = \sqrt{P_{\text{rf}}/Z_{\text{CPW}}}$ was assumed, with a strip impedance of $Z_{\text{CPW}} = 50 \Omega$, while neglecting losses in the transmission lines. Let's consider the case without amplifier, leading to a microwave power of $P_{\text{rf}} = 1 \text{ mW}$. Calculating the H_x^{strip} component at the strip's center ($z \rightarrow 0$) above the surface yields a strength of $\mu_0 H_x^{\text{strip}} = 0.035 \text{ mT}$. Increasing z to $1 \mu\text{m}$ causes $\mu_0 H_x^{\text{strip}}$ to differ only by 1.6% from its surface value. A similar behavior is found by using the amplifier. Here the 27 dB amplification leads to a microwave power of 501 mW and a transversal surface field of $\mu_0 H_x^{\text{strip}} = 0.786 \text{ mT}$ at the strip's center. Again, this value reduces by 1.6% if the height is increased to $z = 1 \mu\text{m}$. In conclusion, field decay effects in magnetic films (thickness below 100 nm) placed on top of the strip are not necessary to be considered, which is of course expected since the film thickness is much smaller than the strip width. Furthermore, the comparably small excitation fields (with respect to the external field) justify the assumption of small deflections, used to solve the LLG equation (2.30). Already an internal magnetic field of 90 mT is sufficient to ensure a precession angle below 0.5° if excitation via amplified microwaves is considered. Although this estimation of the excitation field is rather basic, it gives reasonable values that are comparable with simulations, as shown by Neudecker *et al.* for similar geometries [147]. Of course, for a realistic field profile across the utilized CPW one needs to account for effects caused by the ground planes, its separation to

the center strip, and the influence of the vias. Such calculations are only numerically possible and will especially change the field distribution at the edges of the strip.

Far more important than decaying field strengths along the z direction are field inhomogeneities in the sample's plane. A detailed discussion of the consequences was first given by Council *et al.* [138] and will be presented in the following, again based of the geometry depicted in Fig. 3.1. Due to the limited strip width of $w = 80 \text{ }\mu\text{m}$, much smaller than the in-plane sample dimensions (1 mm^2 up to 1 cm^2), the exciting fields become nonparallel to the surface at the strip edges and, hence, give rise to inhomogeneous excitations. Thereby the inhomogeneities occur only perpendicular to the strip axis, along the x direction. In contrast, parallel the strip along y the strip exceeds the whole sample and produces a homogeneous field. As a result spin waves with $k_{\parallel} \neq 0$ are only emitted perpendicularly to the strip, where the maximum possible wave number is approximately given by the strip width w [138]:

$$k_{\parallel}^{\max} \approx \frac{\pi}{w}. \quad (3.14)$$

To examine the role of generated spin waves, its dispersion relation needs to be considered. Because these waves propagate in-plane, the expression given by Arias and Mills for ultrathin films (2.47) can be used. Certainly, because the exchange length¹¹ of materials to be discussed is much smaller than the strip width w , exchange effects do not need to be taken into account. Therefore, the last term in Eq. (2.47), proportional in D , will be ignored. As it can be seen from (2.47), the deviation of the spin wave frequency $\omega(k_{\parallel}, \varphi_{\mathbf{k}_{\parallel}})$ from the FMR frequency $\omega = \omega(k_{\parallel} = 0)$ is quite small for low $\varphi_{\mathbf{k}_{\parallel}}$ and will increase if the angle between magnetization and spin wave propagation direction increases. In FMR experiments the externally applied field is always perpendicular to the pumping field and, hence, parallel to the strip. Neglecting field-dragging effects, justified for small anisotropies as present in Py, the magnetization aligns parallel with H , which causes $\varphi_{\mathbf{k}_{\parallel}}$ to be 90° . By this, $k_{\parallel} \neq 0$ spin waves have the greatest deviation from the FMR frequency. Assuming a linear response, the measured signal is a superposition of all excited k_{\parallel} states, which in turn will lead to a shift in resonance frequency and a line broadening. For the shift in resonance frequency the authors of Ref. 138 find

$$\delta\omega(k_{\parallel}^{\max}, \varphi_{\mathbf{k}_{\parallel}}) = \frac{1}{2} \left[\omega(k_{\parallel}^{\max}, \varphi_{\mathbf{k}_{\parallel}}) - \omega \right], \quad (3.15)$$

whereas the broadened linewidth is expressed by:

$$\Delta\omega(k_{\parallel}^{\max}, \varphi_{\mathbf{k}_{\parallel}}) = \Delta\omega \sqrt{1 + \left(\frac{\omega(k_{\parallel}^{\max}, \varphi_{\mathbf{k}_{\parallel}}) - \omega}{\Delta\omega} \right)^2}. \quad (3.16)$$

¹¹For example, in case of Py ($\mu_0 M_s = 1 \text{ T}$ and $A = 1.3 \cdot 10^{-11} \text{ J/m}$) the exchange length [see Eq. (2.26)] is just $\Lambda_{\text{ex}} = 5.7 \text{ nm}$ [56].

As in both equations only $k_{||}^{\max} = 3.9 \cdot 10^4 \text{ m}^{-1}$ enters the dispersion relation, the assumption of ultrathin films ($k_{||}d \ll 1$) is justified for all used film thicknesses (below 100 nm).

Using the above presented model, Council *et al.* were able to show that an observed increase in effective Gilbert damping (also seen by others [146, 157]) by 100% at low frequencies (< 3 GHz) is a measurement artifact caused by the stripline. Further experimental verifications using a PIMM observed a shift in resonance frequency that is a function of the ratio between film thickness and CPW width [158]. This in turn has an influence on the determined anisotropy. Also a component of the decay rate depends on this ratio, although no perfect agreement was found at low frequencies of 1 GHz [159]. The consequences of these findings for H -sweep measurements will be discussed along with the experiments in the following chapters.

An extended theory on coplanar waveguides was presented by Kennewell *et al.*, taking the finite conductivity of the sample, screening effects of the CPW metal onto the spin wave dispersion, as well as the ground half-planes into account [160]. For large spacings between the half ground planes and large intrinsic damping the authors find an agreement with the theory of Council *et al.* Otherwise the signal shape depends additionally on the current density, which is a function of the spin wave wave vector.

Despite from inhomogeneous excitation fields, another source of spin wave excitation may originate from the utilized amplifier. Usually, it is operated at a microwave input power of 1 mW. Unfortunately, it is not capable to maintain the amplification of 27 dBm over the whole frequency range up to $f = 50$ GHz, but rather will run into saturation¹². In this case the emitted microwave signal will no longer be sinusoidal, but reaches a cutoff. By this, the signal approaches a square wave shape. Thus, the signal will contain higher harmonics of the input frequency f , which in turn is a source of spin wave excitation. In principle, this additional inhomogeneity will be similar to the ones caused by the CPW geometry. Because higher harmonics are a modulation of the carrier signal, spin wave propagation directions are equal to that discussed above. Considering a Fourier transform of an arbitrary square wave signal reveals a decay of intensities with increasing mode frequency $f_n = nf$, where n is an odd natural number larger than one. Consequently, the increase in harmonic frequency f_n will lower its influence to the FMR signal. Wave numbers $k_{||}$ covered by these harmonics are indeed rather small when compared to the ones caused by the CPW. Here, $k_{||} = 2\pi f_n/c_0$ is comparable to $k_{||}^{\max}$ if $f = 40$ GHz and $n = 49$ is considered. Thus, effects from a saturated amplifier onto the FMR signal will appear (i) only at high frequencies and (ii) will have a smaller impact as the CPW geometry.

Next to the discussed direct influence of excited $k_{||} \neq 0$ spin waves onto the resonance, the

¹²depending on the input power this is in the range between 15 GHz and 25 GHz

precession of the magnetization will induce eddy currents. These may cause damping of spin waves and a renormalization of its dispersion, as it was shown by Almeida and Mills [161]. Restricting the theoretical investigation to Damon-Eshbach modes (in-plane and perpendicularly propagating with respect to \mathbf{M}) the authors find, however, a significant renormalization of the mode dispersion if the skin depth is much smaller than the sample thickness. Here the spin waves become basically confined to a channel defined by the skin depth as well as its dispersion relation is similar to films with thicknesses in the range of the skin depth. Moreover, if propagating spin waves obey the relation $k_{\parallel} \delta_0 \sim 1$, the authors expect a strong damping generated by eddy currents. Thereby, δ_0 is the classical skin depth [$\mu_r = 1$ in (2.55)] without taking the increased susceptibility at resonance into account. Considering Fe, as well as other transition metals, δ_0 is usually in the order of $1 \mu\text{m}$ [161]. As spin waves generated by the CPW have $k_{\parallel}^{\text{max}} = 3.9 \cdot 10^4 \text{ m}^{-1}$ influences may be barely visible.

The last point to mention arises from a conducting sample placed on the CPW, which could cause shorts of the microwave signal. A common practice is to cover the sample by a thin layer (usually $< 1 \mu\text{m}$) of nonconducting photoresist [151, 154]. As there was no difference found, and additionally to exclude influence on sample properties—the resist is baked at a temperature of $200 \text{ }^\circ\text{C}$ —no resist was used for further experiments.

4 Morphology-induced magnetic uniaxial anisotropy in polycrystalline thin films

This chapter addresses the question of morphology influences on static magnetic properties of thin ferromagnetic films. The focus is on induced magnetic anisotropies, originating from the substrate's surface structure after depositing magnetic materials on top. To consider this, the systems investigated showed a polycrystalline structure that reduces magneto-crystalline anisotropies to a minimum. Both was achieved by using ion beam erosion of Si substrates. As this tool provides not only amorphous surfaces that induce polycrystalline metal growth, it gives also an excellent possibility to create well-defined correlated nanostructures. The wavelength of the resulting periodic surface modulation was altered to examine its influence on magnetic properties. As a result, an in-plane uniaxial magnetic anisotropy (UMA) is expected to be induced in the ferromagnetic film, whose origin is found in dipolar effects and scales with the wavelength of the modulation. This effectively provides a possibility to tailor magnetic anisotropy.

A lot of investigations on induced magnetic anisotropies and their physical origin were done in the past, pursuing different mechanisms of roughness control involving the materials Fe, Co, Ni, and Py. Anisotropies basically have been induced by (i) surface erosion of magnetic materials and (ii) by deposition of magnetic materials onto suitable substrates. Sputtering magnetic materials in addition may be divided into single- [34, 162–164] and polycrystalline [35, 165, 166] targets, where sputtering down to the substrate finally leads to the creation of (single-crystalline) nanowires [167]. For anisotropy modifications, achieved during the growth process, likewise several possibilities exist. First, deposition on step-bunched [168] or vicinal substrates [169–172] leads to anisotropy modifications. As well, ripple templates were used for anisotropy and magnetic property modifications [21, 32, 33, 173, 174]. But also in case of flat substrates modifications may be achieved by oblique-angle deposition [175–179] or even via spontaneous pattern formation during film growth [180]. Also a combination of oblique deposition and ion bombardment was used to alter magnetic anisotropies [181]. Finally, using shadow deposition of magnetic materials on self-organized templates [182], or by filling the trenches of a rippled substrate [183], gives similar anisotropy effects.

In case of uniaxial anisotropy observed in single-crystalline films on vicinal surfaces, its origin is generated by broken symmetry at step edges, where the altered electronic structure modifies the spin-orbit interaction [169, 171, 172]. Likewise, the UMA in rippled single-crystals originates from steps along the side walls [34]. Hence, its strength depends on the fluence-dependent ripple formation process [162]. In polycrystalline films the random grain orientation averages out the symmetry breaking and thus purely magnetostatic effects, e. g. dipolar [33, 173, 174] contributions caused by the sample's shape [35, 166], will have an influence on the anisotropy.

The chosen method of rippled Si substrates, against most others introduced above, combines many advantages of earlier investigations. First, in comparison to irradiated films, the surface quality can be determined preliminary to film deposition. In this way, reproducibility can be kept on a high level. Additionally, the film thickness is well known and the surface corrugation is—for thin-enough films—repeated on both interfaces of the magnetic layer. Of course, the last two points are true as well for depositions on vicinal surfaces. But in this case the periodicity of the surface structures are limited to a narrow range, with step heights on the atomic scale. Due to these reasons, magnetic films will be investigated which are deposited on rippled substrates, tunable in wavelength. The roughness of the ripple substrates will be characterized and its influence on magnetic anisotropy will be studied. Thereby, the origin of UMA will be identified and its dependence on surface structure will be discussed. The work was done in collaboration with M. O. Liedke, who prepared the samples and mainly performed the measurements and data evaluation. It was published in Ref. 184.

4.1 Sample preparation and characterization

4.1.1 Preparation procedure

Starting point of each experiment discussed below were flat Si(100) substrates with lateral dimensions of $1 \times 1 \text{ cm}^2$, cut from a commercially available wafer. The ion beam erosion process was mainly done by the Ion Induced Nanostructures division, namely by A. Keller, M. Fritzsche, and M. Ranjan. Here, fluences in the range of $0.2 - 2 \cdot 10^{18} \text{ ions/cm}^2$ and sputter energies in the range of $0.3 - 15 \text{ keV}$ were used to create ripples. Higher-energy sputtering was performed at the institutes implanter facility providing energies up to 40 kV while using the same fluences. Ar^+ and Xe^+ have been used for irradiation, where the beam direction was 67° with respect to the sample's surface normal. By this, wavelengths between 25 nm and 90 nm were achieved. In order to obtain reproducible results, the ripple quality was measured by

atomic force microscopy¹ using a Veeco MultiMode microscope in tapping mode and tips with a typical diameter of 10 nm. The recorded images were image processed using the *WSxM* [186] and *Gwyddion* software [187].

Afterwards, the magnetic layer was deposited by means of molecular beam epitaxy² (MBE). Because the vacuum had to be broken between sputtering, AFM, and layer deposition, all samples underwent a cleaning procedure just before being inserted to the MBE system. In a first step, they were sonicated in an isopropanol bath, which was followed by a heating procedure until the isopropanol started boiling. Finally, the dried samples were inserted into the evaporation system and annealed³ under vacuum conditions (pressure better than 10^{-7} mbar) up to 200 °C in order to evaporate water from the sample's surface. After cooling down to room temperature the samples were transferred to the growth chamber and the magnetic layers were grown using an electron-beam evaporator. Here the pressure during deposition was better than 10^{-9} mbar, while evaporation rates up to 0.2 Å/s were used. The film thickness was monitored *in-situ* by a calibrated quartz microbalance monitor. Between material source and sample a shutter, controlled by stepper motor, was used to get (i) a stable material beam before starting the deposition and (ii) to be able to deposit wedge-shaped films. In the latter case the shutter speed was controlled by the quartz monitor. To prevent oxidation of the magnetic layers a Cr cap was deposited on top, having a thickness of 2 nm. Subsequently, samples were analyzed with respect to their magnetic properties using FMR and magneto-optical Kerr effect (MOKE).

The latter method utilizes a s-polarized laser beam, directed under grazing incidence onto the magnetic sample surface. Reflected light experiences a change in polarization state to typically elliptically polarized light, whose rotation with respect to the incident light is described by the Kerr angle and depends on the sample's magnetization. It is directed into a detector where a Wollaston prism splits the beam into two orthogonally polarized beams and directs them to photodiodes. From the two intensities the Kerr angle can be derived, which is in first order linear to the magnetization component of the sample that is parallel to the plane of light incidence. In this way, recording the Kerr signal as a function of an externally applied magnetic field (from negative to positive and reverse) offers the possibility to record magnetization reversal curves. Compared to FMR the great advantage of this method is the spatial resolution, enabled by focusing the laser beam onto the sample with a spot diameter (for the available setup) below 200 μm.

¹This technique raster scans the surface using a sharp tip (2 – 10 nm in diameter) in order to record a height profile. For details see Ref. 185.

²Here, an atomic beam of the material to be deposited is created by thermal evaporation from an electron-beam (e-beam) evaporator (other sources have not been used in this thesis) and exposed to the sample.

³The samples were heated up to the target temperature and cooled down just by heat conduction and radiation from the sample holder.

4.1.2 Basics of surface characterization

In order to determine the influence of rippled surfaces on magnetic properties the surface structure and its roughness properties need to be evaluated. Due to the fact that the substrates exhibit a correlated roughness the widely used root mean square (RMS) roughness will not be sufficient. Instead, additional parameters such as modulation length are required. When correlated surface structures are present, great care needs to be taken during the measurement. Otherwise, if occurring length scales are ignored, the determined roughness parameters become measurement dependent and thus have no valid meaning. A complete description of rough surfaces, its measurement and characterization, was published in a book by Zhao *et al.* [185]. Here, the focus will be set on a few cases, relevant for later experimental discussions.

First, surfaces need to be classified with respect to their statistical properties, leading to randomly rough surfaces and deterministic rough surfaces⁴. Here, the most important parameters are the height distribution and the root mean square roughness⁵ w , where the latter is defined as [188]:

$$w = \langle [h(\mathbf{r}) - \langle h(\mathbf{r}) \rangle]^2 \rangle. \quad (4.1)$$

In this, the angled brackets denote the spatial average of the expression inside. Considered is an AFM surface image with spatial coordinates $\mathbf{r} = (x, y)$, where $h(\mathbf{r})$ contains the height information. In other words, w expresses the height fluctuations around the average surface height. Usually, when considering deterministic surfaces, w and the height distribution alone do not provide a full representation of the surface's characteristic roughness. Instead, different surface profiles with different fluctuation frequencies may have equal height distributions and RMS values. So, further methods need to be established to fully characterize these surfaces. Here, up to four parameters will be of importance: (i) the root mean square roughness w , (ii) the roughness exponent β , (iii) the correlation length ξ , and (iv) the wavelength λ of periodic surface fluctuations. All these parameters can be deduced from the height-height correlation function (HHCF) given by [185, 188]:

$$C(\mathbf{r}) = \langle [h(\mathbf{r}) - h(0)]^2 \rangle. \quad (4.2)$$

Applied to an AFM image with N_x respectively N_y sampling points along the x and y direction, one finds for the one-dimensional function [188]

$$C(r = ma) = \frac{1}{N_y(N_x - m)} \sum_{l=1}^{N_y} \sum_{n=1}^{N_x - m} [h((m+n)a, la) - h(na, la)], \quad (4.3)$$

⁴Random rough surfaces are best described by a random field, whereas deterministic surfaces can be expressed by a height function.

⁵Sometimes w is also called interface width.

where a is the spacing between two data points and m is an integer value starting from zero and reaching up to $N_x - 1$. The fast scan direction of the microscope was assumed to be the x direction. To determine the mentioned roughness parameters from a HHCF using Eq. (4.3), a suitable model function is essential. In this thesis, two surface types are of importance: (i) self-affine⁶ and (ii) mounded surfaces⁷. The first case is described by [185]

$$C(r) = 2w^2 \left[1 - e^{-\left(\frac{r}{\xi}\right)^{2\beta}} \right] \quad (4.4)$$

and will be used for flat Si substrates. Looking at the limiting case of $r \gg \xi$ the height-height correlation function approaches its saturation value $2w^2$, which provides a possibility to determine the RMS value. In the opposite limit the function is dominated by an exponential increase that is determined by the roughness exponent β , with $0 \leq \beta \leq 1$ [188], and will become smaller the rougher the surface becomes. Furthermore, the roughness exponent is directly related to the surface's fractal dimension: $D_s = 3 - \beta$ [189], which will not be of interest in this study. The HHCF is one out of three equivalent functions, available to describe a rough surface. Alternatively, the power spectrum⁸ $P(k)$ or the autocorrelation function $R(r)$ might be used, where the latter is simply connected to the HHCF by [185]:

$$C(r) = 2w^2 [1 - R(r)]. \quad (4.5)$$

By this a definition of the correlation length ξ can be deduced from the point where the autocorrelation function drops to $1/e$ of its original value at $r = 0$: $R(\xi) = 1/e$. Within a length of ξ height fluctuations can be viewed as being correlated.

Changing to mounded surfaces Eq. (4.4) is expanded by the first-kind Bessel function of zeroth order J_0 [185, 190]:

$$C(r) = 2w^2 \left[1 - e^{-\left(\frac{r}{\xi}\right)^{2\beta}} J_0 \left(\frac{2\pi r}{\lambda} \right) \right]. \quad (4.6)$$

Here, J_0 causes a decaying, oscillatory behavior around the saturation value $2w^2$, where the oscillations are caused by correlated surface roughnesses of the period λ . The impact of roughness on magnetization via demagnetization factors has been in focus for quite some time [11, 191]. In addition, the influence of roughness parameters appearing in Eq. (4.5) and (4.6) on magnetic properties have been linked with the demagnetization factors [14, 192].

⁶A small piece of a self-affine (statistically) recovers the original one, if it is enlarged in different directions by different factors [185].

⁷Mounded surfaces exhibit a correlated roughness.

⁸The power spectrum is derived from the Fourier transform of the autocorrelation function.

Determining roughness parameters from AFM images needs to be done with great care. Not only the resolution of the image plays an important role, but also the recorded field of view. By selecting a too small image view, $C(r)$ is not saturated, which results in field of view dependent RMS values. Also the tip size is of importance, since a too big tip basically acts as a lowpass filter, which removes small fluctuations and hence influences w . A third source influencing w originates from image processing, intended to remove sample tilt or other measurement artifacts. Due to this reason AFM images shown in this thesis undergo a simple flattening procedure subtracting only a line or an offset. Here, too, the image needs to be large enough to deliver saturated RMS [189]. Furthermore, oscillations observed in $C(r)$ may not be caused by a correlated rough surface, but are a result of noise. To clearly distinguish between self-affine and mounded surfaces the noise can be reduced by averaging the correlation functions of several images and by choosing a sufficiently large field of view by considering $\sqrt{\xi^2/(L_x L_y)} \ll 1$ (with $L_i = N_i a$) [188].

A last and important point when dealing with AFM images is the measurement accuracy. That is, in contrast to expectations, not only determined by the sampling points of the image, but also by the correlation length. If the ratio ξ/L_i is settled, no further increase in accuracy can be achieved by increasing the number of data points along the direction i [188].

4.1.3 Substrate characterization

In order to characterize the substrates with respect to their roughness properties AFM images have been recorded and are shown in Fig. 4.1. From these images typical lengths were determined using the AFM software packages mentioned above by calculating the fast Fourier transform (FFT) and the HHCF. The fast scan direction was always aligned perpendicularly to the ripple wavefront to minimize drift effects onto the wavelength determination.

In Fig. 4.1(a) a flat Si substrate is shown, as it would be used for reference samples or as starting point for the ion beam erosion process. Further, panels (b)–(f) show ripple substrates with increasing wavelengths covering a range from 25 to 90 nm. In order to determine the roughness parameters and substrate quality, the height-height correlation functions of the AFM images are plotted in panels (g) and (h), respectively. If one restricts to high r values one finds for each case an increased noise level of the HHCF. This simply results from a decreased number of points available to be averaged at high point distances, which makes the calculation (4.3) more noisy. Nicely visible is also the oscillatory behavior of the HHCFs calculated for the rippled substrates, whereas the flat one simply saturates. From the saturation behavior one finds the RMS values w which basically equals the ones obtained by Eq. (4.1). Most striking is the increase in RMS values by one order of magnitude for rippled samples in comparison to flat Si substrates. RMS results obtained from the two methods introduced above are also listed

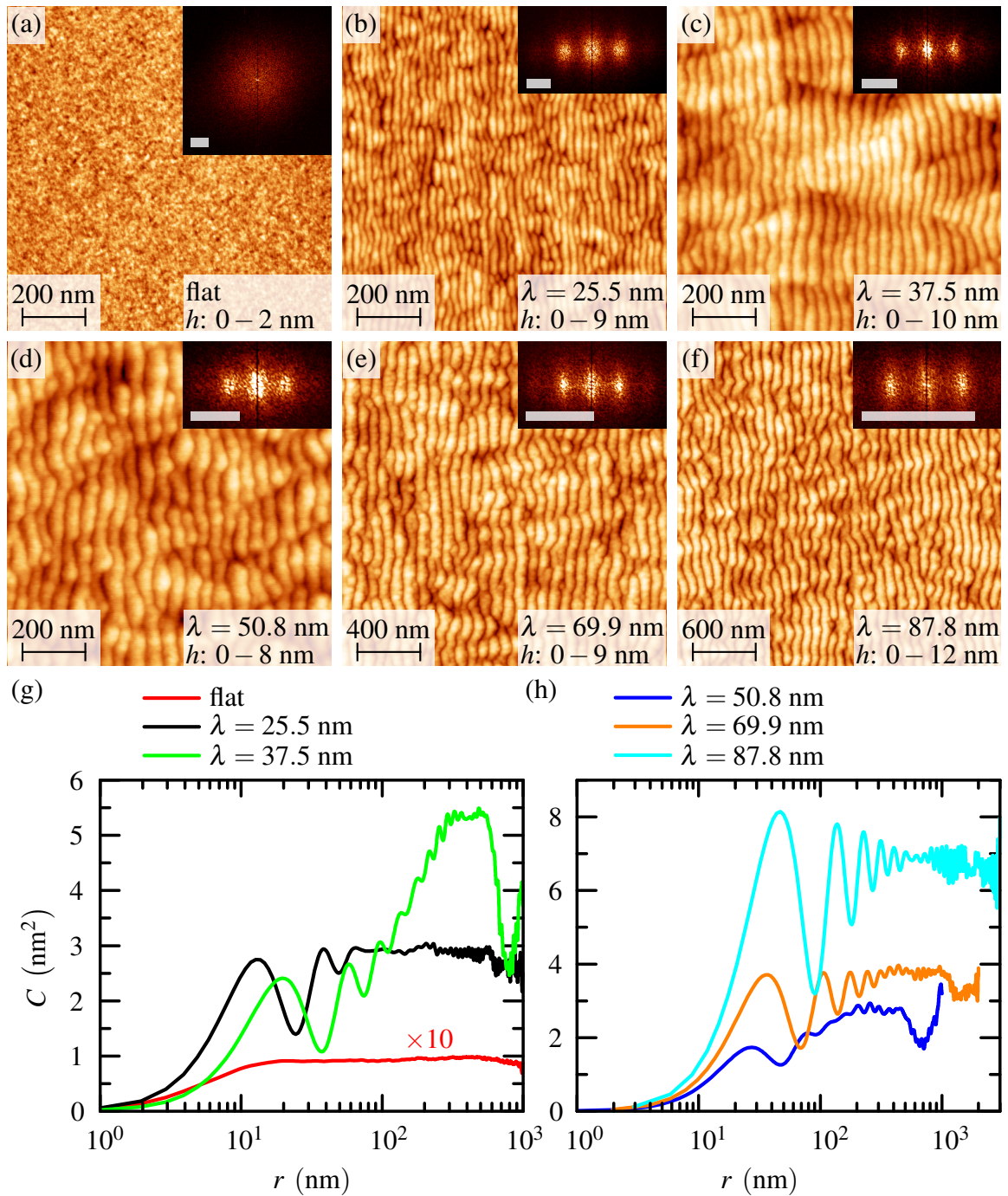


Figure 4.1: Si substrate characterization to determine the wavelength of the surface modulation. For the AFM images (a)–(f) the same color bar was used, where the height scaling h of the images and the ripple wavelength λ are shown at the bottom right corner. The insets show the 2D FFT (color ranges arbitrarily scaled, the white bars correspond to $35 \mu\text{m}^{-1}$), from which λ was derived. Graphs (g) and (h) contain the HHCFs of the AFM images.

sample displayed in Fig. 4.1	wavelength		RMS		ripple	ordering
	FFT	HHCF	Eq. (4.1)	HHCF	amplitude	parameter
	λ_1 (nm)	λ_2 (nm)	w_1 (nm)	w_2 (nm)	v (nm)	ξ_{\perp}/λ_1
(a)	—	—	0.22	0.21	—	—
(b)	25.5	23.2	1.18	1.16	2.3	2.3
(c)	37.5	34.8	1.42	1.07	2.4	2.7
(d)	50.8	48.4	1.08	0.91	2.2	1.4
(e)	69.9	66.1	1.32	1.33	3.3	3.8
(f)	87.8	86.0	1.82	1.81	4.5	6.5

Table 4.1: Roughness parameters for Si samples shown in Fig. 4.1. The ripple amplitude v is determined as peak-to-peak height difference between troughs and crests, whereas the correlation length ξ_{\perp} is the inverse of the FWHM of the first-order satellite peak in the FFT.

in Table 4.1. Two discrepancies from Eq. (4.1) were found, namely at wavelengths of 37.5 nm and 50.8 nm. The reason is due to a hardly distinguishable saturation value of $C(r)$, exhibiting strong noise above $r = 10^2$ nm. Comparing the corresponding AFM images with those yielding a better conformity, one finds an overriding periodicity in the deviating cases. This effect is called wavelength coarsening, which is a nonlinear phenomena of the sputtering process that starts to occur with increasing fluence. Details and further literature on this effect may be found in Ref. 122. Thus, as the determination of w using the HHCF function is highly sensitive to superimposed oscillations, w will be determined directly using Eq. (4.1). Nevertheless, the HHCF function provides a fast impression of the sample quality and—more important—the correct AFM field of view, needed to determine reliable RMS values.

More important than RMS values are wavelengths associated with the surface modulation. Also these values, obtained from the HHCFs, are shown in Tab. 4.1, where additionally wavelengths are displayed that were obtained from the two-dimensional FFT. This function is proportional to the square root of the power spectrum density and, hence, related to the HHCF. The advantage over the HHCF is a two-dimensional representation of characteristic surface periodicities, as shown for each AFM image by the insets in Fig. 4.1. For the flat substrate a concentric ring is observed indicating a spatially homogeneous roughness distribution. This changes dramatically for the rippled substrates. Here the FFT shows satellite peaks, where the distance between these allows to determine the wavelength. As seen from Table 4.1, both approaches provide comparable results with a relative deviation of both values typically below 10%. Compared to the one-dimensional HHCF shown, the 2D FFT has the advantage to determine the correlation length spatially resolved. This is of interest to qualify the ordering of

the rippled substrates and can be gathered numerically by the correlation length ξ_{\perp} , which is determined perpendicularly to the ripple wavefront. From the FFT image this is achieved by taking the inverse of the full width half maximum of the first-order satellite peak [185, 193]. Then, the ratio ξ_{\perp}/λ can be determined, which qualifies the ordering. From this, a steadily increasing ordering is observed with increasing wavelength, which is consistent with literature [193]. The only exception from this trend is the sample with 50.8 nm wavelength. One reason is of course the sample quality, which already was identified to be imperfect. Additionally, the determination of ξ_{\perp} reveals a relatively high relative error of up to 20%.

With respect to ion fluence the surface roughness as well as the average ripple peak-to-peak amplitude v follow a power law or exponential behavior, but reach quickly saturation [32, 193] and are rather linear in ion energy. Here too, the ripple amplitude (relative error below 10%) increases with the wavelength, which is only broken by the $\lambda = 50.8$ nm sample. Comparing the observed ripple amplitudes v against their wavelengths λ , increasing amplitudes were found for rippled Si substrates that typically do not exceed an aspect ratio of 1 : 20 [32].

As already observed in former studies [21, 32, 33], and as it will be shown later using e. g. transmission electron microscope (TEM) images, magnetic films deposited on top of rippled substrates reproduce the substrate's morphology on both interfaces leading to an in-phase modulated film⁹, accompanied with an increase of roughness and amplitude dependent on the film thickness. Therefore, together with the increase of roughness for increasing wavelengths, rippled Si samples provide an excellent base for studying the influence of roughness on magnetic properties via the templates.

4.2 Induced uniaxial magnetic anisotropy

After characterizing the substrates with respect to their roughness properties, magnetic layers of Fe, Co, and Py had been deposited on top. Here, each film had a thickness of 10 nm and was followed by a 2 nm Cr protective layer. Due to the amorphous Si surface the growth of the films is expected to be polycrystalline. Since these samples were prepared in the early stage of the VNA-FMR construction and optimization process, these samples have been measured partially by using a cavity-based FMR setup situated in the Dresden High Magnetic Field Laboratory at the HZDR campus. The cavity setup was a X-band Bruker Elexsys 500 spectrometer equipped with a goniometer operating at a microwave frequency of $f = 9.38$ GHz. In addition, the VNA setup¹⁰ introduced above was used on some samples. Both setups have been operated at room

⁹Consequently, the upper interface is simply shifted upwards by the film thickness and crests (troughs) lay on top of each other. Out-of-phase modulated films may become important in magnetic multilayers [194].

¹⁰As it will be shown in the next chapter the influence of the CPW onto the anisotropy is negligible.

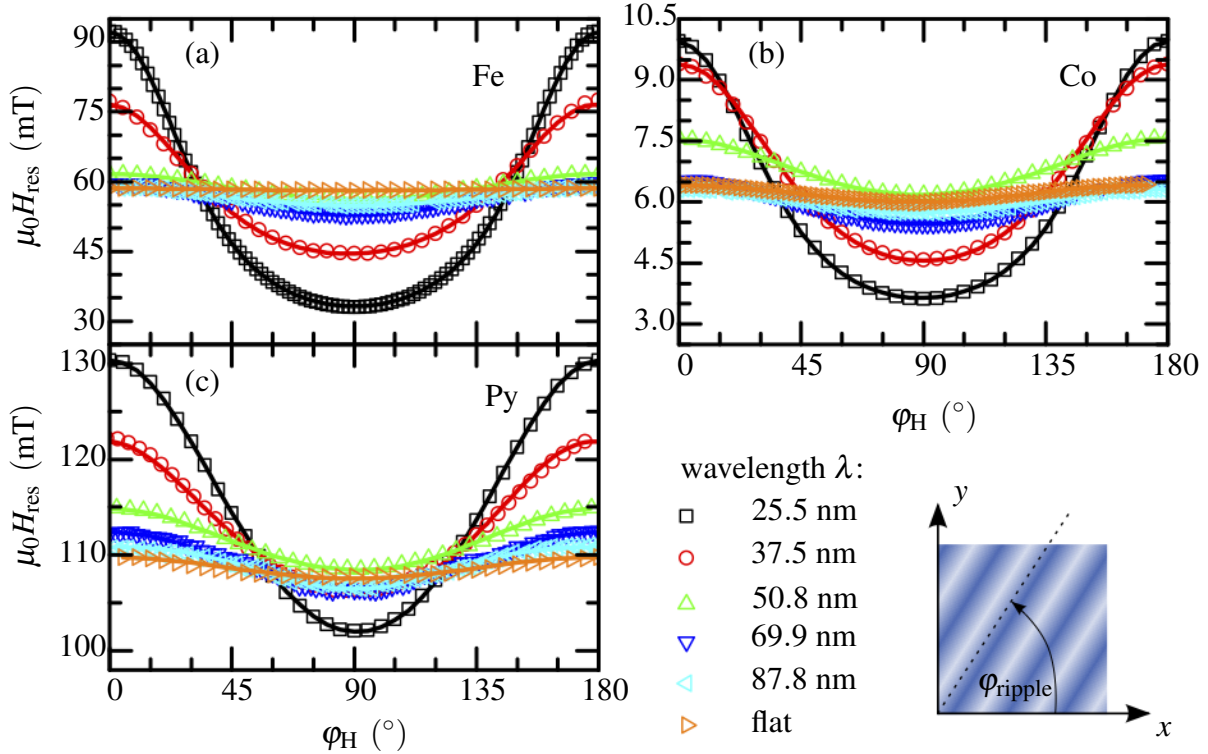


Figure 4.2: In-plane angular dependence of the recorded (symbols) resonance field $\mu_0 H_{\text{res}}$ for (a) Fe, (b) Co, and (c) Py thin films of 10 nm thickness deposited on rippled Si substrates of varying wavelength. The solid lines were obtained by fitting the resonance condition (3.1) to the measured data using the sketched geometry.

temperature. To get the anisotropy contributions originating from the surface morphology the samples were measured with an in-plane applied external magnetic field H , where the field angle φ_H was varied while $\theta_H = 90^\circ$ was kept constant. According to the geometry depicted in Fig. 4.2 the ripple wavefront, whose orientation is known from AFM measurements, was oriented parallel to the y axis ($\varphi_{\text{ripple}} = 90^\circ$). In order to extract anisotropy parameters, Eq. (3.1) has been evaluated using the developed *Matlab* toolbox, introduced in appendix A. Due to the interest in the in-plane anisotropy out-of-plane constants $K_{i\perp}$, except for the effective magnetization $\mu_0 M_{\text{eff}} = \mu_0 M_s - 2 K_{2\perp} / M_s$, will not be discussed. For the g -factors, literature values were assumed, using $g_{\text{Fe}} = 2.088$, $g_{\text{Co}} = 2.18$, and $g_{\text{Py}} = 2.1$ [128, 195].

FMR measurement as well as the corresponding fits are shown in Fig. 4.2. All graphs show a two-fold symmetry that is perfectly reproduced by the model function. The strength of the resonance field is set by the uniaxial in-plane anisotropy constant $K_{2\parallel}$, while the orientation is determined by φ_u , which is, like φ_{ripple} , counted from the x direction (see Fig. 4.2). Since minima of the in-plane resonance field are always observed under $\varphi_H = 90^\circ$ and maxima in turn

occur perpendicularly to this direction along $\varphi_H = 0$ and $\varphi_H = 180^\circ$, the uniaxial anisotropy is found to be $\varphi_u = 90^\circ$. This in turn means that the uniaxial in-plane anisotropy aligns parallel to the ripple wavefront.

In addition, to obtain better fits for Co and Fe it was necessary to include a small four-fold in-plane anisotropy contribution $K_{4||}$, which is, however, two orders of magnitude smaller than $K_{2||}$ and, thus, negligible. The origin of the four-fold anisotropy contribution is caused by intrinsic material properties. Usually, due to the polycrystalline film growth, the random grain orientation is expected to average out this contribution.

As mentioned above, the origin of the uniaxial anisotropy may have mainly three effects: (i) Step edge contributions, (ii) strain effects, and (iii) dipolar effects. If the intrinsic crystal anisotropy is found to average out, the same holds true for randomly oriented grains at the steps. Also strain effects will ease off under random grain orientation. Thus, the most favorable origin of the UMA is due to the dipolar stray fields, caused by the surface morphology. Orienting the magnetization parallel to the ripple ridges causes no disturbance in the micromagnetic structure. All moments can align parallel to each other while at the same time being parallel to the film surface. However, turning the in-plane magnetization perpendicular to the ridge direction, causes an interplay between exchange and dipolar energy. If the exchange interaction would force the magnetization to be homogeneously magnetized in-plane, energetically unfavorable dipolar fields evolve due to the surface roughness. In contrast, if shape contributions drive the magnetization to follow the surface corrugation, the exchange energy would increase instead. Thus, an intermediate state will be occupied, which will have an increased free energy density in comparison to the parallel state and exhibits dipolar stray fields. This effect will be explored in more detail below.

Clearly visible in the measurements shown in Fig. 4.2 is a decrease of peak-to-peak resonance field with increasing ripple wavelength. Since four-fold anisotropy is negligible this originates from the induced UMA. Fig. 4.3(a) shows the observed scaling of the UMA field $2K_{2||}/M_s$ as a function of the ripple wavelength for all three materials investigated. The error of the measurement is within the symbol size. Solid lines serve as guides to the eye only. Especially for the low-wavelength regime ($\lambda < 50$ nm) a strong wavelength dependence can be observed that decays rapidly with increasing λ . Above the wavelength of 50 nm the decay of anisotropy field slows considerably down and reaches finally its saturation value of ≈ 2 mT, observed on flat Si substrates. This decay of UMA strength suggests a dipolar origin, because approaching a flat film will more and more decrease dipolar fields in their strength. However, by comparing the uniaxial anisotropy strengths of Co with the ones of Fe it strikes that Co has the higher values, which is somewhat puzzling. For purely dipolar interaction this in turn should be the opposite, since a higher magnetization should cause a stronger dipolar field and, hence,

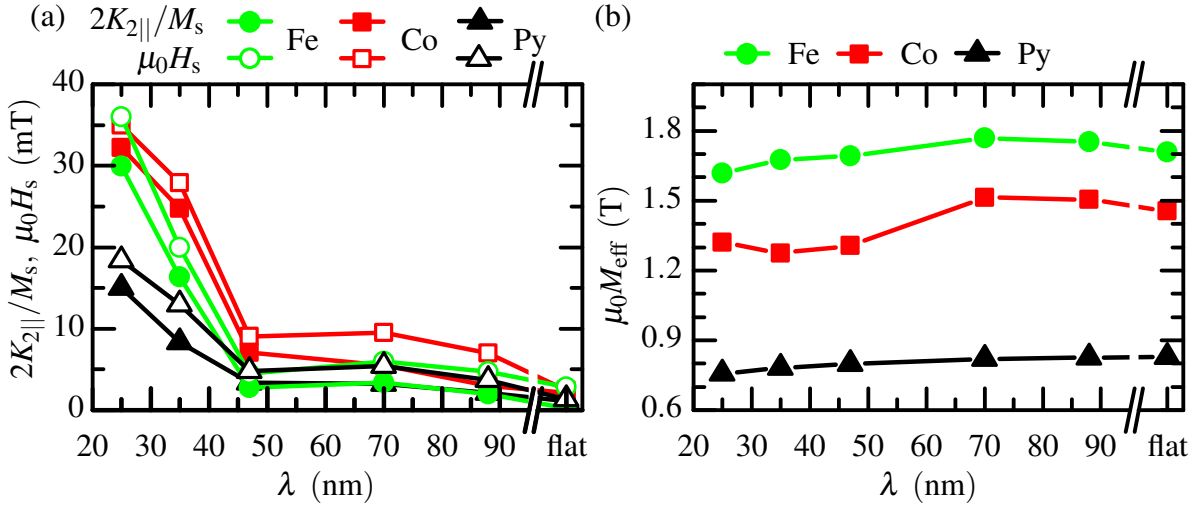


Figure 4.3: Measured wavelength dependence (symbols) of (a) the in-plane uniaxial anisotropy field (solid symbols), the saturation field (open symbols), and (b) the effective magnetization. The solid lines serve as guides to the eye only.

higher anisotropy. This indicates that also other minor contributions must be present, having their origin e. g. in the different crystal structure (cubic vs. hcp) and related texturing or in magnetostrictive interactions.

Besides the uniaxial anisotropy field obtained by FMR measurements Fig. 4.3(a) shows in addition the saturation field¹¹ H_s . It has been obtained by means of MOKE magnetometry where the magnetic field was applied perpendicularly to the ripple wavefronts (along the hard axis). For this case H_s provides an equivalent¹² measure of the UMA with $H_s = 2K_{2||}/M_s$ and is in reasonable agreement with the FMR measurements.

In part (b) of Fig. 4.3 the wavelength dependence of the effective magnetization $\mu_0 M_{\text{eff}}$ is depicted. Again, measurement uncertainties are within the symbol size. Basically no wavelength influence on the effective magnetization can be observed. Even so, the observed effective magnetization $\mu_0 M_{\text{eff}}$ differs by roughly 18% from known bulk values of the saturation magnetization: $\mu_0 M_s^{\text{Fe}} = 2.15$ T, $\mu_0 M_s^{\text{Co}} = 1.76$ T, and $\mu_0 M_s^{\text{Py}} = 1$ T [10, 56]. Due to the definition of the effective magnetization, $\mu_0 M_{\text{eff}} = \mu_0 M_s - 2K_{2||}/M_s$, two origins for the observed deviations are possible. First, the magnetization itself may be reduced and secondly an occurring uniaxial easy out-of-plane anisotropy can lower $\mu_0 M_{\text{eff}}$. The latter may originate from texturing, as it was observed for polycrystalline Co films in the past. In this case a strong

¹¹In magnetization reversal curves H_s is that field value under which a previously unsaturated samples reaches its saturation magnetization while the field magnitude is being increased.

¹²Applies for the present UMA only. Other contributions like four-fold anisotropy will change H_s .

(0001) texture of closely-packed (hcp) Co causes an easy magnetization axis that reduces the effective magnetization [196]. Nevertheless, superconducting quantum interference device (SQUID) magnetometry revealed a saturation magnetization for Co of ≈ 1.7 T, which is close to the bulk value. Hence, the discrepancy between $\mu_0 M_s$ of bulk material and the measured $\mu_0 M_{\text{eff}} = 1.35$ T is caused by an easy axis uniaxial out-of-plane anisotropy in case of Co films. For the case of Fe the impact of texture should be smaller, because in comparison to Co iron exhibits a four-fold cubic crystalline anisotropy instead of a uniaxial one, which makes the effect less pronounced. Indeed, also in this case SQUID measurements reveal a reduction of saturation magnetization down to $\mu_0 M_s^{\text{Fe}} = 1.5$ T.

So far, it was possible to link the creation of an in-plane uniaxial magnetic anisotropy with the correlated roughness, caused by rippled substrates. Here the UMA's strength strongly depends on the periodicity of the corrugation. Further investigations of the suggested dipolar origin will be discussed in more detail in the following section.

4.3 Thickness dependence of the induced UMA

To investigate the contribution of dipolar effects to the UMA, a new set of samples has been prepared. The ripple substrates with the shortest wavelength ($\lambda = 25.5$ nm) have been chosen, because these showed the strongest response in anisotropy. On top magnetic films have been deposited as a wedge going from zero up to 50 nm in thickness d . Finally, the obligatory Cr protective layer has been grown. The chosen sample geometry offers the possibility to study the anisotropy thickness resolved, while keeping the roughness conditions of the substrate. By this, the sample layout made spatially resolved magnetometry investigations necessary that cannot be provided by the FMR setups available. Instead, MOKE magnetometry was applied in longitudinal configuration.

4.3.1 Thickness-dependent magnetization reversal

The first step was to correlate the surface structure with the magnetization reversal behavior. Therefore, the external magnetic field has been applied perpendicularly to the ripple ridges (along the hard magnetization axis) and hysteresis curves have been recorded by means of MOKE magnetometry. In addition, the corresponding regions have been imaged by AFM to obtain the surface profile. Results of both measurements are depicted in Fig. 4.4 for three different layer thicknesses, again for the three materials of interest.

Focusing in the first place on the magnetization reversal curves shows a quite similar behavior for all materials and thicknesses. Depicted are the normalized MOKE signals, scaled by the

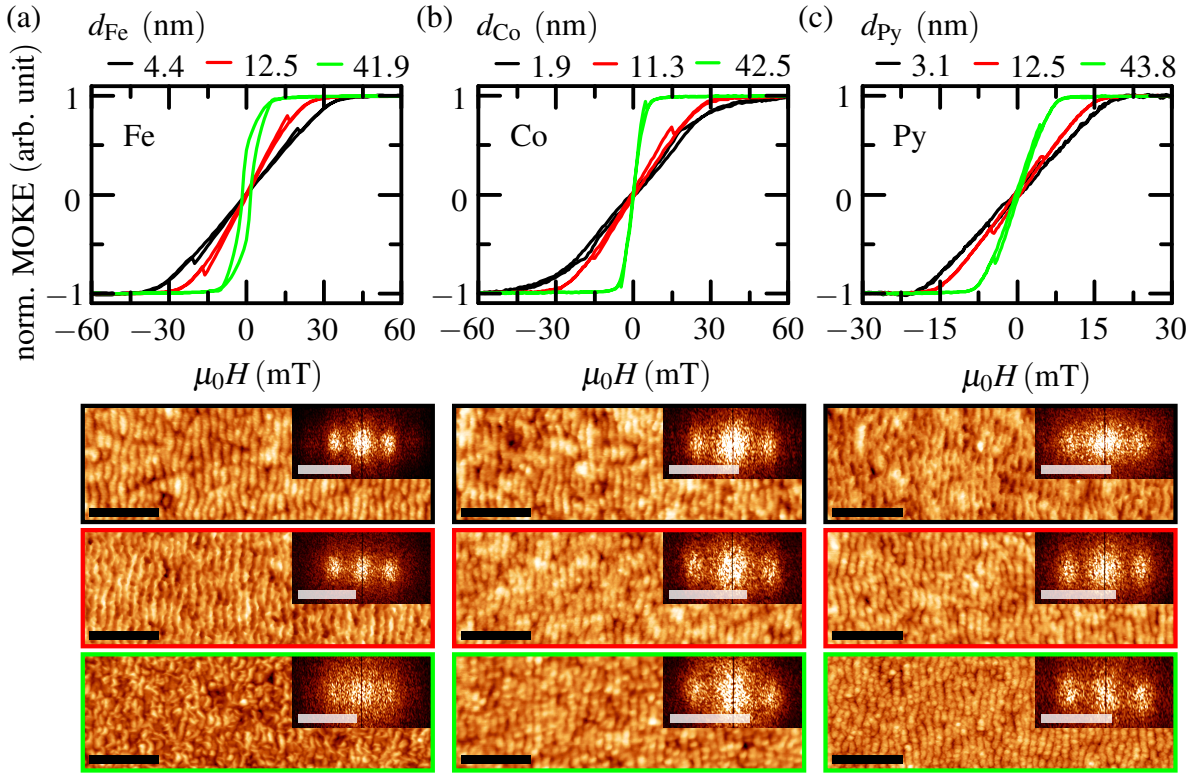


Figure 4.4: Investigations of layer thickness of magnetic films grown on ripples with $\lambda = 25.5$ nm. Panels (a)–(c) depict the behavior for Fe, Co, and Py, respectively. The upper row shows magnetization reversal loops (normalized MOKE signal), whereas the lower rows depict the corresponding AFM images (labeled by colored boxes around images). Black bars correspond to a length of 200 nm. The insets show the corresponding FFTs (color ranges arbitrarily scaled), where white bars correspond to $80 \mu\text{m}^{-1}$.

values measured in saturation for each curve. Basically all curves exhibit the typical features of hard axis magnetization reversals, consisting of a saturated regime for high positive and negative fields, interconnected by a nearly linear field dependence that shows no opening in the middle. This indicates a reversible reorientation process under coherent rotation. The only exception to this is found in a thick iron layer [$d_{\text{Fe}} = 41.9$ nm, Fig. 4.4(c)]. For this case a slight opening of the curve is seen, indicating nonreversible switching processes to be present. The reason for this will be addressed later when discussing the surface structure. With increasing film thickness d the saturation field H_s decreases for all material systems. Together with this also the slope becomes steeper. The reason for the thickness dependence will be addressed in a detailed discussion below. Finally, some of the magnetization reversal curves exhibit a kink on their slope, which is a measurement artifact occurring if the polarization axis of the incident laser beam is slightly misaligned with respect to the sample plane.

Moving on to the AFM images of Fig. 4.4 reveals first an imprinting of the substrate's surface roughness onto the grown magnetic layers. A preferential filling of the valleys, which would reduce the modulation height, cannot be observed. Thus, a closed coverage for small film thicknesses can be assumed. For highest thicknesses a 3D island growth can be observed for Co and Py whereas Fe starts to grow in a complicated microstructure. The surface quality is confirmed by the FFT insets. Except the thickest Fe sample, all FFT images show two satellite peaks, corresponding to the rippled surface structure. The observed wavelength does not change significantly with film thickness, whereas the RMS value slightly increases. Also, for increasing thickness the satellite peaks diminish slightly, suggesting a transition to a random rough surface structure that interconnects the underlying ripples if the thickness would be increased further on.

For the thickest Fe layer such a transition is already quite advanced and the FFT basically shows an isotropic roughness distribution. This might also explain the observed opening in the corresponding magnetization reversal curves for thick iron layers. Due to the increased random surface roughness domain wall nucleation enhances. This shifts the magnetization reversal behavior from coherent rotation to domain accompanied switching, which is noticeable in a splitting of the two branches around zero applied field.

4.3.2 Micromagnetic simulations

To understand roughness-affected magnetization behavior a lot of theoretical work has been done over the past decades. On the one hand, the influence on demagnetization factors has been investigated [11, 14, 191, 192] and, on the other hand, the contribution to magnetostatic energy in general [12, 13, 15, 16, 197]. In particular, the model of Vaz *et al.* [16], developed for single-crystalline films, accounts for the thickness dependence. In that work the authors determine the influence of a random rough surface onto the magnetization state, where the two interfaces of the magnetic film exhibit a coherent modulation. Thereby two thickness regimes evolve, both depicted in Fig. 4.5. For small film thicknesses [Fig. 4.5(a)] and large-enough roughness amplitudes the magnetization is predicted to follow the local roughness profile in order to minimize dipolar energy contributions. The latter arise from "orange-peel" effects [17], which would create dipolar stray fields if the magnetization profile does not follow the surface modulation, but are on cost of increased exchange energy. This state is called undulating state.

In contrast, approaching thicker films [Fig. 4.5(b)] a uniform magnetization state will form due to the linear increase of exchange and anisotropy energy. In this case the magnetization will not follow the surface profile, which creates surface charges and thus dipolar fields. Especially for this state the corresponding magnetostatic energy is well known [14]. Also, for correlation

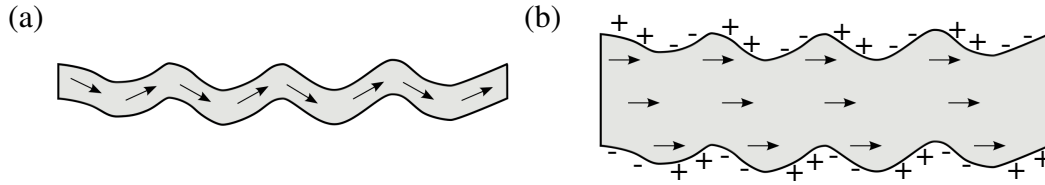


Figure 4.5: Cross-section through a film with correlated roughness in the (a) thin-film regime with undulating magnetization distribution and (b) in the thick regime exhibiting a uniform magnetization state. Arrows denote the local orientation of magnetic moments. Plus and minus symbols mark evolving magnetic “surface charges”.

lengths comparable or smaller than the exchange length the undulating state should be locally uniform. Hence, a competition between anisotropy, exchange, and dipolar energy determines the finally observed magnetization state.

Indeed, the films investigated in this work are non-ideal systems caused by their polycrystalline structure. This makes the model not fully applicable, since the tilt of the magnetization may vary over the film thickness. In order to determine the present magnetization state for various film thicknesses, micromagnetic simulations were performed to account for the complex interplay of energy contributions that may vary over the film thickness. Thus, inconsistencies between the *Vaz et al.* model and the presented experiments were found, e. g. non-vanishing dipolar contributions.

Numeric simulations were performed using *LLG Micromagnetic Simulator* [198] and applying it to rippled Fe films ($\mu_0 M_s = 2.15$ T, $A_{\text{ex}} = 2.1 \cdot 10^{-11}$ J/m) with a thickness between 1 and 30 nm. The choice was in favor of Fe films to benefit from the higher magnetic moment with respect to stray field creation. Furthermore, neither uniaxial nor cubic anisotropy contributions were taken into account in the simulations. Also no external magnetic field was applied to be able to explore the magnetization contribution generated by internal contributions only. Nevertheless, in order to achieve an alignment of magnetization along the hard axis [in the xz plane, see Fig. 4.6(g)], which is perpendicular to the ripple wavefront, a stripe of 100 nm along the y direction was simulated instead of a continuous film. In the x direction periodic boundary conditions were applied to avoid stray field creation at the sample edges. Also, the ripple peak-to-peak amplitude was fixed at $v = 2$ nm and its wavelength to $\lambda = 25$ nm for all layer thicknesses. Note that a perfect sinusoidal surface corrugation was assumed¹³. For the simulation a cell size of $0.2 \times 10 \times 0.1$ nm³ was used and the data obtained were averaged over all slices along the y direction. A corresponding geometry is shown in Fig. 4.6(g).

The simulation results are summarized in Fig. 4.6. Two different thicknesses are depicted

¹³The simulation method uses a finite difference approach, which will cause artifacts at curved interfaces like the ripple surface.

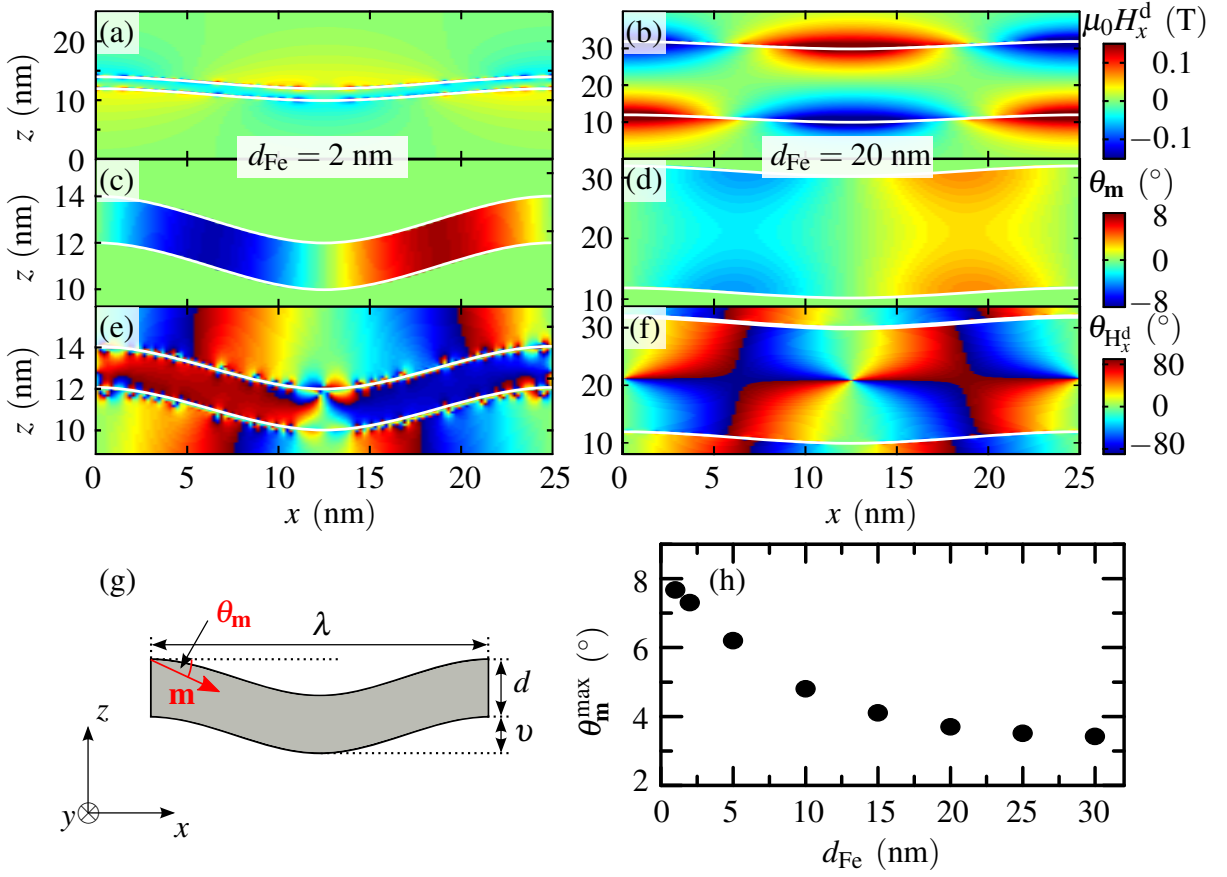


Figure 4.6: Micromagnetic simulations of Fe films with varying thickness d_{Fe} . The left column of the panels (a)–(f) shows a 2 nm film, whereas for the right one $d_{\text{Fe}} = 20$ nm applies. White lines mark ripple/vacuum interfaces. Within the rows the dipolar stray field $\mu_0 H_x^d$ along x [(a), (b)], the angle of magnetic moments θ_m [(c), (d)], and the angle of the in-plane dipolar field $\theta_{H_x^d}$ [(e), (f)] are depicted. Both are counted from the x direction. (g) Underlying geometry and (h) maximum tilt angle θ_m^{max} of the moments over the film thickness.

exemplarily, namely for a 2 nm thin film [Figs. 4.6(a), (c), and (e)] and a 20 nm thick one [Figs. 4.6(b), (d), and (f)]. At first, let's consider the calculated stray field generated in case of thin [Fig. 4.6(a)] and thick [Fig. 4.6(b)] rippled films. In both images the dipolar stray field component H_x^d along the x axis is depicted using the same color bar. For the Vaz model one would expect a strong field for the thick case, but a vanishing one for very thin films. However, the simulations shown provide non-vanishing dipolar fields also for the thin-film case, indicating a deviation of magnetization alignment with respect to the surface corrugation. Albeit, the field strengths for the cases shown is roughly one order of magnitude smaller for the thin film with respect to the thicker one.

Most important, the calculated stray fields are nonuniformly distributed over the film thick-

ness (along the z direction), which is shown in Figs. 4.6(e) and (f) for the thin and thick film, respectively. There, the angle between magnetization direction and x axis is given using the same color code. Plotted is the in-plane angle $\theta_{H_x^d}$ of the dipolar field H_x^d , counted from the x direction. As it can be seen from the graphs for thin films the stray field points basically from one interface to the other, which connects the generated surface charges on both interfaces across the magnetic layer. In contrast, for thick films the interfaces behave almost like two separated ones. There, the flux closure inside the sample is done for each interface separately. This means, especially for thick films a nonuniform magnetization distribution will evolve, which is a function of the film thickness.

This situation is shown for both thicknesses in Figs. 4.6(c) and (d). There, the in-plane angles θ_m of the magnetic moments are plotted. In the thin-film region only a slight variation of the orientation within the film thickness is observed, which in turn changes for thick films. Starting at the film surface the local magnetic moment \mathbf{m} has its strongest deflection θ_m from the averaged surface height (along the x axis), since surface charges are present that offer the highest possible stray field strength. Following into the depth of the film (along the z direction), the dipolar fields decay in strength and, hence, the tilt of the magnetization reduces until it reaches its minimum in the middle of the layer. Therefore, a nonuniform magnetization distribution is observed, which is most pronounced for thick layers. For thin layers the surface charges are quite close together which reduces the decay in strength.

To analyze the influence of the layer thickness on the magnetization, the maximum local tilt angle θ_m^{\max} was computed from images as shown in Fig. 4.6(c). The maximum was taken to circumvent the local variation of the magnetization distribution. To have a reference, θ_m^{\max} was also calculated for a film following perfectly the surface corrugation. Of course, the angle is independent from the layer height and is only given by the surface corrugation. For the ripple sample chosen in this part of the study θ_m^{\max} is equal to 14.1° , which is simultaneously the maximum available distortion from a perfect sinusoidal surface corrugation. The results obtained are summarized in Fig. 4.6(f). Clearly visible is a tilting of the magnetization towards the ripple curvature, however, caused by the interplay of exchange interaction with shape anisotropy in the film plane, the calculated angle θ_m^{\max} is slightly larger than 50% of the expected maximum of 14.1° for ideal films. Furthermore, θ_m^{\max} decreases as a function of the film thickness, marking a fading influence of the surface roughness towards bulk-like behavior. Thus, the amount of surface charges decreases with the film thickness as well.

Finally, the micromagnetic simulations show a clear oscillation of the magnetization vector following the surface corrugation, however, not reaching the perfect case. Therefore, dipolar fields are present, causing an inhomogeneous magnetization distribution over the sample's thickness.

magnetic material	thin film		thick film	
	$\mu_0 H_s^V$ (mT)	$\mu_0 H_s^S$ (mT)	$\mu_0 H_s^V$ (mT)	$\mu_0 H_s^S$ (mT)
Fe	48.5 (1.7)	-4.5 (3.9)	11.8 (0.3)	130.0 (4.1)
Co	58.9 (1.8)	-1.9 (3.1)	2.2 (0.3)	187.1 (4.0)
Py	21.8 (0.4)	0.3 (1.2)	5.4 (0.1)	92.4 (2.0)

Table 4.2: Volume and surface contribution of the UMA, extracted from thickness-dependent magnetization reversal curves. The parameters are determined from the thin- and thick-film regime, shown in Fig. 4.7. The error is given by the standard error of the fit.

4.3.3 Thickness evolution of the anisotropy

Finally, the thickness dependence of the anisotropy is discussed. Here, the MOKE laser was scanned across the metal wedge, recording a hysteresis curve at every point. The applied magnetic field was oriented perpendicularly to the ripple wavefront to measure hard axis loops. From this, the saturation fields have been obtained, which in this case provides a measure of the UMA [$H_s = 2K_{2||}/M_s$, cf. Fig. 4.3(a)]. According to Eq. (2.25) presented earlier, the magnetic anisotropy can be separated into a surface $K_{2||}^S$ and a volume $K_{2||}^V$ contribution. To extract both components, the thickness dependence is plotted linearized in Figs. 4.7(a)–(c). Indeed, two thickness regimes are observed, where the lines are fits using Eq. (2.25). Both regions are separated by a rather sharp kink instead of a transition region. The parameters obtained by the fits are listed in Table 4.2.

Considering at first the thin-film region, the surface contributions H_s^S are much smaller than the volume parts H_s^V for all three materials. The opposite case is given for the thick region. Since the surface contribution H_s^S of the UMA is basically negligible in the thin-film region, dipolar effects (if considered to be the only source of H_s^S) originating from surface charges are negligible as well and volume contributions are dominating. This observation is in nice agreement with the micromagnetic simulations, showing a reduced amount of surface charges for thin films. With respect to the volume contribution of the UMA a possible origin may be found in lattice strain [199], which is most prominent at small layer thicknesses and relaxes with increasing thickness. As already mentioned, the two regimes exhibit a sharp transition. Determining the intersection of the linear fits gives the critical thickness that separates both regions. Here, Fe and Co have a similar critical thickness of $d^{\text{crit}} = 7$ nm, whereas Py exhibits a higher one of $d^{\text{crit}} = 12$ nm. Furthermore, when considering the surface anisotropy contribution for thin films, negative values can be found for Fe and Co. Considering a uniaxial anisotropy a negative anisotropy constant is equivalent to a rotation of the easy axis by 90° . Thus, H_s^S and H_s^V are oriented orthogonal to each other for this case, turning H_s^S perpendicularly to the ripple

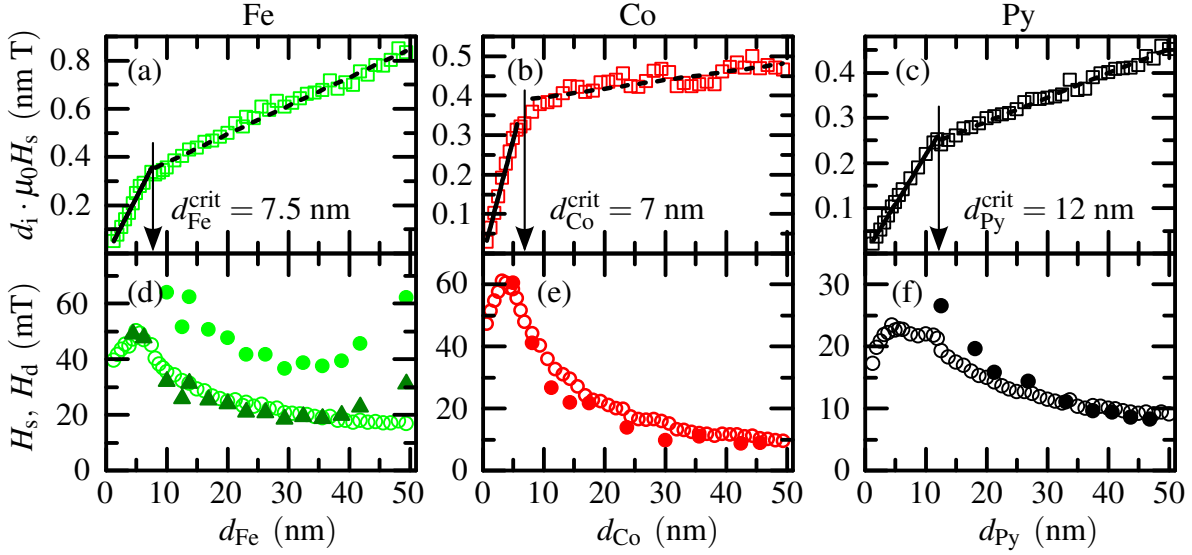


Figure 4.7: Thickness-dependent investigation of (a)–(c) the linearized saturation field $d_i \cdot H_s$ and (d)–(f) the saturation field H_s and the demagnetizing field H_d for the three materials investigated. Open symbols denote the measurement, solid circles the calculated demagnetization fields taking two interfaces into account, and, in case of Fe the solid triangles denote H_d for a single interface. Solid and dashed lines are linear fits for thin and thick regions, where the arrows denote the critical thicknesses d^{crit} between these two regions.

crests. However, the error evolving by taking only the standard error of the fitting procedure into account is—except for Fe—already in the range of the determined anisotropy constant, which makes the observation nonsignificant. Considering further uncertainties, such as the determination of H_s or field error, will increase the experimental error further. Additionally, a reason for such a rotation could not be found in the simulations, which in turn is hard to determine since the volume dominates over the surface contribution (in the discussed region) causing possible spin reorientations to be negligibly small.

Finally, if the UMA is of dipolar origin, it should be possible to directly link the dipolar fields with the observed anisotropy fields for the cases of a dominant surface contribution (thick-film region). Already in 1970 Schlömann presented a theory that calculates the in-plane demagnetization factors [11], and hence the dipolar fields via Eq. (2.11) for arbitrarily rough surfaces with uniform magnetization having a RMS w and a predominant surface modulation λ [11, 33]:

$$H_d = \mu_0 M_s \frac{2\pi w^2}{\lambda d}. \quad (4.7)$$

Here, for all occurring parameters, except M_s where bulk values have been assumed, can be accessed experimentally and are already discussed previously. The results gained by Eq. (4.7)

are plotted in Figs. 4.7(d)–(f) along with the uniaxial anisotropy field H_s . Considering Co and Py a very good agreement is obtained that finally proves the origin of the UMA to be dipolar and caused by surface roughness. In case of Fe only the functional trend can be reproduced by the calculated demagnetization field (solid circles). However, previous investigations in this chapter have proven that Fe on the one hand exhibits a reduced saturation magnetization and on the other hand the surface structure, especially for large thicknesses, does not reproduce the ripple surface anymore. Following the first, a reduction of $\mu_0 M_s$ to 1.23 T would result in a good agreement, which nevertheless is nearly half the bulk value and also far below the SQUID data ($\mu_0 M_s^{\text{Fe}} = 1.5$ T). Therefore, a reduction of $\mu_0 M_s$ is hard to believe even if texture and observed island growth certainly have an influence on the value. To account for the surface structure Eq. (4.7) needs to be slightly modified. The factor of two in the equation originates from the number of interfaces of the film. For perfectly imprinted roughness the modulation is present and correlated on both sides of the magnetic layer. This is in particular the case for Co and Py. However, Fe films develop a microstructure at the top interface when approaching large thicknesses that loses the corrugation to the substrate modulation. Thus, neglecting the factor of two in (4.7) results in the solid triangles shown in Fig. 4.7(d) and hence in a perfect agreement with experimental data, which is of course a simplified picture. In reality both effects will contribute via a reduced $\mu_0 M_s$ and an interface number between one and two, as it is already suggested by the SQUID data. Furthermore, Fig. 4.7(d) shows a rapid increase of H_d for layer thicknesses above 40 nm, which can be related to the increase in roughness and loss of lateral correlation of the surface modulation at the top interface. Apart from these difficulties, this simple theoretical model reflects the experimental situation surprisingly well.

Summarizing the key points of this chapter, it was possible to link the surface-induced roughness of a magnetic film to the generation of dipolar fields, which finally induces a uniaxial magnetic anisotropy whose easy axis is aligned parallel to the ripple crest. The roughness can easily be influenced by the use of rippled substrates, where a smaller wavelength causes a higher UMA. Two thickness regimes have been observed with a dominant dipolar contribution for large thicknesses. In addition, micromagnetic simulations proofed the magnetization to be nonuniform over the sample, following at least partially the surface corrugation.

5 Epitaxial iron on ion beam eroded single-crystalline substrates

Once it was shown in the previous chapter that rippled surfaces are able to induce a UMA to magnetic systems, it is now the aim of this chapter to take this idea further and combine induced with intrinsic crystalline anisotropy. In this way, an insight can be gained into the interplay between this two—fundamentally different—anisotropy contributions on the one hand, and on the other hand a successful combination of both will open a new opportunity of tailoring magnetic properties. In order to study these two aspects a suitable material system is necessary, which has to fulfill several requirements. First, the magnetic material of choice has to be grown easily on top of rippled substrates finally showing an in-plane crystalline anisotropy. The intrinsic anisotropy in turn should have a symmetry that differs from the induced uniaxial one, in order to be able to unambiguously separate both. These requirements are perfectly fulfilled by thin iron films that are epitaxially grown on single-crystalline substrates, showing its intrinsic four-fold magneto-crystalline anisotropy due to the cubic lattice. This was achieved in the past e. g. by using MgO [163, 200–202], Ag [34, 162, 203, 204], or GaAs [146, 205–207] substrates.

If one would start again with the previously used Si ripples, having an amorphous surface layer, a recrystallization by annealing would be necessary. However, annealing the sample after the film growth may have several side effects like diffusion of substrate or cap layer atoms into the magnetic film, imperfect recrystallization, or changing the morphology of the substrate/magnetic film interface. Furthermore, annealing of rippled Si was tried by others in the group leading to a degradation of the surface modulation. Hence, another way of preparing single-crystalline rippled Fe layers is necessary. Taking a look into literature reveals for example the erosion of single-crystalline Fe films [34, 162, 163]. A major disadvantage, however, is the challenging control of layer thickness during the sputtering process, and in addition, having only one modulated interface. Thus, again the bottom-up approach was favored, this time starting with a rippled single-crystalline substrate, as it was e. g. done for Fe on rippled Ag [34]. In order to achieve a good epitaxial relation and to be able to check the rippled substrate

morphology under ambient conditions prior to the Fe growth, MgO(001) was chosen¹. The advantage of MgO against Si is that MgO keeps its crystal structure during sputtering and does not oxidize when exposed to air.

Also this study was done in collaboration with M. O. Liedke, sharing sample preparation and some measurements. The work was published in Ref. 208. Indeed, this time the FMR measurements were completely performed on the VNA-FMR system.

The chapter's structure starts with a summary of the sample preparation followed by a characterization of the rippled MgO substrates (provided by F. Grossmann, M. Ranjan, and S. Facsko) and the Fe films grown on top. As desired, both are single-crystalline. Next, the FMR measurements are discussed revealing a superposition of a UMA onto the magneto-crystalline anisotropy. Both can be adjusted with respect to their relative orientation without restrictions. Finally, the measured FMR linewidth is discussed.

The sample preparation procedure basically equals the one presented in the previous chapter. Using the same method makes the experiments fast in preparation and reliable with respect to sample quality. Here, only ripple substrates with the smallest available wavelength have been considered to gain the strongest UMA contribution. This time commercially available MgO(001) substrates² were used as starting point and were bombarded with Ar⁺ having a primary energy of $E = 0.6$ keV, a fluence of $5 \cdot 10^{17}$ ions/cm², an incident angle of 50°, and a substrate temperature of 0 °C during sputtering. The latter was necessary to ensure a good ripple quality. Most important, the ripple ridge direction ϕ_{ripple} could be set during sputtering to any arbitrary angle with respect to the in-plane MgO $\langle 100 \rangle$ directions. An illustration of the underlying geometry is shown in Fig. 5.1. As above, AFM images were taken prior to film deposition to ensure the substrate's quality. Finally, the samples underwent an identical cleaning procedure (as described in section 4.1.1) and a 10 nm thin Fe film was grown by MBE followed by a Cr cap layer (pressure during growth better than 10^{-9} mbar while using a rate of ≈ 0.2 Å/s). Again, the layer deposition was carried out at room temperature. The Cr layer thickness was varied between 2 and 6 nm. Thicker cap layers were chosen for some samples to achieve a better protection of the surface against scratches caused by the CPW/sample contact. However, no influence of the cap layer thickness on the measurement could be determined. Furthermore, the crystal structure of some samples was examined by means of low energy electron diffraction (LEED) and transmission electron microscopy (TEM), revealing both crystalline growth of Fe on MgO. Finally, magnetometry was carried out by means of VNA-FMR.

¹lattice mismatch between both materials is approximately 4% [176, 201]

²MgO[100] and MgO[010] are parallel to the sample edges, as depicted in Fig. 5.1

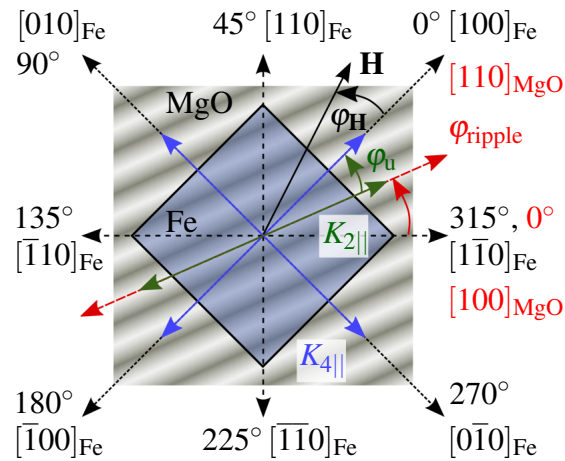


Figure 5.1: Underlying geometry of the rippled Fe/MgO system. In red MgO directions are highlighted, whereas directions in black are counted in the Fe frame. Also the external field \mathbf{H} , the uniaxial anisotropy $K_{2||}$ (green), as well as the four-fold anisotropy $K_{4||}$ (blue) are referred to the Fe frame, whereas the ripple direction is counted in the MgO frame. Both frames are rotated by 45° with respect to each other.

5.1 Sample structure

The surface crystal structure of the MgO substrates and Fe layers can be easily checked by means of LEED. The utilized electron beam has a diameter of less than a millimeter and penetrates the sample's surface within a few monolayers. If the penetrated part exhibits an ordered structure, the reflected beam will be diffracted and a pattern is observed on the screen mapping the reciprocal space of the diffracting periodic structure. Details of this technique are reported e. g. in Refs. 209, 210. Corresponding investigations are shown in Fig. 5.2.

Starting with AFM, the images reveal a loss in image quality when comparing it for example to Fig. 4.1. The reason is mainly due to the insulating MgO and the quite small surface features. If the MgO is charged, e. g. during sputtering, it is difficult to obtain good AFM images since charges repel the AFM tip. Attempts to discharge sample and tip often were not successful. In Fig. 5.2(a) a flat MgO sample is shown that is covered by Fe (10 nm)/Cr (6 nm). Next to the AFM image the corresponding FFT (top) and LEED pattern (bottom) is shown³. From the FFT an almost uniform roughness distribution can be concluded, whereas the LEED pattern reveals a cubic lattice structure. The latter was recorded prior to the Cr cap layer deposition. Next, a rippled MgO sample is compared prior [Fig. 5.2(b)] and after [Fig. 5.2(c)] film deposition. Here, the ripple wavelength is conserved during the film growth, whereas the FFT is slightly diminished. Most important, both LEED patterns show a crystal lattice structure indicating a

³In the center of the LEED image the electron gun blocks the central reflex.

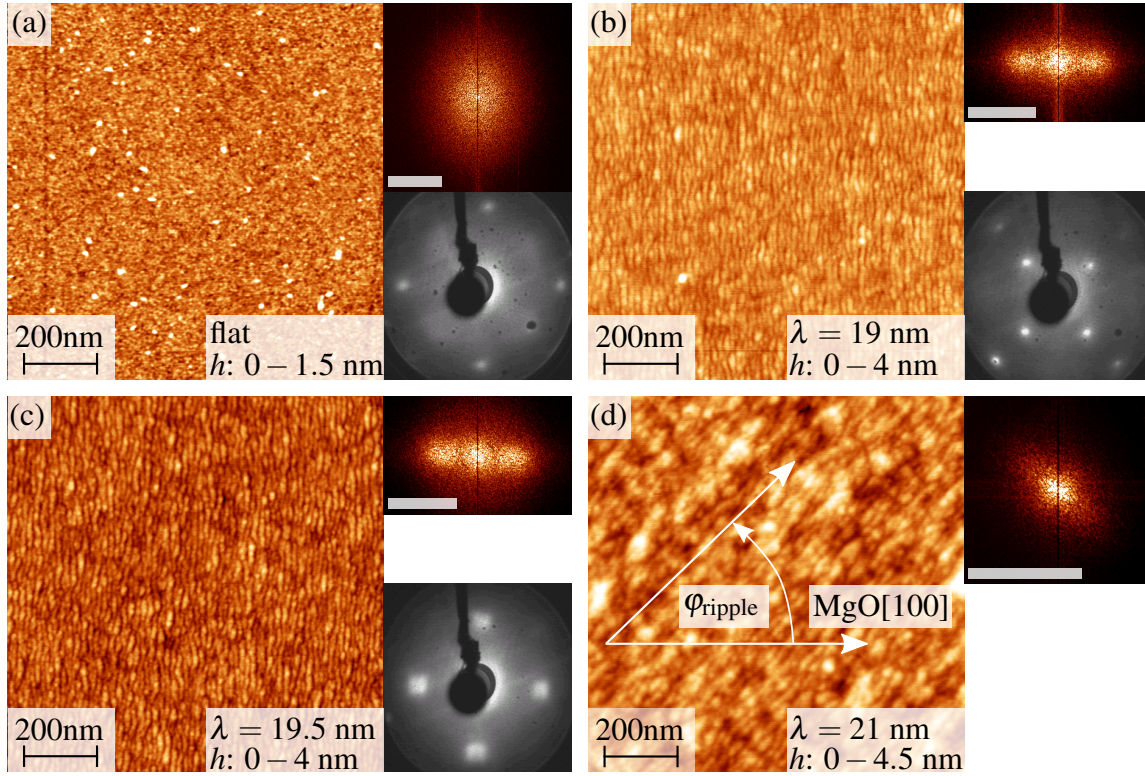


Figure 5.2: Structural investigation of single-crystalline MgO substrates. (a) Flat substrate with Fe (10 nm) / Cr (6 nm) deposited on top. AFM images of: (b) a rippled sample before and (c) after layer deposition and (d) uncovered substrate with ripple ridges rotated with respect to MgO[100]. h denotes the height scaling and λ the ripple wavelength. On the right hand of the images the FFT (top, with arbitrarily scaled color ranges and white bars corresponding to $100 \mu\text{m}^{-1}$) and LEED patterns (bottom, arbitrarily scaled). LEED electron energies are: (a) 120 eV, (b) 162 eV, and (c) 167 eV.

crystalline ripple surface after ion erosion and film growth.

It is well known that Fe grows 45° rotated in-plane with respect to the MgO lattice⁴, which is caused by the mutual lattice mismatch [201]. This rotation is reflected by the LEED patterns in Figs. 5.2(b) and (c), where in panel (b) additionally the high-order diffraction is visible. To compare the uniaxial anisotropy (measured in the Fe system) with the ripple ridge direction (measured in the MgO system), the following conversion

$$\phi_{\text{ripple}}^{\text{Fe}} = \phi_{\text{ripple}} - 45^\circ \quad (5.1)$$

will be used.

Finally, Fig. 5.2(d) shows an eroded MgO surface where the ripple wavefront is rotated

⁴Fe $\langle 110 \rangle$ || MgO $\langle 100 \rangle$, see Fig. 5.1

by $\varphi_{\text{ripple}} = 44^\circ$ with respect to MgO[100]. For this sample the FFT is, already without any layer, too blurry to determine the wavelength. Instead, it was extracted from a ripple profile directly. Thus, the ripple patterns showed a wavelength around $\lambda = 20$ nm and amplitudes of approximately 1 nm. Unfortunately, the AFM image quality did not allow for a satisfying RMS determination, but it can be stated that the values are below the ones from the Si case. Note that the in-plane ripple orientation φ_{ripple} can be set arbitrarily with respect to MgO[100], offering the possibility to study a model system of superimposed uniaxial and cubic magnetic anisotropy.

To further investigate the crystal structure of Fe on MgO, TEM cross-section images have been taken. For this, the samples have been thinned by a polishing process. The results, acquired by A. Mücklich, are shown in Fig. 5.3. Depicted are cross-sectional views perpendicular to the ripple wavefront. Part (a) shows a wide view including several wavelengths. From this, a conformal layer growth can be observed (highlighted by the white dashed lines). Taking a closer look on the lattice structure, shown in a high-resolution image in part (b), reveals a continuous lattice extending from the MgO substrate through the Fe layer up to the Cr cap layer. Additionally, no amorphization was found, underlining the epitaxial, pseudomorphic crystal growth. For better visibility three lattice planes are highlighted by yellow dashed lines.

In the course of the TEM investigations FFTs have been computed to identify the crystal orientation. The respective spacings of the observed planes are shown in Table 5.1. Two important things can be deduced from these values. First, the in-plane lattices of Fe and Cr are parallel to each other and rotated by 45° with respect to the in-plane MgO $\langle 100 \rangle$ orientation. In perpendicular direction the [001] directions of Fe and MgO are parallel. Second, the in-plane spacings differ by 1.5% from the theoretical values for MgO, but 2.5% and 5% for Fe and Cr, respectively. In contrast, the out-of-plane values are close to the expected ones [(002) spacings for Fe and MgO in Table 5.1]. The in-plane lattice expansion is due to the pseudomorphic growth of Fe on the MgO, originating from the lattice misfit. Consequences of this are also present in the TEM image. From the lattice planes highlighted in Fig. 5.3(b) defects are visible (red circles), i. e. dislocations. This indicates strain relaxation to the intrinsically preferred Fe lattice.

To explore this lattice relaxation further, X-ray diffraction experiments have been performed and evaluated on similar systems by A. Shalimov at the ROBL beamline of the ESRF synchrotron source in Grenoble (France). Examination object was a 15 nm Fe film capped by Cr that was grown on flat MgO (001). The investigations confirmed in- and out-of-plane lattice orientations as already observed by TEM investigations. Furthermore, the Fe layer is under ten-

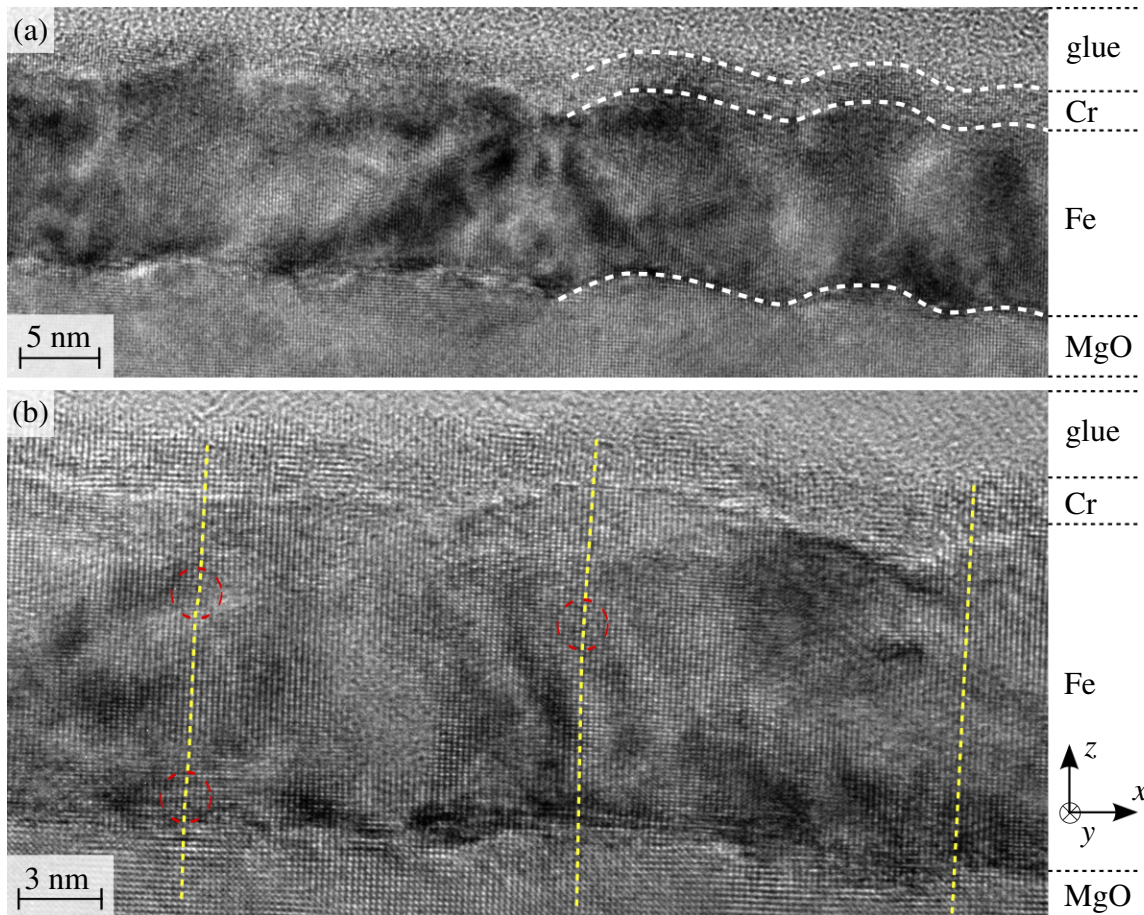


Figure 5.3: TEM cross-section of Fe (10 nm)/Cr (2 nm) deposited on rippled MgO(001). Panel (a) shows a wide view, whereas (b) displays a high-resolution image. White dashed lines mark the rippled interface, yellow dashed lines the observed lattice planes, and red circles lattice defects.

material	plane	lattice spacing	
		theory (nm)	experiment (nm)
MgO	(200), (002)	0.2106	0.214
Fe	(110)	0.2027	0.208
	(002)	0.1433	0.145
Cr	(110)	0.2039	0.215

Table 5.1: Theoretical and experimentally obtained (from a high-resolution TEM image) plane spacings for MgO (fcc), Fe (bcc), and Cr (bcc). Theoretical values can be found in Refs. 176,201,211. The underlying coordinate system is shown in Fig. 5.3.

sile strain⁵ producing a tetragonally distorted unit cell. No difference of the in-plane Fe $\langle 100 \rangle$ directions was observed. Nevertheless, the $\{110\}$ reflection showed, within the systematic error, slightly different values. For this reason, a rhomboidal distortion of the unit cell cannot be fully excluded.

Most important is indeed the determined strain that is given by the relaxation degree:

$$R = \frac{a_{\parallel}^{\text{Fe}} - a_{(110)}^{\text{MgO}}}{a_{\text{bulk}}^{\text{Fe}} - a_{(110)}^{\text{MgO}}}. \quad (5.2)$$

$a_{\parallel}^{\text{Fe}}$ in Eq. (5.2) is the lattice constant for Fe determined in the experiment, and $a_{\text{bulk}}^{\text{Fe}}$ is the bulk Fe lattice parameter that was chosen to $a_{\text{bulk}}^{\text{Fe}} = 2.8686 \text{ \AA}$. To account for the 45° tilt between the Fe and MgO lattice $a_{(110)}^{\text{MgO}}$ has been determined from the (110) plane spacing in MgO. If the determined lattice constant $a_{\parallel}^{\text{Fe}}$ of the Fe film approaches its bulk value $a_{\text{bulk}}^{\text{Fe}}$, the relaxation degree R approaches unity, which indicates a fully relaxed Fe film. In contrary, the Fe film is fully strained if $a_{\parallel}^{\text{Fe}}$ approaches $a_{(110)}^{\text{MgO}}$. Using Eq. (5.2) the relaxation degree for the flat Fe film was found to be $R = -0.14$, indicating a fully strained⁶ film. In contrast, the rippled layer exhibits an almost completely relaxed Fe layer with $R = 0.86$.

In order to compare these findings with the TEM investigations, note that on the one hand the FFT calculations were done on a thinner film (not yet relaxed) and on the other hand taken at the bottom of the Fe film (most strain expected) using a rectangular field of view with less than 5 nm edge length. Thus, predictions from TEM images will give a higher mismatch.

A final proof of the good crystal structure will be given by magnetic investigations discussed below. Here, polycrystalline films would not show a strong cubic anisotropy, which in turn means that also the MgO surface stays single-crystalline after sputtering.

5.2 VNA-FMR investigations

Two different kinds of FMR measurements were performed. First, an in-plane angular scan $H_{\text{res}}(\varphi_{\text{H}})$ was measured determining the behavior of the resonance field at a fixed microwave frequency. From this the easy and hard axes of the sample could be determined, which in turn allowed to measure $f(H)$ dependences along these directions. The latter enabled the possibility to determine the g -factor dependent on the crystallographic direction. Subsequently, it was

⁵the type of strain (tensile or compressive) was determined from calculated strain values (not shown)

⁶A negative sign of R is somehow puzzling as negative values occur for Fe constants being larger than the ones of MgO (usually it is vice versa), which indicates an over-strained Fe film. One possible reason may be the different thermal expansions of both lattices during growth. However, to check this *in-situ* X-ray measurements are necessary.

possible to determine the anisotropy and linewidth behavior of the sample, where the in-plane behavior was considered only.

5.2.1 Direction-dependent g -factor

The reason to determine g —or at least to check it—and not to rely on the literature value of $g_{\text{Fe}} = 2.09$ [212] lies in its possible anisotropic behavior. Based on a relation between spin and orbital momentum ($2\mu_l/\mu_s = g - 2$ [213]), g changes if, e. g., the orbital momentum differs. This was observed for Fe/V superlattices where the momentum reduces at the interface [212, 214]. In addition, the crystal structure can have an effect, although this has not been observed for the case of $3d$ ferromagnets [128]. Nevertheless, if the combination of crystal structure and altered film morphology would turn g anisotropic (e. g. by modified next neighbors at the surface, which should average out for polycrystalline films), the resonance condition has to be modified by including a g -tensor to interpret anisotropies correctly.

To determine the g -factor $f(H)$ measurements have to be evaluated using Eq. (3.1), with $\gamma = g\mu_B/\hbar$. In principle, determining g is also possible from angle-dependent measurements, but by doing so g is simply treated as fitting parameter by which the uncertainties of anisotropy constants enter the g determination. In contrast, this is not the case for measurements at fixed geometries [65, 212]. If measurements are performed along an anisotropy axis, field dragging vanishes as $\varphi = \varphi_H$ applies. Hence, (3.1) simplifies for in-plane measurements ($\theta = \theta_H \equiv 90^\circ$) to:

$$\left(\frac{\omega}{\gamma}\right)^2 = \left\{ \mu_0 H + \left[\mu_0 M_{\text{eff}} + \frac{2K_{2\parallel}}{M_s} \cos^2(\varphi - \varphi_u) + \frac{K_{4\parallel}}{2M_s} (3 + \cos 4\varphi) \right] \right\} \times \left\{ \mu_0 H + \left[\frac{2K_{2\parallel}}{M_s} \cos 2(\varphi - \varphi_u) + \frac{2K_{4\parallel}}{M_s} \cos 4\varphi \right] \right\}. \quad (5.3)$$

Although the expression above contains the angles φ and φ_u inside the squared brackets these terms stay constant during a variation of the external field in magnitude because φ_u is fixed by the sample and φ is settled when measured along an anisotropy axis. Due to this (5.3) further simplifies to

$$\left(\frac{\omega}{\gamma}\right)^2 = (\mu_0 H + c_1)(\mu_0 H + c_2), \quad (5.4)$$

where c_i are constants that depend on the anisotropy. To extract the g -factor from $f(H)$ measurements f^2 over H is plotted and fitted by the parabola $f^2 = \bar{c}_1(\mu_0 H)^2 + \bar{c}_2\mu_0 H + \bar{c}_3$, where the \bar{c}_i are free parameters. While g enters all three parameters \bar{c}_i only \bar{c}_1 has no additional dependence, whereas \bar{c}_2 and \bar{c}_3 include anisotropy constants as well. Hence, using this factor eliminates anisotropy from the calculation completely and g is finally given by $g = 2\pi\sqrt{\bar{c}_1}/\hbar$.

$\varphi_{\text{ripple}}^{\text{Fe}} = -15^\circ$		$\varphi_{\text{ripple}}^{\text{Fe}} = -1^\circ$	
$\varphi_{\text{H}} (^\circ)$	g	$\varphi_{\text{H}} (^\circ)$	g
0.5	2.099 (35)	-88	2.090 (34)
46.0	2.116 (37)	-45	2.125 (58)
90.5	2.088 (29)	1	2.095 (25)
—	—	47	2.11 (3)

Table 5.2: g -factor determined on rippled samples with varying ripple orientation $\varphi_{\text{ripple}}^{\text{Fe}}$. The external field directions φ_{H} correspond to (local) extrema in the lower row of Fig. 5.4.

Uncertainties in g arise from resonance frequency and field only. The resonance frequency is set by the VNA and the error of this continuous wave mode is 1 ppm and thus negligible. Hence, the resonance field determines the error. First, uncertainties from the fitting have to be considered when determining the resonance position and are typically below 0.5 mT. In contrast, the uncertainty of the teslameter is less than 0.01% and can be neglected. Finally, an error for the field determination arises from the hall probe mounted at a pole piece, whereas the sample is located in the center between the poles. This results in large deviations if the poles start to saturate (above 1.4 T). Operating the electromagnet below this point adds another 0.5 mT to the field error. Altogether this yields to errors of g between 0.02 and 0.06.

The introduced method was applied to a variety of samples. Each time the in-plane angular orientation of the magnetization was checked with respect to the external field, where typically deviations below 1° were found. For flat Fe films, g was determined to $g_{[100]} = 2.114(46)$ and $g_{[010]} = 2.096(34)$ along [100] and [010], respectively. Hence, within the order of experimental precision g equals the literature value of 2.09. Furthermore, the g -factor was determined for the rippled samples. The obtained values are shown in Table 5.2. Again, within the given experimental precision, no deviation from the literature value was found.

5.2.2 In-plane anisotropy

The influence of the ripple morphology was investigated in a broad range of ripple orientations with respect to the crystal anisotropy. Figure 5.4 shows a selection of four measurements having different ripple orientations. In Table 5.3 the parameters are summarized for all measured samples. Measurements were performed at a microwave frequency of $f = 15$ GHz and the resonance field was determined for various in-plane field orientations φ_{H} . The measured data are depicted as open circles in Fig. 5.4 whereas the red lines represent fits using the resonance condition, which provides the anisotropy's magnitude and direction. From this, for all measurements good agreements with the model were found. Starting with Fig. 5.4(a), a planar

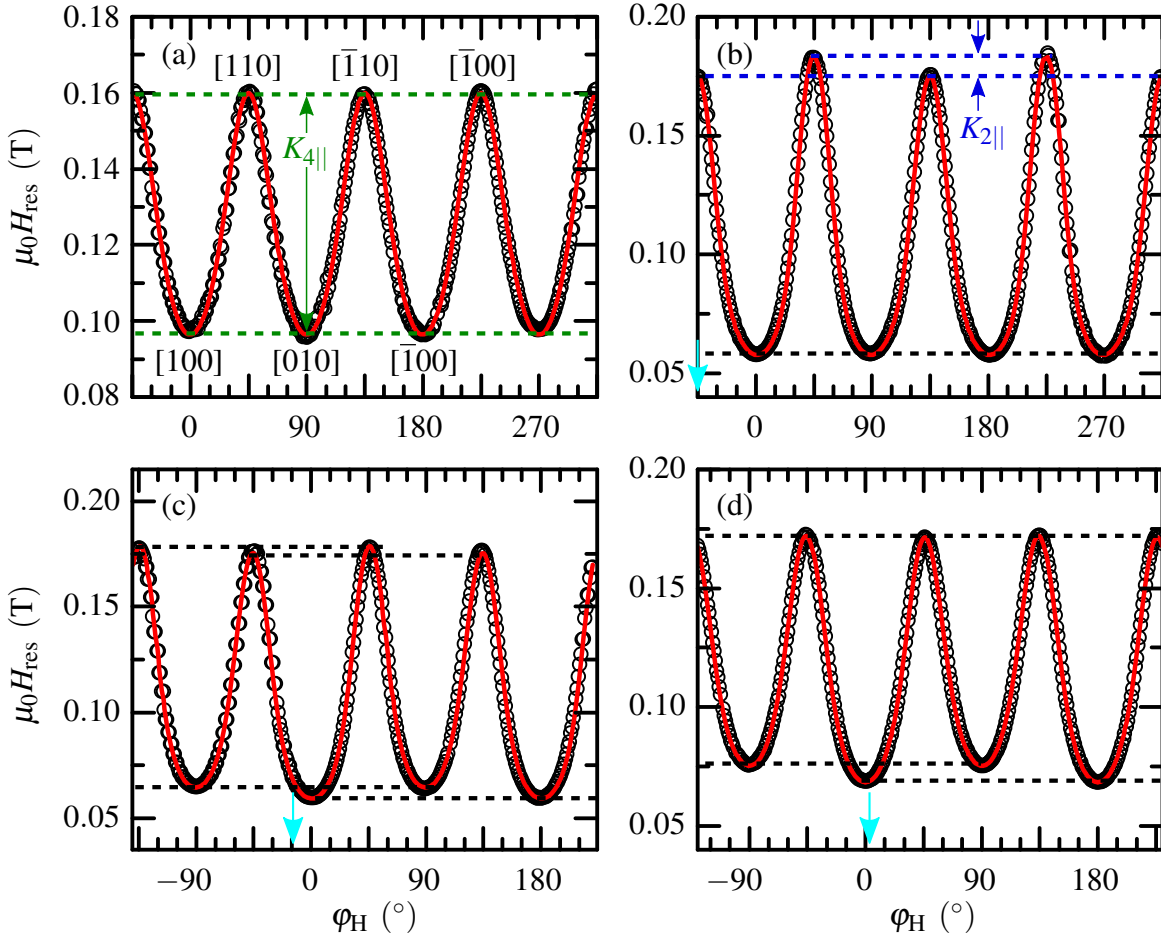


Figure 5.4: Angle-dependent in-plane VNA-FMR measurements of 10 nm Fe epitaxially grown on (a) flat (directions given in Fe lattice) and rippled MgO substrates with (b) $\varphi_{\text{ripple}}^{\text{Fe}} = -45^\circ$, (c) $\varphi_{\text{ripple}}^{\text{Fe}} = -15^\circ$, and (d) $\varphi_{\text{ripple}}^{\text{Fe}} = -1^\circ$. Open symbols are measured data, the red line represents the fit. The obtained uniaxial anisotropy direction φ_u (slightly different from $\varphi_{\text{ripple}}^{\text{Fe}}$, see Table 5.3) is marked by cyan arrows. Dashed lines are guides to the eye.

reference sample is shown exhibiting only an intrinsic four-fold cubic anisotropy, a feature reported in literature years ago [89, 215, 216], that is characterized by an anisotropy field of $2K_{4||}/M_s = 33.2$ mT [sketched in Fig. 5.4(a)]. Thus, all minima and maxima are at the same level, as indicated by the dashed lines. Since the cubic anisotropy refers to the Fe lattice (cf. Fig. 5.1) easy directions (minima in $\mu_0 H$) are found under zero degree and directions shifted by multiple of 90° . Hard axes are by symmetry rotated by 45° with respect to the easy ones.

Now, switching to rippled samples modifies the angular dependence strongly. Aligning the ripples parallel to MgO[100], along the sample edges, results in a ripple ridge direction of $\varphi_{\text{ripple}}^{\text{Fe}} = -45^\circ$ in the iron system [cf. Eq. (5.1)]. This case is depicted in Fig. 5.4(b). As one can see the angular dependence is still dominated by the intrinsic cubic anisotropy

$\varphi_{\text{ripple}} (\text{°})$	$\varphi_{\text{ripple}}^{\text{Fe}} (\text{°})$	$\varphi_{\text{u}} (\text{°})$	$2K_{2 }/M_{\text{s}} (\text{mT})$	$2K_{4 }/M_{\text{s}} (\text{mT})$	$\mu_0 M_{\text{eff}} (\text{mT})$
bulk	—	—	—	55	2144
planar	—	0	0	33.2	1900
0	−45	−45	4.29	63.1	2052
23	−22	−20	3.30	59.4	2037
30	−15	−14	2.94	58.4	2043
44	−1	3	3.54	52.0	2011
52	7	10	2.78	64.8	2072
78	33	30	6.38	63.0	2035

Table 5.3: Parameters of 10 nm Fe grown on single-crystalline flat and rippled substrates.

($2K_{4||}/M_{\text{s}} = 63.1 \text{ mT}$) whereas the height of the maxima is shifted with respect to each other. That is a direct consequence of a uniaxial magnetic anisotropy superimposed onto a cubic one, where the latter in addition is an indirect proof a crystalline MgO surface after sputtering. The obtained direction of the fitted UMA is marked by the cyan arrow in the plot and is rotated by $\varphi_{\text{u}} = -45^\circ$ with respect to the cubic reference system, and hence parallel to Fe[$1\bar{1}0$]. Applying Eq. (5.1) shows a UMA parallel to the ripple crests, as set by the sputter process. Due to coincidence of the easy UMA direction with a hard cubic axis only the maxima differ in height, where the difference is caused by the uniaxial anisotropy field of $2K_{2||}/M_{\text{s}} = 4.29 \text{ mT}$ [sketched in Fig. 5.4(b)]. Here, the two-fold symmetry of the UMA is evident. The opposite case appears if both easy axes align parallel. The corresponding measurement is shown in Fig. 5.4(d) for $\varphi_{\text{u}} = 3^\circ$ causing only the minima to shift in height. Finally, the general case is obtained by setting φ_{u} to an arbitrary direction, e. g. to -14° . Fig. 5.4(c) shows this configuration revealing an influences on both, minima and maxima. Again, for both cases the orientation found for the UMA corresponds to the direction of the ripple crest. Also the cubic anisotropy constants are comparable to the previous ripple sample whereas the UMA slightly changes ($2K_{2||}/M_{\text{s}} = 2.94$ and 3.54 mT).

To further confirm the correlation between ripple ridge direction φ_{ripple} and UMA orientation φ_{u} Table 5.3 lists a number of different ripple orientations, showing a good agreement between φ_{u} and $\varphi_{\text{ripple}}^{\text{Fe}}$. Observed deviations are explained by uncertainties originating from (i) determining φ_{ripple} from the AFM images, which are aligned by eye, and (ii) a fit uncertainty of φ_{u} . Both deviations are of a few degrees only. Furthermore, the table shows the effective magnetization $\mu_0 M_{\text{eff}}$ as well as cubic and uniaxial anisotropy fields $K_{4||}/M_{\text{s}}$ and $K_{2||}/M_{\text{s}}$, respectively. Concerning the first two parameters all rippled films show comparable values indicating that the ripple orientation does not influence the intrinsic Fe properties. The only

exception forms the planar reference sample where the cubic anisotropy is basically half the values of rippled films⁷. However, only minor deviations of up to 12% in cubic anisotropy between rippled samples and bulk values were found. Also the effective magnetization differs remarkably from the bulk value for the planar sample. Considering the planar case, the reason for the strong deviations from bulk values originates from the tensile strain. As discussed in section 5.1, rippled samples underwent a lattice relaxation process that nearly compensated the strain observed in the planar case.

Focusing on the uniaxial anisotropy field a variation in strength between 2.78 mT and 6.38 mT is observed, which originates from the varying quality of the ripple pattern. Here, slight variations in wavelength and ripple amplitude were unavoidable [cf. Fig. 5.2(b) and (d)]. Considering a theoretical description, the formation of the UMA can be understood in the framework of a perturbation theory, recently presented by Landeros and Mills [24], that has been adapted to the current problem by P. Landeros [217]. Details of the theory calculating the spin wave response will be presented in section 6.1. For now, only the basic idea is discussed briefly.

On top of an unperturbed film of thickness $d = 10$ nm a stripe-like periodic defect structure, creating a periodic dipolar field, is placed that has the periodicity⁸ a_0 , a height of $h = 2$ nm, and a width fixed at $w = a_0/2$. A corresponding sketch is shown in Fig. 5.5(a). Due to the presence of stripe defects the resonance condition of the system is modified and reads [24, 217]

$$\omega^2(k_{\parallel} = 0) - \omega^2 - \Gamma_R \sin^4(\varphi - \varphi_{\text{step}}) = 0, \quad (5.5)$$

where $\omega = 2\pi f$ is the angular frequency of the driving microwave field with $f = 15$ GHz and φ_{step} points along the steps. Furthermore, $\omega^2(k_{\parallel} = 0)$ contains the spin wave frequency of the uniform precession⁹ ($k = 0$) and can be calculated from (3.1) using vanishing UMA ($K_{2\parallel} = 0$) and considering only the in-plane case ($\theta = \theta_H \equiv 90^\circ$, $K_{4\perp} = 0$). Finally, Γ_R includes the perturbation originating from dipolar fields created by the stepped surface profile. Note that the perturbation becomes relevant if the magnetization is aligned perpendicularly to the step features¹⁰, and thus introduces a two-fold symmetry. Resonance fields satisfying (5.5) are depicted in Fig. 5.5(b), using the parameters¹¹ given in the figure's caption. Although explicitly the UMA strength was set to zero in the resonance condition a superimposed two-fold UMA contribution can be observed [sketched in panel (b)] additionally to the cubic anisotropy, which originates from dipolar effects of the perturbation (stripes) and is finally due to a shift in

⁷Also a second sample showed a similar behavior.

⁸Note that the assumption $a_0 = \lambda$ is only a rough estimation, which will be discussed in section 6.4.

⁹see also [88] or Eq. (5.6) in the following

¹⁰The term $\sim \sin^4$ becomes unity for \mathbf{M} pointing perpendicularly to the stripes and zero for parallel alignment.

¹¹The role of α and D will become clear in the framework of the perturbation theory presented later.

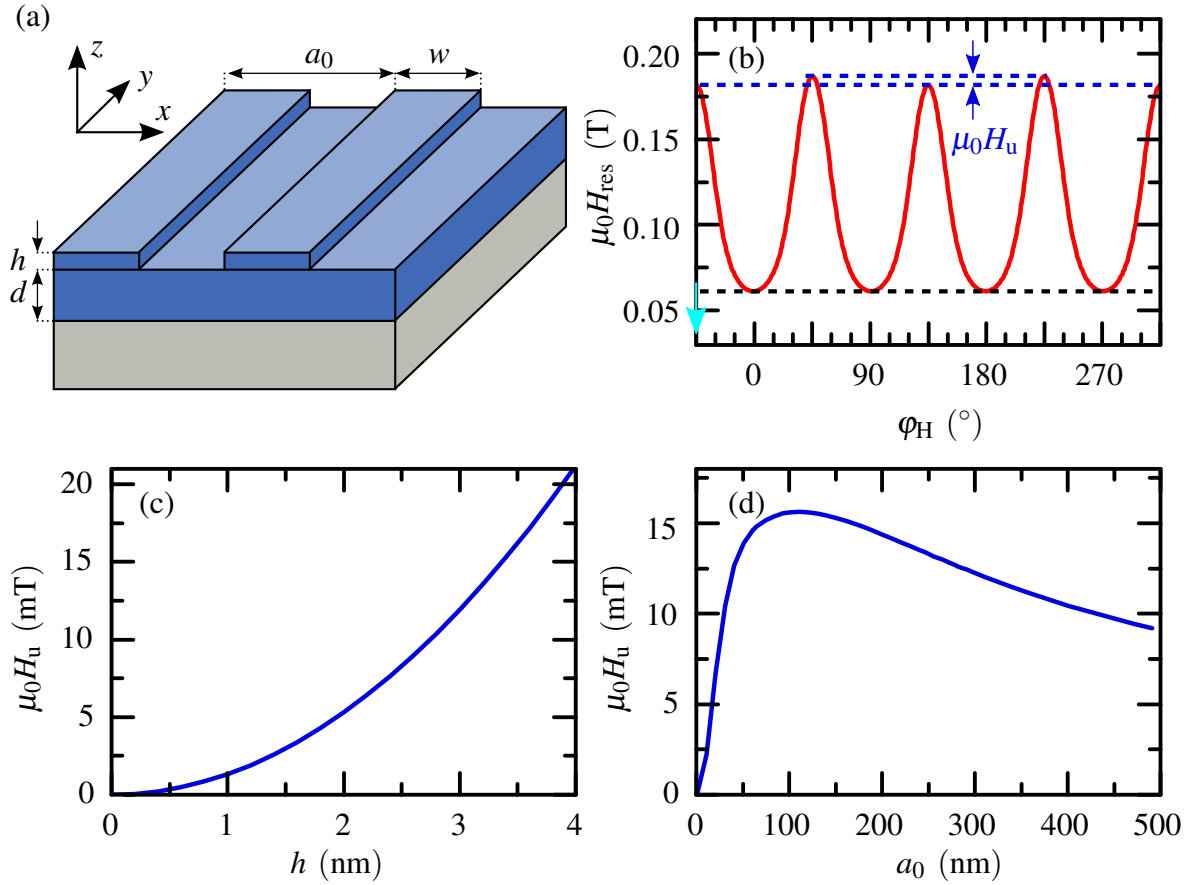


Figure 5.5: Spin wave response of a perturbed Fe film with geometry shown in (a). The model yields (b) the angle-dependent resonance field and the magnitude of the UMA as a function of (c) the defect height and (d) its periodicity [217]. All calculations were done by P. Landeros using $\mu_0 M_{\text{s}} = 2.22$ T, $\mu_0 M_{\text{eff}} = 2010.7$ mT, $g = 2.09$, $\alpha = 0.004$, $D = 27.1$ Tnm², $a_0 = 18$ nm, $d = 10$ nm, $h = 2$ nm, $f = 15$ GHz, $2K_{4\parallel}/M_{\text{s}} = 63.2$ mT, $\varphi_{\text{step}} = 0$ (corresponds to $\varphi_{\text{ripple}}^{\text{Fe}} = -45^\circ$), and $w = a_0/2$.

resonance frequency in (5.5). Hence, already this simplified model (stripes on one side instead of a continuous ripple modulation on both sides) proves the dipolar origin of the UMA.

The evolution of the uniaxial anisotropy field H_{u} , defined as difference between the resonance field along 45° and 135° , as a function of defect height and periodicity can be seen in Figs. 5.5(c) and (d), respectively. While the strength in anisotropy monotonically increases with the defect height h , its dependence peaks with defect periodicity. Recent experiments with increased wavelength of ≈ 30 nm and peak-to-peak amplitude of ≈ 2 nm revealed an enhanced UMA strength of about 19 mT, however, accomplished with a much better ripple quality. To further improve the UMA's strength is thus a task of enhancing the substrate quality. In fact, the ripple quality plays a crucial role for the alignment of the UMA. If rippled substrates with poorly

correlated surface patterns were used at the early stage of the experiments, even no connection between φ_u and ripple ridge direction could be made.

In a last step, the influence of the CPW geometry on the measured anisotropy shall be investigated. In order to do so, Eq. (3.15) will be evaluated. Therefore, the dispersion relation $\omega(k_{\parallel})$ is necessary for a cubic system containing an in-plane UMA and dipolar spin wave interactions. Since the resonance condition (3.1) does not contain spin wave interactions and the spin wave dispersion (2.47) misses UMA and cubic anisotropy, a modified dispersion is needed. For simplicity it is written in the form

$$\omega(k_{\parallel}) = \gamma \sqrt{H_{\parallel}(k_{\parallel}) H_z(k_{\parallel})}, \quad (5.6)$$

where H_{\parallel} , H_z are so-called stiffness fields [22, 88, 217]. Note, that the coordinate system used in this thesis is fixed to the sample geometry [see Figs. 5.5(a) or 2.1], which is a common practice in experiments. In contrast, the theory presented in Refs. 196, 218 uses a coordinate system rotating with the magnetization as it is required to express the Hamiltonian efficiently. Consequently, H_{\parallel} labels a stiffness field that is oriented in the xy plane and perpendicularly to the magnetization. Restricting to the case of an in-plane magnetization ($\theta = \theta_H \equiv 90^\circ$) these fields read:

$$\begin{aligned} H_{\parallel}(k_{\parallel}) = & \mu_0 H \cos(\varphi - \varphi_H) + \frac{2K_{2\parallel}}{M_s} \cos 2(\varphi - \varphi_u) + \frac{2K_{4\parallel}}{M_s} \cos 4\varphi \\ & + \frac{\mu_0 M_s}{2} k_{\parallel} d \sin^2 \varphi_{\mathbf{k}_{\parallel}} + Dk_{\parallel}^2 \end{aligned} \quad (5.7)$$

and

$$\begin{aligned} H_z(k_{\parallel}) = & \mu_0 H \cos(\varphi - \varphi_H) + \mu_0 M_{\text{eff}} + \frac{2K_{2\parallel}}{M_s} \cos^2(\varphi - \varphi_u) + \frac{K_{4\parallel}}{2M_s} (3 + \cos 4\varphi) \\ & - \frac{\mu_0 M_s}{2} k_{\parallel} d + Dk_{\parallel}^2. \end{aligned} \quad (5.8)$$

Setting k_{\parallel} to zero gives (3.1) for the in-plane case, whereas vanishing anisotropy ($K_i = 0$) results in Eq. (2.47). Note also that the ultrathin-film limit is used. Based on the fact that the external magnetic field is always applied along the CPW's center strip and spin waves are emitted perpendicularly to it, the angle between \mathbf{M} and \mathbf{k}_{\parallel} is given by $\varphi_{\mathbf{k}_{\parallel}} = 90^\circ - (\varphi - \varphi_H)$.

To finally apply (3.15) to the measured data it is either necessary to convert the measurement to frequency-sweep data using the resonance condition (3.1) or to express (3.15) in terms of H -sweep data. In the following, both will be discussed to determine its influence on resonance frequency and field position for the case of $\varphi_{\text{ripple}} = -45^\circ$ [cf. Fig. 5.4(b)]. Starting with the conversion approach, Fig. 5.6(a) shows the angle-dependent resonance frequency as it would be

measured if homogeneous excitation is assumed. The external field was fixed at $\mu_0 H = 0.12$ T in order to achieve a resonance frequency around 15 GHz (used in the experiment) and thus be comparable to the measured H -sweep case. Due to the constant external field and by taking only the anisotropy constants into account the calculation in Fig. 5.6(a) displays ideal data exhibiting no experimental noise from the original measurement, or, in other words, deviations between fit and measurement are neglected in Fig. 5.4(b). From the graph it is clear that, in contrast to the measured H -sweep dependence, only the minima are influenced by the UMA for this particular geometry. In addition, minima and maxima are inverted. Using the known anisotropy parameters it is easy to calculate the expected frequency shift δf as a function of k_{\parallel} using Eq. (3.15). The obtained result is depicted in Fig. 5.6(b) for a wide range of possible k_{\parallel} values. Lines shown in this graph are obtained from angle-dependent frequency shifts¹² as e. g. shown in panel (c) for $k_{\parallel} = 3.9 \cdot 10^4 \text{ m}^{-1}$. This point is highlighted by the dashed black line in Fig. 5.6(b). In this figure the minimum frequency shift is represented by the orange line, the maximum by the red line and the difference in peak height by the green line. Due to parallel alignment of all these dependences δf has a linear influence on the resonance frequency f_{res} and increases with k_{\parallel} . However, as discussed in sect. 3.3.3 spin waves emitted from the CPW should have a maximum $k_{\parallel}^{\text{max}}$ of $3.9 \cdot 10^4 \text{ m}^{-1}$ for which the angular dependence of δf is shown in (c). First, an upward shift of about 10 MHz is observed for the easy directions whereas the hard directions exhibit nearly the doubled shift. Therefore, the influence of the used CPW geometry is negligibly small for f -sweep measurements.

To understand the angular dependence of δf the dispersion relation for non-vanishing k_{\parallel} needs to be discussed. Since the anisotropy constants are the same in (3.15) for $\omega(k_{\parallel})$ and $\omega(k_{\parallel} = 0)$ and the equilibrium angle φ does not depend on k_{\parallel} the only source of the oscillation in δf can be $\varphi_{\mathbf{k}_{\parallel}}$, which also enters the calculation. Indeed, plotting the equilibrium angle as a function of the external field orientation [cf. red line in Fig. 5.6(f)] shows a variation around perfect alignment (black dashed line), which in turn is caused by the internal effective field and corresponds¹³ to the oscillations in δf . Thus, changing anisotropy parameters within the experimentally given ranges alters the frequency shift but does not increase it significantly.

To explore the CPW's influence onto the resonance field the used Eq. (3.15) has to be adapted. Due to the point that (3.15) accounts only for the averaged distance of the resonance frequencies caused by a maximum k_{\parallel} and a vanishing one, the corresponding field shift can be expressed by:

$$\mu_0 \delta H(k_{\parallel}^{\text{max}}, \varphi_{\mathbf{k}_{\parallel}}) = \frac{1}{2} \left[\mu_0 H_{\text{res}}(k_{\parallel}^{\text{max}}, \varphi_{\mathbf{k}_{\parallel}}) - \mu_0 H_{\text{res}} \right]. \quad (5.9)$$

The predicted shift is shown in Fig. 5.6(d) as a function of k_{\parallel} . Note that this time it points in the

¹²For all calculations D was set to zero since Dk_{\parallel}^2 is a small quantity in comparison to the anisotropy parameters.

¹³Note that $\varphi_{\mathbf{k}_{\parallel}}$ is shifted by 90° with respect to $\varphi - \varphi_{\text{H}}$.

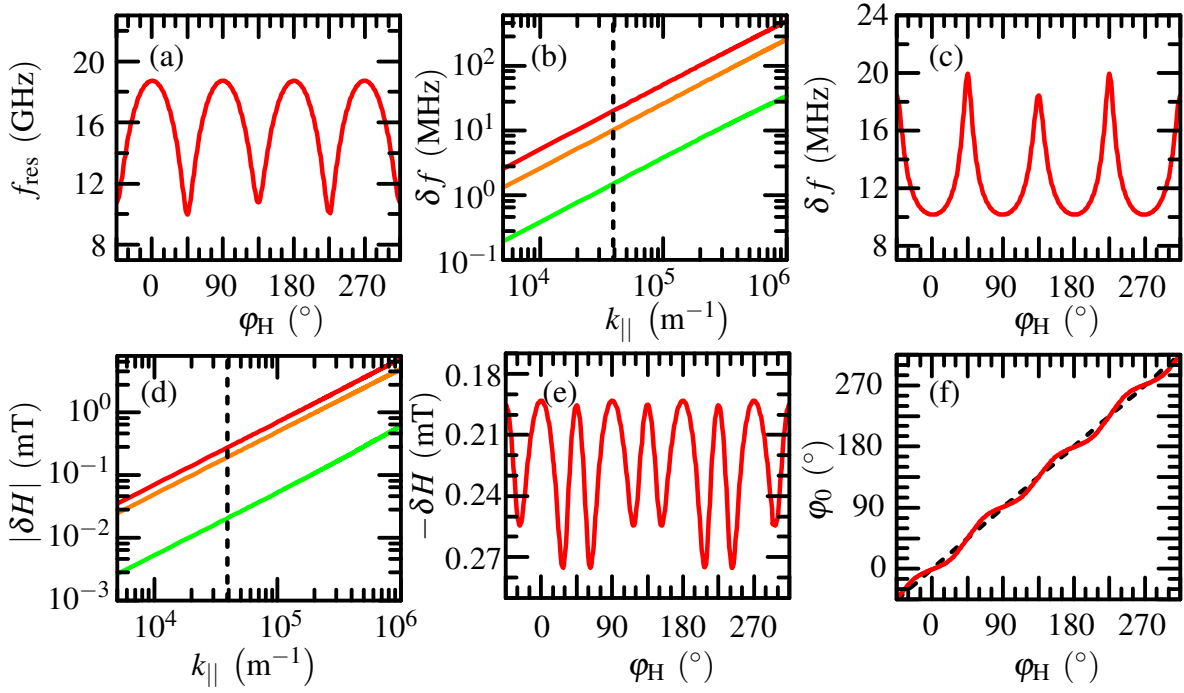


Figure 5.6: CPW influence on resonance measurements for $\varphi_{\text{ripple}}^{\text{Fe}} = -45^\circ$. (a) Resonance frequency calculated from parameters ($\mu_0 H = 0.12$ T) obtained by the fit shown in Fig. 5.4(b). (b) Shift in resonance frequency-dependent on k_{\parallel} and (c) on φ_H with $k_{\parallel} = 3.9 \cdot 10^4 \text{ m}^{-1}$. The corresponding resonance field shifts in dependence of k_{\parallel} and φ_H are shown in (d) and (e), respectively. Panel (f) depicts the equilibrium angle of \mathbf{M} for $k_{\parallel} = 0$. In panel (b) and (d) the dashed black line marks $k_{\parallel} = 3.9 \cdot 10^4 \text{ m}^{-1}$ and orange (red) colors label the minimum (maximum) of the resonance shift, whereas green represents the peak distance between the maxima of the frequency shift and the minima of the field shift [cf. (c) and (e)].

opposite direction as compared to the f -sweep case. Again, comparing δH to the resonance field it is quite small and thus negligible. For example, fitting the shifted resonance dependence $\mu_0 H_{\text{res}} + \mu_0 \delta H$ with the usual resonance condition exhibiting $k_{\parallel} = 0$ for the same sample discussed above yields anisotropy parameters that exhibit only a slight shift of 4 mT in the effective magnetization. All other parameters are basically unaffected by k_{\parallel} . Thus, the only case where the resonance shift might become important is the low-field case of $f(H)$ measurements or measurements at small fields/frequencies. In addition, also the angular dependence, depicted in Fig. 5.6(e), shows an oscillation with φ_H having a more complicated symmetry compared to panel (c). This time not only the anisotropy influence on the equilibrium angle contributes, but also the variation of resonance field with the equilibrium angle, also known as dragging effect.

Summarizing these findings, it was shown that by ion beam erosion rippled surface patterns

can be created on MgO exhibiting a single-crystalline surface structure. Growing Fe on top superimposes the intrinsic cubic anisotropy with a uniaxial induced one, originating from the rippled surface. Here, the latter is of dipolar origin and can be set easily to any arbitrary direction with respect to the cubic anisotropy orientation, which offers a great possibility to tailor the magnetic anisotropy. Furthermore, the CPW geometry has a negligible influence on the resonance condition.

5.3 FMR linewidth

Next, the linewidth influenced by the ripple morphology shall be considered more precisely. With respect to flat Fe films the linewidth has already been subject of investigation. For example, Fermin *et al.* [215] investigated the in-plane angular dependence of the field-sweep linewidth and found two contributing effects. On the one hand, intrinsic Gilbert damping is present, on the other hand mosaicity plays an important role when fitting the experimental data [215]. As underlined by thickness-dependent measurements mosaicity originates from misfit dislocations due to the Fe/MgO lattice mismatch, which is relaxed by mosaics with increasing film thickness [219]. Thereby, mosaicity survives the epitaxial growth by microscopic plane rotations with respect to the sample's normal [215]. Important to note is that these measurements have been done using a cavity-based setup. As already discussed earlier CPW-based approaches may show additional line spreads caused by the inhomogeneous excitation field. This was observed by Mosendz *et al.* [146] following an approach, where Fe deposited on GaAs does not only show Gilbert-like relaxation and mosaicity, but also an influence of the CPW that was comparable in magnitude with the spread in anisotropy.

Performing field-sweep FMR may additionally include field-dragging effects, which would vanish if sweeping the microwave frequency [216]. These effects will become increasingly important the greater the in-plane anisotropy contributions will be and have already been observed in the previous section. Hence, to account for the symmetry present in the sample the introduced dragging function (see section 2.3.1) needs to be adapted to the current situation. Starting from the stiffness fields given by (5.7) and (5.8) in the section above ($k_{\parallel} = 0$ considered), Barsukov *et al.* provided an analytical expression, reading as follows [88, 217]:

$$\Xi = \frac{1}{H_{\parallel} + H_z} \left(H_{\parallel} \frac{dH_z}{dH} + H_z \frac{dH_{\parallel}}{dH} \right). \quad (5.10)$$

With respect to the linewidth, not only Gilbert damping [Eq. (2.53)] has to include this dragging function but also possibly present TMS [Eq. (2.57)]. Thus, the modified TMS

contribution reads [88]:

$$\Delta H_{\text{pp}, 4\text{-fold}}^{2m} = \frac{2}{\sqrt{3}\Xi} \Gamma_{4\text{-fold}} \sin^{-1} \sqrt{\frac{\sqrt{(\omega_0/2)^2 + \omega^2} - \omega_0/2}{\sqrt{(\omega_0/2)^2 + \omega^2} + \omega_0/2}}. \quad (5.11)$$

Note that the scattering matrix was renamed to $\Gamma_{4\text{-fold}}$ to account for the four-fold symmetry of the arcsin function. To be able to observe a two-fold TMS symmetry, possibly introduced by the substrate morphology, a two-fold expression is needed, which also is provided by Barsukov *et al.* [88]:

$$\Delta H_{\text{pp}, 2\text{-fold}}^{2m} = \frac{2}{\sqrt{3}\Xi} \Gamma_{2\text{-fold}} \cos^4(\varphi - \varphi_{2\text{-fold}}). \quad (5.12)$$

In this case $\varphi_{2\text{-fold}}$ accounts for the two-fold TMS direction counted from the Fe[100] direction. In contrast, mosaicity and inhomogeneous line broadening given by Eq. (2.54) account only for spreads in sample parameters and are unaffected by Ξ . With respect to mosaicity $K_{2\parallel}$, $K_{4\parallel}$, φ_u , φ_H , and M_{eff} will be considered in the following as being under spatial variation.

The influence of the CPW geometry on the linewidth can be estimated using Eq. (3.16). In order to obtain frequency units the conversion (2.51) is applied which yields in combination with Eq. (5.9):

$$\mu_0 \Delta H(k_{\parallel}^{\text{max}}, \varphi_{\mathbf{k}_{\parallel}}) = \mu_0 \Delta H \sqrt{1 + \left(\frac{2\mu_0 \delta H(k_{\parallel}^{\text{max}}, \varphi_{\mathbf{k}_{\parallel}})}{\mu_0 \Delta H} \right)^2}. \quad (5.13)$$

From Fig. 5.6(d) a maximum shift in the resonance field of -0.28 mT can be obtained. As shown later, field-swept linewidth values are for this experiment above $\Delta H = 2$ mT, which also makes the linewidth shift negligibly small and hence $\mu_0 \Delta H(k_{\parallel}^{\text{max}}, \varphi_{\mathbf{k}_{\parallel}}) \approx \mu_0 \Delta H$.

In Fig. 5.7 the measured linewidth data and the applied model functions are shown. The contributing linewidth parameters obtained in this way are listed in Table 5.4. Surprisingly, the quite complex linewidth is solely explained by the dragging dominated Gilbert-like intrinsic damping and a single mosaicity contribution originating from the in-plane four-fold anisotropy. In general, obtaining a good linewidth quality for this samples was quite challenging, which is the reason that only a few ripple orientations are listed in the table. The reason why two-magnon scattering cannot be found in these samples will be discussed in the last experimental chapter, investigating the wavelength dependence of TMS. Focusing first on the flat reference sample [Fig. 5.7(a)] reveals a superposition of Gilbert damping and mosaicity. Thereby, the angular dependence of the linewidth is mainly dominated by mosaicity. In contrast, Gilbert damping exhibits only a small angular dependence. Especially along the easy axes (0° and every 90° apart) the resonance curve was difficult to evaluate due to partially shoulder-like features,

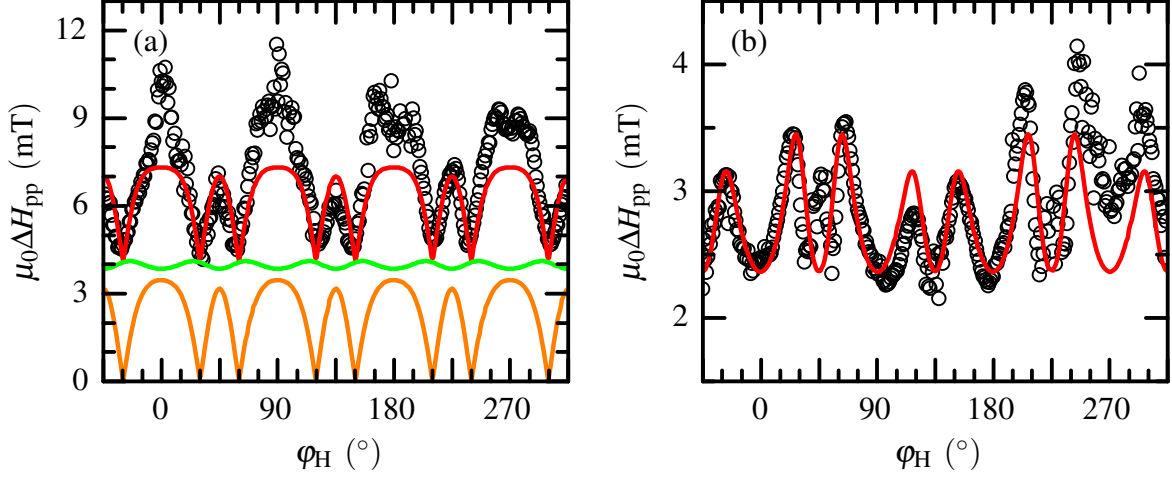


Figure 5.7: Peak-to-peak linewidth of a 10 nm Fe film deposited on (a) planar and (b) rippled MgO with $\varphi_{\text{ripple}}^{\text{Fe}} = -45^\circ$. Black open circles are measured data. Red lines display the overall modeled linewidth composed out of Gilbert damping (green line) and mosaicity of the four-fold in-plane anisotropy (orange line) in panel (a), whereas (b) contains Gilbert damping, only.

suggesting a superposition of two resonance curves. In Fig. 5.8 three measured spectra are exemplarily shown, all taken closely to the extrema presented in Fig. 5.7(a). Especially the curve measured with $\varphi_{\text{H}} = -1^\circ$ shows a strong deviation from the model function, whereas the other two measurements fit reasonably well. Hence, the peak along the easy axis is attributed to a measurement artifact.

The smaller peaks around the hard axes (45° tilted with respect to the easy one) indicate the presence of in-plane mosaicity in this sample. As discussed above, mosaicity is caused by the strain present in the sample. In contrast, rippled layers [Fig. 5.7(b) for $\varphi_{\text{ripple}}^{\text{Fe}} = -45^\circ$] show a remarkable decrease in Gilbert damping α to roughly 66% of the planar value. In comparison, Fermin *et al.* observed a decrease of intrinsic damping constant with increasing

$\varphi_{\text{ripple}} (^\circ)$	$\varphi_{\text{ripple}}^{\text{Fe}} (^\circ)$	α	$\Delta K_{4\parallel}/M_s$ (mT)
planar	—	0.0065 (10)	1.5 (2)
0	-45	0.0040 (2)	0
30	-15	0.0038 (2)	0
44	-1	0.0040 (2)	0.4 (1)
52	7	0.0040 (3)	0

Table 5.4: Linewidth parameters obtained for 10 nm Fe deposited on planar and rippled MgO substrates. The corresponding anisotropy parameters are listed in Table 5.3.

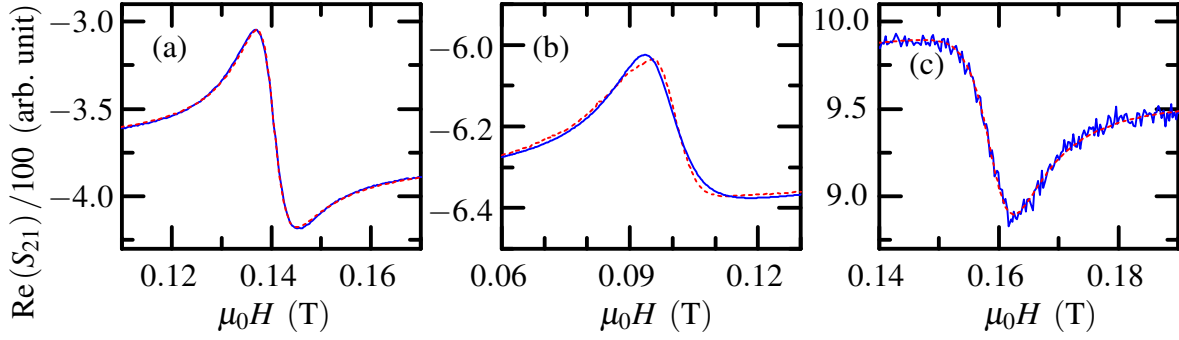


Figure 5.8: Selected FMR spectra of the measurement shown in Fig. 5.7(a). Measurements are depicted in blue and fits in red. The external field positions are (a) $\varphi_H = -31^\circ$, (b) $\varphi_H = -1^\circ$, and (c) $\varphi_H = 43^\circ$.

film thickness [215] and, thus, with ongoing strain relaxation. However, the values obtained from the experiment are much larger than reported in literature, where bulk values around $\alpha = 0.002$ were observed [203]. The best fit was obtained using vanishing mosaicity, which in turn means that the rather complicated behavior originates from Gilbert damping only. Due to the increased in-plane anisotropy, caused by rippled substrates, dragging is important [see Fig. 5.6(f)] and the Gilbert contribution is strongly angle dependent. However, by taking a close look at 45° in Fig. 5.7(b) one observes a little peak remaining from mosaicity. On the other hand the data at 135° do not show such a peak. The only sample with measurable $\Delta K_{4||}/M_s$ was found for 44° of ripple orientation. Also for this case the value is much smaller than for the planar sample. Thus, less pronounced in-plane strain, as observed by X-ray measurements, causes a decrease in mosaicity, which is also in agreement with observations by Fermin *et al.* who investigated a thickness dependence and found an in-plane relaxation of the lattice [215].

Of crucial importance for the linewidth is the sample quality. Forced by the setup, an in-plane angle-dependent scan requires a sample lift-off from the CPW in order to rotate to the next angle φ_H . When reattaching the sample small movements on the CPW may not be fully prevented, which in turn introduce scratches to the sample's surface. This might reintroduce linewidth contributions. Although some measurements were repeated no significant change in was anisotropy found. Remeasuring for example $\varphi_{\text{ripple}} = 30^\circ$ showed unchanged Gilbert damping [$\alpha = 0.0040(2)$] but an increase in $\Delta K_{4||}/M_s$ to $0.7(1)$ mT. Furthermore, scratches might explain the increase of noise visible in Fig. 5.7(b) with increasing angle position.

Summarizing these findings, rippled surfaces enhance the lattice relaxation and thus lead to a decrease of in-plane mosaicity and Gilbert-like damping. Nevertheless, great care has to be taken handling the measurements to not falsify the linewidth parameters.

6 Extrinsic control of magnetic properties in NiFe thin films

The final experimental chapter is dedicated to perturbations entering a thin $\text{Ni}_{81}\text{Fe}_{19}$ film via the surface morphology of rippled Si substrates with the aim to tailor both the magnetic anisotropy and extrinsic relaxation mechanisms, i. e., TMS. Therefore, 30 nm thin Py films were chosen as for this material intrinsic anisotropies are negligibly small if grown on sputtered Si surfaces (amorphous), which thus exhibit only an induced UMA. Magnetic properties of NiFe alloys have already been studied since the late 1950s [220], where the existence of TMS in thick $\text{Ni}_{80}\text{Fe}_{20}$ films (above 50 nm) has been confirmed in the late 1960s by Patton [150]. More recently, TMS has also been observed in thin NiFe films coupled to NiO layers [104]. As mentioned earlier, anisotropic surface structures, e. g. periodic grooves, in $\text{Ni}_{80}\text{Fe}_{20}$ lead to direction-dependent TMS [117], also influencing the frequency-dependent linewidth [112]. Also other ways have been found to specifically alter the linewidth, e. g. by using multilayer stacks where dynamic coupling of a synthetic antiferromagnet to a free $\text{Ni}_{90}\text{Fe}_{10}$ layer allows to tailor the frequency-dependent linewidth [221]. But also simple seed layers alter the dynamic behavior of magnetic films (in this case $\text{Fe}_{65}\text{Co}_{35}$ thin films) [222].

Very recently, Landeros and Mills published a theory on spin waves in periodically perturbed films [24] explaining nonlinear, non-monotonous linewidth observations made by Barsukov *et al.* on periodically patterned, stripe-like perturbed films introducing direction-dependent TMS [144]. The scattering is enabled by a periodically perturbing dipolar field created by surface defects—a feature that was shown to exist also for rippled magnetic layers (see section 4.3.2). Based on this theory and the findings of Barsukov *et al.*, this chapter presents an alternative approach for preparing periodic defect structures. While the stripe defects Barsukov *et al.* used are written by e-beam lithography and subsequent Cr^+ irradiation, rippled samples will offer a much easier preparation approach able to produce large-area samples, while being easily scalable in wavelength and, thus, defect periodicity.

First, the perturbation theory of Landeros and Mills, based on periodic defects at the sample's surface causing dipolar stray fields, will be introduced. Subsequently, the sample preparation and its surface characterization is reviewed before the evolution of stray fields will be monitored directly using MFM and TEM techniques, revealing the dipolar stray field origin. Finally, the

effect of periodic perturbations on polycrystalline Py films is discussed showing an influence on linewidth, well explained by perturbation theory. Also the resonance position is influenced by modulation-dependent two-magnon scattering showing unexpected anisotropy dependences for high wavelengths that are not predicted by observations presented in section 4.2.

6.1 Perturbation theory

First, it is important to review the basic ideas of the perturbation theory presented in Ref. 24 to understand the mechanism behind the influence, which in turn is important to systematically tailor properties. The formalism presented in Ref. 24 is an extension of the response theory presented by Arias and Mills [22] for in-plane magnetized films that was also adapted to the out-of-plane case [196, 218]. It describes the response function of a magnetic film in presence of spin wave scattering and under the influence of stiffness fields (5.7) and (5.8), while in-plane anisotropies are vanishing¹ ($K_{i||} = 0$). Furthermore, phenomenological Gilbert damping α is taken into account.

To introduce a perturbation to a magnetic film, the geometry depicted in Fig. 5.5(a) is considered by placing a stripe-like defect structure on top of a perfect magnetic film, both out of the same material. By exciting such a structure with a time-dependent microwave field of angular frequency ω the uniform precession $k_{||} = 0$ may be scattered into excited spin wave states of $k'_{||} \neq 0$. As discussed earlier (see section 2.3.3), the spin wave dispersion relation has to be degenerated to allow an energy transfer between these two states while fulfilling energy conservation. To further fulfill momentum conservation a scattering potential is mandatory that initializes the scattering and balancing the momentum difference. In reality this shall be given by the stripe defects, whereas in the theory this perturbation is represented by a scattering matrix entering the response function. Thus, the scattering potential must match the given distance in $k_{||}$ space, defined by the dispersion relation $\omega(k_{||}) = \gamma \sqrt{H_{||}(k_{||}) H_z(k_{||})}$ of the unperturbed film. If the periodicity of the perturbation is measured by a_0 [see Fig. 5.5(a)], TMS is only feasible if the condition $\mathbf{k}'_{||} = \mathbf{k}_{||} + \mathbf{g}_m$ is fulfilled, where \mathbf{g}_m is a reciprocal vector pointing perpendicularly to the periodic defects along \mathbf{e}_x with $\mathbf{g}_m = m g_0 \mathbf{e}_x$. Here, m is an integer value and $g_0 = 2\pi/a_0$ the reciprocal lattice parameter. In the theoretical description this case is represented by non-vanishing scattering elements of the matrix. Such a case is depicted in Fig. 6.1 for a set of different external field values and parameters [listed in the figure's caption, substitution (2.49) used] appropriate for best possible visualization of occurring features. The external field was applied perpendicularly to the stripes. Due to neglected anisotropy the

¹Note that for non-vanishing $K_{4||}$ P. Landeros calculated the step-induced UMA in Fe films, shown in Fig. 5.5.

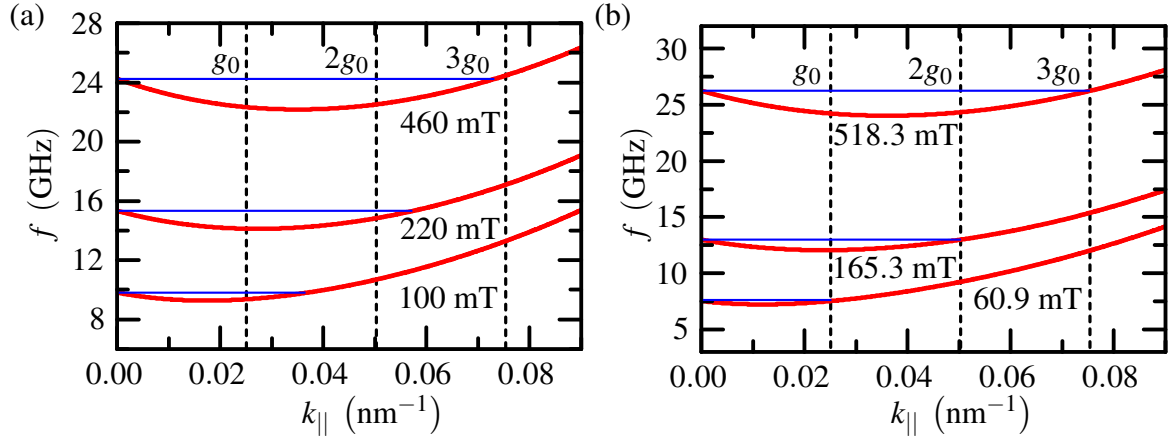


Figure 6.1: Spin wave dispersion relation for an unperturbed magnetic film with $\mu_0 M_s = 1$ T, $d = 30$ nm, $g = 2.11$, $D = 34$ T nm², $a_0 = 250$ nm, and $K_1 = 0$. (a) Shows the situation for external fields not matching the scattering condition $k_{\parallel} = k'_{\parallel} + mg_0$, whereas for (b) the fields are selected to enable TMS. Black dashed lines indicate multiples (one to three times) of the reciprocal lattice parameter g_0 and blue lines mark degenerate spin wave frequencies.

magnetization will align along this direction², turning the angle between \mathbf{M} and \mathbf{k}_{\parallel} to zero and thus giving the maximum possible mode degeneration. In both figures the positions of the reciprocal wave parameter $g_m = mg_0$ are displayed from $m = 1$ to $m = 3$. As one can see in Fig. 6.1(a), the resonance field (set by the excitation frequency) causes a mode degeneration that does not match the periodicity of the scattering potential. In contrast, for Fig. 6.1(b) the field values are chosen such that TMS is enabled. Thus, having a periodically perturbed magnetic film will produce TMS only at distinct resonance fields respectively frequencies, whereas the theory of Arias and Mills (see section 2.3.3 or Ref. 22), relying on random defects, has a much broader acceptance range to fulfill the scattering condition. In addition, by using periodic defects such as stripes or rippled surfaces a direction dependence of the scattering is expected as the spin wave propagation angle $\varphi_{\mathbf{k}_{\parallel}}$ changes with the in-plane orientation of \mathbf{M} , where in the limiting case of parallel alignment no scattering is expected.

To calculate the scattering matrix the stepped geometry shown in Fig. 5.5(a) has to be described analytically. For this purpose the stripes above the nominal surface are expanded in a Fourier series that reads [24]:

$$h^{\text{step}}(x) = \frac{h}{\pi} \sum_{m=-\infty}^{\infty} \frac{\sin(m\pi w/a_0)}{m} \exp(img_0 x). \quad (6.1)$$

²As discussed in the previous chapter the defect-induced UMA is quite weak by what small fields will be enough to align \mathbf{M} perpendicularly to the stripes.

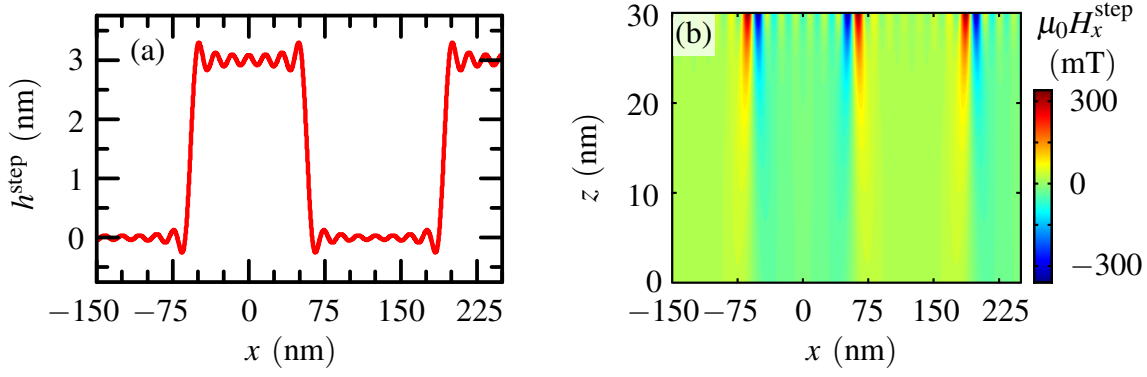


Figure 6.2: Modeling of the perturbation and its influence on the magnetic layer beneath. (a) shows the Fourier expansion (up to $m = 15$) for a modulation height of $h = 3$ nm, periodicity $a_0 = 250$ nm, and step width $w = 115$ nm. In (b) the x component of the emerging stray field is shown within a $d = 30$ nm layer (remaining parameters are identical to Fig. 6.1), where the stripe defects above are omitted.

The origin of the coordinate system is placed at the stripe's center. A visualization of the evolving geometry is shown in Fig. 6.2(a) using the same parameters as for the dispersion relation, but considering a stripe width of $w = 115$ nm. The summation in Eq. (6.1) was carried out between $m = \pm 15$, which turned out to be sufficient when calculating the linewidth later on. From the given surface modulation Landeros and Mills calculated the dipolar stray field component H_x^{step} along the x direction for a magnetization aligning perpendicularly to the stripes. Details on the calculation may also be found in Ref. 15. For the final expression the reader is referred to the publication of Landeros and Mills [Eq. (16) in Ref. 24]. In Fig. 6.2(b) the result obtained for the dipolar field inside a $d = 30$ nm thin magnetic film is depicted. Note that the perturbation-creating stripes are not displayed in the image, but do enter the final response function. Additionally, the stray fields create a modulation of the magnetization inside the layer below the stripes and consequently \mathbf{M} is not uniform anymore. This effect also enters the scattering matrix. Compared to Fig. 6.2(a), the stripes on top of the film create magnetic poles at the step faces causing a periodical stray field modulation along the x direction, where the strength of the field is set by the height h of the defects. Recalling the findings of the first experimental chapter, also rippled films show a periodic modulation of the stray field, which was shown in Fig. 4.6. Thus, although the geometry will differ remarkably from the one used in the model, rippled films—assuming the stray field periodicity can be engineered to g_m values needed for TMS—may be also suitable for defect-induced TMS.

Finally, after the scattering matrix has been derived, the response function of the perturbed

magnetic film can be calculated where its imaginary part reads:

$$\Upsilon^{\text{I}}(\omega) = \gamma M_s \frac{\gamma H_z(0) [\Lambda(0) + \Gamma^{\text{I}}] - \alpha \omega [\omega_{\text{res}}^2 - \omega^2 - \Gamma^{\text{R}}]}{[\omega_{\text{res}}^2 - \omega^2 - \Gamma^{\text{R}}]^2 + [\Lambda(0) + \Gamma^{\text{I}}]^2}. \quad (6.2)$$

In this equation, $\omega_{\text{res}} = \omega(k_{\parallel} = 0)$ is the resonance frequency of the unperturbed film, which can be obtained from (5.6) for vanishing K_i . Γ^{R} and Γ^{I} are the real and imaginary part of a frequency-dependent function $\Gamma(\omega)$ that contains information about the perturbation and $\Lambda(k_{\parallel})$ contains the spin wave dependent stiffness fields. Again, for the explicit form of these functions the reader is referred to Ref. 24. Note that the response function $\Upsilon^{\text{I}}(\omega)$ is defined in k space and may not be directly comparable to the susceptibility measured in real space. As can be seen from Eq. (6.2), Γ^{R} introduces a frequency-dependent shift of the resonance line, which is negligibly small for the case of NiFe perturbed films studied by Barsukov *et al.* [144]. Furthermore, the perturbation couples the uniform mode via dipolar interactions to the degenerate mode, which causes a splitting of the absorption peak into two or more lines.

From the response function it is also possible to calculate the linewidth

$$\Delta H^{\text{stripe}} = \frac{\Lambda(0) + \Gamma^{\text{I}}(\omega_{\text{res}})}{\gamma^2 [H_{\parallel}(0) + H_z(0)]}, \quad (6.3)$$

where TMS scattering is represented by the imaginary part of the perturbation function Γ . It should be noted that in this case the frequency shift mentioned above and the resonance splitting is explicitly neglected since the linewidth is evaluated at the resonance position of the unperturbed film. Hence, predictions made by Eq. (6.3) are only valid for small-enough perturbations. The impact of TMS onto the frequency-dependent linewidth is shown in Fig. 6.3. For a given Py film with $\mu_0 M_s = 1$ T, $\alpha = 0.007$, $g = 2.11$, $a_0 = 250$ nm, and $d = 30$ nm a variation of the defect height h , width w , and exchange stiffness D is presented. All figures have in common that at distinct frequencies the linewidth significantly differs from the Gilbert contribution in form of linewidth peaks. The center position of these peaks is determined by the degenerate states in the dispersion relation matching multiples of the reciprocal lattice vector \mathbf{g}_0 by fulfilling $\omega(k_{\parallel} = 0) = \omega(k_{\parallel} = mg_0)$ with $m > 0$. Furthermore, the peak position depends on material parameters such as D , M_s , K_i , and the properties of the perturbation, namely h , a_0 , and w . As the stiffness field H_{\parallel} depends on the spin wave propagation angle $\varphi_{\mathbf{k}_{\parallel}}$, connected to the external field via the magnetization, the dispersion relation and, thus, the peak position changes with the field orientation. Due to the choice of parameters identical to the ones used for the dispersion relation shown in Fig. 6.1(b) the center of the observed linewidth peaks in Fig. 6.3(a) can be directly related to degenerate states at $f_0 = 7.5$ GHz, $f_1 = 13$ GHz, and $f_2 = 26.2$ GHz corresponding to reciprocal scattering parameters of g_0 , $2g_0$, and $3g_0$. The reason for not observing sharp linewidth peaks is due to intrinsic damping α

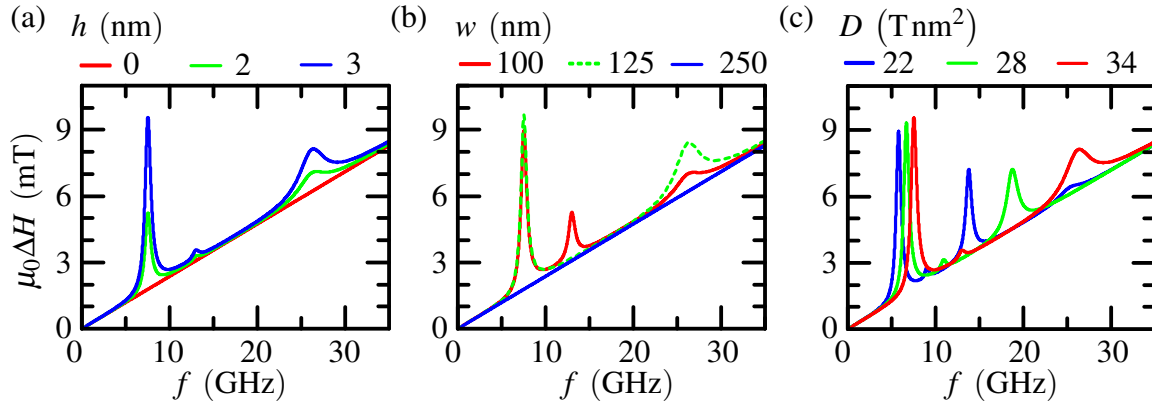


Figure 6.3: Perturbation-influenced frequency-dependent linewidth plotted for (a) varying perturbation height h , (b) perturbation width w , and (c) exchange stiffness D . If nothing else is given parameters are: $\mu_0 M_s = 1$ T, $\alpha = 0.007$, $g = 2.11$, $a_0 = 250$ nm, $d = 30$ nm, $D = 34$ Tnm², $w = 115$ nm, and $h = 3$ nm.

and the microwave frequency, both broadening the peak width by entering Γ^{I} . Furthermore, Fig. 6.3(a) shows the dependence on the defect height h revealing a scaling of the linewidth peaks in height with increasing defect height. A similar effect is observed by increasing M_s (not shown), increasing the peak height but also shifting the peaks to higher frequencies. For h approaching zero the perturbation function vanishes and the frequency-dependent linewidth follows a linear dependence caused by Gilbert damping.

Considering the relative peak height in Fig. 6.3(a) it is striking that the second peak is barely visible whereas the third one is well noticeable. The origin of this behavior is illustrated in Fig. 6.3(b), where the perturbation width w is varied. First, setting the width equal to the defect periodicity $a_0 = 250$ nm naturally yields a vanishing TMS contribution leaving only the Gilbert part. If in turn the ratio of $m\pi w/a_0$ approaches a multiple of π the Fourier component [see Eq. (6.1)] of the corresponding scattering path mg_0 is zero and thus the scattering probability for this peak vanishes. In the depicted case this happens for $w = 125$ nm, which causes the second peak to disappear. Values between the extinction condition lead to increasing respectively decreasing peak heights, as it can be seen for the second and third peak in Fig. 6.3(b) for $w = 100$ nm and $w = 125$ nm.

The relative peak distance is for example influenced by the exchange stiffness D , as shown in Fig. 6.3(c). Here, smaller D values yield to peaks at lower frequencies and a decreased inter-peak distance. Thus, for the smallest value of $D = 22$ Tnm² shown, already the next order of $4g_0$ is visible. The same holds true for increasing the film thickness d (not shown), which in addition influences the peak width. Note that with this knowledge an alternative way to determine the exchange stiffness constant D is given, if at least two linewidth peaks are

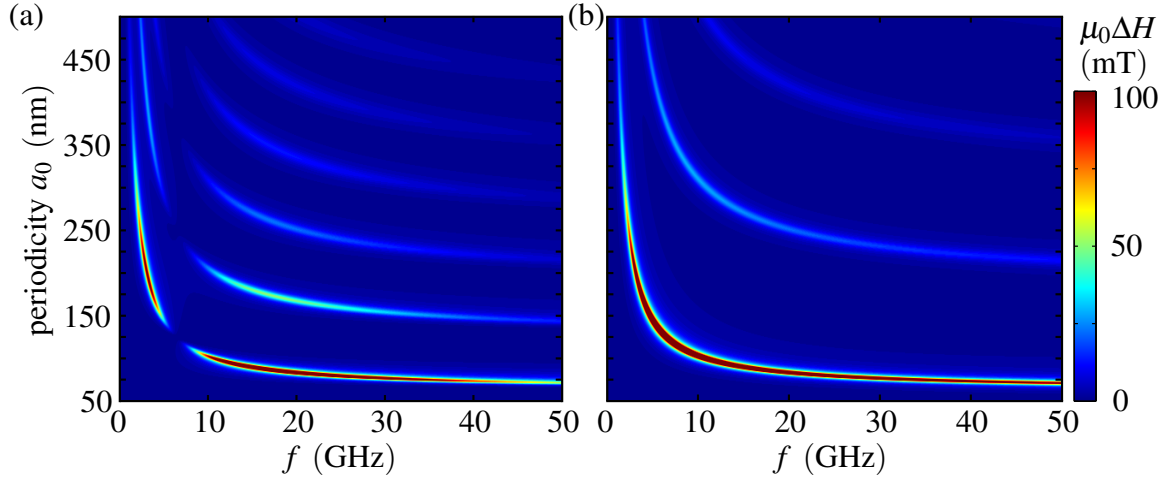


Figure 6.4: Color-coded plot of the linewidth (Gilbert damping term subtracted) as a function of defect periodicity for (a) fixed defect width of $w = 125$ nm and (b) fixed width/periodicity ratio of $w/a_0 = 0.5$. Both images use the same color map. Remaining parameters are equal to Fig. 6.3.

observed.

Finally, it is of interest to determine the defect range in which TMS may occur. To do so, Fig. 6.4 shows two color-coded linewidth calculations depending on the microwave frequency and defect periodicity. The linear background of Gilbert damping is subtracted in both cases. Figure 6.4(a) displays the situation for a fixed defect width of $w = 125$ nm whereas for part (b) the ratio between width and periodicity is fixed to $w/a_0 = 1/2$. In both cases basically no linewidth peak is observed within the given frequency range if the defect periodicity is below the value of $a_0 = 70$ nm. For smaller values the reciprocal lattice parameter g_0 is too big to match the degenerate state in the spin wave dispersion relation. Thus, direction-dependent TMS should not be present in 25 nm wavelength rippled samples, as confirmed in the previous chapter.

For the case of fixed defect width, Fig. 6.4(a) shows nicely the vanishing linewidth peaks if a_0 is equal to w or to its multiples. However, since rippled substrates shall be used in the following, the assumption of fixed periodicity/width ratio is more suitable, although the created dipole pattern will differ from the step case for rippled substrates. For the fixed ratio of $w/a_0 = 1/2$, Fig. 6.4(b) shows a reduced amount of linewidth peaks for the same defect periodicity in comparison to the stripe case. Additionally, these peaks are not interrupted.

To adapt the model in a simple way to the rippled case with respect to surface corrugation, the sum in the Fourier series of the surface modulation in Eq. (6.1) may only be computed between $m = \pm 1$, giving a simple sinusoidal modulation. By doing so, high-order linewidth peaks will disappear leaving only the g_0 peak (the one having highest intensity in the plot) in

sample displayed in Fig. 6.5	wavelength		RMS		ripple	ordering
	FFT	HHCF	Eq. (4.1)	HHCF	amplitude	parameter
	λ_1 (nm)	λ_2 (nm)	w_1 (nm)	w_2 (nm)	v (nm)	ξ_{\perp}/λ_1
(a)	103	97	2.7	2.4	6	6
(b)	222	202	12.3	12.3	30	2.1
(c)	341	298	27.9	25.9	61	2.2
(d)	432	393	16.5	16.6	60	3.2

Table 6.1: Roughness parameters of high-wavelength rippled Si substrates obtained from AFM images.

Fig. 6.4(b). The justification of such an assumption and the appropriate ratio between defect periodicity and width will be discussed below in the context of experimental data.

6.2 Substrate characterization

As defect-induced TMS needs higher-wavelength samples than being discussed up to now this section will shortly report on the substrate properties in this wavelength regime. Due to a possible influence of—if present—TMS on the resonance frequency of the measured magnetic response a discussion of the g -factor and anisotropy behavior will be given in the framework of the evaluation of the perturbation model later on.

Starting with the sample preparation using Si substrates, the same cleaning and evaporation procedure was used as already discussed in section 4.1.1. For this purpose a 30 nm Py layer was deposited followed by a 3 nm Cr protective layer. The only difference regards the sputtering process with respect to the used energy range. To reach higher wavelengths than discussed previously (below 90 nm, details see section 4.1.1) a significant increase in primary ion energy is required that can be simply approximated using Fig. 2.8(c). Ripples sputtered with Xe ions of energies up to 70 keV ($\lambda = 330$ nm) have been produced at the 40 kV implanter station using single- and double-charged ions of a fluence of $5 \cdot 10^{17} \text{ cm}^{-2}$. A further increase of λ could be achieved at the 200 kV facility, where Xe⁺ accelerated to 150 keV yields a wavelength around 420 nm using a fluence of $2 \cdot 10^{17} \text{ cm}^{-2}$. The roughness parameters obtained by AFM are listed in Table 6.1 and the corresponding measurements are depicted in Fig. 6.5. By comparing the roughness values for the high wavelengths with the one presented for low periodicities in Table 4.1 it first strikes that the deviation in wavelength determination between the two methods (HHCF, graphs presented in Figs. 6.5(e), (f), and FFT shown as insets to the AFM images) significantly increased. One reason can be seen by comparing the AFM image for $\lambda = 103$ nm

in Fig. 6.5(c) with the other AFM images shown in this figure. For $\lambda = 103$ nm the ripples are ordered along chains, exhibiting only a few interruptions. By increasing the wavelength these chains lose their homogeneity by forming bumps at the side walls, which in turn increases the error when determining λ . On the other hand, the decreased FFT peak distance in k space yields an increase in the error when determining the peak distance. In contrast, the RMS values for both methods fit quite nicely.

Inhomogeneous ripples also influence the lateral correlation length ξ_{\perp}/λ , which drops for higher wavelength and settles at a value between two and three. With respect to the modulation height, the ripple amplitude drastically increased with respect to the previously utilized samples and is now in the order of the film thickness³. Thus, the question raises if the assumption of a small perturbation acting on the spin dynamics is still justified. An answer to this question will be given in the next section when discussing high-resolution TEM images. Finally, it should be noted that the sample with the largest wavelength shows a strongly reduced RMS value. Here, the AFM images [Fig. 6.5(d)] show a superstructure with a high modulation that locally reduces the ripple amplitude.

6.3 Dipolar stray field observation

The aims of this investigation are two-fold. On the one hand, the layer structure after growth is of interest, since high-wavelength ripple exhibit an amplitude comparable or higher than the film thickness. On the other hand, the spatial distribution of the dipolar stray field is of interest, where especially at long wavelength a vanishing influence from the dipolar interaction is expected from Fig. 4.3. Both are of importance when discussing the perturbation theory of Landeros and Mills and will be investigated by means of MFM and TEM.

MFM is an extension of AFM, where a magnetic tip, magnetized along its cone axis, is used to image the stray field components above a magnetic sample. Therefore, the tip is scanned twice per image line, once in tapping mode close to the surface to record the AFM image and once at an elevated height (around 100 nm) above the surface. During the second scan the previously obtained surface profile is repeated, which leads, together with the distance between surface and tip, to a strong reduction of atomic forces leaving only long-range magnetic interactions. Due to the magnetic configuration of the tip only the stray field component perpendicular to the sample's surface is monitored by a phase shift of the tip excitation and actually recorded tip oscillation. Thus, due to quasi-simultaneously recording of AFM and MFM it is possible to correlate the magnetic with the topographic structure. In addition, an in-plane static magnetic field can be applied to alter the sample's magnetization configuration

³30 nm of Py, deposited after recording the AFM images

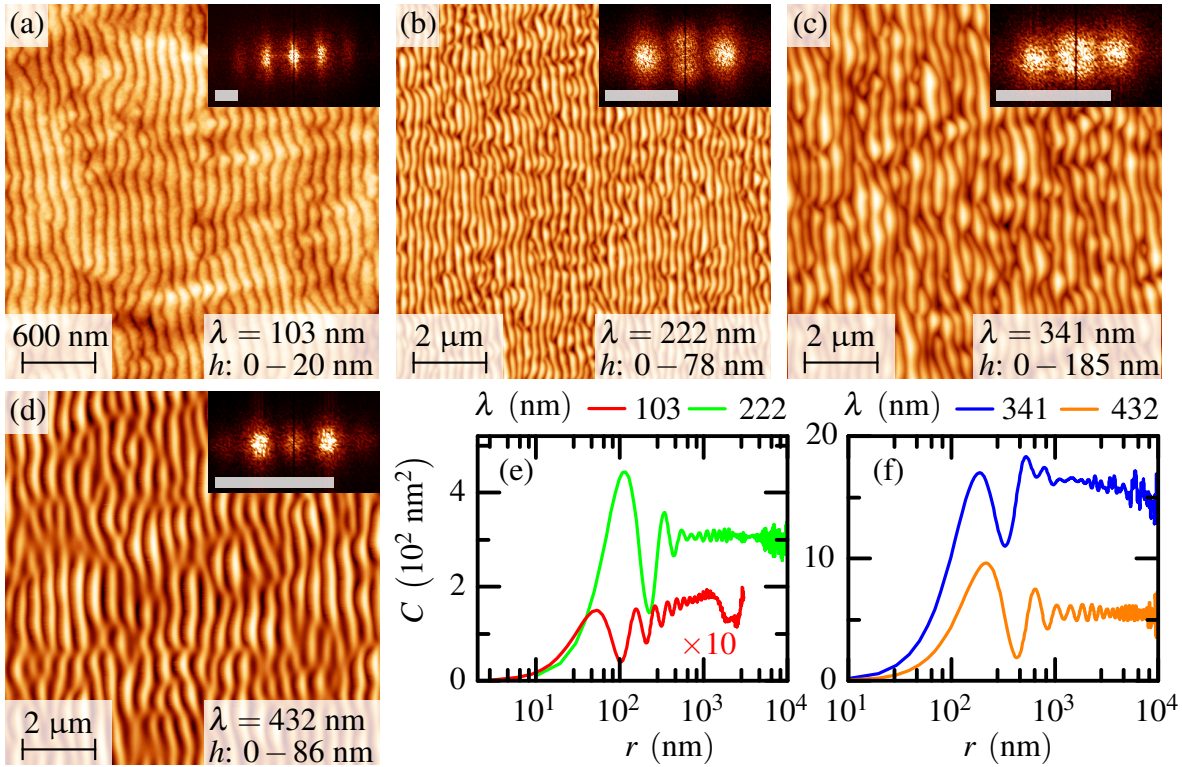


Figure 6.5: Rippled Si substrates exhibiting a high-wavelength pattern. In (a)–(d) AFM images are shown with height scaling h and ripple wavelength λ , both depicted in the bottom right corner of each image. The insets show the 2D FFT (color ranges arbitrarily scaled, the white bars correspond to $8 \mu\text{m}^{-1}$). Corresponding HHCFs are shown in (e) and (f).

during imaging. However, as useful as this method is, it is only limited to near-surface stray fields.

To gain an insight into the sample, TEM images have been taken from the sample's cross-section, revealing the lattice structure as already shown in previous discussions. In order to be able to monitor the magnetism inside the sample a collaboration was established with the Triebenberg laboratory for electron microscopy and electron holography, situated at the University of Dresden. These measurements, provided by F. Röder, allowed to monitor the projected in-plane magnetic induction \mathbf{B} of the rippled layer.

Electron holography uses a Möllenstedt biprism [223] to interfere two electron waves emitted from the same source. One passed the sample while the other crosses free space and thus serves as a reference. By this, an interference pattern is observed providing not only access to the wave's amplitude modulated by the sample, but also to phase shifts. The latter mentioned shifts occur between probe and reference wave if electric or magnetic fields are passed. Accordingly, it is possible to spatially monitor the magnetic induction over the whole film thickness. To

separate electric from magnetic phase shifts two images have to be superimposed numerically where (between both image recordings) either the sample has to be flipped upside-down [224] or the orientation of \mathbf{M} is reversed using a magnetic field of e. g. the objective lens [225]. The latter method has been preferred since it allows to keep the sample's orientation in the microscope. The magnetization reversal was obtained by using the field created by the objective lens, whereas the measurement itself was taken without any external magnetic field using only the aberration corrected Lorentz lens of the FEI TECNAI F20 TEM Cs-corrector. Further details on this technique may be found in Refs. 226–228.

6.3.1 Lamella preparation

A challenging task to perform holography measurements is the sample preparation. The magnetization state of interests exhibiting dipolar magnetic fields appears if \mathbf{M} is perpendicularly aligned to the ripple wavefront, so along the hard magnetization axis of a rippled film. Using conventional TEM preparation techniques⁴ would cause the magnetization to align along the easy axis and consequently dipolar fields will vanish. Also, applying an external magnetic field in a TEM is not possible during the measurement. Nevertheless, to prevent a relaxation of \mathbf{M} to the easy axis of the rippled film the sample geometry needs to be altered redefining the easy axis by tailoring the shape anisotropy (see section 2.1.2).

Instead of an extended, rippled film a lamella, thin enough to realign \mathbf{M} , has been cut out of the sample using a focused ion beam (FIB) technique of Ga^+ ions, which was done by M. Fritzsche using a Zeiss NVision 40 CrossBeam. Since this preparation technique is quite time consuming only three samples have been processed, namely wavelengths of 47 nm, 103 nm, and 222 nm. The usage of scanning electron microscope (SEM) images allowed to image the lamella's geometry during its preparation and helps to search a position having a nicely homogeneous ripple pattern. A side view of two of these lamellas is shown in Fig. 6.6. Noticeable is a thinned area where the lamella has only a thickness (into the plane of view) of ~ 140 nm as shown in panel (a) and less than 100 nm as depicted in panel (b). These two thicknesses were chosen as a first approach and as it turned out, the thinner samples yields better results. The thinned part consists of four different layers, nicely visible in Fig. 6.6(a). Starting from the bottom, the Si substrate is visible, followed by the rippled magnetic stack. On top two carbon layers are deposited. The first one is grown using a precursor gas and the electron beam of the SEM for deposition, and a second layer using the same precursor in combination with the Ga^+ beam of the FIB. Difference in contrast of these layers originates from different Ga concentrations. For the thin lamella depicted in Fig. 6.6(b) these layers are barely visible. Both

⁴the sample is polished in a wedge shape until it is thin enough to transmit electron beams

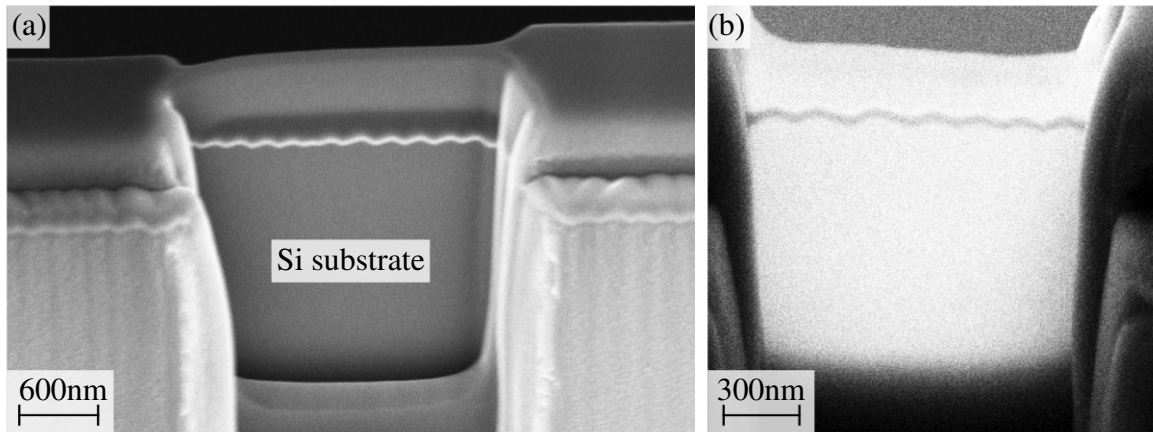


Figure 6.6: Lamella preparation using a crossbeam system. Depicted are SEM images of a lamella with (a) ~ 140 nm thickness (into the plane of view) and (b) a second one below 100 nm in thickness. Lamella preparation and images have been provided by M. Fritzsche.

layers are intended to protect the magnetic film from Ga^+ ions during the milling process from the top while thinning the lamella. Otherwise Ga^+ ions would penetrate the Cr cap and the Py layer, which can dramatically change the magnetic properties. Finally, the lamellas were attached to a grid and transferred to the TEM microscope.

Due to the bar-like geometry of the lamella the magnetization is expected to align along the long axis of the bar and, hence, perpendicular to the ripple wavefront. This can be easily seen by calculating the demagnetization factors for a magnetic film with dimensions of $1 \mu\text{m} \times 100 \text{ nm} \times 30 \text{ nm}$ using the formula given in Ref. 44. As a result $N_{1 \mu\text{m}} = 0.023$, $N_{100 \text{ nm}} = 0.25$, and $N_{30 \text{ nm}} = 0.73$ are obtained, strongly preferring an alignment along the bar's long axis of $1 \mu\text{m}$. From Eq. (2.11) it is evident that the evolving demagnetization fields will easily dominate the small, expected in-plane UMA of several mT.

6.3.2 Sample structure at high wavelengths

Prior to a discussion of the magnetic configuration the structure of the rippled layers will be in focus using high-resolution TEM images. In doing so the question will be answered if it is generally possible to obtain magnetic stray fields at high modulation lengths. Here, Fig. 4.3 suggests a vanishing dipolar influence for the needed ripple wavelengths above 100 nm. From the simple sinusoidal picture of the modulation this should indeed decay drastically, since the modulation is much higher than the exchange length ($\approx 5 \text{ nm}$ in Py), which should cause the magnetization to basically perfectly follow the corrugation to avoid stray fields. However, by increasing the ripple wavelength the shape of the observed surface modulation increasingly

differs from the sinusoidal model. To visualize this, TEM micrographs for three different wavelengths are shown in Fig. 6.7. One can see nicely that one slope of the ripples is always shorter than the other one, which is a consequence of the 67° tilt of the incident ion beam, counted from the sample's normal⁵. Thus, increasing wavelengths lead to partially shadowed surface regions during ion erosion. The shadowing is additionally supported by amorphous regions below the magnetic film (labeled by a-Si in the images), appearing brighter in the TEM image. These are wider below the shorter ripple side, which is evoked by the ion penetration depth.

One might expect a curvature-dependent thickness distribution caused by a varying projected area along the local rippled surface with respect to the material beam during film growth. A modulation in magnetic layer thickness in turn could be a source of dipolar fields. However, observations from the TEM images show a congruent layer growth over the whole surface modulation, which is indicated by the dashed white lines in the images. To obtain both lines the interface between the Si substrate and the Py layer was marked by a first line that was duplicated and parallel shifted to the layer's upper Cr-C interface. For the cases of 47 and 103 nm wavelength a simple upward shift was sufficient. The same applies to the $\lambda = 222$ nm ripple case after correcting the image tilt visible in Figs. 6.7(c) and (d). Hence, no changes in the interface structure were observed. Albeit, as indicated by the yellow bars (scaled to the film thickness of 33 nm) the local thickness differs with respect to the global sample normal along the modulation for the 222 nm wavelength case. Due to the high wavelength two images are presented in Figs. 6.7(c) and (d), highlighting additionally the wavelength variation at different positions. Here the thickness of 33 nm is found along the local normal, which thus is accompanied by a thickness variation between the extrema of the modulation with respect to the global normal. This in turn is a hint that during growth the atoms hit the surface locally normal to the surface, but not, as expected, from the global sample normal. In contrast, for smaller wavelengths a determination between local and global normal thickness cannot be made.

Another evidence to the assertion of local perpendicular growth is found by taking a look at the local lattice structure revealed by FFT images shown in Fig. 6.7. The positions where FFTs were calculated are marked by yellow dashed boxes, although the FFTs were calculated from higher-resolved TEM image than the ones shown. For the shortest ripple wavelength the FFT [Fig. 6.7(a)], calculated over a whole ripple period, reveals the polycrystalline layer structure with two dominant orientations (in the chosen area). In the higher-wavelength cases [Fig. 6.7(b) and (c)] a ring evolves in the FFT indicating the random orientation distribution of the observed lattice planes. Nevertheless, the orientation is not equally distributed over the

⁵The ion beam is directed onto the shorter ripple flank.

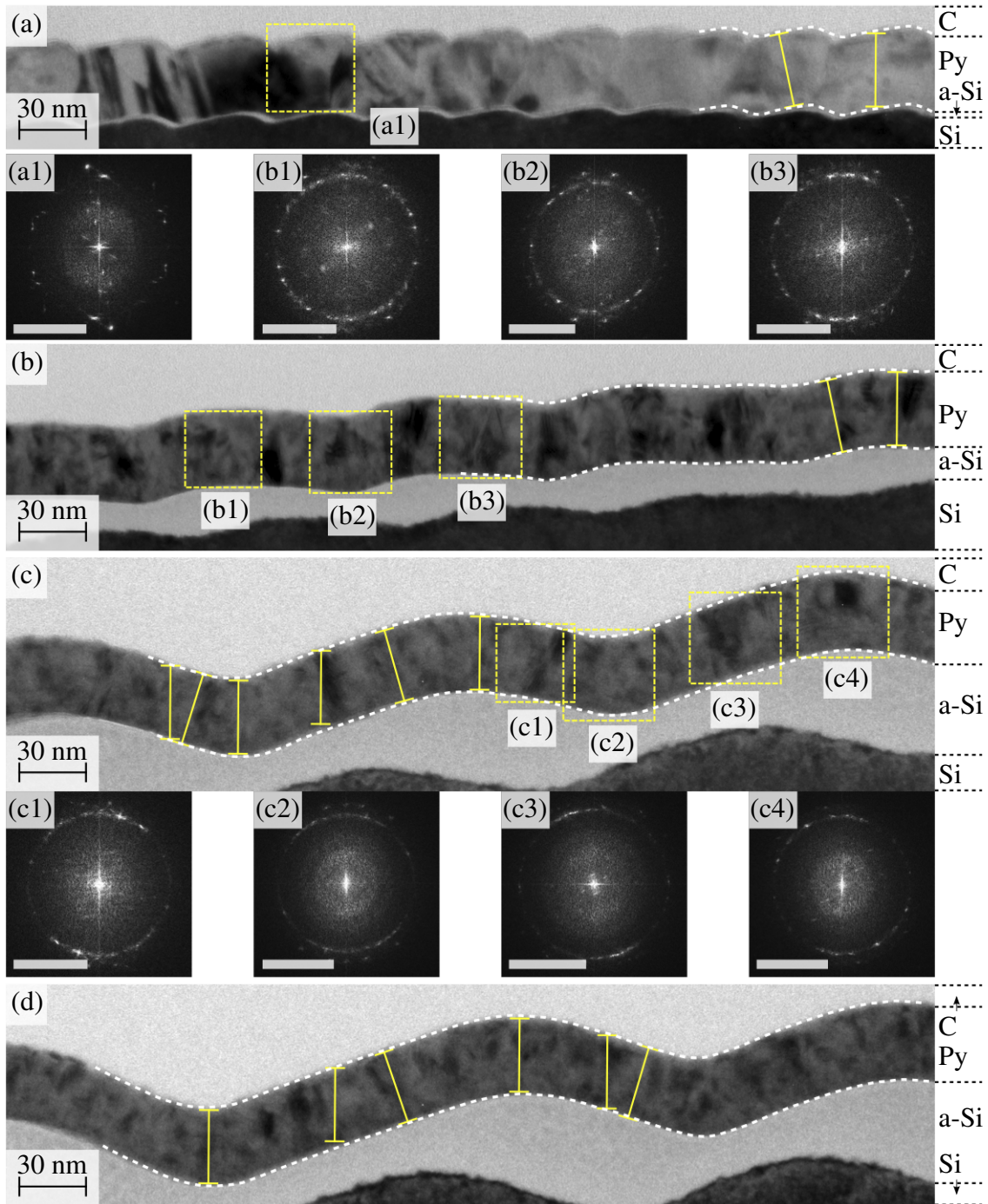


Figure 6.7: TEM micrographs of 30 nm Py (capped by 3 nm Cr) deposited on rippled Si substrates with (a) 47 nm, (b) 103 nm, and (c), (d) 222 nm wavelength. White dashed lines mark the interface between amorphous Si (a-Si) and Py as well as between Cr and the protective C layer. Yellow bars (33 nm length) mark the layer thickness at different positions and yellow dashed boxes label positions where FFTs (above and below TEM images, arbitrary gray scale with white bars of 5 nm^{-1} length) were calculated using high-resolution TEM images.

whole angular range. Especially for the case of $\lambda = 222$ nm [Fig. 6.7(c)] a preferred orientation is given by the local ripple slope, indicating a preferred lattice orientation parallel to the local ripple surface⁶.

With respect to the question whether the Py film may be considered as being perturbed the discussion has to be split into two parts, one for small and another for high wavelengths. Starting with the first, small wavelengths exhibit only a tiny modulation amplitude of a few nanometers, which can be viewed as being small compared to the film thickness of 30 nm. In addition, micromagnetic simulations⁷ presented in section 4.3.2 showed that the magnetization is basically aligned in the film plane (particularly if no external field is applied) showing only a minor canting caused by dipolar stray fields. Thus, in this range the perturbation theory seems to be a valid approximation. With respect to long wavelengths the modulation amplitude is comparable or higher than the layer thickness. However, due to long-range modulations with respect to the exchange length (~ 5 nm in Py), the film can be viewed as locally flat with \mathbf{M} aligned parallel to the local surface for vanishing external fields, which is especially true along the ripple slopes. Basically only at the modulation extrema the magnetic moments will experience an increased distortion from adjacent parallel alignment, caused by the strong curvature. In contrast, high-enough magnetic fields will reorient the magnetic moments towards the field axis.

The emerging magnetic configuration was obtained using the micromagnetic simulation package *OOMMF* [229] ($\mu_0 M_s = 1$ T, $A_{\text{ex}} = 1.3 \cdot 10^{-11}$ J/m) and is depicted in Fig. 6.8 for the cases of vanishing field, $\mu_0 H = 0.1$ T, and $\mu_0 H = 0.5$ T. From the simulated magnetic volume only a single slice (with respect to the y direction) is shown for each case. The sample geometry, especially the ripple shape, was extracted from Fig. 6.7(d) using a *Matlab* image processing script, specially developed for this purpose. Subsequently, the extracted interface was fitted using a polynomial function, which finally was implemented in the *OOMMF* script. In this way a wavelength of 216 nm and a peak-to-peak amplitude of 26 nm were determined. The simulation volume was set to $216 \times 50 \times 100$ nm³ with a cell size of $1 \times 5 \times 0.5$ nm³ and periodic boundary conditions applied along the x direction. In the upper panels of Fig. 6.8 the orientation of the magnetic moments is depicted. As expected, the moments are tilted and try to follow the surface corrugation without externally applied field and start to reorient along the field direction if an external field is present.

In the center and lower panels of Fig. 6.8 the resulting demagnetization field components along x and z are shown. Dipolar stray fields are observable for all cases, even for vanishing external field, since the moments do not perfectly align with the surface corrugation. Due to

⁶The FFT of Fig. 6.7(d) is, due to worse quality with respect to (c), not shown.

⁷Although the calculation was performed for Fe layers on sinusoidal ripples the behavior will only slightly differ in magnetization configuration with respect to Py ripples having minimal asymmetric ripples.

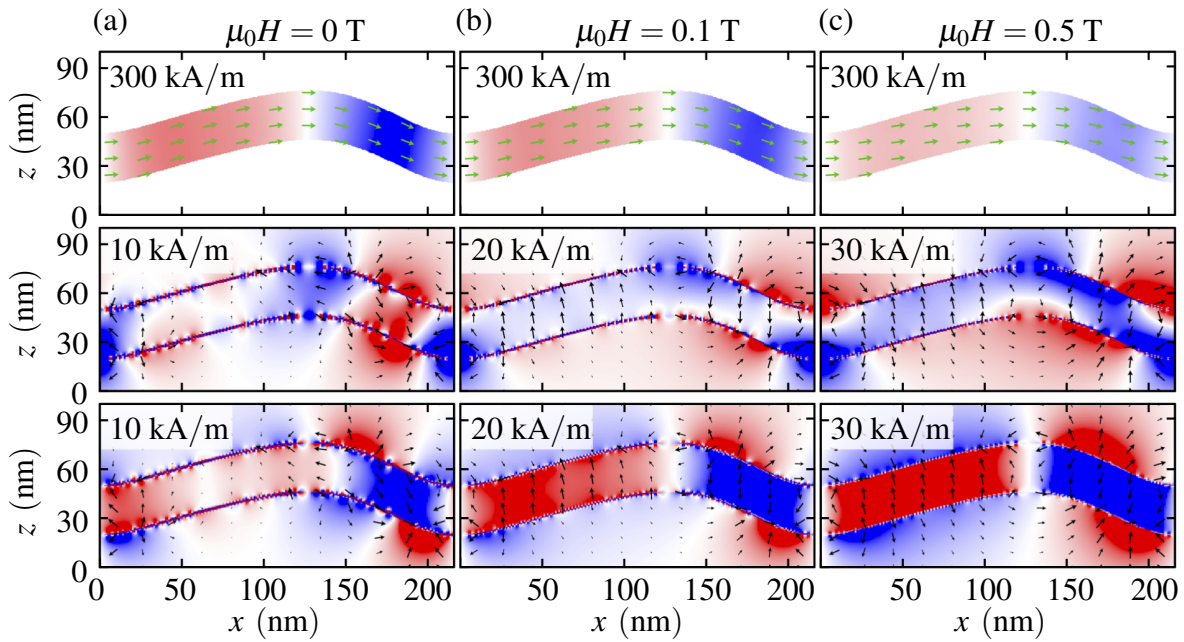


Figure 6.8: Micromagnetic simulations (x periodic) of the ripple profile shown in Fig. 6.7(d) under external fields of (a) 0 T, (b) 0.1 T, and (c) 0.5 T applied along the x direction (hard axis). Upper panels depict the magnetization direction (arrows: x , color: z component), centered ones the demagnetization field along the x direction, and lower ones the stray field along the z direction. The scale is given in the upper left corner of each image, where green (orange) arrows mark positive (negative) orientations of the chosen component and black arrows display the direction only. Red (blue) colors display positive (negative) values of the chosen component. Depicted is a single slice from the center (with respect to y) of the simulated bar.

the presence of stray fields without any external field it is principally possible to observe stray fields in the TEM by electron holography. Increasing the external field strength causes the moments to point towards the ripple slopes, which finally increase the dipolar field strength. However, the emerging dipoles at the film surface are basically unchanged in position but exhibit an increasing pole area with increasing external field. Comparing the magnetization with the evolving stray fields the latter are much smaller and exhibit only a slight influence on the magnetization, which in turn justifies the assumption of a perturbed magnetic film. Nevertheless, the perturbation theory assumes a stepped surface profile, which in turn causes a different shape of the dipolar fields than a ripple profile.

6.3.3 Fields above and inside the magnetic layer

Starting with MFM measurements the dipolar field at the sample surface will be investigated. In order to clearly separate magnetic from topographic contributions it is mandatory to observe

a change in recorded dipolar fields if the magnetization state is switched by an external field. For this reason, nearly all presented measurements are recorded under an external magnetic field that was reversed several times during the scan. Two kinds of MFM tips were used. First, conventional tips with a diameter of 30 nm and ultra sharp ones with 10 nm in diameter (at the smallest point of the cone). Due to the decreased diameter also the magnetic moment of the latter is decreased. Nevertheless, no stray fields could be observed above sample surfaces with $\lambda = 103$ nm or smaller. This might be due to the comparatively large tip diameter with respect to the spatial distribution of the dipolar stray field (recorded 100 nm above the surface), or the reduced magnetic tip moment.

However, moving to high modulations indeed reveals a change in the MFM contrast. The case of $\lambda = 222$ nm modulation period is presented in Fig. 6.9. For all MFM images the tip scan height was 100 nm above the surface and the images were recorded with the slow scan direction along the vertical image axis, starting the scan at the top of each image. During the scans in Figs. 6.9(b) and (c) an applied magnetic fields of 60 mT was reversed several times. The field orientation is labeled by white arrows in the images and field reversal points are marked by the white dashed lines. In each panel the AFM image is placed above the corresponding MFM image. For comparison, micromagnetic simulations showing the z component of the dipolar stray field are presented in panel (d) with applied magnetic field of ± 60 mT along the x axis as well as for vanishing field.

Since MFM investigations were done on a continuous film the simulations presented above (see Fig. 6.8) were repeated using xy periodic boundary conditions on the same geometry. Again, a single slice in the center of the y direction is shown. For all three cases \mathbf{M} was initialized 45° tilted to the x axis within the xz plane and with a negligibly small tilt towards the y axis. The z component of the calculated stray field is shown in Fig. 6.9(d). Considering the case of vanishing external field [center image in Fig. 6.9(d)] the dipolar stray field components are negligibly small since the magnetic moments align with the easy axis along the y direction, which thus creates no stray fields. Nevertheless, applying an external field reorients the moments along the hard x axis showing thus significant stray field components above the sample. In addition, the external field reverses the stray fields, which is equivalent to a switching of the magnetization with respect to the field axis. Note that this switching does not happen if the calculations are repeated with x periodic boundary conditions only, which thus indicates the increased uniaxial shape anisotropy caused by the bar-like structure.

Both simulations in Fig. 6.9(d), calculated with an applied field, show an unexpected feature near the ripple interface, where the z component is reversing several times. This behavior was only observed for the z component and is not repeated by the x periodic simulations shown in Fig. 6.8. It may be attributed to the stepped interface model and the quite small intrinsic

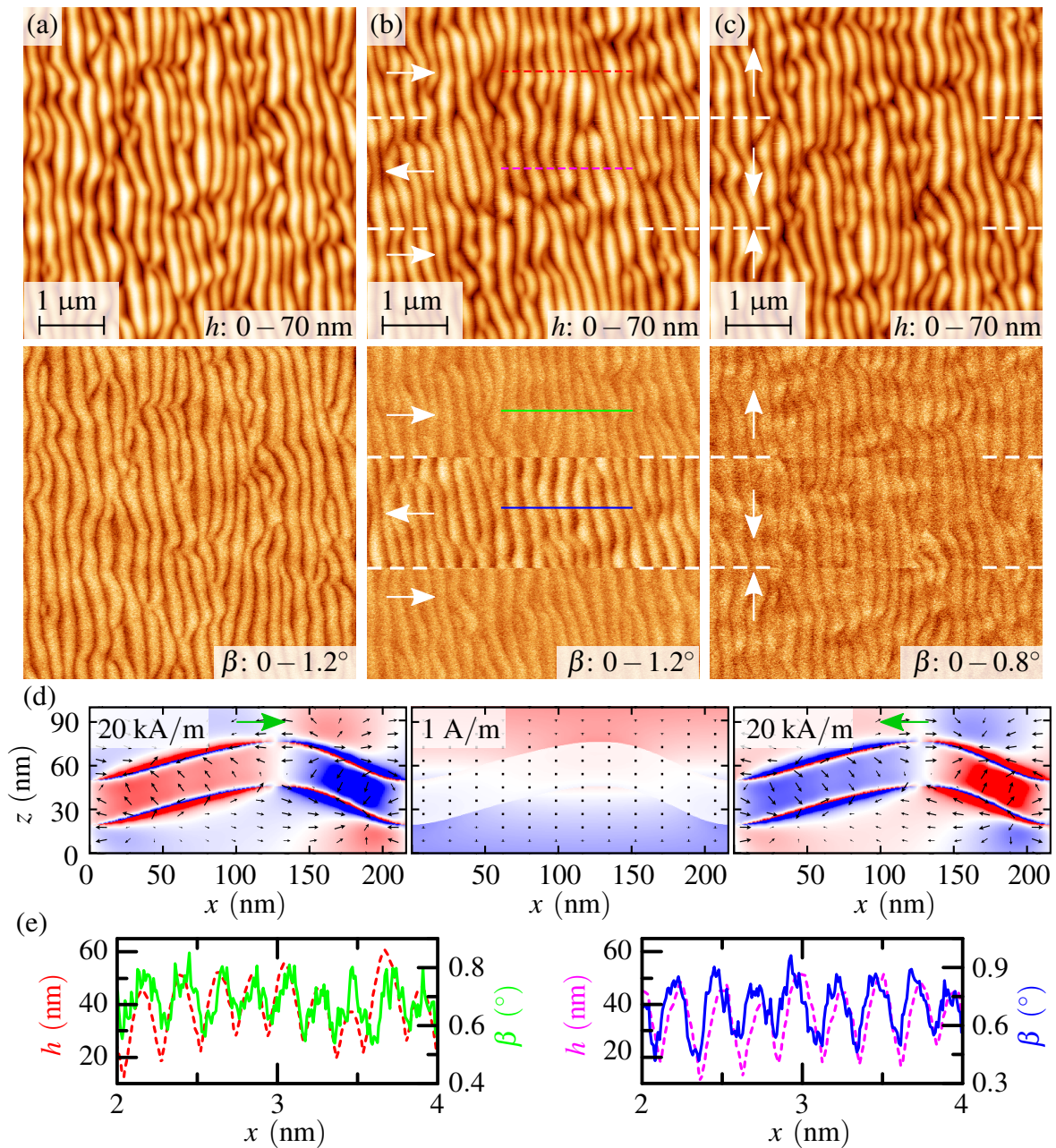


Figure 6.9: AFM (top) and MFM (bottom) investigations of 30 nm Py (capped by 3 nm Cr) on $\lambda = 222\ \text{nm}$ rippled Si under (a) vanishing field, (b) an external field of $\pm 60\ \text{mT}$ perpendicular to the ripple wavefront, and (c) $\pm 60\ \text{mT}$ parallel to the wavefront. White arrows indicate the direction of the applied field, where the points of field reversals are indicated by white dashed lines. The slow scan direction was from top to bottom. Height h and phase scale β are listed in the bottom right corners. In (d) corresponding xy periodic $OOMMF$ simulations (z component) are shown for $\pm 60\ \text{mT}$ (green arrows) and for vanishing field. The color code equals Fig. 6.8. (e) Shows line scans from positions labeled in (b) by solid and dashed colored lines.

anisotropy caused by the modulation and xy periodic boundary conditions. Nevertheless, in comparison to Fig. 6.8, the far field—measured by MFM—is unaffected.

Considering Fig. 6.9(a) the MFM contrast shows a periodic modulation, which in turn is not expected when taking the vanishing z component of the corresponding micromagnetic simulation into account. Furthermore, by overlapping the AFM and MFM image (not shown) no difference was observed in the modulation. Hence, this case reflects only the superimposed topography contrast in the MFM measurements. However, this is not the case if an external field is applied. Fig. 6.9(b) shows the situation for the external field applied perpendicularly to the wavefronts. The AFM part recorded under +60 mT is quite noisy, which is an artifact of the measurement. Apart from this, the AFM image is unaffected by the external field. Especially, no abrupt shifts in the wavefront are observed when the field direction is reversed. In contrast, the MFM image shows a field dependence exactly during reversals of the magnetic field orientation to the opposite direction. At these points, marked by the white dashed lines, the magnetic contrast is shifted, which in other words means that magnetic poles are influenced by the external field. Taking the micromagnetic simulations into account the magnetization flips, which explains the reversed contrast in the MFM image. By overlapping AFM and MFM line scans, as shown in Fig. 6.9(e) [each scan averaged over three lines], a shift of the MFM profile is observed corresponding to the direction of the applied magnetic field. This originates from the fact that the external field tilts the magnetization towards the ripple slope creating magnetic charges at the slope, which can be seen in Fig. 6.9(d). Hence, the magnetic and topographic extrema are shifted with respect to each other.

Opposed to this, the observed shift with the external field vanishes if the magnetic field is applied along the ripple wavefronts [Fig. 6.9(c)], leaving only the topography contrast and underlining unambiguously the dipolar origin of the observation shown in Fig. 6.9(b). The same behavior was in turn observed on even higher wavelengths (not shown).

Next, the magnetic stray fields as well as the internal magnetization configuration is of interest. Both have been investigated using off-axis electron holography measurements. To derive the information of interest the phase shifts, caused by magnetic sample properties, between the object and reference waves were extracted. Such a measurement is shown in Fig. 6.10(a), where the phase signal was numerically amplified for better visibility. Due to this, phase shifts within the magnetic Py layer are clearly visible, which in turn follow the surface corrugation. The direction of the in-plane⁸ magnetic induction \mathbf{B} is derived from equiphase lines to which the projected in-plane component of \mathbf{B} is parallel. Due to the fact that these phase shifts are formed by the total magnetic flux enclosed by the object and reference beams,

⁸with respect to the lamella's side view and thus the cross-section of the film

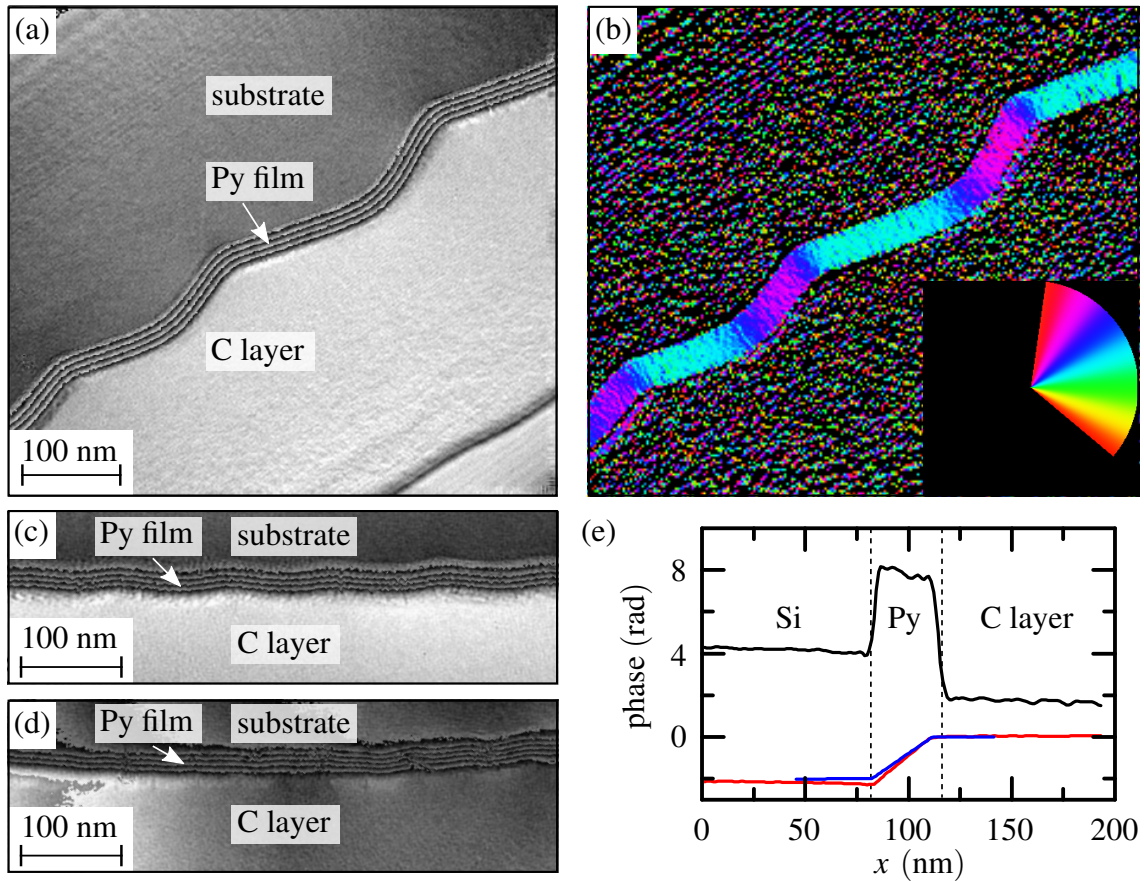


Figure 6.10: Holography cross-section measurements on rippled Py layers. (a) Shows magnetic phase shifts (12 times amplified) from which the magnetic orientation, depicted in (b) was determined (the color wheel shows the direction), both for 222 nm ripples. In (c) the magnetic phase is shown for $\lambda = 103$ nm (17 times amplified) and in (d) for 47 nm wavelength (20 times amplified). The gray scales are arbitrary. (e) Comparison of electric (black), magnetic (red), and simulated magnetic (blue) phases across the lamella. The measurements were done by F. Röder at the Triebenberglaboratory.

it contains information of local magnetization direction and internal magnetic fields inside the layer and dipolar stray fields outside.

First, let's focus on the internal observations. From micromagnetic simulations shown in Fig. 6.8 it can be concluded that inside the Py film the magnetization is the dominant contribution as it is at least one order of magnitude above the calculated stray field values. As a consequence, the magnetization inside the Py layer follows the local surface corrugation. For a better comparison with simulations shown in Fig. 6.8 the magnetization direction, calculated from the phase gradient (which is perpendicular to the in-plane projection of \mathbf{B}), has been

color-coded and is depicted in Fig. 6.10(b). From this, a very good agreement between numerical prediction (Fig. 6.8) and measurement is obtained. Furthermore, Fig. 6.10 shows the magnetization behavior for $\lambda = 103$ nm and 47 nm in panels (c) and (d), respectively. Again, the alignment follows the surface corrugation for $\lambda = 103$ nm and reaches almost the planar case for $\lambda = 47$ nm. At this, the changes in magnetization are too small to be resolved by the measurement.

In Fig. 6.10(e) the phase information (no amplification, taken perpendicularly to a long ripple slope) across the $\lambda = 222$ nm film is shown and, in case of magnetic phases, compared to the micromagnetic simulation. From the electric phase signal (offset set to zero within vacuum region) the sample's composition becomes evident, caused by the different mean inner potentials of the materials. Furthermore, the lamella's thickness (in e-beam direction) was estimated to be within the range of 40 – 45 nm, and is comparable to the thickness roughly determined by SEM during the preparation. The comparison of the magnetic phase signals of measurement and simulation shows a very good agreement, where the magnetic phase has a linear slope of 80 (5) mrad/nm within the Py layer. Deviations of the measured phase signal in the Si region may be due to beam-induced charge fluctuations. Estimating the mean magnetization across the film yields (1.1 ± 0.1) T, which agrees with the literature value of 1 T [56].

Finally, the cross-sectional in-plane dipolar stray field above the sample is of interest. To be able to observe a field contribution outside the magnetic film the unamplified magnetic phase image was contrast-enhanced. By this, large-area in-plane modulations become weakly visible especially above the film, as shown in Fig. 6.11(a). Note that the Py and Si was blackened due to the shifted contrast. Those large phase modulations are visible especially at the shorter ripple slopes (regions II and IV), whereas at the long slopes (regions III and V) the fields are less pronounced. The same behavior is found in the simulation of the in-plane dipolar stray field by plotting it in a similar way, which is shown in Fig. 6.11(b). To be able to compare measurement and simulation directly, Fig. 6.11(b) shows a calculation using the ripple shape depicted in Fig. 6.11(a). Hence, two waves were simulated using periodic boundary conditions along the x direction. The simulation volume was increased to $444 \times 50 \times 100$ nm³ and the cell size was reduced to $0.25 \times 5 \times 0.25$ nm³. In order to compare both, magnetic phase shifts are plotted in Fig. 6.11(c). Due to imperfect flux enclosure of the ferromagnetic film during the experiment the measured signal exhibits a background behavior. However, minima in the phases of measurement and simulation coincide qualitatively very well and confirm the observation of magnetic dipolar stray fields. This is also true for the long slopes, which in turn have no significant features. From the maximum experimental slope of (1 ± 0.5) mrad/nm the magnetic stray field strength was determined to be in the range of 10 – 20 mT, which

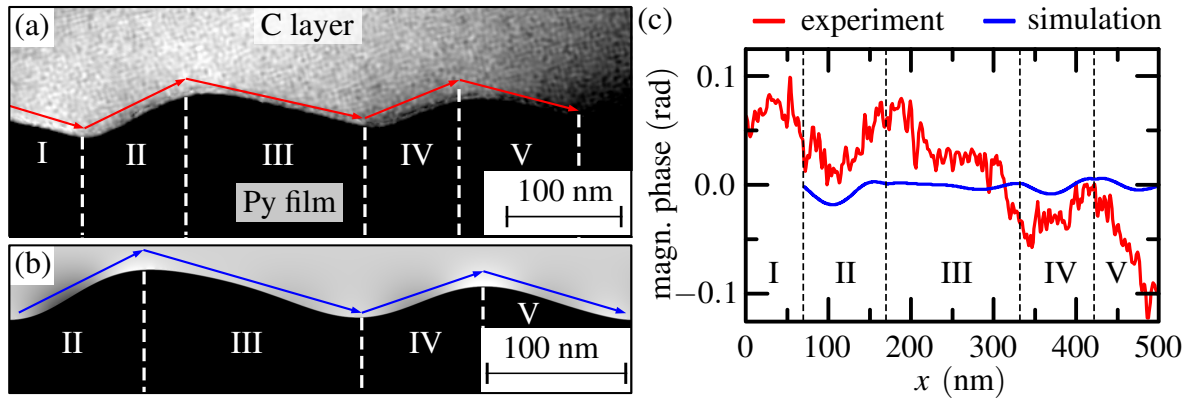


Figure 6.11: Cross-sectional in-plane dipolar magnetic stray fields above the $\lambda = 222$ nm rippled film. (a) Holography measurements and (b) micromagnetic simulation, both with arbitrary gray scale. In (c) the profiles marked in (a) and (b) by the red and blue arrows are plotted. The experiment was performed by F. Röder at the Triebenberglaboratory.

agrees well with the micromagnetic simulation. For the smaller wavelengths investigated by holography the stray fields could not be resolved within the background noise.

In summary, it was demonstrated that the magnetization of rippled layers align with the surface corrugation for long ripple periods. Imaging the magnetization's orientation in the film was achieved by using a holographic technique. In addition, also above the surface stray fields were resolved by MFM measurements. Both measurements agree nicely with micromagnetic simulations. Hence, it is proven that rippled magnetic layers indeed induce a periodic dipolar field that can be utilized to induce TMS.

6.4 Ripple-induced two-magnon scattering

In the final experimental discussion the wavelength dependence of rippled Si substrates onto dynamic magnetic properties of Py films will be discussed. Recalling predictions from perturbation theory (see section 6.1) TMS will not be present in the given frequency range below a modulation periodicity of $a_0 = 70$ nm. To confirm this, a flat reference sample was prepared as well as four samples with different wavelengths of $\lambda = 27$ nm, 35 nm, 47 nm, and 103 nm. Angle-dependent measurements of the planar sample were performed at different frequencies. The obtained anisotropy parameters are presented in Table 6.2.

Starting with the planar sample basically a negligibly small four-fold anisotropy is seen and a tiny intrinsic UMA, typical for planar Py [230]. The effective magnetization seems to decrease with applied microwave frequency, which might be attributed to the fact that at small

f (GHz)	planar			$\lambda = 27$ nm		
	$\mu_0 M_{\text{eff}}$ (mT)	$2K_{2 }/M_s$ (mT)	$2K_{4 }/M_s$ (mT)	$\mu_0 M_{\text{eff}}$ (mT)	$2K_{2 }/M_s$ (mT)	$2K_{4 }/M_s$ (mT)
6	1036	0.66	-0.14	1010	7.42	-0.75
10	1024	0.71	-0.1	999.4	7.72	-0.72
15	1021	0.87	-0.08	997.5	8.32	-0.78
30	1021	0.99	-0.1	995.6	9.34	-0.7

Table 6.2: Anisotropy parameters of a 30 nm thick Py film on a planar Si substrate and a rippled sample with $\lambda = 27$ nm.

frequencies no perfect resonance curves could be recorded, but shoulders in the line were observed⁹. Nevertheless, the effective magnetization is close to the saturation magnetization, indicating a negligibly small out-of-plane anisotropy. Furthermore, within the measurement accuracy the observed linewidth is independent on the angle (not shown). In addition, $f(H)$ measurements were done along the easy as well as hard axis of the samples. From this the g -factor was determined to 2.11 (1) which equals the bulk value. In the past, only for smaller film thicknesses a deviation from this value has been observed [231].

In addition, $f(H)$ and angle-dependent measurements with sufficiently high microwave frequencies (e. g. 30 GHz and above) show an additional mode, as depicted in Fig. 6.12(a) for a measurement of the planar sample along the easy axis. An explanation is found in evolving spin wave modes presented in section 2.2.3. Due to the small exchange length and the comparable large film thickness, PSSW modes are allowed. Fitting the data with Eq. (2.50) for $p = 1$ gives the possibility to determine the spin wave stiffness constant D . Therefore, in-plane anisotropies were neglected and D was determined along the anisotropy axis. Furthermore, in Eq. (2.50) shape anisotropy was included by simply replacing M_s by M_{eff} [cf. Eq. (3.1)]. The latter can be determined easily from the measured angular dependence. By this, the stiffness constant was found to be $D = 23.8(8)$ Tnm² along the easy and $D = 23.6(8)$ Tnm² along the hard axis, respectively. Hence, D can be considered as being isotropic in the planar case.

Besides the field-dependent frequency plot in Fig. 6.12 the frequency dependence of the peak-to-peak linewidth is shown in panel (b). The external field was applied along the easy axis and the linewidth shows a linear frequency dependence. Fitting the dataset gives a Gilbert¹⁰ damping of $\alpha = 0.0062(2)$ and an inhomogeneous line broadening of $\Delta H_{\text{pp}}^{\text{inhom}} = 0.25$ mT.

⁹The observed line broadenings are similar to those seen in section 5.3, which as well might indicate a measurement artifact caused by the setup.

¹⁰The absence of TMS linewidth contributions justifies the g -factor determination described above, because no shifts in resonance position are expected.

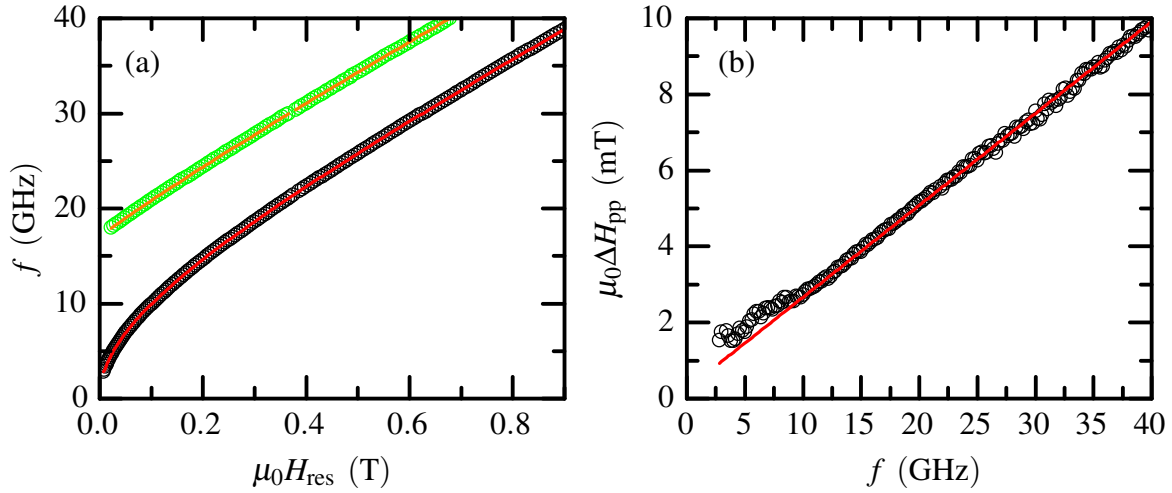


Figure 6.12: Planar reference sample of 30 nm Py measured along the easy axis. (a) Anisotropy plot of the FMR mode (black open circles) and the first PSSW ($p = 1$, green open circles) mode. (b) Peak-to-peak linewidth of the FMR mode. The solid lines are fits using the resonance condition (3.1) and Eq. (2.50).

The same behavior was observed along the hard axis but with slightly different inhomogeneous broadening of $\Delta H_{\text{pp}}^{\text{inhom}} = 0.35$ mT (not shown). An additional important feature of the linewidth can be observed below 10 GHz. Here, the linewidth slightly differs from the ideal Gilbert damping in form of a small peak. This peak originates from the fact that in this frequency range the observed resonance lines are not perfect, but rather exhibit shoulder-like features which already have been mentioned in section 5.3. Nevertheless, the deviation is below 0.5 mT and thus will play only a minor role. Furthermore, above a microwave frequency of $f = 45$ GHz the linewidth noise increases (not shown). On the one hand the measured signal simply decreases due to power limitations with increasing frequency and on the other hand the amplifier reaches its saturation regime, which might cause higher harmonics in the emitted microwaves (see section 3.3.3). Even though, the principal linewidth dependence is not influenced by this.

Next, the rippled samples with wavelengths up to 103 nm will be discussed briefly. First, of course, the UMA strongly increases as it is shown in Table 6.2. Here, as well, a frequency-dependent anisotropy determination is listed. Again, the four-fold anisotropy is negligible and the UMA as well as the effective magnetization follow the same trend as observed in the planar case. This indicates the systematic error of the setup, as the anisotropy is not expected to vary with microwave frequency. Also the in-plane angle-dependent linewidth is found to be isotropic within 1 mT precision for all three wavelengths. From $f(H)$ measurements g as well did not show any noticeable variation from the value of 2.11 (1). Furthermore, the

	planar	$\lambda = 27$ nm	$\lambda = 35$ nm	$\lambda = 47$ nm	$\lambda = 103$ nm
easy axis, α	0.0062	0.0062	0.0061	0.0063	0.0062
hard axis, α	0.0062	0.0063	0.0062	0.0065	0.0064

Table 6.3: Gilbert damping parameters obtained from $f(H)$ measurements along the easy and hard magnetization axis. The absolute fit error of α is less than $2 \cdot 10^{-4}$.

frequency-dependent linewidth shows for all samples a small peak below 10 GHz comparable to the case depicted in Fig. 6.12(b). Apart from that the linewidth is linear in frequency, showing only Gilbert damping and a small inhomogeneous offset (typically below 1 mT). For the damping parameter α no direction dependence can be observed. The values obtained are listed in Table 6.3, where for the sake of completeness also the planar case is included. Also no influence of the rippled substrate on intrinsic damping can be determined within the given error range. Furthermore, in the frequency dependence the first PSSW mode was observed and by this the exchange stiffness was determined. Since this time a small uniaxial anisotropy was present within the plane, Eq. (2.50) was expanded by a $2K_{2||}/M_s$ term according to Eq. (3.1). In Table 6.4 the findings are summarized. Especially for small wavelengths a small influence on the exchange stiffness is visible, whereas modulations of 47 nm and above are quite close to the planar reference sample.

Altogether, it can be said that rippled surfaces do not have a significant influence on intrinsic material properties in the wavelength range below 103 nm. The only exception may be formed with respect to the exchange stiffness for small wavelengths. Also, as predicted by the theory, no extrinsic linewidth contribution can be found below 70 nm of wavelength. However, this was also the case for the 103 nm sample. This might be simply attributed to discrepancies between the model and experiment. Admittedly, the theoretical predictions were made using a higher exchange stiffness of $D = 34 \text{ T nm}^2$, but as Fig. 6.3(c) shows, lower constants shift the peaks to smaller frequencies and thus even lower periodicities are predicted.

The situation changes completely if much higher wavelengths are considered, e. g. above 200 nm. In this case the frequency-dependent linewidth is strongly direction dependent, as pre-

	planar	$\lambda = 27$ nm	$\lambda = 35$ nm	$\lambda = 47$ nm	$\lambda = 103$ nm
easy axis, D (10^{-1} T nm^2)	238 (8)	238 (9)	238 (9)	238 (21)	252 (9)
hard axis, D (10^{-1} T nm^2)	236 (8)	212 (9)	212 (9)	258 (11)	244 (9)

Table 6.4: Exchange stiffness for a planar and rippled Py films up to $\lambda = 103$ nm.

dicted by the perturbation theory, which is a hint for the presence of TMS. The corresponding measurements are depicted in Fig. 6.13. In panel (a) the linewidth is shown once parallel and once perpendicular to the ripple wavefront. While the first case shows a linear, Gilbert-like dependence, the perpendicular orientation reveals a well pronounced linewidth peak. Additionally, both measurements reveal a small peak below 10 GHz as it was already observed in previous experiments and thus can be attributed to measurement artifacts. Compared to the theoretical predictions of the stripe case, only a single peak is observed. In general, this may have three possible reasons: (i) the modulation periodicity equals a multiple of the defect width and corresponding peaks vanish. (ii) The surface modulation approaches a sinusoidal function and the summation over m in Eq. (6.1), describing the surface corrugation, is computed only between $m = \pm 1$. Finally, (iii) the combination of defect periodicity/width and exchange stiffness may lead to high-order peaks above the measurement range. The first can be ruled out immediately if the spatial distribution of the dipolar stray field as well as the symmetry of the surface modulation are considered. Here, Fig. 6.8 shows a strong asymmetry between defect width and periodicity. Due to this, also the second argument is invalid, which thus pleads in favor for the third point.

To compare the perturbation model with the measurement, a valid set of data has to be determined from the evaluation above. With respect to material properties, $\mu_0 M_s = 1$ T and $d = 30$ nm were used for the calculation. The exchange stiffness was once more determined from the first PSSW mode. Here, along the hard [easy] axis $D = (24.6 \pm 1.4)$ T nm² [$D = (26.1 \pm 0.9)$ T nm²] was found, which is comparable to the $\lambda = 103$ nm case. Nevertheless, even if the perturbation may be considered as being small, the evaluation of D is based on the resonance condition of a perfect film. This in turn relies on the assumption of vanishing influences from TMS on the recorded resonance. Therefore, for the g -factor¹¹ and the exchange stiffness¹² the previously determined values of the planar sample were used for further calculations, with $g = 2.11$ and $D = 24$ T nm².

From the TEM image [Fig. 6.7(d)] and the corresponding micromagnetic simulations [Fig. 6.8(c)] one might guess a modulation periodicity equivalent to the wavelength as well as a defect width equal to the length of the ascending or descending ripple slope¹³. However, taking these values the calculated peak appears at a frequency of $f = 6.5$ GHz and is thus well below the observed peak position of $f = (10.7 \pm 0.3)$ GHz. As shown in Fig. 6.4(a), the linewidth peak shifts down in frequency position if the periodicity a_0 is increased. Hence,

¹¹the determination of g is very sensitive on the resonance position

¹²unknown influence of TMS on D

¹³In general two different defect widths can be guessed from the ripple pattern, $w'_1 = 125$ nm and $w'_2 = 97$ nm, set by the asymmetric slopes. However, the linewidth is unaffected by the choice between these two possibilities as long as $w'_1 + w'_2 = a_0$ is fulfilled.

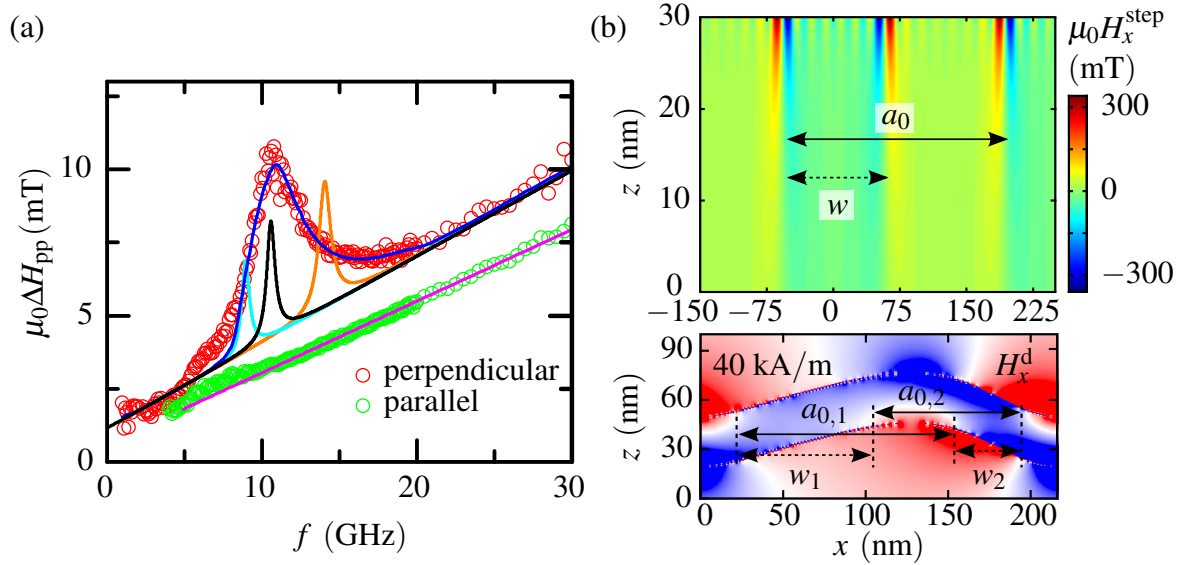


Figure 6.13: Frequency-dependent linewidth obtained for 30 nm Py on $\lambda = 222$ nm rippled Si substrates. In (a) the linewidth is plotted parallel and perpendicularly to the ripple wavefront. Additionally, solid lines show the calculated linewidth using parameters described in the text. (b) Dipolar fields (x component) inside stripe and rippled samples. Solid (dashed) arrows indicate the defect periodicity (width). The upper image equals Fig. 6.2(b) and the lower one is calculated using xy periodic boundaries ($\mu_0 H = 0.5$ T) with color scale and parameters equal to Fig. 6.8(c).

the approximation of a periodicity equal to the wavelength is yet too simple. Instead, from the peak position and the dispersion relation of degenerate spin waves it is easy to obtain a mean periodicity of the perturbation that induces the magnon scattering. If Py bulk values ($D = 24$ T nm², $\mu_0 M_s = 1$ T, and $g = 2.11$) and vanishing in-plane anisotropy are assumed this results in $\bar{a}_0 = (112 \pm 4)$ nm, which is basically half the wavelength.

This can be understood if the dipolar fields entering the model [see Fig. 6.2(b)] are compared with the fields obtained from the simulation [similar to Fig. 6.8(c)]. For a better comparison, both cases are depicted together¹⁴ in Fig. 6.13(b). In case of the stripes the field strongly decreases below the stripe defect, whereas in between the dipolar field is positive and shows poles directly at the stripe edges. Therefore, the field changes its strength inside the sample once per periodicity. For a better visualization the evolving periodicity and defect width is marked by horizontal solid and dashed black arrows. In contrast, the x component of the stray field of the rippled case shows a continuous modulation across the sample from positive to negative stray fields and vice versa. Caused by the two extrema in the rippled film two spatially extended pole

¹⁴In contrast to Fig. 6.8 the simulation is calculated using xy periodic boundary conditions.

regions form along the magnetic film. Due to this, not a single but at least two periodicities evolve with $a_{0,1} = 137$ nm and $a_{0,2} = 88$ nm. Averaging these values gives 112.5 nm, which is remarkably close to the predicted value of $\bar{a}_0 = 112$ nm. It nearly equals half the wavelength of $\lambda = 222$ nm since two adjacent extrema of the surface corrugation—causing dipolar fields of the same periodicity—have a mean distance of $\lambda/2$. Furthermore, the defect widths are $w_1 = 62$ nm and $w_2 = 39$ nm, which gives an average value of $\bar{w} = 50$ nm. Next to the defect periodicity and width also the modulation height h obviously cannot be taken from the TEM images. In this case a 26 nm height would definitely not be a small perturbation anymore and moreover, the expected dipolar fields of such a structure would be around a Tesla. Instead, numerical calculations presented in Fig. 6.13(b) suggest a field strength below 40 mT, which is easily given by a defect height of $h = 1$ nm.

Finally, the evolving linewidth calculations are shown in Fig. 6.13(a) by solid lines. The Gilbert damping parameter α and the inhomogeneous line broadening were approximated to the measurement by $\alpha = 0.0075$ (3) and $\mu_0\Delta H_{pp}^{\text{inhom}} = 1$ mT for perpendicular alignment with respect to the ripple wavefront. The Gilbert value is slightly larger than for samples discussed above and will be addressed later. Along the easy axis (magenta line) $\alpha = 0.0062$ (2) was measured ($\mu_0\Delta H_{pp}^{\text{inhom}} = 0.6$ mT), which is in nice agreement with the Gilbert damping parameter obtained from the reference samples and thus indicates the vanishing influence of TMS parallel to the surface modulation. The three periodicities $a_{0,1}$, $a_{0,2}$, and the averaged case \bar{a}_0 , obtained from the micromagnetic simulation, are additionally shown in Fig. 6.13(a). Considering the averaged peak (black), it fits quite well in its center position with respect to the measured one, whereas $a_{0,1} = 137$ nm (cyan) and $a_{0,2} = 88$ nm (orange) form the lower and upper limit of the measured data.

Simply averaging these three peaks would not reflect the measurement. Instead, since the dipolar stray field changes continuously in the rippled case (the step case has a relatively sharp field transition), scattering will occur continuously within the range of $a_{0,1}$ and $a_{0,2}$ leading to a superposition of numerous linewidth peaks located at different frequencies. This assumption is underlined by the measured peak width, which is in general much broader for the rippled films than for the stripe simulation. In order to approximate the measured linewidth peak of the rippled film by a superposition of single peaks from the stripe model, a series of 200 curves was averaged where the defect periodicity a_0 was changed linearly between 72 and 139 nm. Compared to the previously determined values for $a_{0,1}$ and $a_{0,2}$ slight variations are observed that originate from uncertainties of the graphical evaluation of the micromagnetic simulation. Additionally, the simulation is based on a single ripple wave¹⁵ that was periodically repeated, which in turn neglects spatial variations of the ripple quality and wavelength. The latter for

¹⁵the wavelength of 216 nm is close to the average wavelength of 222 nm

example were observed by AFM (Fig. 6.5 shows broadened satellite peaks in the FFT) and TEM (Fig. 6.7 shows cross-section for two wavelengths) micrographs. Contrary to the defect periodicity the defect width does not influence the linewidth peak position and, hence, cannot be approximated by a fit to the measured data. Therefore, w was varied linearly between 39 and 62 nm.

Finally, the defect height h had to be adapted, since it quantifies the strength of the scattering potential and, as a result, the height of the linewidth peak. The best fit was obtained by changing h linearly. Starting with $h = 1.2$ nm at the lower limit of the a_0 range, h was gradually increased to 3.5 nm until the center of the peaks was reached. Subsequently, h was gradually decreased down to 1.2 nm until the upper limit of the periodicity range a_0 was reached. This dependence is justified by the micromagnetic simulation shown in Fig. 6.13(b). Here, the extrema in the dipolar field are roughly separated by half the wavelength, whereas smaller dipolar fields are separated by shorter/longer periods. Note that the defect height h assumed for the ripple case cannot be compared to the height of a stripe defect. Choosing a value of $h = 3.5$ nm would cause much higher linewidth peaks than observed. Due to the averaging the peaks h may be considered as an effective height that scales the scattering strength.

Using these parameters the perturbation model (based on stripe-like defects) nicely reproduces the experimental observations made on rippled Py films, which confirms the presence of TMS. The corresponding fit is shown in Fig. 6.13(a) by a blue solid line. Next to the peak position the asymmetry of the peak's slope is reproduced by the fit. The latter is caused by the increasing linewidth of single linewidth peaks with increasing frequency and is also visible by comparing the cyan and orange curve shown in Fig. 6.13(a). The small deviation below 10 GHz can be attributed to a measurement artifact observed in many experiments, which is also visible for the parallel orientation of external field and ripple wavefront.

Additionally to the influence of TMS on the linewidth, the perturbation theory predicts a shift in resonance frequency as well as a splitting of the response function. Note that both is neglected when evaluating the linewidth using Eq. (6.3). Especially the latter leads to an apparent line broadening since two superimposed peaks may be too close to each other to be separated in the experiment. In the present case the linewidth is averaged over a broad range of perturbation parameters a_0 , w , and h . Especially for high values of h the perturbation is significant and the response function [given by Eq. (6.2)] of a single a_0 , w , and h set will differ remarkably from the unperturbed film (splitting of the resonance and shifted position, not shown). However, by averaging over the whole parameter range the resulting line shape allows a determination of a single resonance position and linewidth. Also in the experiment no splitting of the resonance curves, leading to Fig. 6.13(a), was observed. Nevertheless, this leads to the conclusion that the observed line broadening results from a superposition of neighboring

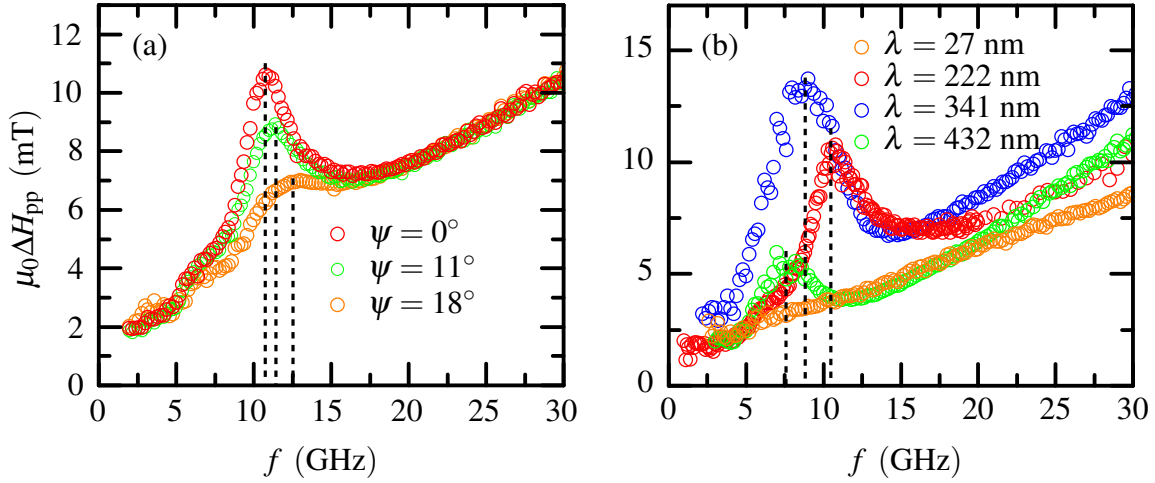


Figure 6.14: Frequency-dependent linewidth for (a) orientations around perpendicular alignment with respect to the ripple wavefront of the $\lambda = 222$ nm case and (b) as a function of the ripple wavelength. The angle ψ is counted between ripple wave vector and externally applied field. Dashed lines mark the peak maxima.

resonances and, thus, is apparent. Drawing conclusions on the damping will become only possible by investigating the intrinsic damping of the—by TMS—excited $k_{\parallel} \neq 0$ modes. Apart from this, the presented model supports the understanding of the basic physics behind the measured data.

In Fig. 6.14 the angular dependence of the linewidth and its frequency dependence are shown for the sample with 222 nm wavelength. Panel (a) depicts the frequency-dependent linewidth for field orientations close to the ripple wave vector, which in turn is aligned normal to the wavefront. With increasing angles between the modulation wave vector and the external field, the observed linewidth peak starts to decrease in height and the peak frequency slightly increases as indicated by the dashed lines. The decrease in peak height is understood in the framework of dipolar field strength, which triggers TMS. Turning the external field away from the perpendicular orientation towards the easy axis steadily decreases the field component that aligns the magnetization along the hard axis, which in turn will follow the external field. Hence, the magnetic dipoles at the surface will be weakened in strength and finally vanish if the easy axis alignment is reached. A decrease in dipolar fields is, however, accompanied with a decreasing number of TMS scattering events, which finally lowers the peak.

In the language of the theory the perturbation function Γ^I entering the linewidth scales with $\cos^4 \psi$, as pointed out by Landeros and Mills [24]. Here, ψ is the angle between magnetization and ripple wave vector. To explain the upward shift in frequency the resonance condition (5.6)

has to be taken into account, where three influencing mechanisms are conceivable: (i) the change in resonance frequency to higher frequencies (lower fields) when approaching the easy axis, (ii) slight shifts in the defect's periodicity with decreasing external field along the hard axis, and (iii) the influence of the magnetization with respect to the spin wave propagation direction $\varphi_{\mathbf{k}_{\parallel}}$. Especially the second point should be quite small or negligible, since Fig. 6.8 does not suggest a significant change in periodicity of the dipoles along the x direction with decreasing external field component. In addition, an increase of the projected wavelength along the external field direction and its accompanied increase in defect periodicity would lead to a shift downwards in peak frequency. The same holds true for the influence of the UMA, which additionally decreases the peak frequency by up to 0.1 GHz. Thus, the peak frequency is mainly influenced by the angle $\varphi_{\mathbf{k}_{\parallel}}$. As the perturbation direction triggering the spin waves is set by the ripple ridges, the angle between magnetization and spin wave propagation increases when \mathbf{M} is rotated towards the easy axis¹⁶. This finally alters the dispersion relation causing the upward shift in peak frequency. A similar trend was also observed on samples with higher wavelengths.

Next to the angular orientation with respect to the surface modulation, the ripple wavelength has an influence on the peak position and its height. Fig. 6.14(b) shows this dependence for the three high-wavelength samples with modulations between 222 and 432 nm. For comparison the $\lambda = 27$ nm case was added. This time a decrease in peak frequency is observed with increasing wavelength. In this case the average scattering periodicity set by the surface modulations increases with the wavelength, which thus decreases the reciprocal lattice parameter g_0 . Hence, the scattering condition is fulfilled at lower external fields (cf. Fig. 6.1) corresponding to lower microwave frequencies. This finally explains the downwards shift of the linewidth peak. Note that the peaks caused by wavelengths above 222 nm are at least partially below 10 GHz and, hence, in the region where measurement artifacts influence the measured spectra increasing the noise. The frequency positions of the peaks are (8.6 ± 0.6) GHz and (7.5 ± 0.8) GHz, which finally leads to average periodicities of (146 ± 14) nm and (182 ± 30) nm. Considering the given errors and the uncertainties in wavelength determination using the two methods listed in Table 6.1, the averaged periodicities again reflect half the wavelength of the surface modulation.

Furthermore, it seems in Fig. 6.14(b) that the peak amplitudes change unsystematically, since the amplitude of the $\lambda = 222$ nm peak is higher than for $\lambda = 432$ nm, but smaller than for the $\lambda = 341$ nm case. An answer to this question can be given by considering Fig. 6.13(a) [solid lines] or Fig. 6.3(b) where the same behavior is observed for the modeled linewidth. In both examples the only thing that changes is the ratio between defect width and periodicity. Hence,

¹⁶Note that increasing $\varphi_{\mathbf{k}_{\parallel}}$ above a certain threshold causes the degenerate spin wave state to vanish [see Fig. 2.7(b)] and TMS is shut off.

it can be assumed that for increasing wavelength this ratio slightly changes, which produces the observed height differences.

Another interesting feature in Fig. 6.14(b) can be observed above 15 GHz. In this region the linewidth slope of samples containing TMS ($\lambda \geq 222$ nm) differ remarkably from the pure Gilbert contribution ($\lambda = 27$ nm) as well as among each other. Therefore, Gilbert damping may not be the only contribution in this frequency range, but a second linewidth peak may evolve. Such a peak is also one reason of observing an increased Gilbert damping for perpendicular alignment to the ripple wavefront. As proven by TEM investigations (cf. Fig. 6.7) the surface modulation is not perfectly sinusoidal, which thus allows high-order peaks due to $|m| > 1$ in Eq. (6.1). Considering for example $a_{0,1} = 137$ nm and $w_1 = 62$ nm would cause a second peak at 23 GHz, which is barely visible in Fig. 6.13(a) for the cyan curve as its amplitude is only 0.2 mT (the main peak has an amplitude of 5 mT). The two remaining parameter sets did not show any additional contributions in the computed range up to 40 GHz. Higher-frequency positions of second-order peaks may evolve for smaller periodicities, e. g. caused by imperfect ripples. These high-order peaks are in general more broadened than the main peak and may vanish in the background function causing different slopes of the TMS-influenced samples. In addition, the ripple geometry will further broaden these peaks, as it is also the case for the main peak. Further evidences of high-order peaks are given by comparing the slopes against each other. The slope of the $\lambda = 432$ nm sample equals the slope for $\lambda = 27$ nm up to a frequency of 20 GHz, from where it is higher, which suggests the starting point of an additional peak. Furthermore, the $\lambda = 432$ nm and $\lambda = 341$ nm case exhibit comparable slopes that are different to the $\lambda = 222$ nm case. This coincides with the positions of the main peaks that are closer to each other for $\lambda = 432$ nm and $\lambda = 341$ nm than for $\lambda = 222$ nm. Conversely, this means that second-order peaks for the first two cases are nearly at the same position resulting in a comparable slope. However, the parameter set introduced above for the $\lambda = 222$ nm case does not predict high-order peaks¹⁷ in the linewidth. Therefore, other (smaller) defect periodicities may be present that are neglected by the model.

Next to the frequency dependence the angle-dependent resonance fields and linewidths are influenced by TMS and will be discussed. Both are shown in Fig. 6.15 for the $\lambda = 222$ nm sample. In panel (a) the in-plane angular dependence of the linewidth is depicted for different choices of microwave frequency. Interestingly, the linewidth strongly depends on the excitation frequency and shows a two-fold symmetry with high (low) linewidth values perpendicular (parallel) to the ripple wavefront. For the lowest frequency of $f = 6$ GHz only a tiny two-fold

¹⁷ $m > 1$ used

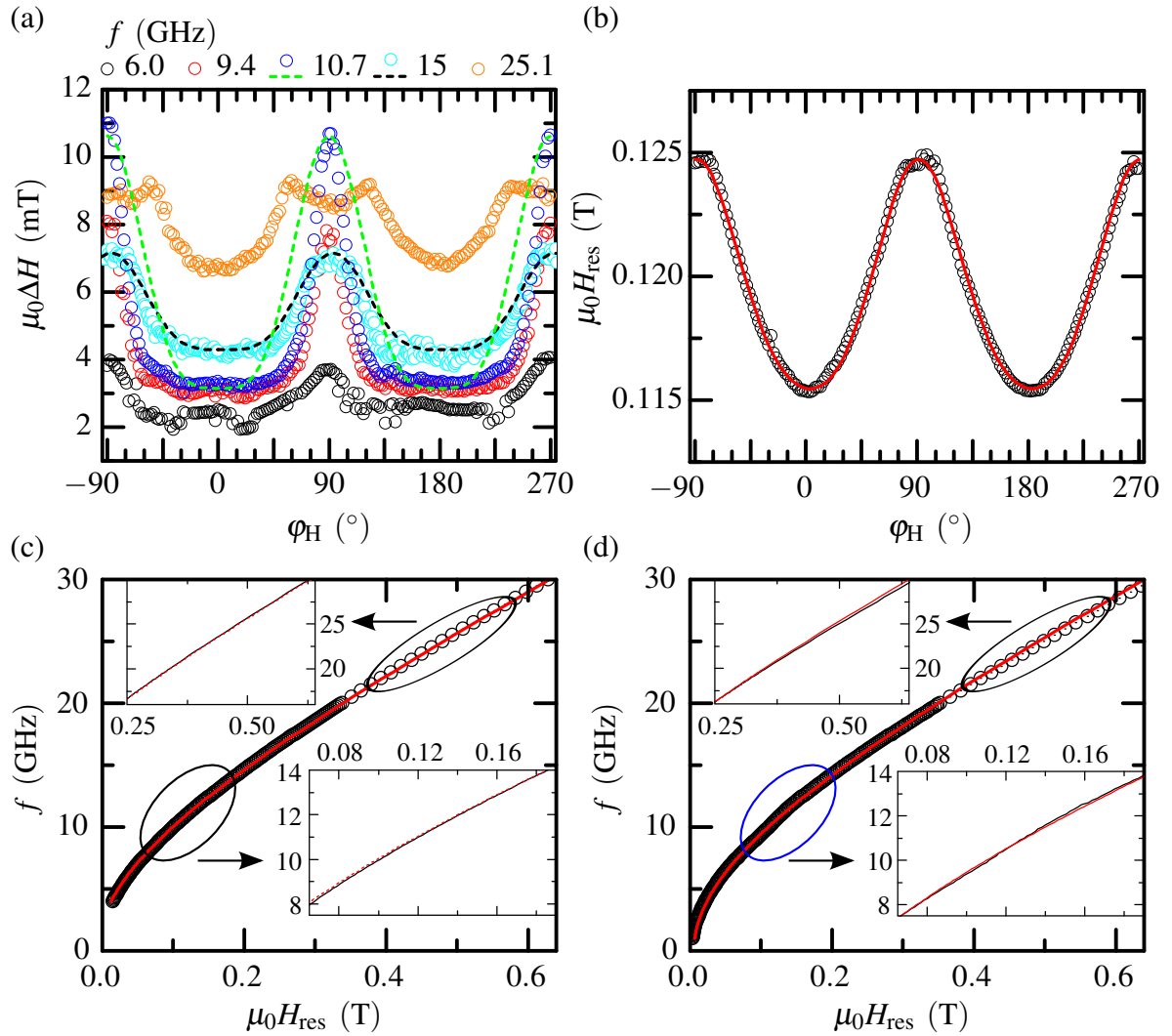


Figure 6.15: Perturbation influence on 30 nm Py grown on 222 nm rippled Si. Angular dependence of (a) the linewidth and (b) the resonance field ($f = 10.7$ GHz). For $\phi_H = 0$ the external field is aligned along the ripple wavefront. The frequency dependence of the resonance is shown along (c) the easy and (d) along the hard axis. Red lines are fits using parameters obtained from (b) and the insets are magnifications at low and high fields.

symmetry is observed that strongly increases if the microwave frequency approaches the peak in the frequency-dependent linewidth [$f = 10.7$ GHz in Fig. 6.13(a)]. For higher frequencies the linewidth exhibits an even more complicated shape. This increase in peak-to-peak amplitude is accompanied by the evolving peak in the frequency-dependent linewidth [see Fig. 6.13(a)] that starts to differ from the Gilbert contribution when approaching the scattering condition given by the surface modulation. Therefore, a frequency selected close to the peak in the

frequency-dependent linewidth—but not perfectly matching the scattering condition¹⁸—causes only a reduced TMS contribution. However, this does not explain the angular dependence for the highest frequency of $f = 25.1$ GHz. Comparing the parallel ($\varphi_H = 0$) and perpendicular ($\varphi_H = 90^\circ$) direction for the $f = 25.1$ GHz case, shown in Fig. 6.13(a), reveals that even if no obvious linewidth peak is observed in the frequency-dependent linewidth [see also Fig. 6.14(b)] at high frequencies both directions still differ if linewidth values for different directions at the same frequency are compared. As discussed above, this might be due to high-order peaks. Thus, the angle-dependent linewidth for $f = 25.1$ GHz is influenced by TMS as well. The upward shift of the $f = 25.1$ GHz curve in Fig. 6.15(a) in general is caused by the upward shift in linewidth with increasing microwave frequency. However, the kink around the maximum in the angular dependence still remains unclear and needs further theoretical investigations.

The symmetry of the angular dependence in Fig. 6.15(a) is directly given by the symmetry of the rippled surface, where maxima in the linewidth correspond to a perpendicular orientation between external field and ripple wavefront. In order to extract linewidth parameters Eq. (5.12) was applied to get an idea of the relaxation. However, the model function does not fit perfectly as it is shown for the $f = 10.7$ GHz case in Fig. 6.15(a). There the modeled peak width is much broader than the measured one. Obviously the formula will fail completely for the highest frequency of 25.1 GHz. In contrast, the case of $f = 15$ GHz is nearly perfectly reproduced. Table 6.5 summarizes the obtained parameters, indicating the increasing influence of TMS when approaching the linewidth peak. However, it should be noted that these values are only a very rough estimation, since the model is not entirely appropriate. Nevertheless, the two-fold TMS parameter is strongly increased if the excitation frequency corresponds to the maximum in the frequency-dependent linewidth. The Gilbert damping in turn steadily decreases with increasing microwave frequency. However, this parameter might be misleading since the sample does not exhibit any dragging, and thus the Gilbert contribution cannot be separated from mosaicity of e. g. the effective magnetization since both exhibit the same (vanishing) angular dependence. Hence, this parameter reflects an effective linewidth contribution.

Besides the TMS linewidth contribution the uniaxial anisotropy is listed in Table 6.5 showing a frequency dependence which certainly does not follow the trend of the TMS influenced linewidth. Recalling that the $\lambda = 27$ nm reference sample showed a linear trend of the UMA with frequency (see Table 6.2), which in addition was much smaller, the influence of direction-dependent TMS on the resonance condition is evident. Although the angle-dependent resonance field, depicted in Fig. 6.15(b) does not show significant deviations from the model function above 10 GHz (below the measurement does, but the typical measurement artifacts cannot be

¹⁸The reason why TMS occurs also for imperfect matches between the reciprocal lattice vector and the degenerate state lies in intrinsic damping. In contrast, if α approaches zero, the linewidth peak is sharp in frequency.

f (GHz)	$\mu_0 M_{\text{eff}}$ (mT)	$2K_{2 }/M_s$ (mT)	α_{eff}	$\gamma\Gamma_{2\text{-fold}}$ (MHz)
6.0	9935	3.64	0.0085 (5)	290 (30)
9.4	9866	5.0	0.0083 (3)	760 (30)
10.7	9880	4.87	0.0077 (4)	1220 (40)
15.0	9848	5.66	0.0070 (4)	460 (40)
25.1	9704	11.33	0.0070 (2)	—

Table 6.5: Frequency-dependent anisotropy and linewidth parameters for 30 nm Py on 222 nm rippled substrates.

fully excluded), the frequency-dependent resonance field in turn does. This becomes clear if the dependence along the easy and hard axis are compared as shown in Figs. 6.15(c) and (d). For the easy axis the resonance condition (3.1) fits quite well over the whole field range, whereas along the hard axis a deviation is observed especially at high fields above 0.4 T. Moreover, the measurement differs from the model in the field range exhibiting the linewidth peak (marked by the blue ellipse), which indicates that the TMS has a strong influence of the resonance condition. Such influences are predicted by Landeros and Mills [24] in the framework of the perturbation theory. Stripe-patterned samples recently showed several splittings in the $f(H)$ dependence and the response functions. Both observations are well covered by the theory and are in the focus of further investigations. In case of the rippled films the splitting in the $f(H)$ dependence—such as for the response function—mostly averages out leaving only a small indication in the area marked by the blue ellipse.

Hence, it is not possible to apply the ordinary resonance condition anymore, since it relies on a uniformly magnetized film, which is certainly not given in the perturbation regime. Due to this, an evaluation of g and D may be invalid since it relies on the same assumptions as the resonance condition, as it is derived from it. The other wavelengths of $\lambda = 341$ nm and 432 nm show a similar behavior and are, therefore, not shown. In agreement with Fig. 6.14(b), $\lambda = 341$ nm showed the biggest influence of TMS ($\gamma\Gamma$ up to 1.6 GHz) and 432 nm the lowest one ($\gamma\Gamma$ up to 400 MHz).

Summarizing the findings of this section, TMS was found for samples with wavelengths of 222 nm and above, whereas samples with smaller wavelength showed Gilbert damping only. From the latter the exchange stiffness was determined and found to be isotropic for modulations above 47 nm and slightly anisotropic below. Also Gilbert damping in these samples does not show an angular dependence. Most important are the findings for long wavelengths revealing direction-dependent TMS, where a peak in the frequency-dependent linewidth occurs for

perpendicular alignment of the external field (and thus the magnetization) with the ripple ridges. In combination with micromagnetic simulations the position of the evolving linewidth peak in the frequency dependence could be explained as well as its broadening. For this purpose, a superposition of modes covering a broad range of TMS parameters was used. Due to this the observed linewidth broadening is apparent and cannot be linked to an increase in damping. Furthermore, TMS strongly influences the angular dependence of the linewidth and the resonance field due to an introduced frequency dependence, which makes it impossible to apply the LLG equation throughout the whole frequency range.

7 Summary and outlook

In conclusion, it was shown that rippled substrates have a strong influence on magnetic layers grown on top, suitable to tailor static and dynamic magnetic properties. The advantage of ripples over other preparation techniques such as lithographic patterning, is the easy and fast preparation using ion beam erosion techniques. This in turn allows for large-area samples and wavelengths that simply scale with the primary ion energy. The change in film morphology induces a uniaxial magnetic anisotropy of dipolar origin for all wavelengths considered (starting from $\lambda = 20$ nm and going up to 432 nm). In addition, long-range modulations, starting from $\lambda = 222$ nm, introduce perturbations in the magnetic layer that match degenerate states in the spin wave dispersion relation, and, thus, induce direction-dependent two-magnon scattering. To gain these findings, the thesis was divided into three experimental sections clarifying first the origin of the magnetic anisotropy of polycrystalline systems of different magnetic materials. Secondly, the induced UMA was superimposed to a magneto-crystalline anisotropy of Fe, and finally the FMR linewidth containing two-magnon scattering in Py systems was addressed.

Starting with the first experimental chapter the UMA was in focus. After reviewing the ripple preparation process the evaluation of the surface morphology using AFM revealed an increase in ripple ordering with increasing wavelength. Also the RMS roughness increases with the wavelength, which both makes ripples suitable for morphology investigation over a wide range of surface modulations. Only the ripple amplitude is fixed by the sputtering process to the ripple wavelength by a nearly constant aspect ratio. Due to the ion erosion process and by natural oxidation Si substrates are amorphous at the surface, which in turn results in polycrystalline layer growth on top. By this, magnetic films deposited on these substrates exhibit basically no—or only a quite weak—magneto-crystalline anisotropy and, thus, provide an excellent system to study induced anisotropies. Indeed, due to the surface modulation a uniaxial magnetic anisotropy forms with easy axis along the ripple ridges and a hard axis perpendicular to it. The anisotropy is found to be strongest for the lowest wavelength possible and decreases with the same. Other parameters such as effective magnetization are not influenced by the ripples in this wavelength regime. Evaluating thickness-dependent measurements revealed the dipolar origin of the UMA. Two characteristic regions were found with competing uniaxial volume and surface anisotropy where the volume contribution is dominant in the thin region and the thick region is controlled by dipolar stray fields at the surface. Here, the dipolar stray field

could be correlated with the RMS roughness of the film and its modulation period. Increasing the first increases the dipolar field, whereas the latter has the opposite effect. Under the use of micromagnetic simulations the spatial distribution of the dipolar field and the magnetization could be resolved in dependence of the film thickness and modulation period. The magnetic anisotropy is formed by evolving dipoles at the film surface if the magnetization is unable to follow the corrugation. Due to the direction-dependent roughness of the ripples an alignment of \mathbf{M} parallel to the ridges is energetically favored as the perpendicular orientation forms, under the cost of energy, the surface dipoles and thus the stray field. By this, the hard magnetization axis lies perpendicularly to the ripple ridges and the easy axis parallel to it. In contrast to a model proposed by Vaz *et al.* the magnetization never perfectly follows the surface corrugation (caused by the interplay between exchange and dipolar energy), which in turn means that dipolar fields are always present. However, increasing λ causes the magnetization to align with the average film height and, additionally, decreases tilts between adjacent moments. Hence, the origin of the UMA and its scaling with the ripple period have been proven.

Next, the ripple-induced UMA was combined with the crystal anisotropy of Fe layers of 10 nm thickness, epitaxially grown on MgO single-crystalline substrates. In parallel to rippled samples with $\lambda = 20$ nm wavelength, planar reference samples were used to examine the modulation influence. First, AFM confirmed that the ripple structure created on MgO substrates can be oriented along any direction with respect to the underlying MgO lattice. Moreover, as proved by LEED, the MgO keeps its crystal structure at the surface after ion beam erosion, which makes it possible to epitaxially grow Fe on top. However, in comparison to the Si case the ripple quality is slightly reduced, which is e. g. noticeable in small ripple amplitudes of 1 nm. Structural investigations after the film growth indeed revealed a single-crystalline iron layer whose in-plane [100] direction is 45° rotated with respect to MgO[100]. This behavior is already known since years for flat films and is caused by the lattice mismatch between both materials. Depending on film thickness and lattice mismatch defect structures evolve in the film that relax the strain. TEM micrographs showed such defects in the rippled Fe layer indicating a relaxation. Further investigations by means of X-ray diffraction confirmed that the flat Fe layer is still under tensile strain whereas the rippled one is nearly fully relaxed. Magnetic investigations were done by means of VNA-FMR measurements determining the in-plane angular dependence of the resonance field as well as its $f(H)$ dependence. From the latter the g -factor was determined, where the obtained values did not show deviations from literature values for planar and rippled samples. Contrary, the in-plane anisotropy is strongly influenced by the rippled surface modulation. While the planar reference sample revealed the expected four-fold anisotropy of cubic Fe, a superposition of induced UMA with crystalline anisotropy was observed for the rippled samples. Most important is the point that UMA and

crystal anisotropy can be oriented independently from each other by simply selecting the ripple orientation with respect to the MgO crystal lattice. This in turn is easily achieved by choosing the direction of the incident ion beam when fabricating ripple substrates. With respect to anisotropy, theoretical calculations by P. Landeros underlined the dipolar origin of the UMA. Its strength is one order of magnitude smaller than the intrinsic cubic anisotropy and variations in strength are caused by the varying ripple quality. The intrinsic four-fold anisotropy and the effective magnetization for rippled samples are in turn much closer to bulk values than the planar case, which can be attributed to the present tensile strain found for the reference samples. Finally, the magnetization relaxation was in focus revealing two dominant linewidth contributions, namely intrinsic Gilbert damping and mosaicity of the cubic anisotropy. Further contributions like extrinsic two-magnon scattering could not be observed, mainly caused by the too small ripple period. The Gilbert damping in turn showed a complex angular dependence generated by magnetization dragging caused by the strong in-plane anisotropy. Like the intrinsic anisotropy it is also affected by the strain, where the rippled films are closest to the bulk values, but still twice as large. The same holds true for mosaicity, which nearly vanished for the rippled films and was most dominant in the flat case. Thus, rippled films offer a possibility to combine intrinsic and induced anisotropies with any preselected orientation possible. In addition, the rippled morphology enhances the lattice strain relaxation and, thus, brings intrinsic anisotropy and damping closer to the bulk values than it is the case for the planar reference sample.

In the final experimental chapter the extrinsic linewidth contributions were investigated. Outgoing from the two-magnon scattering theory introduced by Arias and Mills the spin wave dispersion relation exhibits degenerate states that offer the possibility to transfer energy from the excited FMR mode into higher $k_{||}$ spin waves, which in turn effectively transfers energy away from the initial, uniform precession. To fulfill besides the energy conservation also the conservation of momentum, scattering centers are essential to trigger that process, which was ensured in the theory by random defect structures located at the sample surface. Based on this, Landeros and Mills presented an extended theory by considering periodic defect structures that create periodic dipolar magnetic fields and thus act as scattering centers to finally activate the energy transfer. To do so, the periodicity of the defect structure has to match the degenerate energy states in the spin wave dispersion. In this framework, rippled magnetic films provide an excellent tool to tailor the surface modulation and, thus, the periodicity of the evolving dipolar fields over a wide range starting from $\lambda \approx 20$ nm up to several hundred nanometers in wavelength by simultaneously being fast and easy to prepare. The wavelength expected to enable TMS in Py thin films should be at higher wavelengths than those used in previous investigation. Hence, a series of magnetic films deposited on different ripple periodicities was

prepared to investigate the influence due to induced extrinsic relaxation effects. To exclude other influences such as crystal structure Py was chosen as material, whereas Si ripples provided an amorphous substrate surface suppressing crystal anisotropy. This means that dragging effects vanish and the intrinsic damping contribution is angle independent, which in contrast was not observed in the case of Fe on MgO exhibiting a strong in-plane anisotropy. In a first step rippled substrates with wavelengths up to $\lambda = 432$ nm were investigated by AFM revealing a drop in correlation length and, as expected, a further increase of modulation amplitude with wavelengths reaching and exceeding the thickness of the Py layer. This in turn raised the question if the assumption made by the theory of a small perturbing defect structure placed on top of the magnetic layer is still justified. In addition, the dipolar field assumed by Landeros and Mills originating from stripe-like defects may significantly differ in its shape from the one created by the ripples. Furthermore, previous investigations suggested negligible dipolar fields at high wavelengths. Hence, the dipolar field configuration was of interest and has been explored using TEM holography and MFM measurements. A clear signature of dipolar fields was observed by MFM for rippled Py films with a wavelength of $\lambda = 222$ nm. The origin of these fields was determined by TEM investigations using holography. Cross-sectional images revealed an asymmetric ripple structure with ripple slopes of different length and sign as well as increasing asymmetry the greater the wavelength. Due to this, linear increasing branches are connected by quite narrow regions in which the film changes its orientation to match both, ascending and descending slope. The magnetization in turn follows the surface corrugation, which has been imaged and proven by TEM holography. Thereby, dipoles evolve at the film surface caused by imperfect parallel alignment along the surface modulation and the magnetization reorientation at the venue of both ripple branches. Also the stray fields have been imaged with TEM holography. In addition, from the TEM images the ripple profile was extracted and the magnetization configuration modeled using micromagnetic simulations to extract the exact shape of these dipolar fields and the underlying magnetization configuration. Both are in agreement with the experimental findings. With respect to the magnetic properties FMR measurements were performed for in-plane configuration and for the $f(H)$ dependence. Besides a planar reference sample rippled films with a modulation up to $\lambda = 103$ nm did not show any significant changes in intrinsic Gilbert damping α and g -factor. Compared to the epitaxially grown Fe on MgO the polycrystalline Py film does not exhibit a lattice mismatch and, therefore, strain and its relaxation does not influence intrinsic damping. Due to the chosen film thickness of 30 nm of Py PSSW modes evolve, which offered the possibility to determine the exchange stiffness and showed a slight dependence on the surface modulation for ripple wavelengths smaller than 47 nm. The magnetic anisotropy observed in this wavelength range was dominated, as expected, by the UMA as it was observed in the previous experiments.

Most important are the findings for rippled Py of $\lambda = 222$ nm and above. In these cases the frequency-dependent linewidths show a clear direction dependence. Here, a measurement with applied magnetic field parallel to the ripple wavefront showed the typical linear dependence caused by Gilbert damping as it was observed for any anisotropy direction of the reference and rippled samples below $\lambda = 222$ nm. In contrast, orienting the external magnetic field perpendicularly to the ripple wavefront a distinct linewidth peak evolves for $\lambda \geq 222$ nm that clearly is caused by two-magnon scattering. The peak frequency position and width can be understood using the theory of Landeros and Mills including the knowledge from the TEM investigations. In comparison to the stripe defects assumed in the theory the ripple modulation shows a significantly different dipolar stray field that does not exhibit sharp transitions at the defect boundaries but rather continuously changes along the surface modulation. Also, due to two branches with opposing slopes for the ripples no sharp defect width and periodicity can be determined but rather a continuous range develops that in turn leads to a superposition of occurring modes and, thus, to a linewidth peak and apparent line broadening. In addition, its position in frequency is determined by the average defect width—basically half the wavelength—matching the degenerate spin wave state in the dispersion relation. Hence, the peak position changes with increasing ripple wavelength to smaller frequencies. For a fixed wavelength the peak height can be decreased by simply turning the external field away from the perpendicular orientation, which in turn slightly increases the peak's frequency position. With respect to the angular dependence of the TMS process a frequency-dependent two-fold symmetry was observed matching the symmetry of the substrate, but it is deviating from conventionally known angular dependences. Indeed, direction-dependent deviations from conventional models are also found for the resonance position, indicating the influence of the TMS process on both, linewidth and resonance.

Summing up all these findings, rippled substrates offer a fast and easy method to effectively tailor the static and dynamic properties of single- and polycrystalline magnetic materials grown on top. This approach offers an additional UMA due to dipolar effects that also—given that the surface modulation matches degenerate states governed by the spin wave dispersion—activates TMS. Especially the latter can be utilized to design novel devices having a strongly increased in-plane linewidth within a certain frequency range, which simply can be switched off by changing the external magnetic field direction.

Future activities on subjects presented in this thesis will be mainly directed towards two-magnon scattering. While an improvement of ripple quality would increase the UMA strength—especially needed for the rippled MgO case to be relevant for applications in e. g. sensors—the main task is to further enhance the understanding of the direction-dependent defect-induced

magnon scattering process in polycrystalline thin films. Finally, intrinsic damping influenced by crystal anisotropy via dragging may be combined with extrinsic TMS contributions to further tailor dynamic magnetic properties. Therefore, it is mandatory to expand the understanding of TMS and to bring theory and experiment in line by either modifying the theoretical description matching the rippled case or by changing the sample layout. The latter has already been done by Barsukov *et al.* using ion implantation on Py films partially covered by resist stripes to shadow the ion beam. Using Cr^+ ions reduces the saturation magnetization in the irradiated area and thus forms stripe-like surface defects. The resist in turn was patterned by e-beam lithography, which makes the sample preparation time consuming and limited to small areas, but in return allows to freely chose defect width, periodicity, and height. By choosing this method remarkable good agreements between theory and experiment have been achieved recently with respect to peak position and width in the frequency-dependent linewidth, observing also high-order peaks. In addition, the $f(H)$ dependence does not show a single mode, but a splitting of resonances into several lines, as predicted by the theory of Landeros and Mills. For this case the spatial distribution of the magnetization in the occurring modes is of interest, which may be explored by micromagnetic simulations. In addition, the question needs to be answered if the observed linewidth broadening in the frequency dependence is due to energy transfer to degenerate states or simply caused by the superposition of two closely positioned modes. In this framework the intrinsic damping of the excited high-order modes needs to be addressed. Finally, the described sample structure can be improved further since ion implantation reduces M_s inhomogeneously within the implantation profile, whereas the theory assumes free space between the stripe defects, such as e. g. in magnonic crystals.

A Software toolbox for FMR data evaluation

In the framework of this thesis a data evaluation software was developed using *Matlab 7.8*, partly in collaboration with D. Ball. It covers all the functionality to process the data acquired by the VNA-FMR measurement such as measurement series varying the external magnetic field angle [$f_{\text{res}}(\theta_{\text{H}}, \varphi_{\text{H}})$ or $H_{\text{res}}(\theta_{\text{H}}, \varphi_{\text{H}})$] or magnetic field strength, respectively excitation frequency [$f(H)$]. The basic workflow of the developed toolbox is depicted in Fig. A.1 showing all the tools and its interplay.

As mentioned in sect. 2.2.2, FMR spectra can be obtained by two different measurement methods: (i) by sweeping the external magnetic field while keeping the frequency constant (field sweep) or (ii) by fixing the externally applied magnetic field and sweeping the microwave frequency (frequency sweep). The latter case ends with a set of measured data as well as reference data that have to be converted to the dynamic magnetic susceptibility by using an algorithm described by Bilzer *et al.* [140] in order to obtain correct linewidth values. To do so, *FMR_convert* is used taking the geometry of the stripline into account. After conversion the data are automatically handed over to the next tool, *Pseudocolor*, displaying it as a color-coded map depending on the chosen measurement series. If the data are obtained by field-sweep mode it can be directly loaded to *Pseudocolor*. The obtained color map gives a good overview on occurring modes, even for weak ones that cannot be evaluated in subsequent steps. Finally, plots and created data tables can be stored using a newly introduced file format (.cdat). This allows to load/modify it with third-party software, e. g. *OriginLab*, as well as to further evaluate the data by other tools described later in the text.

If a signal was observed in the color map the characteristic parameters of the resonances are extracted by *FMR_LoFi*. It is capable of fitting normal as well as complex Lorentzian curves (see sect. 3.1 and 3.3.2) to the spectra fully automatically and even superimposes the Lorentzian curves in case of overlapping resonances. Again, the data are stored in a special data format (.fdat files) allowing to load and modify it later on, but also to import it in third-party software. Additionally, .fdat files are recognized by *FMR_gFi* and *FMR_AngFi* handling the final evaluation steps.

To extract the direction-dependent g -factor (see section 5.2.1) of the sample *FMR_gFi* is

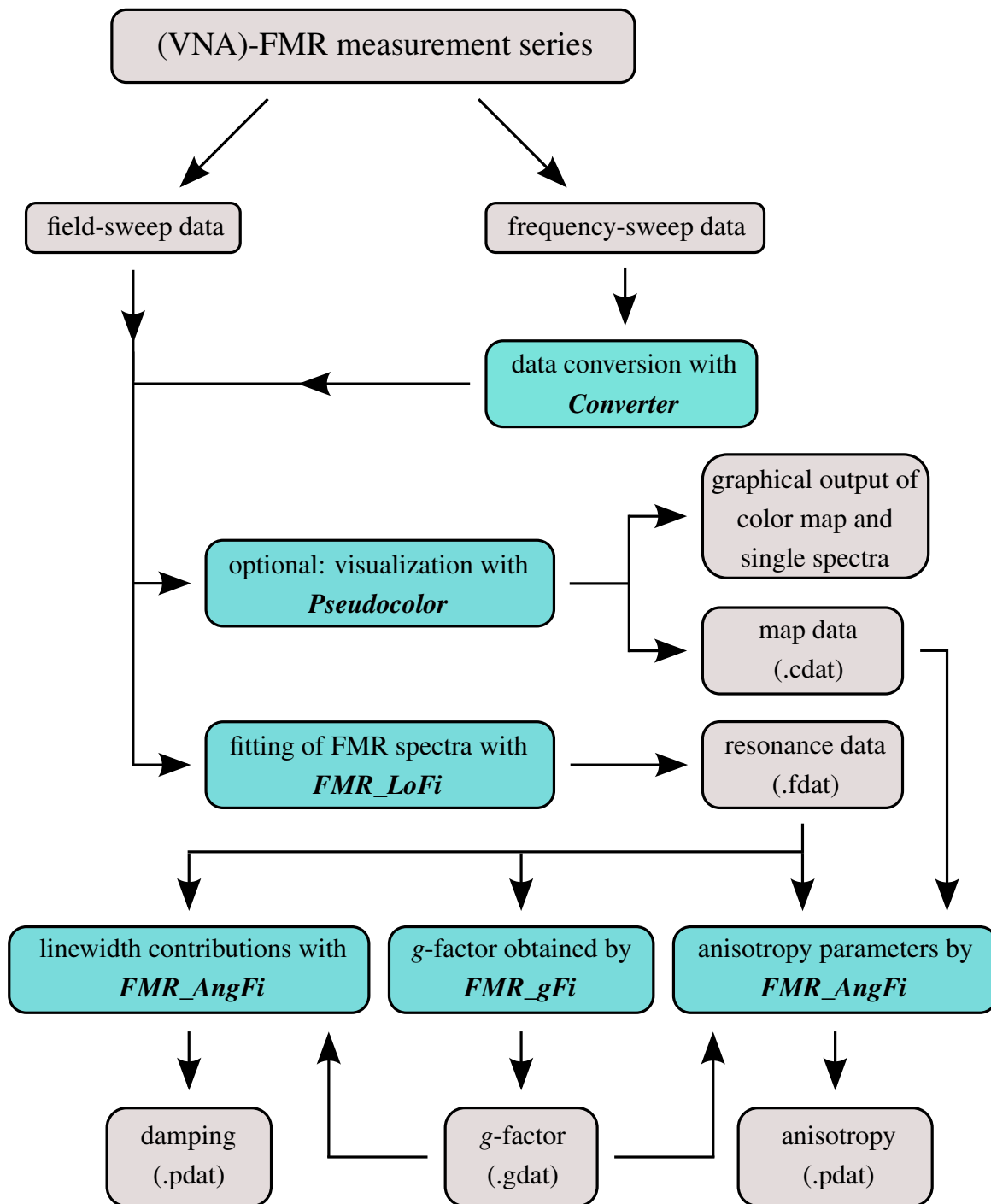


Figure A.1: Workflow of the developed toolbox showing included programs (bold face) and its interplay. As main output magnetic anisotropy and linewidth/damping parameters as well as the g -factor are obtained. Cyan colored elements highlight the toolbox components.

used, evaluating $f(H)$ curves recorded under fixed measurement geometries. The geometrical restriction to $f(H)$ curves allows to separate the g -factor from magnetic anisotropy contributions and, hence, reducing the error to the field and frequency uncertainties of the measurement.

Finally, .cdat, .fdat, and other text files that contain resonance data are used in *FMR_AngFi* to distinguish magnetic anisotropy contributions. While the .cdat approach is only a graphical approximation suitable for small signals (too small for fitting with *FMR_LoFi*) performed manually by the user, .fdat files are fitted fully automatic. Furthermore, results are stored in a *FMR_AngFi*-owned file format (.pdat), which allows modifications later on. In addition, .fdat files or any other text file containing linewidth data is used to determine linewidth contributions of the measurement. Both, anisotropy as well as linewidth can be evaluated for fixed [$f(H)$] or angle-dependent geometries (polar and azimuthal).

Additionally, the developed data evaluation toolbox contains some minor tools (not included in Fig. A.1) handling file renaming, phase shifting of the measured signal, and additional conversion steps used to test other operation modes of the VNA. A much more detailed explanation of the introduced tools can be found in the corresponding manuals (written by T. Schneider) covering the full workflow from raw data processing/visualization to final parameter extraction. By focusing on user-friendly automated evaluation algorithms these tools allow a fast evaluation and, hence, in combination with the fully automated measurement system, a high point density for each measurement. Screenshots of the tools are shown in Figs. A.2–A.6.

Subsequently, the most important features are summarized:

Converter:

- Conversion from complex S -parameters to dynamic susceptibility χ using the approach of Bilzer *et al.* [140]
- Parameter extraction from file names and automatic measurement geometry detection (polar, azimuthal) as well as sorting of spectra
- Angle-dependent adaption of sample length on CPW for azimuthal measurements
- Parameter extraction (microwave frequency/magnetic field or current and field angle) from file names (one file per recorded spectra) and, if necessary, conversion from current to magnetic field values
- Data and settings transfer to the *Pseudocolor* tool

Pseudocolor:

- Parameter extraction from file names and automatic measurement geometry detection as well as sorting of spectra

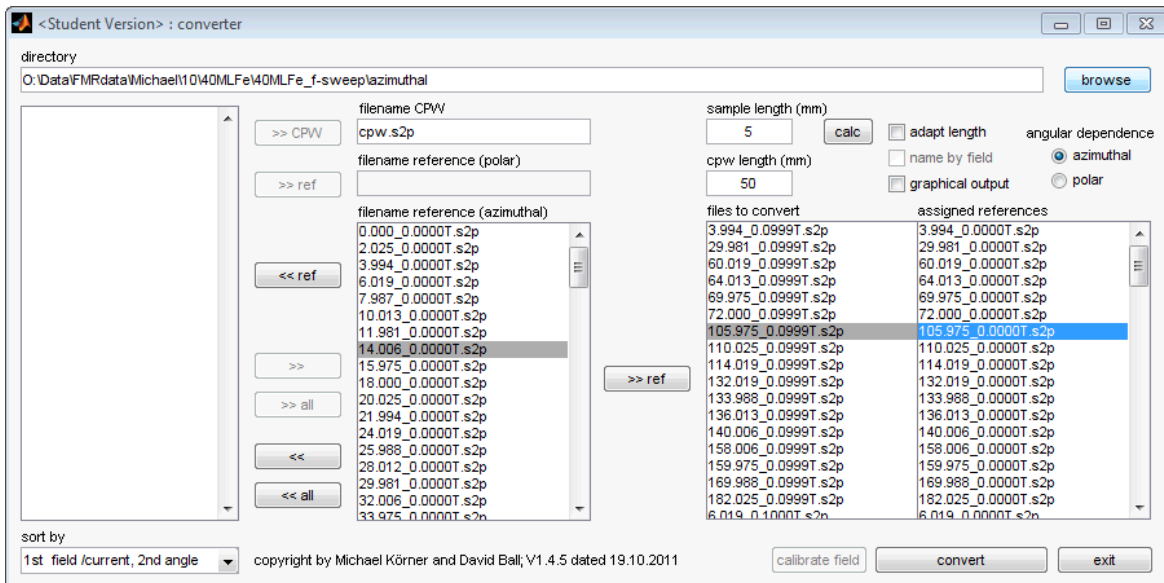


Figure A.2: Converter tool to calculate the dynamic susceptibility from the measured S -parameters obtained in the f -sweep mode.

- Calculation of absolute values for complex measurements
- Automatic measurement set detection (different sets may have different fixed parameters, e. g. angular dependence at different frequencies in H -sweep mode)
- Field axis averaging for H -sweep mode and calculation of standard deviation at each point (x axis has not exactly the same values for each spectrum)
- Display up to two color plots (e. g. real and imaginary part of a complex measurement or simply its absolute value)
- Plot modifications (labels, axes scaling and tics, contrast, brightness, manual exclusion of bad data points, level spectra to same offset, and color scheme)
- Graphical output as .png files (color plots, single spectra, deviation from averaged x axis)
- Data output as .cdat files (matrices for color plots)

FMR_LoFi:

- Parameter extraction from file names and automatic sorting of spectra
- Subtraction of background measurements, individually for each measured spectra

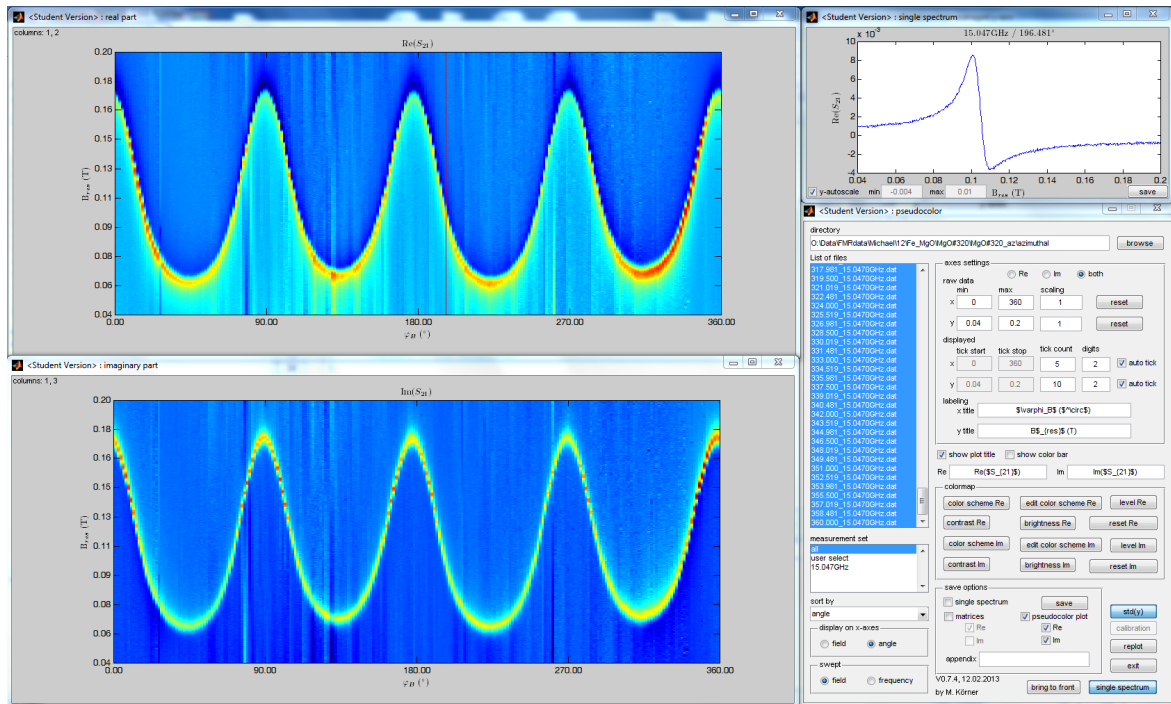


Figure A.3: Pseudocolor tool to display a whole set of measured data using a color code.

- Automatic estimation (three different options available) for initial fit values to initialize the fitting algorithm
- Fully automatized fit (robust fit possible as well as using an iterative approach)
- Selectable fit region
- Batch fit option that runs through whole measurement series and may abort automatically (e. g. in case of bad fit results)
- User-selectable parameter variation/fixation during automatic fit
- Model functions: single Lorentzian functions [based on Eqs. (3.2)–(3.5) as well as Eqs. (3.11), (3.12)] superimposed by a linear background as well as a superposition of two Lorentzian functions of the same type including a linear background
- Fitting of multiple modes in a single spectrum
- Manual modification of initial and final fit parameters via graphical or value editing
- Live plot of fitted resonance as well as a second user-selectable parameter, both for the chosen modes (all or a single one)
- Navigation from live plot data point to corresponding measured spectrum

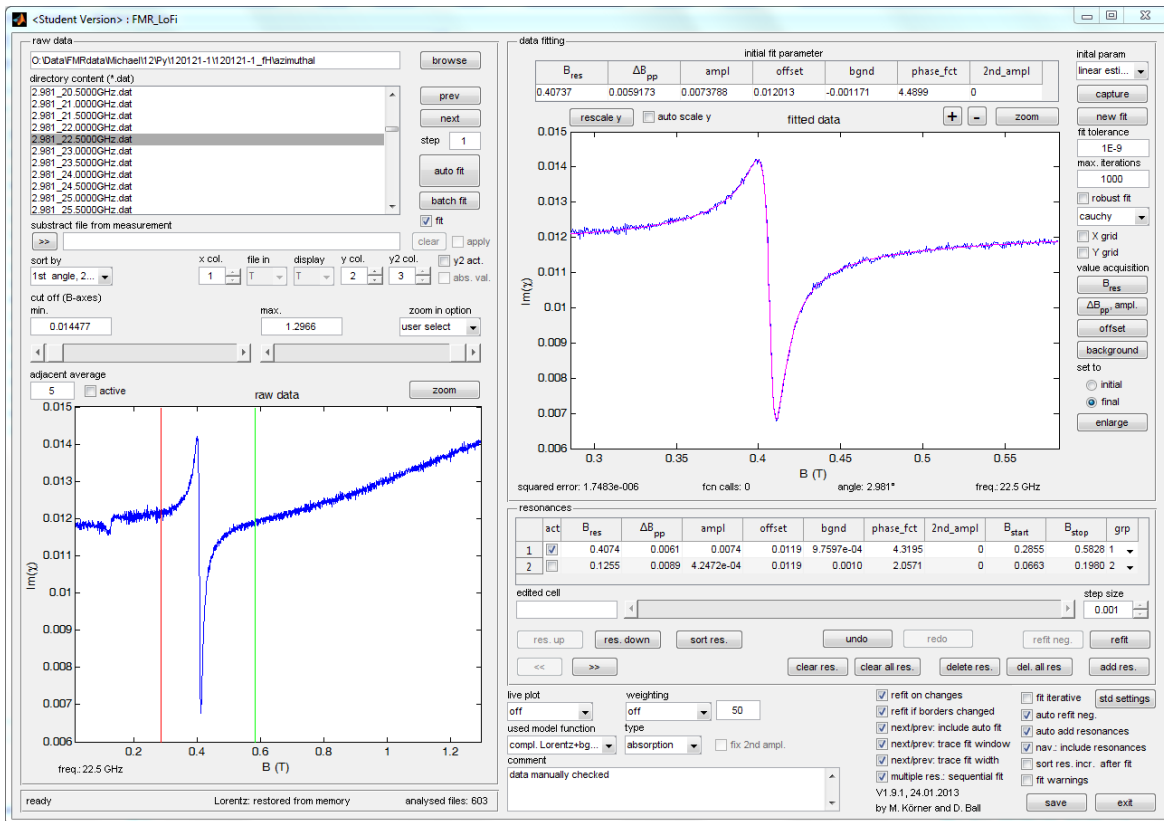


Figure A.4: *FMR_LoFi* tool to extract parameters like linewidth and resonance position for the acquired spectra.

- Shortcuts for enhanced data evaluation
- Automatic refit options for incorrect values (e. g. negative linewidth)
- Settings stored individually for each spectrum
- User-defined fit range, traceable in width and position when moving to the next spectrum
- Graphical output as .png files (single fits, live plots)
- Output of fit results as .fdat file (containing fit parameters and used options to fully reload the evaluation project)

FMR_gFi:

- Reads .fdat files (automatic column detection if .fdat files are used)
- Automatic measurement set detection and sorting of spectra

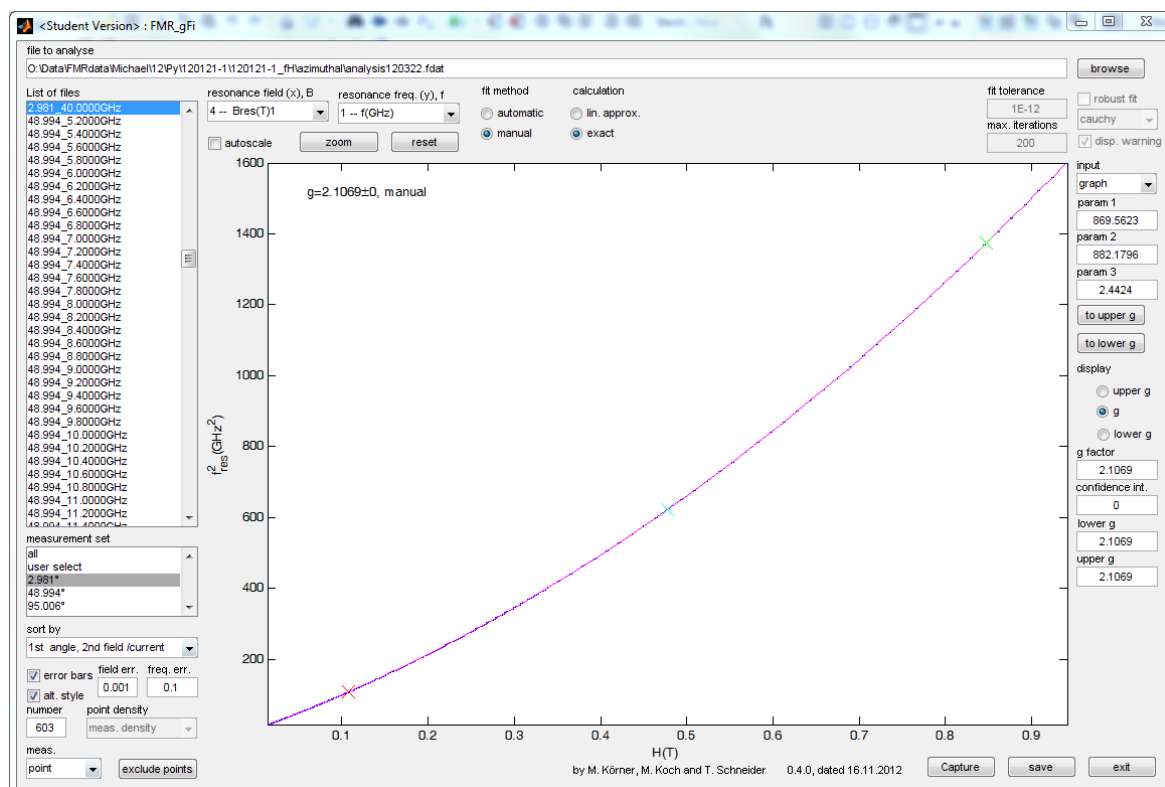


Figure A.5: *FMR_gFi* tool to calculate the g -factor for the obtained resonance positions in dependence of the external field.

- Automatic (robust fit available) as well as manual g -factor determination for linear approximation and exact (quadratic) solution
- Error for manual and automatic fit
- Manual exclusion of bad data points and selectable fit region
- Graphical output as .png file (measurement including fit)
- Data output as .gdat (containing results and options for fully reload)

FMR_AngFi:

- Reads .fdat (automatic column detection in case of .fdat files) and .cdat files
- Automatic measurement set detection, geometry, and sorting of points
- User-selectable fit range and manual exclusion of bad data points
- Included anisotropy models: tetragonal (including UMA) for some fixed geometries (also including spin wave energy and $k_{||} \neq 0$ modes), tetragonal for all geometries

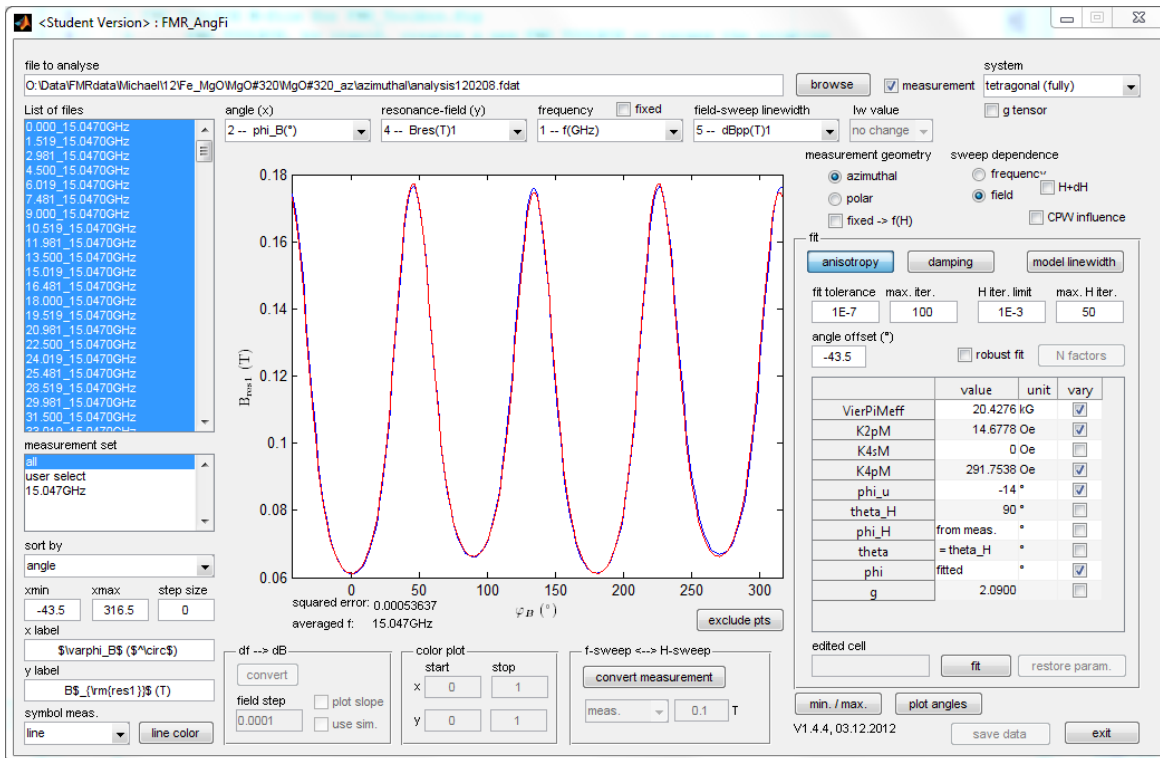


Figure A.6: *FMR_AngFi* tool to fit the linewidth as well as the resonance positions in angle- and frequency-dependent measurements to obtain linewidth and anisotropy parameters.

(including UMA, with and without demagnetization factors and interlayer exchange coupling), and hexagonal systems for all measurement geometries

- Automatic (robust fit available) as well as manual parameter adaption for angular and $f(H)$ dependences in f - and H -sweep mode and manual fit in color plot
- Calculation of magnetization equilibrium angles (in-plane, out-of-plane, or both)
- Linewidth evaluation including: inhomogeneous broadening, Gilbert damping, two-fold and four-fold TMS, and mosaicity under consideration of dragging
- Conversion from frequency- to field-sweep linewidth and resonance data
- Automatic determination of easy and hard axes directions in case of angle-dependent measurements
- Graphical output as .png file (measurement including fit, progress of equilibrium vs. expected saturation angles)
- Data output as .pdat file (contains results and settings for fully reload)

Bibliography

- [1] E. du Trémolet de Lacheisserie, D. Gignoux, and M. Schlenker, editors, “Magnetism Fundamentals”, Springer (2005).
- [2] I. S. Jacobs, “Role of Magnetism in Technology”, *J. Appl. Phys.* **40**, 917 (1969).
- [3] S. A. Wolf, D. D. Awschalom, R. A. Buhrman, J. M. Daughton, S. von Molnár, M. L. Roukes, A. Y. Chtchelkanova, and D. M. Treger, “Spintronics: A Spin-Based Electronics Vision for the Future”, *Science* **294**, 1488 (2001).
- [4] C. H. Marrows and B. J. Hickey, “New directions in spintronics”, *Phil. Trans. R. Soc. A* **369**, 3027 (2011).
- [5] M. N. Baibich, J. M. Broto, A. Fert, F. N. Van Dau, F. Petroff, P. Eitenne, G. Creuzet, A. Friederich, and J. Chazelas, “Giant Magnetoresistance of (001)Fe/(001)Cr Magnetic Superlattices”, *Phys. Rev. Lett.* **61**, 2472 (1988).
- [6] P. Grünberg, R. Schreiber, Y. Pang, M. B. Brodsky, and H. Sowers, “Layered Magnetic Structures: Evidence for Antiferromagnetic Coupling of Fe Layers across Cr Interlayers”, *Phys. Rev. Lett.* **57**, 2442 (1986).
- [7] M. P. Kostylev, A. A. Serga, T. Schneider, B. Leven, and B. Hillebrands, “Spin-wave logical gates”, *Appl. Phys. Lett.* **87**, 153501 (2005).
- [8] A. Khitun, M. Bao, and K. L. Wang, “Spin Wave Magnetic NanoFabric: A New Approach to Spin-Based Logic Circuitry”, *IEEE Trans. Magn.* **44**, 2141 (2008).
- [9] S. S. P. Parkin, K. P. Roche, M. G. Samant, P. M. Rice, R. B. Beyers, R. E. Scheuerlein, E. J. O’Sullivan, S. L. Brown, J. Bucchigano, D. W. Abraham, Y. Lu, M. Rooks, P. L. Trouilloud, R. A. Wanner, and W. J. Gallagher, “Exchange-biased magnetic tunnel junctions and application to nonvolatile magnetic random access memory (invited)”, *J. Appl. Phys.* **85**, 5828 (1999).
- [10] R. Skomski, “Simple Models of Magnetism”, Oxford University Press (2008).
- [11] E. Schlömann, “Demagnetizing Fields in Thin Magnetic Films Due to Surface Roughness”, *J. Appl. Phys.* **41**, 1617 (1970).

- [12] P. Bruno, “Dipolar magnetic surface anisotropy in ferromagnetic thin films with interfacial roughness”, *J. Appl. Phys.* **64**, 3153 (1988).
- [13] C.-R. Chang, “Influence of roughness on magnetic surface anisotropy in ultrathin films”, *J. Appl. Phys.* **72**, 596 (1992).
- [14] Y.-P. Zhao, G. Palasantzas, G.-C. Wang, and J. T. M. De Hosson, “Surface/interface-roughness-induced demagnetizing effect in thin magnetic films”, *Phys. Rev. B* **60**, 1216 (1999).
- [15] R. Arias and D. L. Mills, “Theory of roughness-induced anisotropy in ferromagnetic films: The dipolar mechanism”, *Phys. Rev. B* **59**, 11871 (1999).
- [16] C. A. F. Vaz, S. J. Steinmuller, and J. A. C. Bland, “Roughness-induced variation of magnetic anisotropy in ultrathin epitaxial films: The undulating limit”, *Phys. Rev. B* **75**, 132402 (2007).
- [17] L. Néel, “Sur un problème de magnétostatique relatif à des couches ferromagnétiques”, *C. R. Acad. Sci.* **255**, 1545 (1962).
- [18] L. Néel, “Sur un nouveau mode de couplage entre les aimantations de deux couches minces ferromagnétiques”, *C. R. Acad. Sci.* **255**, 1676 (1962).
- [19] J. Zhang and R. M. White, “Topological coupling in magnetic multilayer films”, *J. Appl. Phys.* **79**, 5113 (1996).
- [20] P. Fuchs, U. Ramsperger, A. Vaterlaus, and M. Landolt, “Roughness-induced coupling between ferromagnetic films across an amorphous spacer layer”, *Phys. Rev. B* **55**, 12546 (1997).
- [21] M. Körner, K. Lenz, M. O. Liedke, T. Strache, A. Mücklich, A. Keller, S. Facsko, and J. Fassbender, “Interlayer exchange coupling of Fe/Cr/Fe thin films on rippled substrates”, *Phys. Rev. B* **80**, 214401 (2009).
- [22] R. Arias and D. L. Mills, “Extrinsic contributions to the ferromagnetic resonance response of ultrathin films”, *Phys. Rev. B* **60**, 7395 (1999).
- [23] A. Azevedo, A. B. Oliveira, F. M. de Aguiar, and S. M. Rezende, “Extrinsic contributions to spin-wave damping and renormalization in thin Ni₅₀Fe₅₀ films”, *Phys. Rev. B* **62**, 5331 (2000).
- [24] P. Landeros and D. L. Mills, “Spin waves in periodically perturbed films”, *Phys. Rev. B* **85**, 054424 (2012).

- [25] K. Y. Guslienko, “Magnetic anisotropy in two-dimensional dot arrays induced by magnetostatic interdot coupling”, *Phys. Lett. A* **278**, 293 (2001).
- [26] S. Tacchi, M. Madami, G. Gubbiotti, G. Carlotti, H. Tanigawa, T. Ono, and M. P. Kostylev, “Anisotropic dynamical coupling for propagating collective modes in a two-dimensional magnonic crystal consisting of interacting squared nanodots”, *Phys. Rev. B* **82**, 024401 (2010).
- [27] J. Lindner and M. Farle, “Magnetic Anisotropy of Heterostructures”, in “Magnetic Heterostructures”, Springer Berlin / Heidelberg (2007).
- [28] B. K. Kuanr, R. E. Camley, and Z. Celinski, “Extrinsic contribution to Gilbert damping in sputtered NiFe films by ferromagnetic resonance”, *J. Magn. Magn. Mater.* **286**, 276 (2005).
- [29] C. P. Poole and H. A. Farach, editors, “Handbook of Electron Spin Resonance”, volume 2, Springer, Berlin (1999).
- [30] C. Vieu, F. Carcenac, A. Pépin, Y. Chen, M. Mejias, A. Lebib, L. Manin-Ferlazzo, L. Couraud, and H. Launois, “Electron beam lithography: resolution limits and applications”, *Appl. Surf. Sci.* **164**, 111 (2000).
- [31] R. M. Bradley and J. M. E. Harper, “Theory of ripple topography induced by ion bombardment”, *J. Vac. Sci. Technol. A* **6**, 2390 (1988).
- [32] J. Fassbender, T. Strache, M. O. Liedke, D. Markó, S. Wintz, K. Lenz, A. Keller, S. Facsko, I. Mönch, and J. McCord, “Introducing artificial length scales to tailor magnetic properties”, *New J. Phys.* **11**, 125002 (2009).
- [33] M. O. Liedke, B. Liedke, A. Keller, B. Hillebrands, A. Mücklich, S. Facsko, and J. Fassbender, “Induced anisotropies in exchange-coupled systems on rippled substrates”, *Phys. Rev. B* **75**, 220407 (2007).
- [34] F. Bisio, R. Moroni, F. B. de Mongeot, M. Canepa, and L. Mattera, “Isolating the Step Contribution to the Uniaxial Magnetic Anisotropy in Nanostructured Fe/Ag(001) Films”, *Phys. Rev. Lett.* **96**, 057204 (2006).
- [35] K. Zhang, F. Rotter, M. Uhrmacher, C. Ronning, J. Krauser, and H. Hofsäss, “Ion induced nanoscale surface ripples on ferromagnetic films with correlated magnetic texture”, *New J. Phys.* **9**, 29 (2007).
- [36] G. Czycholl, “Theoretische Festkörperphysik: Von den klassischen Modellen zu modernen Forschungsthemen”, second edition, Springer-Verlag (2004).

-
- [37] J. H. van Vleck, “On the Anisotropy of Cubic Ferromagnetic Crystals”, *Phys. Rev.* **52**, 1178 (1937).
- [38] H. J. F. Jansen, “Magnetic anisotropy in density-functional theory”, *Phys. Rev. B* **38**, 8022 (1988).
- [39] P. Bruno, “Physical origins and theoretical models of magnetic anisotropy”, in “Magnetismus von Festkörpern und Grenzflächen: 24. IFF–Ferienkurs”, R. Hölzle, editor, Forschungszentrum Jülich GmbH (1993).
- [40] S. Blügel, “Magnetische Anisotropie und Magnetostriktion (Theorie)”, in “Magnetische Schichtsysteme: 30. IFF–Ferienkurs”, R. Hölzle, editor, Forschungszentrum Jülich GmbH (1999).
- [41] P. A. M. Dirac, “The Quantum Theory of the Electron”, *Proc. R. Soc. Lond. A* **117**, 610 (1928).
- [42] A. Hubert and R. Schäfer, “Magnetic Domains: The Analysis of Magnetic Microstructures”, Springer Berlin Heidelberg (1998).
- [43] E. R. Callen and H. B. Callen, “Anisotropic magnetization”, *J. Phys. Chem. Solids* **16**, 310 (1960).
- [44] A. Aharoni, “Demagnetizing factors for rectangular ferromagnetic prisms”, *J. Appl. Phys.* **83**, 3432 (1998).
- [45] S. Chikazumi, “Physics of Ferromagnetism”, second edition, Oxford University Press (2010).
- [46] H. Brooks, “Ferromagnetic Anisotropy and the Itinerant Electron Model”, *Phys. Rev.* **58**, 909 (1940).
- [47] P. Bruno, “Tight-binding approach to the orbital magnetic moment and magnetocrystalline anisotropy of transition-metal monolayers”, *Phys. Rev. B* **39**, 865 (1989).
- [48] J. G. Gay and R. Richter, “Spin anisotropy of ferromagnetic slabs and overlayers (invited)”, *J. Appl. Phys.* **61**, 3362 (1987).
- [49] G. H. O. Daalderop, P. J. Kelly, and M. F. H. Schuurmans, “First-principles calculation of the magnetocrystalline anisotropy energy of iron, cobalt, and nickel”, *Phys. Rev. B* **41**, 11919 (1990).
- [50] G. H. O. Daalderop, P. J. Kelly, and F. J. A. den Broeder, “Prediction and confirmation of perpendicular magnetic anisotropy in Co/Ni multilayers”, *Phys. Rev. Lett.* **68**, 682 (1992).

- [51] J. G. Gay and R. Richter, "Spin Anisotropy of Ferromagnetic Films", *Phys. Rev. Lett.* **56**, 2728 (1986).
- [52] N. S. Akulov, "Über das magnetische Quadrupolmoment des Eisenatoms", *Z. Phys. A* **57**, 249 (1929).
- [53] G. Bihlmayer, "Reduced Dimensions II: Magnetic Anisotropy", in "Magnetism goes Nano: 36. IFF-Ferienkurs", S. Blügel, T. Brückel, and C. M. Schneider, editors, Forschungszentrum Jülich GmbH (2005).
- [54] T. L. Gilbert, "A phenomenological theory of damping in ferromagnetic materials", *IEEE Trans. Magn.* **40**, 3443 (2004).
- [55] J. Miltat, G. Albuquerque, and A. Thiaville, "An Introduction to Micromagnetics in the Dynamic Regime", in "Spin Dynamics in Confined Magnetic Structures I", B. Hillebrands and K. Ounadjela, editors, Springer Berlin / Heidelberg (2002).
- [56] J. K. Ha, R. Hertel, and J. Kirschner, "Micromagnetic study of magnetic configurations in submicron permalloy disks", *Phys. Rev. B* **67**, 224432 (2003).
- [57] C. L. Dennis, R. P. Borges, L. D. Buda, U. Ebels, J. F. Gregg, M. Hehn, E. Jouguelet, K. Ounadjela, I. Petej, I. L. Prejbeanu, and M. J. Thornton, "The defining length scales of mesomagnetism: a review", *J. Phys.: Condens. Matter* **14**, R1175 (2002).
- [58] S. V. Vonsovskii, editor, "Ferromagnetic Resonance", Pergamon Press (1966).
- [59] K. Baberschke, "Investigation of Ultrathin Ferromagnetic Films by Magnetic Resonance", in "Handbook of Magnetism and Advanced Magnetic Materials", H. Kronmüller and S. S. Parkin, editors, John Wiley & Sons, Ltd. (2007).
- [60] L. Landau and E. Lifshitz, "On the theory of magnetic permeability in ferromagnetic bodies", *Phys. Z. Sowjetunion* **8**, 153 (1935).
- [61] J. Mallinson, "On damped gyromagnetic precession", *IEEE Trans. Magn.* **23**, 2003 (1987).
- [62] F. Bloch, "Nuclear Induction", *Phys. Rev.* **70**, 460 (1946).
- [63] N. Bloembergen, "On the Ferromagnetic Resonance in Nickel and Supermalloy", *Phys. Rev.* **78**, 572 (1950).
- [64] N. Bloembergen and S. Wang, "Relaxation Effects in *Para* - and Ferromagnetic Resonance", *Phys. Rev.* **93**, 72 (1954).

- [65] K. Baberschke, “Ferromagnetic resonance in nanostructures, rediscovering its roots in paramagnetic resonance”, *J. Phys.: Conf. Ser.* **324**, 012011 (2011).
- [66] D. L. Mills and S. M. Rezende, “Spin Damping in Ultrathin Magnetic Films”, in “Spin Dynamics in Confined Magnetic Structures II”, B. Hillebrands and K. Ounadjela, editors, Springer Berlin / Heidelberg (2003).
- [67] C. Kittel, “Interpretation of Anomalous Larmor Frequencies in Ferromagnetic Resonance Experiment”, *Phys. Rev.* **71**, 270 (1947).
- [68] C. Kittel, “On the Theory of Ferromagnetic Resonance Absorption”, *Phys. Rev.* **73**, 155 (1948).
- [69] J. Smit and H. G. Beljers, “Ferromagnetic Resonance Absorption in $\text{BaFe}_{12}\text{O}_{19}$, a highly anisotropic crystal.”, *Philips Res. Rep.* **10**, 113 (1955).
- [70] H. Suhl, “Ferromagnetic Resonance in Nickel Ferrite Between One and Two Kilomegacycles”, *Phys. Rev.* **97**, 555 (1955).
- [71] L. Baselgia, M. Warden, F. Waldner, S. L. Hutton, J. E. Drumheller, Y. Q. He, P. E. Wigen, and M. Maryško, “Derivation of the resonance frequency from the free energy of ferromagnets”, *Phys. Rev. B* **38**, 2237 (1988).
- [72] D. D. Stancil and A. Prabhakar, “Spin Waves: Theory and Applications”, Springer (2009).
- [73] D. Polder, “VIII. On the theory of ferromagnetic resonance”, *Philos. Mag.* **40**, 99 (1949).
- [74] A. G. Gurevich and G. A. Melkov, “Magnetization Oscillations and Waves”, CRC Press (1996).
- [75] M. Sparks, “Ferromagnetic-Relaxation Theory”, McGraw-Hill, New York (1964).
- [76] S. O. Demokritov and B. Hillebrands, “Spinwaves in Laterally Confined Magnetic Structures”, in “Spin Dynamics in Confined Magnetic Structures I”, B. Hillebrands and K. Ounadjela, editors, Springer Berlin / Heidelberg (2002).
- [77] C. Herring and C. Kittel, “On the Theory of Spin Waves in Ferromagnetic Media”, *Phys. Rev.* **81**, 869 (1951).
- [78] C. E. Patton, “Magnetic excitations in solids”, *Physics Reports* **103**, 251 (1984).
- [79] M. J. Hurben and C. E. Patton, “Theory of magnetostatic waves for in-plane magnetized isotropic films”, *J. Magn. Magn. Mater.* **139**, 263 (1995).

- [80] B. A. Kalinikos and A. N. Slavin, “Theory of dipole-exchange spin wave spectrum for ferromagnetic films with mixed exchange boundary conditions”, *J. Phys. C: Solid State Phys.* **19**, 7013 (1986).
- [81] A. N. Slavin, S. O. Demokritov, and B. Hillebrands, “Nonlinear Spinwaves in One- and Two-Dimensional Magnetic Waveguides”, in “Spin Dynamics in Confined Magnetic Structures I”, B. Hillebrands and K. Ounadjela, editors, Springer Berlin / Heidelberg (2002).
- [82] A. A. Serga, A. V. Chumak, and B. Hillebrands, “YIG magnonics”, *J. Phys. D: Appl. Phys.* **43**, 264002 (2010).
- [83] R. W. Damon and J. R. Eshbach, “Magnetostatic modes of a ferromagnet slab”, *J. Phys. Chem. Solids* **19**, 308 (1961).
- [84] C. Kittel, “Excitation of Spin Waves in a Ferromagnet by a Uniform rf Field”, *Phys. Rev.* **110**, 1295 (1958) and *Phys. Rev.* **112**, 2139 (1958).
- [85] B. Heinrich, “Spin Relaxation in Magnetic Metallic Layers and Multilayers”, in “Ultrathin Magnetic Structures III: Fundamentals of Nanomagnetism”, J. A. C. Bland and B. Heinrich, editors, Springer-Verlag (2005).
- [86] K. Zakeri, J. Lindner, I. Barsukov, R. Meckenstock, M. Farle, U. von Horsten, H. Wende, W. Keune, J. Rucker, S. S. Kalarickal, K. Lenz, W. Kuch, K. Baberschke, and Z. Frait, “Spin dynamics in ferromagnets: Gilbert damping and two-magnon scattering”, *Phys. Rev. B* **76**, 104416 (2007) and *Phys. Rev. B* **80**, 059901 (2009).
- [87] S. S. Kalarickal, P. Krivosik, M. Wu, C. E. Patton, M. L. Schneider, P. Kabos, T. J. Silva, and J. P. Nibarger, “Ferromagnetic resonance linewidth in metallic thin films: Comparison of measurement methods”, *J. Appl. Phys.* **99**, 093909 (2006).
- [88] I. Barsukov, P. Landeros, R. Meckenstock, J. Lindner, D. Spoddig, Z.-A. Li, B. Krumme, H. Wende, D. L. Mills, and M. Farle, “Tuning magnetic relaxation by oblique deposition”, *Phys. Rev. B* **85**, 014420 (2012).
- [89] Y. V. Goryunov, N. N. Garif’yanov, G. G. Khaliullin, I. A. Garifullin, L. R. Tagirov, F. Schreiber, T. Mühge, and H. Zabel, “Magnetic anisotropies of sputtered Fe films on MgO substrates”, *Phys. Rev. B* **52**, 13450 (1995).
- [90] B. Heinrich, R. Urban, and G. Woltersdorf, “Magnetic relaxations in metallic multilayers”, *IEEE Trans. Magn.* **38**, 2496 (2002).

- [91] R. E. Camley and D. L. Mills, “Theory of microwave propagation in dielectric/magnetic film multilayer structures”, *J. Appl. Phys.* **82**, 3058 (1997).
- [92] W. S. Ament and G. T. Rado, “Electromagnetic Effects of Spin Wave Resonance in Ferromagnetic Metals”, *Phys. Rev.* **97**, 1558 (1955).
- [93] M. Kostylev, “Strong asymmetry of microwave absorption by bilayer conducting ferromagnetic films in the microstrip-line based broadband ferromagnetic resonance”, *J. Appl. Phys.* **106**, 043903 (2009).
- [94] B. Heinrich, D. Fraitová, and V. Kamberský, “The Influence of s-d Exchange on Relaxation of Magnons in Metals”, *Phys. Stat. Sol.* **23**, 501 (1967).
- [95] R. J. Elliott, “Theory of the Effect of Spin-Orbit Coupling on Magnetic Resonance in Some Semiconductors”, *Phys. Rev.* **96**, 266 (1954).
- [96] V. Kamberský, “On the Landau–Lifshitz relaxation in ferromagnetic metals”, *Can. J. Phys.* **48**, 2906 (1970).
- [97] J. Seib, D. Steiauf, and M. Fähnle, “Linewidth of ferromagnetic resonance for systems with anisotropic damping”, *Phys. Rev. B* **79**, 092418 (2009).
- [98] V. Kamberský, “On ferromagnetic resonance damping in metals”, *Czech. J. Phys. B* **26**, 1366 (1976).
- [99] V. Kamberský, “FMR linewidth and disorder in metals”, *Czech. J. Phys.* **34**, 1111 (1984).
- [100] R. C. LeCraw, E. G. Spencer, and C. S. Porter, “Ferromagnetic Resonance Line Width in Yttrium Iron Garnet Single Crystals”, *Phys. Rev.* **110**, 1311 (1958).
- [101] M. Sparks, R. Loudon, and C. Kittel, “Ferromagnetic Relaxation. I. Theory of the Relaxation of the Uniform Precession and the Degenerate Spectrum in Insulators at Low Temperatures”, *Phys. Rev.* **122**, 791 (1961).
- [102] M. J. Hurben, D. R. Franklin, and C. E. Patton, “Angle dependence of the ferromagnetic resonance linewidth in easy-axis and easy-plane single crystal hexagonal ferrite disks”, *J. Appl. Phys.* **81**, 7458 (1997).
- [103] M. J. Hurben and C. E. Patton, “Theory of two magnon scattering microwave relaxation and ferromagnetic resonance linewidth in magnetic thin films”, *J. Appl. Phys.* **83**, 4344 (1998).
- [104] R. D. McMichael, M. D. Stiles, P. J. Chen, and W. F. Egelhoff, “Ferromagnetic resonance linewidth in thin films coupled to NiO”, *J. Appl. Phys.* **83**, 7037 (1998).

- [105] R. Arias and D. L. Mills, “Extrinsic contributions to the ferromagnetic resonance response of ultrathin films”, *J. Appl. Phys.* **87**, 5455 (2000).
- [106] J. Lindner, K. Lenz, E. Kosubek, K. Baberschke, D. Spoddig, R. Meckenstock, J. Pelzl, Z. Frait, and D. L. Mills, “Non-Gilbert-type damping of the magnetic relaxation in ultrathin ferromagnets: Importance of magnon-magnon scattering”, *Phys. Rev. B* **68**, 060102 (2003).
- [107] R. P. Erickson and D. L. Mills, “Magnetic instabilities in ultrathin ferromagnets”, *Phys. Rev. B* **46**, 861 (1992).
- [108] D. Mills and R. Arias, “The damping of spin motions in ultrathin films: Is the Landau-Lifschitz-Gilbert phenomenology applicable?”, *Physica B* **384**, 147 (2006).
- [109] M. L. Spano and S. M. Bhagat, “Ferromagnetic resonance in amorphous alloys”, *J. Magn. Magn. Mater.* **24**, 143 (1981).
- [110] B. Heinrich, J. F. Cochran, and R. Hasegawa, “FMR linebroadening in metals due to two-magnon scattering”, *J. Appl. Phys.* **57**, 3690 (1985).
- [111] Z. Celinski and B. Heinrich, “Ferromagnetic resonance linewidth of Fe ultrathin films grown on a bcc Cu substrate”, *J. Appl. Phys.* **70**, 5935 (1991).
- [112] D. J. Twisselmann and R. D. McMichael, “Intrinsic damping and intentional ferromagnetic resonance broadening in thin Permalloy films”, *J. Appl. Phys.* **93**, 6903 (2003).
- [113] K. Lenz, H. Wende, W. Kuch, K. Baberschke, K. Nagy, and A. Janossy, “Two-magnon scattering and viscous Gilbert damping in ultrathin ferromagnets”, *Phys. Rev. B* **73**, 144424 (2006).
- [114] G. Woltersdorf and B. Heinrich, “Two-magnon scattering in a self-assembled nanoscale network of misfit dislocations”, *Phys. Rev. B* **69**, 184417 (2004).
- [115] R. D. McMichael, D. J. Twisselmann, and A. Kunz, “Localized Ferromagnetic Resonance in Inhomogeneous Thin Films”, *Phys. Rev. Lett.* **90**, 227601 (2003).
- [116] R. D. McMichael and P. Krivosik, “Classical model of extrinsic ferromagnetic resonance linewidth in ultrathin films”, *IEEE Trans. Magn.* **40**, 2 (2004).
- [117] R. D. McMichael, D. J. Twisselmann, J. E. Bonevich, A. P. Chen, W. F. Egelhoff, and S. E. Russek, “Ferromagnetic resonance mode interactions in periodically perturbed films”, *J. Appl. Phys.* **91**, 8647 (2002).

- [118] J. Fassbender, J. von Borany, A. Mücklich, K. Potzger, W. Möller, J. McCord, L. Schultz, and R. Mattheis, “Structural and magnetic modifications of Cr-implanted Permalloy”, *Phys. Rev. B* **73**, 184410 (2006).
- [119] W. Möller and W. Eckstein, “Tridyn – A TRIM simulation code including dynamic composition changes”, *Nucl. Instr. and Meth. in Phys. Res. B* **2**, 814 (1984), download available under <http://www.hzdr.de>.
- [120] W. Möller, W. Eckstein, and J. P. Biersack, “Tridyn-binary collision simulation of atomic collisions and dynamic composition changes in solids”, *Comput. Phys. Commun.* **51**, 355 (1988).
- [121] W. L. Chan and E. Chason, “Making waves: Kinetic processes controlling surface evolution during low energy ion sputtering”, *J. Appl. Phys.* **101**, 121301 (2007).
- [122] A. Keller and S. Facsko, “Ion-Induced Nanoscale Ripple Patterns on Si Surfaces: Theory and Experiment”, *Materials* **3**, 4811 (2010).
- [123] M. A. Makeev, R. Cuerno, and A.-L. Barabási, “Morphology of ion-sputtered surfaces”, *Nucl. Instr. and Meth. in Phys. Res. B* **197**, 185 (2002).
- [124] P. Sigmund, “A mechanism of surface micro-roughening by ion bombardment”, *J. Mater. Sci.* **8**, 1545 (1973).
- [125] D. Markó, K. Lenz, T. Strache, R. Kaltofen, and J. Fassbender, “Measuring the Saturation Magnetization in Samples With Unknown Magnetic Volume”, *IEEE Trans. Magn.* **46**, 1711 (2010).
- [126] Z. Celinski, K. B. Urquhart, and B. Heinrich, “Using ferromagnetic resonance to measure the magnetic moments of ultrathin films”, *J. Magn. Magn. Mater.* **166**, 6 (1997).
- [127] C. P. Poole, “Electron Spin Resonance: A Comprehensive Treatise on Experimental Techniques”, Interscience Publishers (1967).
- [128] M. Farle, “Ferromagnetic resonance of ultrathin metallic layers”, *Rep. Prog. Phys.* **61**, 755 (1998).
- [129] K. C. Gupta, R. Garg, I. Bahl, and P. Bhartia, “Microstrip Lines and Slotlines”, second edition, Artech House Inc (1996).
- [130] Agilent Technologies, “Network Analyzer Basics”, USA, 5965-7917E (2004).
- [131] Agilent Technologies, “S-Parameter Design”, USA, Application Note 154 (2000).
- [132] D. M. Pozar, “Microwave Engineering”, third edition, John Wiley & Sons, Inc (2005).

- [133] Agilent Technologies, “Service Guide E8362B, E8363B, E8364B Agilent Technologies PNA Series Microwave Network Analyzers”, USA, E8364-90026 (2008).
- [134] Agilent Technologies, “De-embedding and Embedding S-Parameter Networks Using a Vector Network Analyzer”, USA, Application Note 1364-1 (2004).
- [135] Agilent Technologies, “Applying Error Correction to Network Analyzer Measurements”, USA, Application Note 1287-3 (2002).
- [136] D. Markó, “Magnetostatics and Dynamics of Ion Irradiated NiFe/Ta Multilayer Films Studied by Vector Network Analyzer Ferromagnetic Resonance”, Ph.D. thesis, TU Dresden (2010).
- [137] D. Pain, M. Ledieu, O. Acher, A. L. Adenot, and F. Duverger, “An improved permeameter for thin film measurements up to 6 GHz”, *J. Appl. Phys.* **85**, 5151 (1999).
- [138] G. Counil, J.-V. Kim, T. Devolder, C. Chappert, K. Shigeto, and Y. Otani, “Spin wave contributions to the high-frequency magnetic response of thin films obtained with inductive methods”, *J. Appl. Phys.* **95**, 5646 (2004).
- [139] G. Counil, J.-V. Kim, K. Shigeto, Y. Otani, T. Devolder, P. Crozat, H. Hurdequint, and C. Chappert, “Inductive measurement of the high frequency permeability of a Permalloy thin film”, *J. Magn. Magn. Mater.* **272**, 290 (2004).
- [140] C. Bilzer, T. Devolder, P. Crozat, C. Chappert, S. Cardoso, and P. P. Freitas, “Vector network analyzer ferromagnetic resonance of thin films on coplanar waveguides: Comparison of different evaluation methods”, *J. Appl. Phys.* **101**, 074505 (2007).
- [141] C. Bilzer, “Susceptibilité micro-ondes de couches minces ferromagnétiques: métrologie et analyse de la dynamique de l’aimantation. (Microwave susceptibility of thin ferromagnetic films: metrology and insight into magnetization dynamics)”, Ph.D. thesis, Faculté des sciences d’Orsay, Université Paris-Sud 11 (2007).
- [142] W. B. Weir, “Automatic measurement of complex dielectric constant and permeability at microwave frequencies”, *Proc. IEEE* **62**, 33 (1974).
- [143] W. Barry, “A Broad-Band, Automated, Stripline Technique for the Simultaneous Measurement of Complex Permittivity and Permeability”, *IEEE Trans. Microw. Theory Tech.* **34**, 80 (1986).
- [144] I. Barsukov, F. M. Römer, R. Meckenstock, K. Lenz, J. Lindner, S. Hemken to Krax, A. Banholzer, M. Körner, J. Grebing, J. Fassbender, and M. Farle, “Frequency dependence of spin relaxation in periodic systems”, *Phys. Rev. B* **84**, 140410(R) (2011).

- [145] Anritsu, “Understanding Directivity”, USA, Application Note (2010).
- [146] O. Mosendz, B. Kardasz, D. S. Schmool, and B. Heinrich, “Spin dynamics at low microwave frequencies in crystalline Fe ultrathin film double layers using co-planar transmission lines”, *J. Magn. Magn. Mater.* **300**, 174 (2006).
- [147] I. Neudecker, G. Woltersdorf, B. Heinrich, T. Okuno, G. Gubbiotti, and C. H. Back, “Comparison of frequency, field, and time domain ferromagnetic resonance methods”, *J. Magn. Magn. Mater.* **307**, 148 (2006).
- [148] F. Zighem, Y. Roussigné, S.-M. Chérif, P. Moch, J. B. Youssef, and F. Paumier, “Magnetic properties of exchange biased and of unbiased oxide/permalloy thin layers: a ferromagnetic resonance and Brillouin scattering study”, *J. Phys.: Condens. Matter* **22**, 406001 (2010).
- [149] W. Dietrich and W. E. Proebster, “Millimicrosecond Magnetization Reversal in Thin Magnetic Films”, *J. Appl. Phys.* **31**, S281 (1960).
- [150] C. E. Patton, “Linewidth and Relaxation Processes for the Main Resonance in the Spin-Wave Spectra of Ni-Fe Alloy Films”, *J. Appl. Phys.* **39**, 3060 (1968).
- [151] Y. Ding, T. J. Klemmer, and T. M. Crawford, “A coplanar waveguide permeameter for studying high-frequency properties of soft magnetic materials”, *J. Appl. Phys.* **96**, 2969 (2004).
- [152] E. Moraitakis, L. Kompotiatis, M. Pissas, and D. Niarchos, “Permeability measurements of permalloy films with a broad band stripline technique”, *J. Magn. Magn. Mater.* **222**, 168 (2000).
- [153] B. K. Kuanr, R. E. Camley, and Z. Celinski, “Exchange bias of NiO/NiFe: Linewidth broadening and anomalous spin-wave damping”, *J. Appl. Phys.* **93**, 7723 (2003).
- [154] H. T. Nembach, T. J. Silva, J. M. Shaw, M. L. Schneider, M. J. Carey, S. Maat, and J. R. Childress, “Perpendicular ferromagnetic resonance measurements of damping and Landé g -factor in sputtered $(\text{Co}_2\text{Mn})_{1-x}\text{Ge}_x$ thin films”, *Phys. Rev. B* **84**, 054424 (2011).
- [155] K. J. Kennewell, M. Kostylev, N. Ross, R. Magaraggia, R. L. Stamps, M. Ali, A. A. Stashkevich, D. Greig, and B. J. Hickey, “Magnetization pinning at a Py/Co interface measured using broadband inductive magnetometry”, *J. Appl. Phys.* **108**, 073917 (2010).
- [156] O. Karlqvist, “Calculation of the magnetic field in the ferromagnetic layer of a magnetic drum”, *Trans. R. Inst. Tech. Stockholm* **86**, 3 (1954).

- [157] T. J. Silva, C. S. Lee, T. M. Crawford, and C. T. Rogers, “Inductive measurement of ultrafast magnetization dynamics in thin-film Permalloy”, *J. Appl. Phys.* **85**, 7849 (1999).
- [158] M. L. Schneider, A. B. Kos, and T. J. Silva, “Finite coplanar waveguide width effects in pulsed inductive microwave magnetometry”, *Appl. Phys. Lett.* **85**, 254 (2004).
- [159] M. L. Schneider, T. Gerrits, A. B. Kos, and T. J. Silva, “Gyromagnetic damping and the role of spin-wave generation in pulsed inductive microwave magnetometry”, *Appl. Phys. Lett.* **87**, 072509 (2005).
- [160] K. J. Kennewell, M. Kostylev, and R. L. Stamps, “Calculation of spin wave mode response induced by a coplanar microwave line”, *J. Appl. Phys.* **101**, 09D107 (2007).
- [161] N. S. Almeida and D. L. Mills, “Eddy currents and spin excitations in conducting ferromagnetic films”, *Phys. Rev. B* **53**, 12232 (1996).
- [162] F. Bisio, R. Moroni, F. B. de Mongeot, M. Canepa, and L. Mattera, “Tuning the magnetic anisotropy of ultrathin Fe/Ag(001) films from biaxial to uniaxial by ion sculpting”, *Appl. Phys. Lett.* **89**, 052507 (2006).
- [163] F. Büttner, K. Zhang, S. Seyffarth, T. Liese, H.-U. Krebs, C. A. F. Vaz, and H. Hofsäss, “Thickness dependence of the magnetic properties of ripple-patterned Fe/MgO(001) films”, *Phys. Rev. B* **84**, 064427 (2011).
- [164] R. Moroni, F. Bisio, F. Buatier de Mongeot, C. Boragno, and L. Mattera, “Kink contribution to the magnetic anisotropy of nanostructured ultrathin Co/Cu(001) and Fe/Ag(001) films”, *Phys. Rev. B* **76**, 214423 (2007).
- [165] H. Hofsäss, F. Rotter, M. Uhrmacher, K. Zhang, C. Ronning, and J. Krauser, “Sputter erosion of ferromagnetic thin films”, *Surf. Coat. Technol.* **201**, 8477 (2007).
- [166] K. Zhang, M. Uhrmacher, H. Hofsäss, and J. Krauser, “Magnetic texturing of ferromagnetic thin films by sputtering induced ripple formation”, *J. Appl. Phys.* **103**, 083507 (2008).
- [167] R. Moroni, D. Sekiba, F. Buatier de Mongeot, G. Gonella, C. Boragno, L. Mattera, and U. Valbusa, “Uniaxial Magnetic Anisotropy in Nanostructured *Co/Cu*(001): From Surface Ripples to Nanowires”, *Phys. Rev. Lett.* **91**, 167207 (2003).
- [168] A. Encinas-Oropesa and F. N. V. Dau, “Origin of magnetic anisotropy in thin films deposited on step-bunched substrates”, *J. Magn. Magn. Mater.* **256**, 301 (2002).

- [169] A. Berger, U. Linke, and H. P. Oepen, "Symmetry-induced uniaxial anisotropy in ultrathin epitaxial cobalt films grown on Cu(1 1 13)", *Phys. Rev. Lett.* **68**, 839 (1992).
- [170] D. S. Chuang, C. A. Ballentine, and R. C. O'Handley, "Surface and step magnetic anisotropy", *Phys. Rev. B* **49**, 15084 (1994).
- [171] Y. Z. Wu, C. Won, and Z. Q. Qiu, "Magnetic uniaxial anisotropy of Fe films grown on vicinal Ag(001)", *Phys. Rev. B* **65**, 184419 (2002).
- [172] C. Boeglin, S. Stanescu, J. P. Deville, P. Ohresser, and N. B. Brookes, "In-plane magnetocrystalline anisotropy observed on Fe/Cu(111) nanostructures grown on stepped surfaces", *Phys. Rev. B* **66**, 014439 (2002).
- [173] K. V. Sarathlal, D. Kumar, and A. Gupta, "Growth study of Co thin film on nanorippled Si(100) substrate", *Appl. Phys. Lett.* **98**, 123111 (2011).
- [174] K. V. Sarathlal, D. Kumar, V. Ganesan, and A. Gupta, "In-situ study of magnetic thin films on nanorippled Si (100) substrates", *Appl. Surf. Sci.* **258**, 4116 (2012).
- [175] Y. Park, E. E. Fullerton, and S. D. Bader, "Growth-induced uniaxial in-plane magnetic anisotropy for ultrathin Fe deposited on MgO(001) by oblique-incidence molecular beam epitaxy", *Appl. Phys. Lett.* **66**, 2140 (1995).
- [176] O. Durand, J. R. Childress, P. Galtier, R. Bisaro, and A. Schuhl, "Origin of the uniaxial magnetic anisotropy in Fe films grown by molecular beam epitaxy", *J. Magn. Magn. Mater.* **145**, 111 (1995).
- [177] J. H. Wolfe, R. K. Kawakami, W. L. Ling, Z. Q. Qiu, R. Arias, and D. L. Mills, "Roughness induced in plane uniaxial anisotropy in ultrathin Fe films", *J. Magn. Magn. Mater.* **232**, 36 (2001).
- [178] S. van Dijken, G. Di Santo, and B. Poelsema, "Influence of the deposition angle on the magnetic anisotropy in thin Co films on Cu(001)", *Phys. Rev. B* **63**, 104431 (2001).
- [179] J. L. Bubendorff, S. Zabrocki, G. Garreau, S. Hajjar, R. Jaafar, D. Berling, A. Mehdaoui, C. Pirri, and G. Gewinner, "Origin of the magnetic anisotropy in ferromagnetic layers deposited at oblique incidence", *Europhys. Lett.* **75**, 119 (2006).
- [180] C. Teichert, "Self-organized semiconductor surfaces as templates for nanostructured magnetic thin films", *Appl. Phys. A* **76**, 653 (2003).
- [181] S. Iwatsubo and M. Naoe, "Surface morphology and uniaxial magnetic anisotropy of Fe films deposited by dual ion beam sputtering", *IEEE Trans. Magn.* **37**, 2298 (2001).

- [182] C. Teichert, J. Barthel, H. P. Oepen, and J. Kirschner, “Fabrication of nanomagnet arrays by shadow deposition on self-organized semiconductor substrates”, *Appl. Phys. Lett.* **74**, 588 (1999).
- [183] B. Borca, O. Fruchart, P. David, A. Rousseau, and C. Meyer, “Kinetic self-organization of trenched templates for the fabrication of versatile ferromagnetic nanowires”, *Appl. Phys. Lett.* **90**, 142507 (2007).
- [184] M. O. Liedke, M. Körner, K. Lenz, M. Fritzsche, M. Ranjan, A. Keller, E. Čížmár, S. A. Zvyagin, S. Facsko, K. Potzger, J. Lindner, and J. Fassbender, “Crossover in the surface anisotropy contributions of ferromagnetic films on rippled Si surfaces”, *Phys. Rev. B* **87**, 024424 (2013).
- [185] Y. P. Zhao, G. C. Wang, and T.-M. Lu, “Characterization of Amorphous and Crystalline Rough Surface – Principles and Applications: 37 (Experimental Methods in the Physical Sciences)”, Academic Press (2001).
- [186] I. Horcas, R. Fernandez, J. M. Gomez-Rodriguez, J. Colchero, J. Gomez-Herrero, and A. M. Baro, “WSXM: A software for scanning probe microscopy and a tool for nanotechnology”, *Rev. Sci. Instrum.* **78**, 013705 (2007).
- [187] “Gwyddion”, available under <http://gwyddion.net/>.
- [188] H.-N. Yang, Y.-P. Zhao, A. Chan, T.-M. Lu, and G.-C. Wang, “Sampling-induced hidden cycles in correlated random rough surfaces”, *Phys. Rev. B* **56**, 4224 (1997).
- [189] J. D. Kiely and D. A. Bonnell, “Quantification of topographic structure by scanning probe microscopy”, *J. Vac. Sci Technol. B* **15**, 1483 (1997).
- [190] Y.-P. Zhao, H.-N. Yang, G.-C. Wang, and T.-M. Lu, “Diffraction from diffusion-barrier-induced mound structures in epitaxial growth fronts”, *Phys. Rev. B* **57**, 1922 (1998).
- [191] E. Schlömann and R. I. Joseph, “Surface-Roughness-Induced Demagnetizing Fields in Thin Films and Their Influence Upon the Approach to Saturation”, *J. Appl. Phys.* **41**, 1336 (1970).
- [192] G. Palasantzas, Y.-P. Zhao, J. Hosson, and G.-C. Wang, “Roughness effects on magnetic properties of thin films”, *Physica B* **283**, 199 (2000).
- [193] B. Ziberi, F. Frost, T. Höche, and B. Rauschenbach, “Ripple pattern formation on silicon surfaces by low-energy ion-beam erosion: Experiment and theory”, *Phys. Rev. B* **72**, 235310 (2005).

- [194] J. Zhang and R. M. White, "Topological coupling in spin valve type multilayers", *IEEE Trans. Magn.* **32**, 4630 (1996).
- [195] R. A. Reck and D. L. Fry, "Orbital and Spin Magnetization in Fe-Co, Fe-Ni, and Ni-Co", *Phys. Rev.* **184**, 492 (1969).
- [196] J. Lindner, I. Barsukov, C. Raeder, C. Hassel, O. Posth, R. Meckenstock, P. Landeros, and D. L. Mills, "Two-magnon damping in thin films in case of canted magnetization: Theory versus experiment", *Phys. Rev. B* **80**, 224421 (2009).
- [197] S.-B. Choe and S.-C. Shin, "Generic method for calculations of magnetic dipolar anisotropy energy in rough thin films", *J. Magn. Magn. Mater.* **221**, 255 (2000).
- [198] M. R. Scheinfein, "LLG Micromagnetic Simulator", available under <http://llgmicro.home.mindspring.com>.
- [199] S. Blundell, "Magnetism in Condensed Matter", Oxford University Press (2001).
- [200] T. Kanaji, K. Asano, and S. Nagata, "Behaviour of impurity atoms and adsorbed oxygen atoms on (001) face of iron epitaxial film", *Vacuum* **23**, 55 (1973).
- [201] H. Fuke, A. Sawabe, and T. Mizoguchi, "Structural and Magnetic Properties of (001) Fe Films", *Jpn. J. Appl. Phys.* **32**, L1137 (1993).
- [202] C. M. Boubeta, J. L. Costa-Krämer, and A. Cebollada, "Epitaxy, magnetic and tunnel properties of transition metal/MgO(001) heterostructures", *J. Phys.: Condens. Matter* **15**, R1123 (2003).
- [203] B. Heinrich, K. B. Urquhart, A. S. Arrott, J. F. Cochran, K. Myrtle, and S. T. Purcell, "Ferromagnetic-resonance study of ultrathin bcc Fe(100) films grown epitaxially on fcc Ag(100) substrates", *Phys. Rev. Lett.* **59**, 1756 (1987).
- [204] M. Stampanoni, A. Vaterlaus, M. Aeschlimann, and F. Meier, "Magnetism of Epitaxial bcc Iron on Ag(001) Observed by Spin-Polarized Photoemission", *Phys. Rev. Lett.* **59**, 2483 (1987).
- [205] K. B. Hathaway and G. A. Prinz, "First-Order Magnetic Phase Transitions in Fe", *Phys. Rev. Lett.* **47**, 1761 (1981).
- [206] G. A. Prinz, G. T. Rado, and J. J. Krebs, "Magnetic properties of single-crystal 110 iron films grown on GaAs by molecular beam epitaxy (invited)", *J. Appl. Phys.* **53**, 2087 (1982).
- [207] J. J. Krebs, F. J. Rachford, P. Lubitz, and G. A. Prinz, "Ferromagnetic resonance studies of very thin epitaxial single crystals of iron", *J. Appl. Phys.* **53**, 8058 (1982).

- [208] M. O. Liedke, M. Körner, K. Lenz, F. Grossmann, S. Facsko, and J. Fassbender, “Magnetic anisotropy engineering: Single-crystalline Fe films on ion eroded ripple surfaces”, *Appl. Phys. Lett.* **100**, 242405 (2012).
- [209] M. Henzler and W. Göpel, “Oberflächenphysik des Festkörpers”, second edition, B. G. Teubner Stuttgart (1994).
- [210] K. Heinz, “LEED and DLEED as modern tools for quantitative surface structure determination”, *Rep. Prog. Phys.* **58**, 637 (1995).
- [211] E. Fawcett, “Spin-density-wave antiferromagnetism in chromium”, *Rev. Mod. Phys.* **60**, 209 (1988).
- [212] A. N. Anisimov, M. Farle, P. Pouloupoulos, W. Platow, K. Baberschke, P. Isberg, R. Wäppling, A. M. N. Niklasson, and O. Eriksson, “Orbital Magnetism and Magnetic Anisotropy Probed with Ferromagnetic Resonance”, *Phys. Rev. Lett.* **82**, 2390 (1999).
- [213] A. J. P. Meyer and G. Asch, “Experimental g' and g Values of Fe, Co, Ni, and Their Alloys”, *J. Appl. Phys.* **32**, S330 (1961).
- [214] A. Scherz, H. Wende, P. Pouloupoulos, J. Lindner, K. Baberschke, P. Blomquist, R. Wäppling, F. Wilhelm, and N. B. Brookes, “Induced V and reduced Fe moments at the interface of Fe/V(001) superlattices”, *Phys. Rev. B* **64**, 180407 (2001).
- [215] J. R. Fermin, A. Azevedo, F. M. de Aguiar, B. Li, and S. M. Rezende, “Ferromagnetic resonance linewidth and anisotropy dispersions in thin Fe films”, *J. Appl. Phys.* **85**, 7316 (1999).
- [216] G. Counil, J.-V. Kim, T. Devolder, P. Crozat, C. Chappert, and A. Cebollada, “Magnetic anisotropy of epitaxial MgO/Fe/MgO films studied by network analyzer ferromagnetic resonance”, *J. Appl. Phys.* **98**, 023901 (2005).
- [217] P. Landeros, private communication (2012).
- [218] P. Landeros, R. E. Arias, and D. L. Mills, “Two magnon scattering in ultrathin ferromagnets: The case where the magnetization is out of plane”, *Phys. Rev. B* **77**, 214405 (2008).
- [219] P. F. Miceli, C. J. Palmstrøm, and K. W. Moyses, “X-ray scattering study of lattice relaxation in ErAs epitaxial layers on GaAs”, *Appl. Phys. Lett.* **58**, 1602 (1991).
- [220] D. O. Smith, “Static and Dynamic Behavior of Thin Permalloy Films”, *J. Appl. Phys.* **29**, 264 (1958).

- [221] S. Schäfer, N. Pachauri, C. K. A. Mewes, T. Mewes, C. Kaiser, Q. Leng, and M. Pakala, “Frequency-selective control of ferromagnetic resonance linewidth in magnetic multilayers”, *Appl. Phys. Lett.* **100**, 032402 (2012).
- [222] L. Lu, J. Young, M. Wu, C. Mathieu, M. Hadley, P. Krivosik, and N. Mo, “Tuning of magnetization relaxation in ferromagnetic thin films through seed layers”, *Appl. Phys. Lett.* **100**, 022403 (2012).
- [223] G. Möllenstedt and H. Düker, “Beobachtungen und Messungen an Biprisma-Interferenzen mit Elektronenwellen”, *Z. Phys.* **145**, 377 (1956).
- [224] A. Tonomura, T. Matsuda, J. Endo, T. Arii, and K. Mihama, “Holographic interference electron microscopy for determining specimen magnetic structure and thickness distribution”, *Phys. Rev. B* **34**, 3397 (1986).
- [225] R. E. Dunin-Borkowski, M. R. McCartney, D. J. Smith, and S. S. P. Parkin, “Towards quantitative electron holography of magnetic thin films using in situ magnetization reversal”, *Ultramicroscopy* **74**, 61 (1998).
- [226] M. R. McCartney and D. J. Smith, “Electron Holography: Phase Imaging with Nanometer Resolution”, *Annu. Rev. Mater. Res.* **37**, 729 (2007).
- [227] H. Lichte and M. Lehmann, “Electron holography—basics and applications”, *Rep. Prog. Phys.* **71**, 016102 (2008).
- [228] F. A. M. Ramírez, editor, “Holography - Different Fields of Application”, InTech (2011).
- [229] M. Donahue and D. Porter, “The Object Oriented MicroMagnetic Framework (OOMMF) project at ITL/NIST”, available under <http://math.nist.gov/oommf/>.
- [230] M. D. de Sihues, C. A. Durante-Rincón, and J. R. Fermin, “A ferromagnetic resonance study of NiFe alloy thin films”, *J. Magn. Magn. Mater.* **316**, e462 (2007).
- [231] J. P. Nibarger, R. Lopusnik, Z. Celinski, and T. J. Silva, “Variation of magnetization and the Landé g factor with thickness in Ni–Fe films”, *Appl. Phys. Lett.* **83**, 93 (2003).

Publications

Articles

- M. Körner, K. Lenz, M. Fritzsche, R. A. Gallardo, A. Mücklich, S. Facsko, J. Lindner, P. Landeros, and J. Fassbender
“Two-magnon scattering in Permalloy thin films due to rippled substrates”
submitted to Phys. Rev. B (2013)
- R. A. Gallardo, K. Lenz, A. Banholzer, M. Körner, J. Lindner, J. Fassbender, and P. Landeros
“Ferromagnetic resonance response of thin films with one- and two-dimensional patterned arrays of periodic perturbations”
submitted to Phys. Rev. B (2013)
- M. O. Liedke, M. Körner, K. Lenz, M. Fritzsche, M. Ranjan, A. Keller, E. Čížmár, S. Zviagin, S. Facsko, K. Potzger, and J. Fassbender
“Crossover in the surface anisotropy contributions of ferromagnetic films on rippled Si surfaces”
Phys. Rev. B **87**, 024424 (2013)
- S. Wintz, C. Bunce, A. Neudert, M. Körner, T. Strache, M. Buhl, A. Erbe, S. Gemming, J. Raabe, C. Quitmann, and J. Fassbender
“Topology and origin of effective spin meron pairs in ferromagnetic multilayer elements”
Phys. Rev. Lett. **110**, 177201 (2013)
- S. Wintz, C. Bunce, A. Banholzer, M. Körner, T. Strache, R. Mattheis, J. McCord, J. Raabe, C. Quitmann, A. Erbe, and J. Fassbender
“Interlayer coupled spin vortex pairs and their response to external magnetic fields”
Phys. Rev. B **85**, 224420 (2012)
- S. Wintz, T. Strache, M. Körner, C. Bunce, A. Banholzer, I. Mönch, R. Mattheis, J. Raabe, C. Quitmann, J. McCord, A. Erbe, K. Lenz, and J. Fassbender

- “Control of vortex pair states by post- deposition interlayer exchange coupling modification”
Phys. Rev. B **85**, 134417 (2012)
- M. O. Liedke, M. Körner, K. Lenz, F. Grossmann, S. Facsco, and J. Fassbender
“Magnetic Anisotropy Engineering: Single-crystalline Fe Films on Self- organized Ripple Surfaces”
Appl. Phys. Lett. **100**, 242405 (2012)
 - I. Barsukov, F. M. Römer, R. Meckenstock, K. Lenz, J. Lindner, S. Hemken To Krax, A. Banholzer, M. Körner, J. Grebing, J. Fassbender, and M. Farle
“Frequency dependence of spin relaxation in periodic systems”
Phys. Rev. B **84**, 140410(R) (2011)
 - S. Wintz, T. Strache, M. Körner, M. Fritzsche, D. Markó, I. Mönch, R. Mattheis, J. Raabe, C. Quitmann, J. McCord, A. Erbe, and J. Fassbender
“Direct observation of antiferromagnetically oriented spin vortex states in magnetic multilayer elements”
Appl. Phys. Lett. **98**, 232511 (2011), erratum: Appl. Phys. Lett. **99**, 149901 (2011)
 - A. Puzic, T. Korhonen, B. Kalantari, J. Raabe, C. Quitmann, P. Juellig, L. Bommer, D. Goll, G. Schuetz, S. Wintz, T. Strache, M. Körner, D. Markó, C. Bunce, and J. Fassbender
“Photon Counting System for Time- resolved Experiments in Multibunch Mode”
Synchrotron Radiation News **23**, 26 (2010)
 - M. Körner, K. Lenz, M. O. Liedke, T. Strache, A. Muücklich, A. Keller, S. Facsco, and J. Fassbender
“Interlayer Exchange Coupling of Fe/Cr/Fe Thin Films on Rippled Substrate”
Phys. Rev. B **80**, 214401 (2009)

Talks

- “Morphology induced magnetic anisotropy and damping in thin films”
Seminar talk at Lawrence Berkeley National Lab, Berkeley (CA), USA (2012)
- “Morphology induced magnetic anisotropy and damping in thin films”
Seminar talk at HGST, a Western Digital company, San Jose (CA), USA (2012)
- “Morphology induced magnetic anisotropy and damping in thin films”
Seminar talk at IBM Almaden Research Center, San Jose (CA), USA (2012)

- M. Körner, K. Lenz, M. Fritzsche, S. Facsko, and J. Fassbender
“Morphology induced two-magnon scattering in thin NiFe films”
INTERMAG 2012, IEEE International Magnetism Conference, Vancouver, Canada (2012), including a travel grant and a “Student Best Presentation Award” nomination
- M. Körner, K. Lenz, A. Banholzer, J. Grebing, I. Barsukov, F. M. Römer, J. Lindner, M. Farle, and J. Fassbender
“Extrinsically controlled spin relaxation in NiFe thin films induced by a periodic scattering potential”
Frühjahrstagung der Deutschen Physikalischen Gesellschaft (DGP), Berlin, Germany (2012)
- M. O. Liedke, M. Körner, K. Lenz, T. Strache, A. Shalimov, M. Ranjan, S. Facsko, J. McCord, and J. Fassbender
“Magnetic anisotropy engineering: single crystalline Fe films on ripple surfaces”
Intermag 2011, IEEE International Magnetism Conference, Taipei, Taiwan (2011)
- M. Körner, K. Lenz, M. O. Liedke, T. Strache, A. Keller, S. Facsko, and J. Fassbender
“Morphology Induced Magnetic Phenomena”
Seminar talk at TU München, Garching, Germany (2010)
- M. Körner, M. O. Liedke, T. Strache, S. Dzenisevich, S. Keller, S. Facsko, and J. Fassbender
“Influence of Rippled Substrate Morphology on the Interlayer Exchange Coupling in Fe/Cr/Fe Thin Films”
Frühjahrstagung der Deutschen Physikalischen Gesellschaft (DGP), Dresden, Germany (2009)

Posters

- M. Körner, K. Lenz, M. Fritzsche, S. Facsko, and J. Fassbender
“Morphology induced two-magnon scattering in thin NiFe films”
International Colloquium on Magnetic Films and Surfaces (ICMFS), Shanghai, China (2012)
- M. Körner, I. Barsukov, F. M. Römer, K. Lenz, R. Meckenstock, S. Hemken To Krax, A. Banholzer, J. Grebing, J. Lindner, M. Farle, and J. Fassbender
“Frequency dependence of spin relaxation in periodic systems”
International Colloquium on Magnetic Films and Surfaces (ICMFS), Shanghai, China (2012)

- M. Körner, M. O. Liedke, K. Lenz, M. Ranjan, M. Fritzsche, S. Facsko, J. Fassbender, U. von Hörsten, B. Krumme, and H. Wende
“Morphology Induced Magnetic Anisotropy of Thin Films Deposited on Nanoscale Ripple Substrates”
IEEE Magnetics Society Summer School, New Orleans, USA (2011)
- M. Körner, M. O. Liedke, K. Lenz, M. Ranjan, M. Fritzsche, S. Facsko, J. Fassbender, U. von Hörsten, B. Krumme, and H. Wende
“Morphology Induced Magnetic Anisotropy of Thin Films Deposited on Nanoscale Ripple Substrates”
Frühjahrstagung der Deutschen Physikalischen Gesellschaft (DGP), Dresden, Germany (2011)
- M. Körner, M. O. Liedke, T. Strache, S. Dzenisevich, A. Keller, S. Facsko, K. Lenz, and J. Fassbender
“Tailoring the Magnetic Coupling of Fe/Cr/Fe Trilayers by Using Substrates with Nanometer Scale Ripples”
Nanofair 2010, 8th International Nanotechnology Symposium, Dresden, Germany (2010)
- M. Körner, K. Lenz, M. O. Liedke, T. Strache, A. Mücklich, A. Keller, S. Facsko, and J. Fassbender
“Influence of Rippled Substrate Morphology on the Interlayer Exchange Coupling in Fe/Cr/Fe Thin Films”
Nanoscale Modification of Surfaces and Thin Films (workshop), Rathen, Germany (2009)

In case of talks and posters only self-presented contributions are listed.

Acknowledgments

Of course, all the works presented would not have been possible without the help of many people contributing! To those I would like to express my thanks:

- Prof. Dr. Jürgen Faßbender for giving me the opportunity to pursue my research at the HZDR, the support, and discussions
- Prof. Dr. Joachim Wosnitza for refereeing my dissertation
- Dr. Kilian Lenz, my supervisor who was always available for discussions and solving problems, for teaching me FMR, carefully reviewing my thesis/publications, and for the great support and supervision
- Dr. Jürgen Lindner for lots of discussions and support during the final part of my work
- Dr. Maciej Oskar Liedke for giving me an introduction in AFM, MFM, MOKE, and MBE as well as for the excellent collaboration concerning experiments on ripples
- Prof. Dr. Pedro Landeros for the great collaboration and support on numerous questions on the theory of two-magnon scattering
- Andreas Henschke for the excellent and fast technical support in every situation
- Rodolfo E. Gallardo for giving me an insight in the theory of two-magnon scattering
- Dr. Arndt Mücklich for the TEM investigations
- Dr. Artem Shalimov for the XRD experiments
- Tobias Schneider for the assistance of some FMR measurements, testing the *Matlab* tools and finding/fixing some “undocumented features”, writing the manuals, and finally taking over the programming
- Dr. Adrian Keller, Dr. Mukesh Ranjan, and Fabian Grossmann for providing ripple substrates
- Dr. Stefan Facsko for discussions on the subject of ripples
- Monika Fritzsche for the ripple and lamella preparation

- Falk Röder for the holography measurement and great collaboration to visualize the dipolar fields and magnetization
- Markus Koch for assisting in *Matlab* programming
- Ingolf Winkler and Frank Ludewig for the ion irradiation
- Sven Stienen for the introduction and support with *OOMMF*
- Sebastian Wintz for the introduction to *LLG micromagnetics* and the possibility to join some great measurement trips to Switzerland
- Dr. David Ball for the support on programming and the funny time in our office and on business trips
- Dr. Christine Baumgart for the great support in various situations, numerous after work activities, and inspiring coffee breaks
- Dr. Christopher Bunce for support and after work activities
- Dr. Alina Maria Deac for networking and support

In addition, I would like to thank all members of the FWIN division and the FWIN-D junior research group for the friendly and cooperative atmosphere, from which I benefited and which I enjoyed a lot. I would also like to thank the public relations and school laboratory teams for their cooperations. The financial support from the DFG (grant No. FA 314/6-1) is gratefully acknowledged.

Last but not least, I would like to thank my flat mates for their patience and support during writing my thesis and especially I would like to thank my parents for their great support in every situation possible!

—Thank you—

Erklärung

Diese Dissertation wurde am Institut für Ionenstrahlphysik und Materialforschung des Helmholtz-Zentrums Dresden-Rossendorf e. V. unter der wissenschaftlichen Betreuung von Prof. Dr. Jürgen Faßbender angefertigt.

Hiermit versichere ich, dass ich die vorliegende Arbeit ohne unzulässige Hilfe Dritter und ohne Benutzung anderer als der angegebenen Hilfsmittel angefertigt habe; die aus fremden Quellen direkt oder indirekt übernommenen Gedanken sind als solche kenntlich gemacht. Die Arbeit wurde bisher weder im Inland noch im Ausland in gleicher oder ähnlicher Form einer anderen Prüfungsbehörde vorgelegt.

Ich versichere weiterhin, dass bislang keine Promotionsverfahren stattgefunden haben.

Ich erkenne die Promotionsordnung der Fakultät Mathematik und Naturwissenschaften an der Technischen Universität Dresden vom 23.02.2011 an.

Dresden, 07. Mai 2013

(Michael Körner)